PHOTOMETRIC ANALYSES AND ATTITUDE ESTIMATION OF INACTIVE BOX-WING GEOSYNCHRONOUS SATELLITES

ANALYSE PHOTOMÉTRIQUE ET ESTIMATION DE L'ORIENTATION DE SATELLITES GÉOSYNCHRONES INACTIFS DE FORME 'BOX-WING'

A Thesis Submitted to the Division of Graduate Studies
of the Royal Military College of Canada

by

Michael Anthony Earl, MSc

In Partial Fulfillment of the Requirements for the Degree of
Doctor of Philosophy

May 2017

This thesis is dedicated to those who have significantly supported me throughout my journeys:

Ms. Mary Theresa Earl

Major Anthony Lloyd Earl

Mr. Lowell O. Christensen

LCol Philip W. Somers

Dr. Thomas J. Racey

Mr. Paul G. Comision

Ms. Jane Elizabeth Yaeger

My deepest gratitude.

ACKNOWLEDGEMENTS

ABSTRACT

Earl, Michael Anthony

Doctor of Philosophy

Royal Military College of Canada

May 2017

**Photometric Analyses and Attitude Estimation
of Inactive Box-Wing Geosynchronous Satellites**

Supervisor: Gregg A. Wade, Ph.D.

Determining the attitude dynamics of non-operational box-wing geosynchronous satellites using ground-based observations can be difficult because of their small apparent motion with respect to the Earth's rotation and to the Sun's position. Due to their very large solar panels, these satellites are especially susceptible to solar radiation pressure disturbance torques. Because of these torques, some of these satellites might experience constantly varying spin periods and spin axis orientations. The torques will vary due to the Earth's orbit motion and due to the short or long term satellite orientation variation with respect to the Sun and other, possibly significant, light flux sources (such as the Earth and the Moon).

For the first time, a long term and high temporal resolution significant broadband photometric survey of 11 non-operational box-wing geosynchronous satellites has been conducted. Spin periods, angular accelerations, and light curve morphologies have been inferred from each observation in order to qualitatively determine and compare how each satellites' attitude dynamics are varying over the short term and the long term. These observations have qualitatively confirmed that the attitude dynamics of these satellites are diverse with respect to one another. Some of these satellites have exhibited consistently short spin periods of less than 1000 seconds. Other satellites have longer spin periods of between 1000 seconds and 5000 seconds. Other satellites have significantly variable spin periods of between 200 seconds and 3000 seconds. Finally, other satellites have such complex light curves that a spin period determination was very difficult or was inconclusive.

A previously suggested relationship between a box-wing satellite's spin period variation amplitude and its average spin period has been found not to fit the new data acquired in the 11-satellite survey. However, a very strong relationship between Telstar-401's power spectrum ratio (PSR) and its spin period variation has been observed. This is the first time that a quantitative relationship has been established between a box-wing satellite's attitude variation (suggested by the light curve morphology) and its spin variation.

The Echostar-2 satellite was selected for spin axis orientation estimation because its light curves suggested the most stable spin axis variation relative to those of the other 10 satellites. It was found that Echostar-2's spin axis remained within 30 degrees of the North Celestial Pole (for prograde rotation) or within 30 degrees of the South Celestial Pole (for retrograde rotation). Echostar-2's spin axis was also observed to have moved approximately 180 degrees in right ascension between September and March (and between March and September) 2012-2015, throughout the survey time span. This motion suggested a spin axis precession about an angular momentum vector that was roughly oriented about the North Celestial Pole (or the South Celestial Pole).

A simulation of Echostar-2's angular acceleration and spin period variation was conducted for a time spanning over 10 years from the date of the first observation. The simulation was based on a numerical modeling of the solar radiation pressure torques affecting Echostar-2 over each single spin period within the 10-year time scale. The simulated angular acceleration and spin period variations compared well with the observations. The model successfully simulated the general shapes of the

angular acceleration curve and spin period variation curve. The model also successfully simulated the decreasing average spin period and the decreasing spin period variation amplitude. Most importantly, the model simulated the areas of spin period inflection (between a variation maximum and minimum), in which the angular acceleration magnitude would decrease for several days before increasing again.

RÉSUMÉ

Earl, Michael Anthony

Docteur en philosophie
Collège militaire royal du Canada

mai 2017

**Analyse photométrique et estimation de l'orientation
de satellites géosynchrones inactifs de forme 'box-wing'**

Superviseur: Gregg A. Wade, Ph.D.

La détermination de la dynamique de l'orientation des satellites géosynchrones inactifs à l'aide d'observations terrestres peut être difficile en raison de leurs petits mouvements apparents par rapport à la rotation de la Terre et à la position du Soleil. En raison de leurs très grands panneaux solaires, ces satellites sont particulièrement sensibles aux perturbations causées par la pression du rayonnement solaire. Par conséquent, certains de ces satellites peuvent connaître des périodes de rotation variables ainsi que des orientations variables de leurs axes de rotation. Les couples varieront en raison du mouvement orbital de la Terre et du fait de la variation à court ou à long terme de l'orientation du satellite par rapport au Soleil et d'autres sources - possiblement significatifs - de flux lumineux, comme la Terre et la Lune.

Cette thèse décrit une première étude photométrique à bande large à long terme et à haute résolution temporelle de 11 satellites géosynchrones non-opérationnels. Les périodes de rotation, les accélérations angulaires et les morphologies de leurs courbes de lumière ont été déduites à partir de chaque observation afin d'évaluer la manière dont la dynamique de l'orientation de chaque satellite varie à court terme et à long terme. Ces observations ont confirmé qualitativement que la dynamique d'attitude de ces satellites est très diversifiée l'une par rapport à l'autre. Selon ces observations, certains satellites ont affiché régulièrement des périodes de rotation courtes de moins de 1000 secondes tandis que d'autres satellites ont des périodes de rotation plus longues, entre 1000 secondes et 5000 secondes. Par contre, d'autres satellites ont des périodes de rotation significativement variables entre 200 secondes et 3000 secondes. Enfin, d'autres satellites ont des courbes de lumière si complexes que la détermination d'une période de rotation était très difficile ou n'était pas concluante.

Une relation, précédemment suggérée, entre l'amplitude de la variation de la période de rotation des satellites et leurs périodes de rotation moyennes a été trouvée d'être en contradiction avec les nouvelles données acquises dans cette étude. Cependant, une relation très forte entre le rapport de spectre de puissance de Telstar-401 et la variation de sa période de rotation a été observée. C'est la première fois qu'une relation quantitative a été établie entre la variation de l'orientation d'un satellite (inféré selon la morphologie de sa courbe de lumière) et la variation de sa période de rotation.

Le satellite Echostar-2 a été sélectionné pour l'estimation de l'orientation de son axe de rotation car ses courbes de lumière ont suggéré que son axe de de rotation variait de manière la plus stable parmi les 11 satellites observés. Cette étude a constaté que l'axe de rotation du satellite Echostar-2 a resté à moins de 30 degrés du pôle Nord céleste (pour une rotation prograde) ou à moins de 30 degrés du pôle Sud céleste (pour une rotation rétrograde). Selon les observations, l'axe de rotation du satellite Echostar-2 s'est déplacé d'environ 180 degrés en ascension droite entre septembre et mars ainsi qu'entre mars et septembre 2012-2015. Cette motion a suggéré une précession de l'axe de rotation autour d'un vecteur de moment angulaire qui était à peu prés orienté au pôle Nord céleste (ou le pôle Sud céleste).

Une simulation de l'accélération angulaire du satellite Echostar-2 et de l'évolution de sa période de rotation pendant une période de plus de 10 ans a été effectuée. La simulation a été basée sur une modélisation numérique des couples de pression de rayonnement solaire affectant Echostar-2 sur chaque période de rotation unique dans l'échelle de temps de 10 ans. Les variations simulées de l'accélération angulaire et de la période de rotation se comparent bien aux observations. Le modèle a reproduit avec succès les formes générales de la courbe de l'accélération angulaire et de la courbe de variation de la période de rotation. Le modèle a également reproduit avec succès la période de rotation décroissante à long terme, et l'amplitude des variations de la période de rotation à court terme. En plus, le modèle a simulé les zones d'inflexion de la période de rotation (entre une variation maximale et minimale), dans laquelle la grandeur d'accélération angulaire diminue pendant plusieurs jours avant de reprendre.

CO-AUTHORSHIP STATEMENT

All of the satellite observations and scientific research discussed within this thesis was performed exclusively by the PhD candidate and primary author, Mr. Michael A. Earl. Mr. Earl performed all of the writing of the thesis and the three research papers within, with the exception of some French translations for the title page and Résumé sections.

A number of data analysis procedures were suggested by the PhD candidate's thesis advisor, Dr. Gregg A. Wade. Examples include: suggesting Lomb-Scargle periodogram analysis of satellite light curves and suggesting the development and comparison of the power spectrum ratios extracted from the satellite light curves to investigate the light curve morphology quantitatively.

This entire thesis, including the three research papers contained within, were thoroughly reviewed by Dr. Gregg A. Wade. Dr. Wade provided editing suggestions concerning significant portions of this thesis. Dr. Wade is listed as a co-author in all three of the papers contained within.

Additional advice for thesis preparation and research paper preparation was provided by Dr. Konstantin Kabin (assistant professor), Maj. Donald Bédard PhD (assistant professor), and LCol (retd.) Philip W. Somers (adjunct professor); all at the Royal Military College of Canada.

TABLE OF CONTENTS

LIST OF TABLES

LIST OF FIGURES

NOMENCLATURE

$^{\circ}$C	degrees Celsius
$<>$	if negative, value between brackets is considered zero
a	cube side length
A	original coordinate matrix before transformation
A'	final coordinate matrix after transformation
A	solar panel area
α	equatorial right ascension coordinate
α_{b}	right-handed azimuthal body frame angle from x_{b} axis
α_{eq}	equatorial right ascension coordinate of surface normal unit vector
$\alpha_{\text{n(ps)}}$	equatorial right ascension coordinate of normal; solar panel 'p', side 's'
α_{L}	equatorial right ascension coordinate of angular momentum vector
$\dot{\alpha}_{\text{L}}$	time derivative of α_{L}
α_{obs}	equatorial right ascension coordinate of observer viewed by satellite
α_{PAB}	equatorial right ascension coordinate of phase angle bisector
α_{PAB1}	equatorial right ascension coordinate of first phase angle bisector
α_{PAB2}	equatorial right ascension coordinate of second phase angle bisector
α_{sat}	equatorial right ascension coordinate of satellite from observer
α_{spin}	equatorial right ascension coordinate of spin axis
α_{spin1}	equatorial right ascension coordinate of first spin axis orientation
α_{spin2}	equatorial right ascension coordinate of second spin axis orientation
$\alpha_{\text{spin(p)}}$	equatorial right ascension coordinate of prograde spin axis
$\alpha_{\text{spin(r)}}$	equatorial right ascension coordinate of retrograde spin axis
α_{sun}	equatorial right ascension coordinate of the Sun
$\alpha_{\tau\text{tot}}$	equatorial right ascension coordinate of total torque vector
α_{ω}	right-handed azimuthal spin frame angle from x_{ω} axis
b	histogram spin percentage bin width
B	first Euler rotation matrix
B	histogram bin number
β	original azimuthal coordinate before transformation
β'	final azimuthal coordinate after transformation
β_1	the half angle of the phase angle at time t_1
β_2	the half angle of the phase angle at time t_2
β_{sun}	ecliptical latitude coordinate of the Sun
c	speed of light in vacuum
c	value of histogram bin center position
C	second Euler rotation matrix
γ	original elevation coordinate before transformation
γ	angle between satellite spin axis unit vector and net torque vector
γ'	final elevation coordinate after transformation
d	intensity of diffusely reflected light
d	dish indicator (1 or 2)
dd	day of month
dd1	day of month: first observation
dd2	day of month: second observation
D	specular reflectance distribution function
D	third Euler rotation matrix
δ	equatorial declination coordinate

$\delta_{1,s}$	Kronecker Delta comparing '1' with solar panel side number
$\delta_{2,s}$	Kronecker Delta comparing '2' with solar panel side number
δ_b	elevation angle from body frame x-y plane toward z_b axis
δ_{eq}	equatorial declination coordinate of surface normal unit vector
$\delta_{n(ps)}$	equatorial declination coordinate of normal; solar panel 'p', side 's'
δ_L	equatorial declination coordinate of angular momentum vector
δ_{obs}	equatorial declination coordinate of observer viewed by satellite
δ_{PAB}	equatorial declination coordinate of phase angle bisector
δ_{PAB1}	equatorial declination coordinate of first phase angle bisector
δ_{PAB2}	equatorial declination coordinate of second phase angle bisector
δ_{sat}	equatorial declination coordinate of satellite from observer
δ_{spin}	equatorial declination coordinate of spin axis
δ_{spin1}	equatorial declination coordinate of first spin axis orientation
δ_{spin2}	equatorial declination coordinate of second spin axis orientation
$\delta_{spin(p)}$	equatorial declination coordinate of prograde spin axis
$\delta_{spin(r)}$	equatorial declination coordinate of retrograde spin axis
δ_{sun}	equatorial declination coordinate of the Sun
δ_ω	elevation angle from spin frame x-y plane toward z_ω axis
Δt	temporal difference
$\delta_{\tau tot}$	equatorial declination coordinate of total torque vector
ΔT	temporal difference between synodic and sidereal spin periods
ΔT_p	ΔT from a prograde spin axis
ΔT_r	ΔT from a retrograde spin axis
e	orbit eccentricity
ϵ	cross-residual (broadband magnitude difference)
ϵ	obliquity of the ecliptic plane
ϵ	spin angle between satellite synodic and sidereal spin periods
ϵ_B	residual of simulated and observed broadband magnitudes
ϵ_i	cross-residual of ith light curve data point
η	angle between surface normal and observer
frac	keep only decimal component of determined value
F	Fresnel reflectance function
$\vec{F}_{ps}$	instantaneous force on solar panel 'p', side 's'
ϕ	Euler rotation angle: first coordinate rotation about original z-axis
ϕ_b	Euler rotation angle: first rotation about z_b-axis
ϕ_{ps}	angle between Sun and solar panel 'p', side 's' unit vector
Φ_s	solar irradiance at 1 Astronomical Unit from the Sun
ϕ_ω	Euler rotation angle: first rotation about z_ω-axis
G	light masking function (self-shadowing)
hh	hours
θ	Euler rotation angle: second rotation about intermediate x-axis
θ_b	Euler rotation angle: second rotation about intermediate x-axis
θ_ω	Euler rotation angle: second rotation about intermediate x-axis
i	cube side indicator (1 to 6)
i	orbit inclination
i	individual element
I	moment of inertia tensor
I_i	sunlight incident on surface
$I_{ic(i)}$	sunlight intensity incident on cube side i

$I_{\text{id(ds)}}$	sunlight intensity incident on dish d, side s
$I_{\text{is(ps)}}$	sunlight intensity incident on solar panel p, side s
I_{r}	sunlight intensity reflected from a surface
$I_{\text{rc(i)}}$	sunlight intensity reflected from cube side i
$I_{\text{rd(ds)}}$	sunlight intensity reflected from dish d, side s
$I_{\text{rs(ps)}}$	sunlight intensity reflected from solar panel p, side s
$I_{\text{r(tot)}}$	total sunlight intensity reflected from all box-wing surfaces
I_{xx}	moment of inertia about x_{b}-axis
I_{yy}	moment of inertia about y_{b}-axis
I_{zz}	moment of inertia about z_{b}-axis
j	individual element
J	inverse cost function
J	inverse of the sum of the squares of magnitude residuals
J	Julian reference frame
l_{p}	length of solar panel
l_{tot}	total length of box-wing (wing span)
L	angular momentum magnitude
L_{bx}	body frame x component of angular momentum magnitude
L_{by}	body frame y component of angular momentum magnitude
L_{bz}	body frame z component of angular momentum magnitude
L_{x}	inertial frame x component of angular momentum magnitude
L_{y}	inertial frame y component of angular momentum magnitude
L_{z}	inertial frame z component of angular momentum magnitude
$\vec{\text{L}}$	angular momentum vector
λ	wavelength
λ_{sun}	ecliptical longitude coordinate of the Sun
m_{aveobs}	observed average broadband magnitude in histogram bin
m_{b}	brightness: broadband magnitude
m_{B}	broadband magnitude coordinate of a light curve's data point
m_{BOL}	satellite mass after orbit insertion (beginning of life)
m_{box}	satellite central cube mass
m_{dry}	satellite dry mass (no on board fuel remaining)
m_{fBOL}	satellite fuel mass after orbit insertion (beginning of life)
m_{fEOL}	satellite fuel mass at end of life
m_{obs}	observed broadband magnitude
m_{p}	satellite single solar panel mass
m_{sim}	simulated broadband magnitude
m_{tot}	total satellite mass
mm	month of year
μ	surface smoothness factor
$\mu_{\text{c(i)}}$	surface smoothness factor for cube side i
$\mu_{\text{s(ps)}}$	surface smoothness factor for solar panel p, side s
$\mu_{\text{d(ds)}}$	surface smoothness factor for dish d, side s
n	orbit mean motion
$\hat{n}$	surface normal unit vector
$\hat{n}_{\text{b}}$	surface normal unit vector in body frame
$\hat{n}_{\text{eq}}$	surface normal unit vector in equatorial frame
$\hat{n}_{\text{obs}}$	unit vector from surface to observer
$\hat{n}_{\text{ps}}$	orthogonal unit vector of solar panel 'p', side 's'

$\hat{n}_{\mathrm{PAB}}$	surface normal unit vector of phase angle bisector in equatorial frame
$\hat{n}_{\mathrm{spin}}$	unit vector of spin axis
$\hat{n}_{\mathrm{sun}}$	unit vector from surface to Sun
N	number of histogram bins
N	number of light curve cycle comparisons
ν	satellite orbit true anomaly
ξ	sunlight incidence angle
p	solar panel number indicator (1 or 2)
p_{a}	proportion of reflected light from ambient source
p_{d}	proportion of diffusely reflected light
$p_{\mathrm{dc(i)}}$	proportion of diffusely reflected light for cube side i
$p_{\mathrm{ds(ps)}}$	proportion of diffusely reflected light for solar panel p, side s
$p_{\mathrm{dd(ds)}}$	proportion of diffusely reflected light for dish d, side s
p_{s}	proportion of specularly reflected light
$p_{\mathrm{sc(i)}}$	proportion of specularly reflected light for cube side i
$p_{\mathrm{ss(ps)}}$	proportion of specularly reflected light for solar panel p, side s
$p_{\mathrm{sd(ds)}}$	proportion of specularly reflected light for dish d, side s
P	phase percentage
P_{full}	maximum frequency-space power corresponding to a full spin period
P_{half}	maximum frequency-space power corresponding to the half spin period
P_{SRP}	solar radiation pressure
q_{ps}	reflectivity of solar panel 'p', side 's'
$\hat{r}_{\mathrm{p}}$	orthogonal unit vector of solar panel 'p'
$\vec{r}$	arbitrary radial vector
ρ	phase angle at satellite subtended by Sun and observer
ρ_1	satellite phase angle at time t_1
s	intensity of specularly reflected light
s	side indicator (of solar panel or dish) (1 or 2)
σ_{p}	solar panel area mass density
t_1	observation time of first bright specular reflection
t_{j}	time coordinate of j$^{\mathrm{th}}$ light curve data point
t_{inc}	time increment
t_{lc}	time coordinate of light curve data point
t_{ph}	light curve temporal phase offset time
T	light curve period or satellite spin period
T	rotational kinetic energy
T_{orb}	satellite orbit period
T_{p}	sidereal spin period with prograde spin axis
T_{r}	sidereal spin period with retrograde spin axis
T_{sid}	sidereal spin period
T_{syn}	synodic spin period
τ_{c}	constant torque factor
τ_{ij}	$\sin(\delta_{\mathrm{PABi}})\cos(\delta_{\mathrm{PABj}})$ where i, j = 1, 2 or 2, 1
τ_{x}	body frame torque x component
τ_{y}	body frame torque y component
τ_{z}	body frame torque z component
$\vec{\tau}_{\mathrm{net}}$	instantaneous net solar radiation pressure torque on system
$\vec{\tau}_{\mathrm{ps}}$	instantaneous torque due to sunlight on solar panel 'p', side 's'
$\vec{v}_{\phi}$	tangential velocity vector

w_{p}	width of solar panel
x	x coordinate of original A matrix before transformation
x'	x coordinate of final A$'$ matrix after transformation
$\hat{x}$	inertial Cartesian x unit vector
$\hat{x}_{\mathrm{b}}$	body frame Cartesian x unit vector
x_{b}	satellite body frame "pitch" axis
x_{PAB}	phase angle bisector Cartesian x-axis
χ_{α}	right ascension offset angle between solar panels
χ_{δ}	declination offset angle between solar panels
y	y coordinate of original A matrix before transformation
y'	y coordinate of final A$'$ matrix after transformation
$\hat{y}$	inertial Cartesian y unit vector
$\hat{y}_{\mathrm{b}}$	body frame Cartesian y unit vector
y_{b}	satellite body frame "roll" axis
y_{PAB}	phase angle bisector Cartesian y-axis
yy	years
ψ	Euler rotation angle: third coordinate rotation about final z-axis
ψ_{b}	Euler rotation angle: third rotation about z$_{\omega}$-axis
ψ_{ω}	Euler rotation angle: third rotation about z$_{\mathrm{eq}}$-axis
$\psi_{\omega\mathrm{L}}$	angle between the spin angular velocity vector and $\vec{\mathrm{L}}$
Ψ	angle between surface normal unit vector and phase angle bisector
$\vec{\omega}$	angular velocity vector
ω	angular velocity magnitude
ω_{x}	body frame x component of angular velocity vector
ω_{y}	body frame y component of angular velocity vector
ω_{z}	body frame z component of angular velocity vector
z	z coordinate of original A matrix before transformation
z'	z coordinate of final A$'$ matrix after transformation
$\hat{z}$	inertial Cartesian z unit vector
$\hat{z}_{\mathrm{b}}$	body frame Cartesian z unit vector
z_{b}	satellite body frame "yaw" axis
z_{PAB}	phase angle bisector Cartesian z-axis

LIST OF ABBREVIATIONS AND ACRONYMS

2-D	2-dimensional
3-D	3-dimensional
ave	average
ADCS	Attitude Determination and Control System
ADU	Analog to Digital Units
AEOS	Advanced Electro-Optical Sensor
AIAA	American Institute of Aeronautics and Astronautics
AMOS	Affordable Modular Optimized Satellite
AS	[GE] Astro Space
ASAT	Anti-Satellite
AsiaSat	Asia Satellite
AT&T	Atlantic Telephone and Telegraph
AU	Astronomical Unit
BOL	Beginning of Life
CASTOR	Canadian Astronomy, Satellite Tracking, and Orbit Research
CCD	Charge-Coupled Device
COSPAR	Committee on Space Research
COTS	Commercial Off The Shelf
CRT	Cross-Residual Technique
dd	day
dec	declination
DARPA	Defense Advanced Research Projects Agency
DBS	Direct Broadcast Satellite
DT	[GEO] Drifting
eq	equatorial
EOL	End of Life
FOV	Field of View
FWHM	Full Width at Half Maximum
GE	General Electric
GEO	Geosynchronous
GOES	Geostationary Operational Environmental Satellite
GPS	Global Positioning System
GY	[GEO] Graveyard Orbit
HEO	High Earth Orbit
HS	Hughes Space
HGS	Hughes Global Services
I-band	600 to 900 nm IR
inc	increment
IMAGE	Imager for Magnetopause-to-Aurora Global Exploration
IR	Infra-red
J2000.0	Julian 2000 Epoch of Equinox
JFCC SPACE	Joint Functional Component Command for Space
JSR	[AIAA] Journal of Spacecraft and Rockets
lim	limit
LEO	Low Earth Orbit
LM	Lockheed Martin
L-S	Lomb-Scargle

mm	month
MATLAB	Matrix Laboratory
MEV	Mission Extension Vehicle
MOI	Moment of Inertia
MSc	Master of Science
NASA	National Aeronautics and Space Administration
NCP	North Celestial Pole
NORAD	North American Aerospace Defense Command
obs	observation
orb	orbit
OOS	On-Orbit Servicing
p	prograde
PA	Phase Angle
PAB	Phase Angle Bisector
PAS	PanAmSat
PhD	Doctor of Philosophy
P-P	Peak-to-Peak
PSR	Power Spectrum Ratio
r	retrograde
RA	right ascension
RMCC	Royal Military College of Canada
RSGS	Robotic Servicing of Geosynchronous Satellites
sat	satellite
sid	sidereal
sim	simulated
syn	synodic
SATMEX	Satellite Mexico
SBIG	Santa Barbara Instrument Group
SBS	Satellite Business Systems
SEC	Securities and Exchange Commission
SPRL	Société Privée à Responsabilité Limitée
SRP	Solar Radiation Pressure
SSA	Space Situational Awareness
SSN	Space Surveillance Network
tot	total
US	United States (of America)
UTC	Coordinated Universal Time
UV	Ultra-Violet
yy	2-digit year

CHAPTER 1: INTRODUCTION

The majority of people in the modern world benefit from the services provided by satellites. These services include: worldwide communications (including phone, television, and Internet); real-time weather monitoring for any location on Earth; environmental monitoring; precise time and geodetic coordinates of any location on the Earth (via GPS satellites); remote sensing (of domestic and foreign territory); and even financial transactions[1]. Many do not realize their dependence on satellites for the roles that they play in routine, day-to-day tasks. The known satellite population is tracked on an almost daily basis because of the roles satellites play in daily life.

Satellites are constantly at risk from dangers that include; collision with natural objects (meteorites); collision with other man-made objects (dead satellites and satellite debris); space weather (highly charged solar ions, ultra-violet (UV) radiation, and solar radiation pressure (SRP)), gravitational perturbations (from the Earth, the Sun, and the Moon); critical systems malfunctions (including power systems and attitude control systems); and interference (physical and radio-frequency) from foreign and domestic sources. This means that in order to guarantee 24-hour reliable satellite services to customers, satellite owners must be on standby around the clock in the event that their satellite malfunctions. Contingency plans must be implemented immediately in the event their satellite fails.

The surface of the Earth is protected from many sources of radiation (including gamma ray, X-ray, UV and some infra-red (IR)) and highly charged ions. However, the area above the Earth's atmospheric strata is a very different environment that can be very harmful to equipment that relies on semiconductor technology. Many satellites are manufactured with shielding that blocks the majority of harmful particles from interacting with the on-board electronics. However, from time to time, a particle will get through and flip a "0" to a "1" (or vice-versa) (bit flip), possibly causing a single event upset[2]. This seemingly small change can trigger a critical system shutdown that could affect attitude control, communications or the entire power system. Sometimes the fault can easily be resolved from the ground; however, sometimes the malfunction is permanent and the satellite ceases operation. Vital services to customers will be disrupted. This results in financial loss for the satellite owner and any company that procures time on the satellite. There have been instances in which satellite failures have caused major disruption in services. Some of these are described in Section D.

Nearly 60 years after the launch of the first artificial satellite (Sputnik I), not a single satellite maintenance or satellite repair service is currently in operation that actively maintains, rescues, repairs, or salvages satellites (of any orbit type). Such services are collectively known as "on-orbit servicing" (OOS). Such an OOS service does not include sporadic maintenance on spacecraft such as the Hubble Space Telescope or the International Space Station. Some satellites are designed to deliver services to customers for up to 20 years [1]. Such reliability requires: an adequate supply of maneuvering fuel; sufficient radiation shielding and radiation-resistant electronic components; sufficient critical system redundancy; sufficiently large solar panels (to compensate for efficiency degradation); and a well-coordinated contingency plan in the event of malfunction. Such a design requires extra fuel, redundancy, and contingency planning, which significantly increases design and launch costs [2].

Studies have been conducted that explore the feasibility, advantages, and disadvantages of OOS as compared to the status quo[3]. The results of one study are included in Section E. An overall

---

[1]Kota, S., et al., "Satellite ATM Network Architectural Considerations and TCP/IP Performance", https://arxiv.org/ftp/cs/papers/9809/9809062.pdf, Accessed 04/04/17.

[2]NASA, "Single Event Effects", https://radhome.gsfc.nasa.gov/radhome/see.htm, Accessed 04/04/17.

[3]NASA, "On-Orbit Satellite Servicing Study - Project Report", https://sspd.gsfc.nasa.gov/images/nasa_satellite%20servicing_project_report_0511.pdf, Accessed 04/04/17.

advantage of OOS is that satellites can be designed with less on-board fuel (if OOS can refuel satellites), less redundancy, and less contingency planning, thus significantly reducing design costs and overall spacecraft mass, and thereby reducing the launch costs. However, servicing a satellite is not as easy as it sounds because of the external forces and torques that are constantly acting on all satellites.

When a satellite is healthy, its attitude determination and control system (ADCS) is constantly detecting and correcting for the effects of external disturbance torques acting on the spacecraft. These torques include: SRP; magnetic (Lorentz) forces; gravitational perturbations from the Earth, the Sun, and the Moon (including gravity gradient torque); atmospheric drag (for lower altitude satellites); and minor collisions with micro-meteorites and small man-made debris. When a satellite's ADCS is malfunctioning, the spacecraft is still affected by these external disturbance torques but the ADCS ceases to effectively correct for them. As a result, the net torque causes a change in the spacecraft's angular momentum, which in turn changes the magnitude (spin period) and direction (spin axis orientation) of the spacecraft's angular velocity vector. Once a spacecraft's attitude can no longer be controlled from the ground, the spacecraft's communications dishes likely begin to point away from the Earth, thus disrupting its important communications services. Communications between the satellite and the ground station(s) may also be severely affected, assuming that the communications and power systems are still operational. The satellite's spin period and attitude begin to vary in ways that were not planned for during the satellite's design phases.

Satellite motions have very complex rectilinear (orbit motion) and rotational (attitude dynamics) components that can constantly vary due to disturbance forces and disturbance torques, respectively. Additionally, satellites are not constrained; therefore, when describing their motion, the maximum degrees of freedom are possible. This is the main reason why satellite orbit elements need to be updated on a regular basis. Although orbit motion models can predict a satellite's location in its orbit, the accuracy (for a specific set of orbit elements) can significantly decrease over a matter of days because the orbit perturbation models are so complex.

An OOS module approaching a malfunctioning satellite will likely be approaching a spinning target [3, 4, 5, 6]. To dock with the satellite, the module must either find a point that lies along the apparent spin axis (a point with no transverse velocity) or rotate such that a point on the spacecraft appears stationary with respect to the module. Some satellites have very large solar panels that can "swat" an approaching module, thus causing damage to both the module and the spacecraft as well as releasing additional debris into an already crowded environment.

An investigation into the requirements for an OOS mission and what maneuvering steps the OOS modules would be required to take during rendezvous and docking with a tumbling spacecraft could partially depend on the attitude dynamics characteristics of the target spacecraft's design. The worst case scenario for an OOS module is a satellite that has been tumbling uncontrollably for a number of months, such that the satellite's ADCS attitude control components (including any reaction wheels or momentum-bias wheels) have transferred all of their angular momentum into the spacecraft system. In such a scenario, the OOS module would be required to repair the ADCS, communications, and the power systems (whichever is required) and restart the ADCS.

A GEO satellite's reflected sunlight can be detected with ground-based electro-optical equipment consisting of small aperture telescopes and charge-coupled device (CCD) cameras. A tumbling GEO satellite's detected brightness will appear to vary over time with an apparent period that is related to the satellite's true spin period. Photometric measurements of the satellite's reflected sunlight can be obtained over time to infer the satellite's spin period as well as its spin axis orientation.

Several short-term (less than one year) photometric studies of tumbling spacecraft have been conducted in advance of OOS mission designs [4, 5]. However, additional long term (one year or more) studies that include the investigation of satellite light curve morphology and quantitative

attitude determination would be more beneficial. A description of the short term surveys are included in Chapter 2. A number of the satellite samples would have to be more closely studied to determine the satellites' spin axis orientations and variations with time. The satellites chosen would have to exhibit photometric light curves that appear similar over a long period of time in order to construct dynamics models with the minimum amount of free parameter assumptions.

This thesis describes the results of a research project whose goals were:

- to conduct an in-depth photometric study of a large sample of non-operational telecommunications satellites;

- to infer the apparent (synodic) spin periods and angular accelerations of these satellites;

- to investigate a satellite's light curve morphology over the long term;

- to geometrically determine a satellite's spin axis orientation and variation;

- to compare a satellite's synodic and sidereal spin periods over the long term; and

- to determine and verify a satellite's attitude dynamics.

In this thesis, the term "broadband" was defined to refer to an unfiltered optical system with a detected flux spanning the entire detectable optical spectrum. The thesis presents results from an 11-satellite broadband photometric survey that was conducted from March 2012 to January 2016. Furthermore, the thesis highlights one of these satellites for an investigation of its attitude dynamics. Finally, the thesis reports the results of a numerical model that simulates the highlighted satellite's angular acceleration and spin period variations.

A   Geostationary and Geosynchronous Satellite Orbits

For every parent body in the universe, such as a star or a planet, a specific average orbit radius (semi-major axis) exists in which the orbit period will be identical to the parent body's rotation period. For the Earth, with a rotation period of one sidereal day (23 hours, 56 minutes, and 4.0921 seconds [7]), this specific orbit radius is 42,161 km; an altitude of 35,783 km. A satellite orbiting at that specific distance from the Earth would be able to continuously access the same portion of the Earth. Consequently, that same portion of the Earth's surface would be able to access the satellite on a continuous basis. This is why consumer satellite dishes do not need to be realigned throughout the day and night to access a telecommunication satellite's signal.

A "geostationary" Earth orbit is one which has a sidereal day period, is perfectly circular (orbit eccentricity of 0), and has a plane coincident with the Earth's equatorial plane (orbit inclination of 0). A "geosynchronous" Earth orbit (GEO) is one which has a sidereal day period, but can have any eccentricity or inclination. In effect, a geostationary orbit can be considered to be a GEO orbit, but not vice-versa.

B   The Box-wing Satellite Design

The "box-wing" satellite design consists of a number of critical components: a roughly cube-shaped central bus with sides of approximately 2.5m; two large solar panels that are each approximately 10m long and 3m wide; and two large parabolic dish antennas, each approximately 2m in diameter. The solar panel size depends on the specific power requirements of the satellite. The total length (wing span) of a box-wing satellite can currently be as large as 35m. An illustration of the Echostar-2 box-wing satellite is shown in Fig. 1 [6].
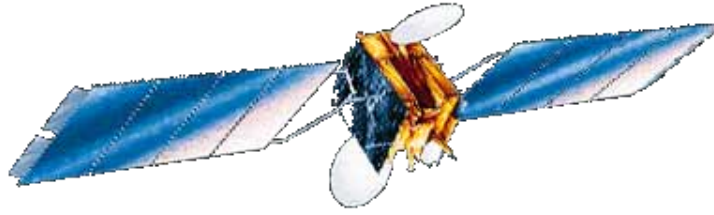
Figure 1   The Echostar-2 satellite: An example of the box-wing design[4]

C   Active and Inactive Box-wing GEO Satellites

For the purposes of this thesis, an "active" box-wing satellite has been defined as one whose ADCS is at least partially functional, such that the satellite's attitude can be stabilized and controlled from the ground station. Typically, an active box-wing satellite has a geostationary orbit; however, some box-wings near their "End of Life" (EOL) stages can still be active while in inclined GEO orbits [8]. When active, a box-wing satellite's longest axis, that axis running through the lengths of the two solar panels shown in Fig. 1, is oriented orthogonally to the satellite's orbit plane (typically coincident with the Earth's equatorial plane) [9].

An active box-wing's solar panels will slowly rotate about their long axes so that sunlight is consistently at a minimum incidence angle to the solar panel surface, in order to generate the nominal power output. At the same time, the box-wing's central cube portion is aligned such that the parabolic dish antennas (shown in Fig. 1) are constantly pointed toward the Earth's surface. This alignment is accomplished by rotating the box portion at the same rate as the satellite's orbit motion. By performing these tasks, the satellite will maintain its nominal power levels (including charging on-board batteries used in eclipses), will maintain its communications with the ground station, and will maintain its delivery of telephone, television, and/or Internet services to its ground-based customers.

For the purposes of this thesis, an "inactive" box-wing satellite has been defined as one whose ADCS is no longer functioning due to any reason. An inactive box-wing satellite's attitude can no longer be controlled (automatically or manually); therefore, its spin axis orientation and its spin period can be influenced by external disturbance torques, most likely SRP, acting on the satellite's large solar panels [6].

A box-wing satellite can become inactive either by intentional deactivation (at EOL) or by catastrophic malfunction including; power failure; single event upset; component malfunction; or collision with debris (man-made or natural). Just before a box-wing satellite is intentionally retired (deactivated), its orbit radius is raised above the geostationary belt by several hundred kilometers [10]. Technically, this slight orbit radius increase changes the satellite's orbit type to "super-synchronous" (also known as High Earth Orbit (HEO)); however, the satellite is still considered to be in a near-GEO orbit. The slight increase in orbit radius will cause the newly inactive satellite's orbit period to be slightly larger than the Earth's rotation period. The satellite will therefore appear to slowly drift from east to west in a ground-based observer's sky. At times, a successfully retired satellite will be below an observer's local horizon for an extended time (depending on the new orbit period), so that it will be inaccessible. Therefore, a newly retired box-wing GEO satellite will no longer be continuously accessible from a single position on the Earth's surface.

When a satellite is deactivated by a catastrophic malfunction, its orbit radius cannot be raised

---

[4]Krebs, G., Gunter's Space Page - EchoStar 1,2, http://space.skyrocket.de/doc_sdat/echostar-1.htm, Accessed 04/04/17.

above the geostationary altitude. As a result, the satellite remains in a geostationary orbit for several weeks. However, the perturbations due to the Sun, the Moon, and the obliquity of the ecliptic plane, causes the newly inactive satellite's orbit inclination to increase to a maximum of approximately 15º [11]. This increase in inclination causes the satellite to assume a GEO orbit. This inclination increase also occurs for box-wing satellites that are purposely retired and parked outside of the geostationary belt. Since these satellites are not parked outside of the geostationary belt, they can be observed to oscillate back and forth about one of the two stable gravitational zones. Depending on how close a satellite was to one of these stable zones, the angle of oscillation could be large enough to cause the satellite to drop below an observer's horizon for a time.

D   Critical Box-wing Satellite Malfunctions

A box-wing satellite is typically designed to continuously and reliably deliver its products to its customers over a lifetime of between 15 and 20 years. Once a box-wing satellite is placed within its geostationary orbit slot, it is physically on its own. This means that apart from software maintenance, there is no way of maintaining the satellite's hardware or replenishing its fuel over its lifetime. Therefore, component reliability and hardware redundancy are required to increase the probability of a successful 15-20-year lifetime. Despite this costly preparedness, several box-wing satellites have malfunctioned, both temporarily and permanently, before their designed EOLs, mainly due to high energy solar particles emanating from coronal mass ejections (CMEs).

In January 1994, both Canadian Anik-E (E1 and E2) box-wing satellites temporarily failed within nine hours of one another [12]. The malfunctions caused both satellites' to lose ADCS attitude control, thereby causing communications loss as their communications dishes moved away from Earth-pointing orientation. Many of the Canadian cable and satellite television channels became unavailable (especially in the far north of Canada) and news agencies could not receive or deliver up-to-date press releases, except by land-line telephone and fax. Neither satellite was insured [12]. Telesat Canada (the owners of both satellites), managed to restore all communications within three days; however, at considerable financial and public relations costs [12]. Both satellites were launched in 1991, therefore they were only in their fourth year of operation.

The most widely publicized satellite malfunction occurred on January 11, 1997, when the AT&T-owned Telstar-401 box-wing satellite suddenly ceased all operation because of satellite charging due to high solar activity. Unlike the Anik-E events, Telstar-401 ceased all communications with the ground stations, thus cutting off all possibility of a rescue. Telstar-401 had delivered telephone and satellite television services to much of the contiguous United States (US). After the malfunction, these services had to be rerouted to other active geostationary satellites; a process that required several days and the realignment of thousands of consumers' satellite dishes. Telstar-401 continued to orbit the Earth up to the present day and will do so for hundreds, if not thousands, of years to come.

Another critical malfunction occurred over one year later on May 19, 1998 when the (now defunct) PanAmSat's (PAS's) Galaxy IV satellite suddenly ceased all operations, including communications. Just two weeks earlier, the Earth's magnetosphere suffered an extreme compression due to very high solar wind activity [13], thus exposing the geostationary belt to highly charged ions. Prior to its failure, Galaxy IV was responsible for the majority of the pager traffic (including those used by medical professionals) and some of the credit card and ATM transactions in the US at the time [5]. After the malfunction, Galaxy IV customers had to realign their satellite dishes after PanAmSat rerouted Galaxy IV traffic to active geostationary satellites.

---

[5]Zuckerman, L., "Satellite Failure is Rare, and Therefore Unsettling", The New York Times, May 21, 1998, http://www.nytimes.com/1998/05/21/business/satellite-failure-is-rare-and-therefore-unsettling.html, Accessed 03/11/17.

More recent box-wing malfunctions have occurred. Echostar-2 is a box-wing telecommunications satellite originally designed by General Electric's (GE's) Astro Space (AS) with an AS-7000[6] bus design. The satellite was launched on September 11, 1996[7] to service customers in North and South America[8] for 15 years. On July 14, 2008, the satellite suffered "a substantial failure that appears to have rendered the satellite a total loss"[9]. Echostar-2 could no longer be controlled from the ground and therefore could not be parked in the GEO graveyard orbit.

Each of the substantial box-wing failures described here have inconvenienced customers and cost their owners millions of dollars. However, a new paradigm is being considered by a number of military and commercial organizations, in which critically malfunctioned box-wing satellites do not have to be abandoned. OOS modules that promise to rendezvous, dock, refuel and service telecommunications satellites might be demonstrated by as early as the end 2018 [10].

E   On-orbit Servicing Projects

To date, no OOS demonstrations have been conducted in GEO. However, an OOS service module that is aimed at servicing telecommunications satellites in GEO orbits is currently being designed by the US Defense Advanced Research Projects Agency (DARPA) [4, 5]. The goals of DARPA's "Robotic Servicing of Geosynchronous Satellites" (RSGS) program include: to demonstrate a GEO robotic servicing vehicle that can perform safe, reliable, and efficient operations that can adapt to varying conditions; to demonstrate servicing mission operations on active GEO satellites; and to support development of satellite-servicing spacecraft that can perform a number of missions over several years. [11].

Orbital ATK [12] has also been developing an OOS mission called the "Mission Extension Vehicle" (MEV). The main goals of the MEV include; fuel replenishment; spacecraft inspection and repair; and parts replacement. [13]. Unlike the DARPA RSGS mission, the MEV mission does not specify the orbit types of the satellites that would eventually be serviced.

NASA has also been developing its own OOS mission called "Restore-L". The goals of Restore-L include; autonomous rendezvous; docking; refueling; satellite relocation; incorporation servicing technologies into other NASA missions; transferring technology knowledge to the commercial sector; and assisting with the creation of a satellite servicing industry [14]. To date, the intended satellite clients are located in the LEO orbit realm and not GEO.

---

[6]Also known as the Lockheed Martin (LM) designation "LM-7000".

[7]Joint Functional Component Command for Space (JFCC SPACE)/J3, Space Track, https://www.space-track.org, Accessed 05/01/16.

[8]Krebs, G., Gunter's Space Page, Echostar 1, 2, http://space.skyrocket.de/doc_sdat/echostar-1.htm, Accessed 05/01/16.

[9]US Securities and Exchange Commission (SEC), "Form 8-K: Current Report Pursuant to Section 13 or 15(d) of the Securities Exchange Act of 1934", http://apps.shareholder.com/sec/viewerContent.aspx?companyid=DISH&docid=6046093, Accessed 05/01/16.

[10]Clark, S., "NASA selects builder for robotic satellite servicing craft", https://spaceflightnow.com/2016/12/09/nasa-selects-builder-for-robotic-satellite-servicing-mission, Accessed 03/18/17.

[11]Roesler, G., Robotic Servicing of Geosynchronous Satellites (RSGS), DARPA, http://www.darpa.mil/program/robotic-servicing-of-geosynchronous-satellites, Accessed 03/17/17.

[12]The result of a 2014 merger of Orbital Sciences Corporation and the aerospace division of Aliant Techsystems (ATK).

[13]Orbital Mission Extension Vehicle fact sheet, https://www.orbitalatk.com/space-systems/human-space-advanced-systems/mission-extension-services/docs/MEV_Rev01-17.pdf, Accessed 03/17/17.

[14]NASA Restore-L Robotic Servicing Mission fact sheet, https://sspd.gsfc.nasa.gov/documents/Restore_L_Factsheet_113016.pdf, Accessed 03/17/17.

All of these OOS programs can benefit from an in-depth, long term, and ground-based photometric survey of the inactive GEO box-wing satellite population. The surveys could provide OOS design engineers with vital box-wing satellite environmental information including; the range of spin periods (spin rates) that could be encountered; the spin rate variation and variation timescale; the range of spin axis orientations that could be encountered (within the spacecraft frame and within the inertial frame of reference); the spin axis variations due to precession and external disturbance torques; the timescale of the precessional motions; and the effect of SRP on a box-wing satellite's attitude dynamics. This information would provide OOS design engineers with data that could be used to predict the risks and difficulty of a docking of a robotic servicing module with a spinning spacecraft.

F   Thesis Scope

1   Long Term Photometric Survey

The first goal of this thesis was to conduct a long term (over one year) and high temporal resolution (one observation per week per satellite, weather and access permitting) ground-based broadband photometric survey of inactive AS-7000 and HS-601[15] box-wing GEO satellites (illustrated in Fig. 2) over at least one year. Echostar-2, illustrated in Fig. 1, was one of the AS-7000 design satellites that were observed. An "observation" would consist of a number of images of a box-wing satellite over one hour or more, depending on the satellite's synodic spin period. Each image would consist of a star field with a foreground box-wing satellite appearing as a dot spanning several pixels. A photometric analysis software tool was developed in Matrix Laboratory (MATLAB) to automatically extract the broadband photometric information from each image obtained over an observation.

A ground-based photometric survey is financially advantageous when compared with using space-based and radar facilities. However, there are limitations, such as inclement weather conditions and sky transparency, including the attenuation of optical wavelengths due to the atmosphere. These limitations will reduce the minimum size and the maximum phase angle of detectable satellites assuming a constant detector aperture size.

a) AS-7000[16]   b) HS-601[17]
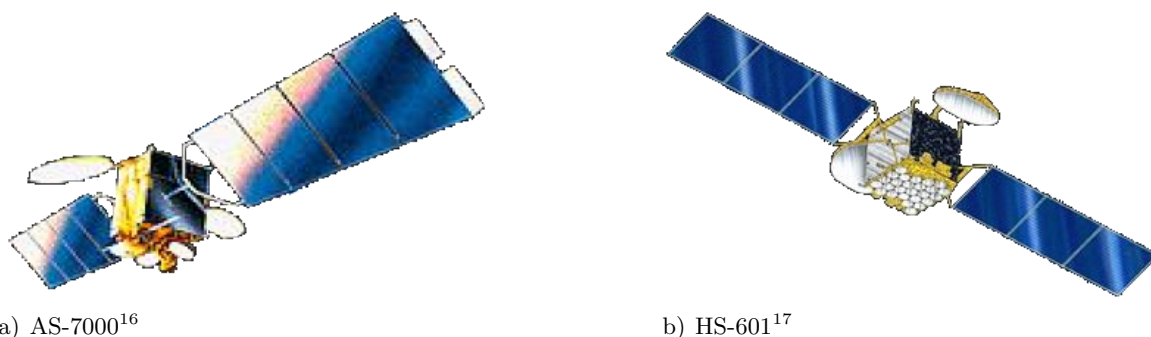
Figure 2   Artists' conceptions of AS-7000 and HS-601 models

All photometric observations conducted for this thesis were obtained with commercial off the shelf (COTS) electro-optical equipment consisting of a small-aperture computer-controlled telescopes and research-grade CCD cameras listed in Table 1. Broadband imagery was conducted; to

---

[15]Hughes Space

[16]Encyclopedia Astronautica, AS-7000, http://www.astronautix.com/a/as7000.html, Accessed 09/14/16.

[17]Encyclopedia Astronautica, HS-601, http://www.astronautix.com/h/hs601.html, Accessed 09/14/16.

maximize the amount of signal being detected by the CCD camera; to maximize the sampling rate; to maximize the light curve resolution; and to avoid light curve aliasing. Chapter 3 presents a subset of the light curves obtained from observations of AS-7000 and HS-601 box-wing satellites.

Table 1 Electro-optical hardware chosen for this research

Hardware	Brand and Model	Specifications
Optical Telescope	Celestron NexStar 11 GPS	Aperture: 0.28m (11 inches) Mount type: Fork equatorial
CCD Camera	Santa Barbara Instrument Group (SBIG) ST-9XE[18]	Detector: Kodak KAF-0261E Array size: 512 x 512 pixels Pixel size: 20 μm (square) Quantum efficiency: 67% at λ=600nm Chip cooling: 40°C below ambient
CCD Camera	SBIG ST-8XE[19]	Detector: Kodak KAF-1603ME Array size: 1530 x 1020 pixels Pixel size: 9 μm (square) Quantum efficiency: 83% at λ=640nm Chip cooling: 40°C below ambient

In all cases a continuous series of one-second CCD integration times was used over a time scale of between one and two hours. Observations of each satellite were typically conducted twice per week, weather permitting. The sampling cadence for a 1-second integration time was 3.32±0.05 seconds (one duty cycle). In all cases the telescope's sidereal tracking was switched off to prevent the satellite from streaking on the image plane. Each satellite was allowed to drift across the field of view (FOV) until it reached an edge of the FOV. Depending on the satellite's orbit inclination and its position in its orbit, this time could be 2 minutes to 30 minutes. The telescope was then manually slewed so that the satellite appeared on the opposite side of the FOV so that the satellite could slowly drift across the FOV once again. This routine was repeated throughout each 1-2 hour observation session. The CCD automatically imaged during the entirety of each observation session and each image was automatically stored. No filters were used in order to allow the CCD to detect the maximum satellite signal and to allow the maximum sampling cadence.

Photometric data was only obtained when the Sun's elevation was less than -12° (nautical twilight) and the Moon's phase (when above the local horizon) was less than 50%. The satellite's phase angle had to be between 10° and 90° (to maximize detected signal) and the satellite's elevation had to be greater than 15° to avoid excessive atmospheric signal absorption. The CCD detector chip's maximum temperature during observation was not to exceed -20°C to minimize dark (thermal) currents.

2 Comparisons of Box-wing Light Curve Characteristics

The second goal of this thesis was to compare the characteristics of the light curves' morphologies, spin period variations and angular acceleration variations. A satellite's light curves can contain encoded information about its attitude, how the attitude varies over time, and the rate at

---

[18]SBIG, Operating Manual: CCD Camera Models ST-7XE/XME, ST-8XE, ST-9XE, ST-10XE/XME and ST-674 2000XM/XCM With High Speed USB Interface, 1.4 ed., June 2004.

[19]Ibid.

which the attitude can vary. Be decoding and interpreting this information, the range of possible satellite spin periods, spin angular accelerations, spin axis orientations, and the rates of each, may be inferred for box-wing satellites. Chapter 3 presents results for the AS-7000 and HS-601 box-wing satellites.

3   Relations between Light Curve Morphologies and Spin Period Variations

The third goal of this thesis was to investigate evidence of potential relationships between box-wing light curve morphologies and their spin period variations. Light curve morphologies can indicate how a box-wing's attitude dynamics can vary over time. Spin period variation can be caused by a net external torque. Evidence of a potential relationship between these two phenomenon can be used to prove a potential link between a box-wing satellite's photometric light curve morphology and the net external torque acting on the spacecraft. Chapter 3 presents results for two AS-7000 box-wing satellites.

4   Spin Axis Orientation Estimation

The fourth goal of this thesis was to estimate the spin axis orientation of one box-wing chosen from the satellite sample. The selection criterion was a slowly varying light curve morphology over a long time scale. This criterion would have to suggest a minimal spin axis precession over the long term. The satellite chosen would have a light curve morphology that exhibited little to no change in its characteristics. The rationale of this goal was that it would be easier to develop spin axis orientation models of a satellite with attitude dynamics that vary over time scales of several weeks or several months than to develop models for a box-wing satellite whose attitude dynamics vary over timescales of several minutes or several hours. Chapter 4 presents the results of the spin axis orientation determination of the Echostar-2 box-wing satellite.

5   Difference between Synodic Spin Period and Sidereal Spin Period

The fifth goal of this thesis was to determine the difference between the chosen satellite's synodic spin period and its estimated sidereal spin period using the (synodic) spin period variations previously inferred and the spin axis orientation estimations previously estimated. Assessing the effects on the synodic spin period of the sidereal spin period and the effects of the angle between a reflecting surface's normal unit vector and the satellite's phase angle bisector (PAB) would reveal how much the satellite's synodic spin period can differ from its sidereal spin period over the study's time scale. Such a determination can also be used to verify the estimated spin axis orientation. Chapter 5 presents the results of the synodic-sidereal spin period difference of Echostar-2, based on the satellite's spin axis orientation determined in Chapter 4.

6   Simulating Spin Period Variation and Angular Acceleration Variation

The final goal of this thesis was to develop a first-order attitude dynamics model to investigate how the primary disturbance torque (due to SRP) could vary the chosen satellite's spin period and its angular acceleration over a long time scale (approximately 10 years). This SRP torque model was used to simulate the chosen satellite's observed spin period and angular acceleration variations and to predict future variations. Chapter 5 presents a 10-year simulation of the Echostar-2 satellite's spin angular acceleration and spin period variation, based on the satellite's spin axis orientation determined in Chapter 4.

G   Thesis Format

This thesis was prepared in the article-based format, as described in the latest version of the RMCC's Thesis Preparation Guidelines[20], published on May 6, 2015. Therefore, some repetition might exist between the general Introduction and Literature Review Chapters and the Introduction and Background Sections of each article (Chapters 3, 4, and 5).

This thesis was prepared with LaTeX TEXnicCenter, Version 2.0. This thesis has adopted the American spelling style throughout in order to meet formatting requirements of American scientific journals, such as the American Institute of Aeronautics and Astronautics' (AIAA's) Journal of Spacecraft and Rockets (JSR). The author has formatted this thesis according to the latest version of the RMCC's Thesis Preparation Guidelines, published on May 6, 2015.

---

[20]This document is available at https://www.rmcc-cmrc.ca/en/academic-wing/thesis-preparation-guidelines.

CHAPTER 2:   LITERATURE REVIEW

Several important realizations came to light when researching previously published research papers concerning photometric observation, spin axis orientation determination, synodic-sidereal spin period transformation, and spin period variation simulation of inactive box-wing GEO satellites. Firstly, there were very few papers addressing these subjects. Only one of these papers reported on long term photometric observation; however, the resolution (number of times observed) of these observations were low; a maximum of one or two observations per month. Several papers reported on high resolution observations; however the observations were carried out over the short term; a maximum of several months. Many of the papers reported findings based on short term and low resolution observations. None of the published papers discussed the results of inactive box-wing spin axis orientation determination or discussed simulations of box-wing spin period variations.

A   Photometric Observations and Light Curve Morphology Analysis

Papushev, et al. (2009) surveyed the long term variability of the optical characteristics of a number of inactive Russian Raduga, Gorizont, and Ekran satellites from 1990 to 2004 by obtaining high temporal resolution broadband light curves [3]. They observed a large and periodic brightness variability, which suggested spinning motion. They reported that the satellites' inferred (synodic) spin periods slowly varied over time [3]. However, when they observed Raduga-14, they noticed a sudden and significant spin period increase, then a sudden decrease over a several day interval [3]. Their light curves exhibited broad features (relative to a full inferred spin period) with amplitudes of between 2 to 3 magnitudes (between 14th and 11th visual magnitude) adjacent to features that were thin, sharp, and tall (relative to the broad features) with amplitudes between 4 and 8 magnitudes (between 14th and 6th magnitude for Raduga-14) [3]. They attributed the tall, sharp features to specular sunlight reflections (glints) from the large-area solar panels [3]. The estimated synodic spin periods of the Raduga, Gorizont, and Ekran satellites fell into a broad range of between 0.3 minutes and 7.2 minutes. A single broadband light curve of Raduga-18, observed by Payne, et al. (2007) on June 7, 2007, exhibited shapes that were similar to those obtained by Papushev, et al. but was reported by Payne, et al. to have a synodic spin period of approximately 30 minutes [14].

Binz, et al. (2014) surveyed a number of American box-wing satellites from January to May 2012 [5]. Some of their reported synodic spin periods were longer than those reported by Papushev, et al. (up to 100 minutes), while other synodic spin periods could not be determined. Synodic spin period variations were not reported.

Cognion (2014) surveyed the American GOES[21]-8, 9, 10, 11, and 12 satellites from December 2013 to August 2014 [4]. GOES satellites have a single solar panel and a small solar sail which balances the SRP torque from the solar panel, as described in [4]. Cognion observed adjacent broad and sharp light curve features that appeared to be similar to those observed by Papushev, et al. and Binz, et al. Cognion reported that the GOES satellites' light curves, when phased according to their inferred (synodic) spin periods, appeared to be unexpectedly different from each other, suggesting a "very different rotational behavior" [4]. GOES-8 and GOES-10 light curves revealed repeating patterns from cycle to cycle. The five satellites' synodic spin periods and spin period variability rates were reported to differ significantly. Ryan and Ryan (2015) estimated GOES-8's synodic spin period to be 22.951±0.001s, based on observations made on April 24, 2014 [15]. This period was between the 16.48s and 75.66s values which were reported by Cognion in February and July 2014, respectively. This suggests that GOES-8's synodic spin period was increasing over the first half of 2014. Ryan and Ryan could not infer GOES-8's spin period from a light curve obtained on September 12, 2015 because a repeating pattern could not be identified [15]. Similarly, Cognion's observations of GOES-9, 11, and 12 revealed light curves that varied significantly from cycle to

---

[21]Geostationary Operational Environmental Satellite.

cycle. Cognion had reported that most of the GOES satellite synodic spin periods appeared to be between several minutes and tens of minutes, and that the spin period determination of GOES-12 was unsuccessful [4].

Earl and Wade (2015) reported broadband photometric observations of four inactive box-wing satellites; Solidaridad-1, Telstar-401, Echostar-2, and HGS[22]-1 (formerly Asiasat-3) (Table 2) with the equipment and observation procedure described in [6][23]. Broadband (rather than color) observations were conducted to allow long term and high temporal resolution imaging (to minimize the possibility of aliasing), and to allow a rigorous observation schedule (a minimum of one observation per week per satellite, weather and access permitting). It was reported that these satellites appeared to be spinning with diverse synodic spin periods ranging from 2.4 minutes (Telstar-401) to 30.8 minutes (HGS-1) [6]. Their synodic spin periods were consistently and smoothly varying, but the spin periods did not vary as suddenly as Papushev had reported for Raduga-14. In all four cases, the spin period could be determined with ease, in contrast with the difficulties reported by Cognion, Binz, and Ryan and Ryan. The spin period variations of Telstar-401, Echostar-2, and HGS-1 appeared cyclical, while Solidaridad-1's spin period variations appeared secular [6]. Results from all of the aforementioned box-wing photometric studies suggested complex rotational behaviors with unknown origins.

1   Previous Observations of Echostar-2

In November 2010, amateur satellite observers reported that Echostar-2 was flashing "very brightly" to the naked eye (likely due to brief specular sunlight reflections), with an apparent period of 240.3s[24]. Long term and high temporal resolution broadband photometric observations of Echostar-2 were conducted from March 2012 to November 2015 [16] with the equipment and procedure described in [6]. In Earl and Wade (2016), it was reported that Echostar-2's spin period varied cyclically, with a minimum of 272.1s and a maximum of 532.2s [16, 17]. The satellite's spin period variation amplitude was observed to significantly decrease from 186.8s (in 2012-13) to 31.3s (in 2014-15) [16]. Brief and bright (naked eye brightness) specular flares from Echostar-2 were observed in March and September of 2012, 2014, and 2015. Two contiguous specular flares corresponded to half an inferred spin period[25].

All light curves of Echostar-2 contained four distinct and alternating features over each inferred spin period; two broad (likely diffuse reflection) features and two thin and sharp (likely specular reflection) features that suggested four sides of the box-wing satellite's box portion [16, 17]. Figure 3 shows an example of an Echostar-2 folded broadband light curve for September 12, 2012 [16]. The thin, sharp features appeared similar in shape and amplitude and were consistently separated by 50% of a spin period [16], suggesting that two reflective surfaces, 180º of a rotation apart, were specularly reflecting sunlight to the observer during each satellite rotation. This further suggested that the two highly reflective mirrored radiators[26], and not the solar panels, were the sources of the bright specular flares observed in 2012, 2014, and 2015 [16].

---

[22]Hughes Global Services.

[23]also Earl, M., Observation and Analysis of the Spin Period Variations of Inactive Box-wing Telecommunications Satellites in Geosynchronous Orbit, Master of science (MSc) thesis, Royal Military College of Canada (RMCC), May 2013, http://www.castor2.ca/08_Papers/earl_thesis.pdf, Accessed 03/27/16.

[24]McCants, M., "Very bright flashes from Echostar-2", http://www.satobs.org/seesat/Nov-2010/0052.html, Accessed 05/01/16.

[25]Earl, M., Observation and Analysis of the Spin Period Variations of Inactive Box-wing Telecommunications Satellites in Geosynchronous Orbit, MSc thesis, RMCC, May 2013, http://www.castor2.ca/08_Papers/earl_thesis.pdf, Accessed 03/27/16.

[26]The radiators dissipate heat away from the temperature-sensitive electrical components within the box portion.
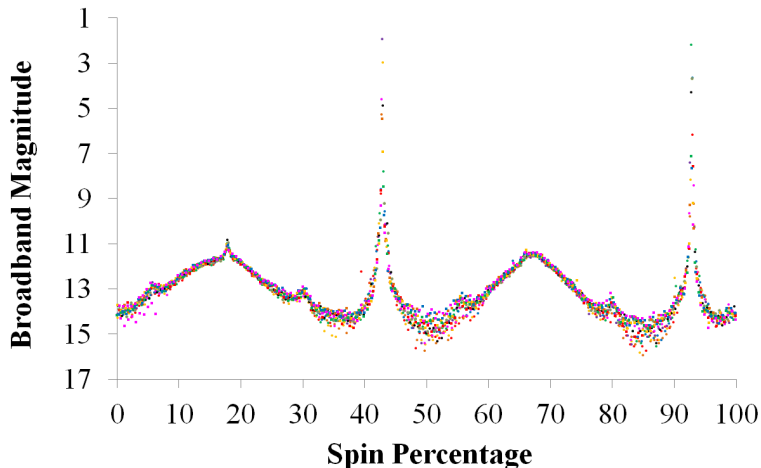
Figure 3   Echostar-2 folded light curve for September 12, 2012. 375.9s period

An inactive box-wing satellite's light curve morphology depends on the satellite's spin axis orientation with respect to the satellite's body frame, to the Sun, and to the observer. Echostar-2's light curve morphology was reported to have been similar over time; always containing the two alternating broad (diffuse) and sharp (specular) features over an inferred spin period (as shown in Fig. 3), but with varying specular brightness amplitudes over a weekly timescale. The light curve morphologies of the remaining ten satellites listed in [16] were observed to vary significantly over timescales between a single spin period (typically minutes or hours) and several months [16]. Echostar-2's light curve specular magnitude amplitudes appeared to vary cyclically with a timescale of approximately half a year [16]. Echostar-2's brightest broadband specular magnitudes were consistently observed in several weeks of March and September of 2012, 2014, and 2015. One of the brightest specular flares, of approximately broadband magnitude 2 (Fig. 3), was observed on September 12, 2012.

B   Synodic and Sidereal Spin Periods of GEO Satellites

One example of the possibly significant difference between a synodic and a sidereal spin period (also known as the "synodic effect") is a non-spinning (infinitely long sidereal spin period) GEO satellite observed from some single location on the Earth's surface. The observer would see the satellite appear to spin with a 24-hour (synodic) period because the GEO satellite is orbiting the Earth at the same angular rate as the Earth's rotation and it is moving with the Earth as it orbits the Sun[27]. Therefore, the satellite's light curve would appear to have a 24-hour period, even though the satellite is not spinning at all.

Evidence of the synodic effect was presented by Lambert, et al. (2003) based on their observations of the cylindrical SBS[28]-B and SBS-C HS-376 [29] design GEO satellites with the Advanced Electro-Optical Sensor (AEOS) facility in Maui, Hawaii from 2002 to 2003 [18]. Lambert, et al. observed bright reflections which were seen as brief temporal duration and bright magnitude features on their I-band photometric light curves, as shown in [18]. They reported that on June 15, 2003, SBS-B's light curve period (inferred from the light curve features) appeared to lengthen from 50s

---

[27]Earl, M., Observation and Analysis of the Spin Period Variations of Inactive Box-wing Telecommunications Satellites in Geosynchronous Orbit, MSc thesis, RMCC, May 2013, http://www.castor2.ca/08_Papers/earl_thesis.pdf, Accessed 10/11/16.

[28]Satellite Business Systems.

[29]Hughes 376, later Boeing 376.

to nearly 200s over a timescale of 2.5 hours from 10:30 to 13:00 UTC[30]. They also reported that on December 20, 2002, SBS-C's light curve period appeared to suddenly increase from 30s to 60s at approximately 08:40 UTC [18].

Lambert, et al. concluded that the SBS-B and SBS-C light curves they observed were inconsistent with those of active HS-376 satellites. They suggested that after these spacecraft were retired, they underwent a change in their dynamics, wherein their spin axes transitioned from their minimum to their maximum moments of inertia (MOIs), resulting in a pure tumble (also known as "flat spin") [18]. Lambert, et al. reported that the satellites' synodic spin periods increased suddenly and significantly. They suggested that the cause in each case was the PAB (corresponding to the normal of a satellite surface responsible for the bright reflections), nearly aligning with the satellite's spin axis [18]. An extreme example of such a lengthening of the synodic period occurs when a surface's PAB is aligned with the spin axis and the observer can see a sunlight reflection from the corresponding surface. In this case, the light curve should show a continuous and constant reflected brightness until the PAB is no longer aligned with the spin axis, or, until the viewing geometry between the Sun, the observer, and the satellite ceases to be favorable for a sunlight reflection to the observer.

Hall, et al. (2006) obtained I-band light curves of NASA's[31] IMAGE[32] satellite in January and February 2006, soon after the satellite ceased transmitting telemetry in December 2005 [19]. They observed IMAGE with the AEOS 3.6m aperture telescope atop Haleakala mountain in Maui, Hawaii on January 28, 31, February 3, and May 30, 2006 in order to estimate the satellite's spin axis orientation and sidereal spin period. They reported varying synodic spin periods of between 121.6 and 126.5s (rates of between 0.49342 and 0.47431 revolutions$\cdot$min^{-1}) over a timescale of approximately 45 minutes. Their estimations were compared with the spin rate contained within the final IMAGE telemetry received by NASA on December 12, 2005. The sidereal spin period contained within the satellite's final transmitted telemetry was 0.47594$\pm$0.00012 revolutions$\cdot$min^{-1}, a spin period of 126.066$\pm$0.032s [19].

Much like a light curve morphology variation, a satellite's synodic spin period can be varied by relative motions of the satellite, the observer, and the Sun. This includes the satellite's spin axis orientation with respect to the PAB [19]. For example, if a spinning satellite is moving quickly with respect to an observer, that observer will measure a synodic spin period that might significantly deviate from its sidereal spin period [19]. In the case of GEO satellites (observed by Cognion, Binz, Earl and Wade, and Lambert, et al.), the relative motion between the satellite and observer is very small and could therefore be negligible.

Hall, et al. reported that they had measured IMAGE's spin frequency on January 28, 2006 to within 0.00142$\pm$0.00043 revolutions$\cdot$min^{-1} of the spin frequency (0.38$\pm$0.11s of the spin period) as measured by NASA on December 12, 2005. They also reported that their subsequent measurements had revealed that IMAGE's spin frequency was decreasing at a rate of approximately (3.1$\pm$0.3) $\times$ 10^{-5} revolutions$\cdot$min^{-1} $\cdot$ d^{-1}. This rate corresponds to a steady spin period increase of 0.0074$\pm$0.0011s $\cdot$ d^{-1}. This sidereal spin rate was approximately three times faster than that observed during the final two years of IMAGE's active operation. Hall, et al. also confirmed that the IMAGE satellite was not able to receive commands by NASA to increase its spin rate, based on the satellite's apparently continued spin rate decrease after the commands were sent on February 16 and March 2, 2006 [19].

---

[30]Coordinated Universal Time.

[31]National Aeronautics and Space Administration.

[32]Imager for Magnetopause-to-Aurora Global Exploration.

C   Box-wing Spin Axis Orientation Estimation

The "spin axis orientation" was defined in [20] as the inertial right ascension (RA) (α_{spin}) and declination (dec) (δ_{spin}) direction of a satellite's spin angular velocity vector ($\vec{\omega}$). These two angles are related to the Euler transformation angles between a satellite's spin axis reference frame and the equatorial (inertial) reference frame, as described in [20].

A spinning satellite's synodic-sidereal spin period difference depends on its spin axis orientation [19] with respect to its inertial frame. Hall, et al. estimated the IMAGE satellite's spin axis orientation from their synodic spin period measurements inferred from I-band photometric light curves obtained with the AEOS facility.

Hall, et al. estimated IMAGE's spin axis orientation with the "epoch method", a method which is also used within the asteroid observation community, as described in [19]. An advantage of the epoch method is that it does not depend on the satellite's shape and its reflectivity characteristics. This method assumes that the satellite's spin axis state is stable (not chaotic) and that the measured synodic spin period corresponds to a full rotation of the PAB (responsible for the observed reflections and the inferred spin periods) about the satellite's spin axis [19].

Hall, et al. reported that the estimated IMAGE satellite spin axis orientation, based on combined synodic frequencies determined from observations conducted on January 28, 2006, was within 8.5º of the last known spin axis orientation reported by NASA on December 12, 2005. They reported that IMAGE's spin axis orientation remained stable during the 170 days after NASA's final telemetry reception [19]. NASA sent commands to the spacecraft to attempt to increase its spin rate to 0.52 revolutions·min^{-1}. Hall, et al. reported that IMAGE's spin rate did not increase. This suggests that either the spacecraft did not receive this command or was unable to increase the spin rate.

In Earl and Wade (2015), the apparent angular accelerations of four inactive box-wing GEO satellites were studied. It was concluded that SRP was a primary contributor to a net external torque causing each of the accelerations. In the case of box-wing GEO satellites, the epoch method might not be a viable option for spin axis orientation determination because of the constantly varying apparent spin periods that are not solely caused by geometry between the satellite, the Sun and the observer. Since inactive GEO satellites appear to move very slowly with respect to an observer when compared with satellites in lower altitude orbits, the primary contributor to the apparent spin period variations would likely be the effects of SRP on the GEO satellites' sidereal spin periods and not the varying geometry. Should this be the case, then an alternative method of spin axis orientation determination will be required. This thesis describes and investigates a geometrical method that relies on very bright specular reflections observed over a number of days.

D   Box-wing Angular Acceleration and Spin Period Variation

Papushev, et al. (2009) presented several reasons for their reported box-wing spin period variations, including: light pressure force (interpreted as the force originating from SRP); Lorentz force acting upon the charged satellite surfaces by the Earth's magnetic field; and micro-jet (internal) forces caused by small fissures in the hermetically sealed satellite buses [3]. They reported that these forces were on the order of between 30 and 100 mdyn (between 0.3 and 1 μN). Papushev, et al. did not present models or calculations that verified the hypothesized spin period variation causes or the force magnitude range.

In Earl and Wade (2015), the observed angular accelerations of four inactive box-wing GEO satellites and the maximum possible angular acceleration determined from a first-order box-wing external torque model were presented [6]. It was concluded that SRP was the largest contributor to the observed angular accelerations and therefore contributed to the apparent spin period variations. It was reported that Lorentz forces could not significantly contribute to the angular accelerations,

due to the large distance of the GEO circular orbit radius from the Earth's magnetic poles. The micro-jet hypothesis that was originally proposed by Papushev, et al., was not tested because the four box-wing satellites studied had been inactive for at least four years [6] when the study commenced.

In Earl and Wade (2017), the long term[33] and high temporal resolution[34] broadband photometric observations of 11 inactive box-wing GEO satellites were presented. These observations were conducted to further study the satellites' light curve morphologies and their apparent spin period variations [16]. It was concluded that all 11 satellites' light curves and inferred spin period variations were diverse, when compared to each other, with few similarities [16]. Some satellites' light curves varied slowly over a timescale of weeks or months, while the light curves of other satellites varied more quickly over timescales of minutes or hours. Echostar-2's light curves appeared to be the most stable, with similar features observed over a nearly 4-year timescale. It was suggested in [16] that Echostar-2's spin axis orientation was either nearly constant or that it could have a small precession angle [16].

In Earl and Wade (2015), evidence was presented that suggested that a box-wing satellite's spin angular acceleration (and therefore its spin period variation) is dependent upon; the satellite's orientation with respect to the Sun; the solar panel(s) orientation(s) with respect to the Sun; the solar panels' orientations with respect to each other (if more than one); and the solar panel reflectivity (on each of the panel sides) [6]. A simple first order model was presented to simulate the HGS-1 satellite's spin angular acceleration and its spin period variation from mid-2012 to late-2013. HGS-1 has only one deployed solar panel[35] [6] and therefore is not the typical example of a 2-panel box-wing satellite. Echostar-2 has two fully deployed solar panels.

It was reported in Earl and Wade (2015 and 2017) that Echostar-2's spin period variation appeared to be cyclical [6, 16]. However, the variations were not sinusoidal and included points of inflection where the spin period variation magnitude would appear to decrease for a number of days before resuming its previous rate of change, as illustrated in [16]. Echostar-2's spin period variation amplitude also appeared to decrease over time; from 156.2s in 2012-13 to 39.4s in 2015, as described in [16]. This decrease appeared to correlate with the overall decrease in Echostar-2's average spin period.

In Earl and Wade (2017), a strong quantitative relationship between Telstar-401's light curve morphology and its spin period was reported, which suggested a quantitative relationship between the satellite's attitude and its spin period variation [16]. This relationship suggested that SRP was varying Telstar-401's attitude, which in turn was varying the satellite's spin period over time. A similar, albeit weaker, correlation was also found for Echostar-2 [16].

---

[33]Early March 2012 to early January 2016.

[34]One observation of each satellite per week, weather and access permitting.

[35]HGS-1's southern solar panel could not be deployed after launch.

CHAPTER 3: PHOTOMETRIC OBSERVATIONS

As of April 2017, no mission has conducted up-close imaging or has performed a rendezvous with any satellite (including box-wing) in a GEO orbit. A number of ground-based efforts involved observing the light curve characteristics of a number of American and Russian box-wing GEO satellites. One goal of these observations was to qualitatively assess their attitude dynamics prior to OOS missions that would rendezvous with GEO satellites [4, 5].

Results inferred from some previously published light curves of inactive satellites were not accompanied by suitably long term and/or high temporal resolution observations. These previous observations included: long term (more than one year) with a low temporal resolution (a maximum of two observations per month), short term (several weeks to several months) with at least one observation per month, or short term with a low temporal resolution. Prior to 2015, no results from a photometric survey conducted over the long term (greater than one year) combined with a high temporal resolution (at least one observation per week per satellite, weather and access permitting) had been published.

One goal of this thesis was to conduct a long term and high temporal resolution photometric survey of a large sample of inactive box-wing GEO satellites exhibiting synodic (apparent) spin periods of greater than 100s. The survey contained a total of 11 satellites with synodic spin periods of between 145s and 4315s. The survey was conducted from March 5, 2012 to January 3, 2016. The results based on this survey confirmed all of the results previously published and discovered phenomena that included a significant quantitative relationship between a box-wing satellite's light curve morphology and its spin period variation.

This Chapter focuses on: the photometric observations of AS-7000 and HS-601 box-wing satellites obtained for this thesis; a comparison of three spin period determination methods; the comparison of the satellites' light curve morphologies, the spin period variations and spin angular accelerations; and the relationship between light curve morphology and spin period variation. This Chapter was initially formatted as a research paper, which is currently in peer review for publication in the American Institute of Aeronautics and Astronautics' (AIAA's) Journal of Spacecraft and Rockets (JSR).

Analysis of the Long Term Photometric Variations of Inactive Box-wing Geosynchronous Satellites

Michael A. Earl* and Gregg A. Wade†

Royal Military College of Canada, Kingston, Ontario, Canada, K7K 7B4

This paper has been submitted, both in its full form and as a technical note, to the American Institute of Aeronautics and Astronautics' Journal of Spaceraft and Rockets. Peer review is currently in progress.

A   Introduction

NEARLY 60 years after the launch of the first Sputnik, Space Situational Awareness (SSA) continues to protect our highly valuable active satellite population from threats that include satellite collision, malevolent physical interference, and communications interference. SSA includes space object characterization, which can be used to determine a satellite's identity, nation of origin, status (active or inactive), orbit characteristics, attitude (orientation), size, and/or component make-up. The ability to perform suitably high resolution SSA (including space object characterization) has recently become much more important, and more complicated, due to the Chinese anti-satellite (ASAT) test on Fengyun-1C and the Iridium-Cosmos satellite collision. The GEO population is steadily increasing due to its continued and increasing importance to the telecommunications industry and due to the consequently increasing number of spent rockets and payloads in the GEO graveyard orbits. An important component of GEO spacecraft characterization is long term and high cadence observation that can be used to study the light curve morphology and spin period variability of GEO debris and to test the reliability of attitude dynamics models. The reliability of such models could mean the difference between a successful and failed OOS mission.

The GEO population consists of satellites orbiting at approximately 35,785 km in altitude with nearly circular prograde orbits inclined at between 0° and 15° from the Earth's equatorial plane[36][37]. Approximately 95% of orbiting satellites is comprised of inactive debris [21], including some of the GEO box-wing satellites (illustrations shown in [6, 22]). Ground-based photometric observations of some inactive box-wing GEO satellites have been reported since the early 1990s. A number of observation programs have been conducted in advance of OOS missions to GEO to begin a qualitative assessment of their attitude dynamics [4, 5].

B   Background

1   Previous Research

Papushev, et al. (2009) surveyed the long term variability of the optical characteristics of a number of inactive Russian Raduga, Gorizont, and Ekran satellites from 1990 to 2004 by obtaining

---

*PhD Candidate, Department of Physics, Royal Military College of Canada, P.O. Box 17000 Station Forces Kingston, Ontario, Canada, K7K 7B4.

†Professor and Department Head, Department of Physics, Royal Military College of Canada, P.O. Box 17000 Station Forces Kingston, Ontario, Canada, K7K 7B4.

[36]JFCC SPACE/J3, Space Track, https://www.space-track.org, Accessed 03/25/16.

[37]The first three Sirius radio satellites are also GEOs, despite orbit eccentricities of 0.27 and orbit inclinations of nearly 65°.

high temporal resolution broadband light curves [3]. They observed a large and periodic brightness variability, which suggested spinning motion. They reported that the satellites' inferred (synodic) spin periods slowly varied over time [3]. However, when they observed Raduga-14, they noticed a sudden and significant spin period increase, then a sudden decrease over a several day interval [3]. Their light curves exhibited broad features (relative to a full inferred spin period) with amplitudes of between 2 to 3 magnitudes (between 14th and 11th visual magnitude) adjacent to features that were thin, sharp, and tall (relative to the broad features) with amplitudes between 4 and 8 magnitudes (between 14th and 6th magnitude for Raduga-14) [3]. They attributed the tall, sharp features to specular sunlight reflections (glints) from the large-area solar panels [3]. The estimated synodic spin periods of the Raduga, Gorizont, and Ekran satellites fell into a broad range of between 0.3 minutes and 7.2 minutes. A single broadband light curve of Raduga-18, observed by Payne, et al. (2007) on June 7, 2007, exhibited shapes that were similar to those obtained by Papushev, et al. but was reported by Payne, et al. to have a synodic spin period of approximately 30 minutes [14].

Binz, et al. (2014) surveyed a number of American box-wing satellites from January to May 2012 [5]. Some of their reported inferred (synodic) spin periods were longer than those reported by Papushev, et al. (up to 100 minutes), while other satellite periods could not be determined. Synodic spin period variations were not reported.

Cognion (2014) surveyed the American GOES-8, 9, 10, 11, and 12 satellites from December 2013 to August 2014 [4]. GOES satellites have a single solar panel and a small solar sail which balances the SRP torque from the solar panel, as described in [4]. Cognion observed adjacent broad and sharp light curve features that appeared to be similar to those observed by Papushev, et al. and Binz, et al. Cognion reported that the GOES satellites' light curves, when phased according to their inferred (synodic) spin periods, appeared to be unexpectedly different from each other, suggesting a "very different rotational behavior" [4]. GOES-8 and GOES-10 light curves revealed repeating patterns from cycle to cycle. The five satellites' synodic spin periods and spin period variability rates were reported to differ significantly. Ryan and Ryan (2015) estimated GOES-8's synodic spin period to be 22.951±0.001s, based on observations made on April 24, 2014 [15]. This period was between the 16.48s and 75.66s values which were reported by Cognion in February and July 2014, respectively. This suggests that GOES-8's synodic spin period was increasing over the first half of 2014. Ryan and Ryan could not infer GOES-8's spin period from a light curve obtained on September 12, 2015 because a repeating pattern could not be identified [15]. Similarly, Cognion's observations of GOES-9, 11, and 12 revealed light curves that varied significantly from cycle to cycle. Cognion had reported that most of the GOES satellite synodic spin periods appeared to be between several minutes and tens of minutes, and that the spin period determination of GOES-12 was unsuccessful [4].

2 This Research

In this paper, the term "broadband" was defined to refer to an unfiltered optical system with a detected flux spanning the entire detectable optical spectrum. From March 2012 to December 2013, Earl and Wade (2015) conducted broadband photometric observations of four inactive box-wing satellites; Solidaridad-1, Telstar-401, Echostar-2, and HGS-1 (formerly Asiasat-3) (Table 2) with the equipment and observation procedure described in [6][38]. Broadband (rather than color) observations were conducted to allow long term and high temporal resolution imaging (to minimize the possibility of aliasing), and to allow a rigorous observation schedule (a minimum of one observation per week per satellite, weather and access permitting). These satellites also appeared to be spinning with diverse synodic spin periods ranging from 2.4 minutes (Telstar-401) to 30.8 minutes

---

[38]also Earl, M., Observation and Analysis of the Spin Period Variations of Inactive Box-wing Telecommunications Satellites in Geosynchronous Orbit, MSc thesis, RMCC, May 2013, http://www.castor2.ca/08_Papers/earl_thesis.pdf, Accessed 03/27/16.

(HGS-1) [6]. Their synodic spin periods were consistently and smoothly varying, but the spin periods did not vary as suddenly as Papushev had reported for Raduga-14. In all four cases, the spin period could be determined with ease, in contrast with the difficulties reported by Cognion, Binz, and Ryan and Ryan. The spin period variations of Telstar-401, Echostar-2, and HGS-1 appeared cyclical, while Solidaridad-1's spin period variations appeared secular [6].

Results from the aforementioned box-wing studies suggested complex rotational behavior with unknown origins. In this study, the aim is to establish the empirical foundations to develop a more accurate theoretical model of the rotational dynamics of inactive box-wing GEO satellites. The time baseline of high cadence photometric observations of the original four satellites has been significantly extended. The satellite sample size has nearly tripled (refer to Table 2); however, the focus on AS-7000 and HS-601 bus designs (refer to Fig. 4) remains. The monitoring of the long term spin period variability of the initial four satellite sample was continued in order to evaluate and confirm periodicity and long term trends. The linear trend originally proposed by Earl and Wade (2015) [22] was re-evaluated using the new photometric data. A search for systematics in the light curve morphology and variability that are attributable to specific bus design is described in which relationships between light curve and spin period evolution behavior are identified. The research began with the determination of instantaneous synodic spin periods of each satellite implicitly evaluating three different methods of period determination. Next, an examination of the short term and long term behavior of the morphology of their rotational light curves was conducted. Finally, a characterization of the satellites' rotational period evolutions and a search for relationships between light curve morphology (which can be associated with satellite orientation and observational geometry) and spin period behavior was conducted.

All observed spin periods presented in this paper have not been corrected for the synodic effect. Therefore, all mention of spin periods for the remainder of this paper are to be understood to mean synodic spin periods.
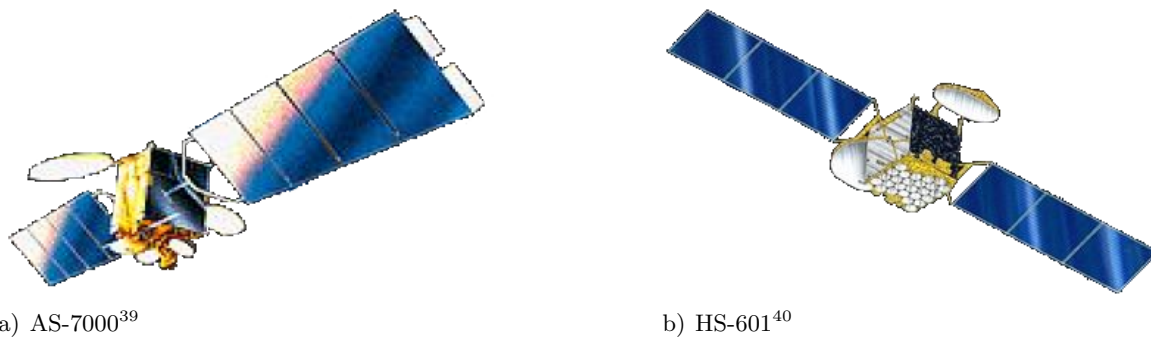

a) AS-7000[39]   b) HS-601[40]

Figure 4 Artists' conceptions of AS-7000 and HS-601 models

C Box-wing Satellite Selection

Additional broadband photometric observations of the satellites studied by Earl and Wade (2015) were conducted from January 2014 to January 2016 with the same equipment and observation procedure described in [6, 22]. Seven satellites were added to the sample, totaling 11 satellites (five AS-7000 and six HS-601), allowing light curve comparisons between satellites of similar design and from two different manufacturers. The three additional AS-7000 satellites (Table 2) were

---

[39]Encyclopedia Astronautica, AS-7000, http://www.astronautix.com/a/as7000.html, Accessed 09/14/16.

[40]Encyclopedia Astronautica, HS-601, http://www.astronautix.com/h/hs601.html, Accessed 09/14/16.

chosen because they were predicted to have inaccessibility times of less than 100d. Furthermore, Telstar-402R and Telstar-401 had identical designs[41]. All of the satellites studied are shown in Table 2.

DirecTV-2 was suggested as an additional satellite of interest by Dr. Mark Skinner, who observed it in both the thermal IR (8 to 13 μm) and the visible wavelengths [21, 23]. One year after it was retired, Solidaridad-2 was suggested as an additional satellite of interest by Dr. Jeremiah Salvatore[42] because it has an identical design to Solidaridad-1[43]. Light curves of a satellite that had been inactive for nearly 15 years (Solidaridad-1) could then be compared with those of an identical satellite that had been inactive for only one year (Solidaridad-2).

Table 3 lists the inclination (i), the eccentricity (e), the mean motion (n), the local observed azimuth, and the inactivity status of each of the 11 satellites. The two values listed for each satellite's inclination, eccentricity, and mean motion refer to those orbit elements at the beginning observation date and the ending observation date, respectively, listed for the corresponding satellite in Table 2. The two values listed for each satellite's local azimuth refer to the minimum and maximum azimuths that were observed in the local observing venue's sky over the total observation range shown in Table 2. A value of 'All' refers to a satellite that can appear to orbit the observer over several weeks because it is no longer a truly GEO satellite. The satellites' inclinations also refer roughly to the absolute values of the apparent equatorial declination. There are two specific values for the final status column in Table 3. The value DT (drifting) refers to a GEO satellite that had suffered a malfunction such that it could not be maneuvered into the GEO graveyard orbit. As a result, the GEO satellite drifted within the geostationary belt and natural forces varied the satellite's orbit elements. The value GY (graveyard) refers to a GEO satellite that had been maneuvered into the GEO graveyard orbit after it had been decommissioned. Note the distinct difference between the mean motions of the DY satellites and those of the GY satellites. All of the satellites' orbits remained nearly circular (orbit eccentricity of nearly 0) after several years. HGS-1's relatively large eccentricity is likely due to the manner in which its orbit was initially circularized. HGS-1's orbit was circularized from geostationary transfer orbit using the Moon's gravity because the satellite's 4th rocket stage malfunctioned during the final Hohmann transfer phase.

Table 3 indicates that all of the satellites' orbit inclinations were increasing by several degrees over several years, their orbit eccentricities remained roughly circular, and all of their mean motions were fairly constant over a long time frame. However, some of the eccentricities increased and others decreased, possibly because of external perturbations, including those due to J2 and SRP effects.

---

[41]Telstar-401 and Telstar-402R were part of the "Telstar-4" series.

[42]Solidaridad-2 was retired in December 2013.

[43]Personal correspondence with Dr. Jeremiah Salvatore, retired Boeing senior research fellow: October 23, 2014.

[44]North American Aerospace Defense Command.

[45]Committee on Space Research.

[46]Direct Broadcast Satellite

[47]High power version of HS-601 containing larger solar panels.

[48]Only one solar panel successfully deployed after launch and rescue from the GEO transfer orbit.

Table 2 Satellite sample

NORAD[44]	COSPAR[45]	Common Name	Design	Observations (mm/dd/yy)
22911	1993-073-A	Solidaridad-1	HS-601	06/16/12 to 09/23/15
22927	1993-077-A	Telstar-401	AS-7000	03/05/12 to 09/23/15
23192	1994-047-A	DirecTV-2 (DBS-2)[46]	HS-601	11/14/14 to 01/08/16
23313	1994-065-A	Solidaridad-2	HS-601	11/14/14 to 11/04/15
23670	1995-049-A	Telstar-402R (Telstar-4)	AS-7000	07/16/13 to 10/12/15
23723	1995-064-A	AMOS-5i (Asiasat-2)	AS-7000	10/01/13 to 10/10/15
23764	1996-002-A	Intelsat-3R (PAS-3R)	HS-601HP[47]	02/16/13 to 10/13/14
23779	1996-006-A	Paksat-1 (Anatolia-1)	HS-601	10/11/13 to 10/12/15
24313	1996-055-A	Echostar-2	AS-7000	03/11/12 to 11/04/15
24846	1997-031-A	Intelsat-802	AS-7000	01/20/15 to 11/04/15
25126	1997-086-A	HGS-1 (Asiasat-3)	HS-601HP[48]	06/16/12 to 11/04/15

D   Comparison of Spin Period Determination Methods

Spin period determination involves the careful analysis of light curves in order to identify repeating characteristics over a suitable timescale that indicate a satellite's likely synodic rotation period. This process can involve visual (manual) inspection of the light curve or more automated methods, such as Fourier analysis. Three methods of spin period determination were evaluated: P-P, L-S (discrete Fourier), and CRT.

Table 3 Satellite orbit particulars

Common Name	i (°)	e (10^{-3})	n (orbits·d^{-1})	Local Azimuth (°)	Status
Solidaridad-1	10.2-12.2	0.4517-1.0227	1.00266-1.00274	216-220	DT
Telstar-401	12.3-14.2	1.2701-0.8702	1.00269-1.00266	210-236	DT
DirecTV-2	6.8-7.4	1.0314-1.0965	0.98633-0.98635	All	GY
Solidaridad-2	5.6-6.2	0.4640-0.6098	0.98864-0.98863	All	GY
Telstar-402R	8.6-10.0	0.3882-0.5867	1.00296-1.00302	195-237	DT
AMOS-5i	2.5-3.9	0.5864-0.9958	0.99308-0.99303	All	GY
Intelsat-3R	3.0-4.3	1.0709-1.5088	0.99088-0.99085	All	GY
Paksat-1	1.6-3.1	1.1058-0.9655	0.99594-0.99592	All	GY
Echostar-2	3.2-5.9	0.4388-0.4106	1.00344-1.00242	158-275	DT
Intelsat-802	3.3-3.9	2.8259-2.8671	0.98110-0.98108	All	GY
HGS-1	4.1-6.7	4.6425-4.0112	1.00280-1.00289	130-270	DT

Photometric analyses of raw broadband CCD images were performed using MATLAB software that is described in [6, 22][49]. The software automatically detects the satellite of interest within the images and sequentially extracts the photometric data. Significant modifications were made early

---

[49]also Earl, M., Observation and Analysis of the Spin Period Variations of Inactive Box-wing Telecommunications Satellites in Geosynchronous Orbit, MSc thesis, RMCC, May 2013, http://www.castor2.ca/08_Papers/earl_thesis.pdf, Accessed 03/27/16.

in 2015 that included automated light curve generation, user-friendly interfaces, and a spin period determination module. An example light curve from this software resulting from Echostar-2 raw photometric data obtained on April 29, 2015, is shown in Fig. 5 (a).

The spin periods of all 11 satellites shown in Table 2 were inferred from the high cadence broadband photometric measurements. Example illustrations of the three spin period methods are shown in Fig. 5 (b), (c), and (d). The "Power" axis in Fig. 5 (c) refers to the significance value of the specific frequency shown in the horizontal axis. A Power value of 1 or greater refers to a significant frequency.
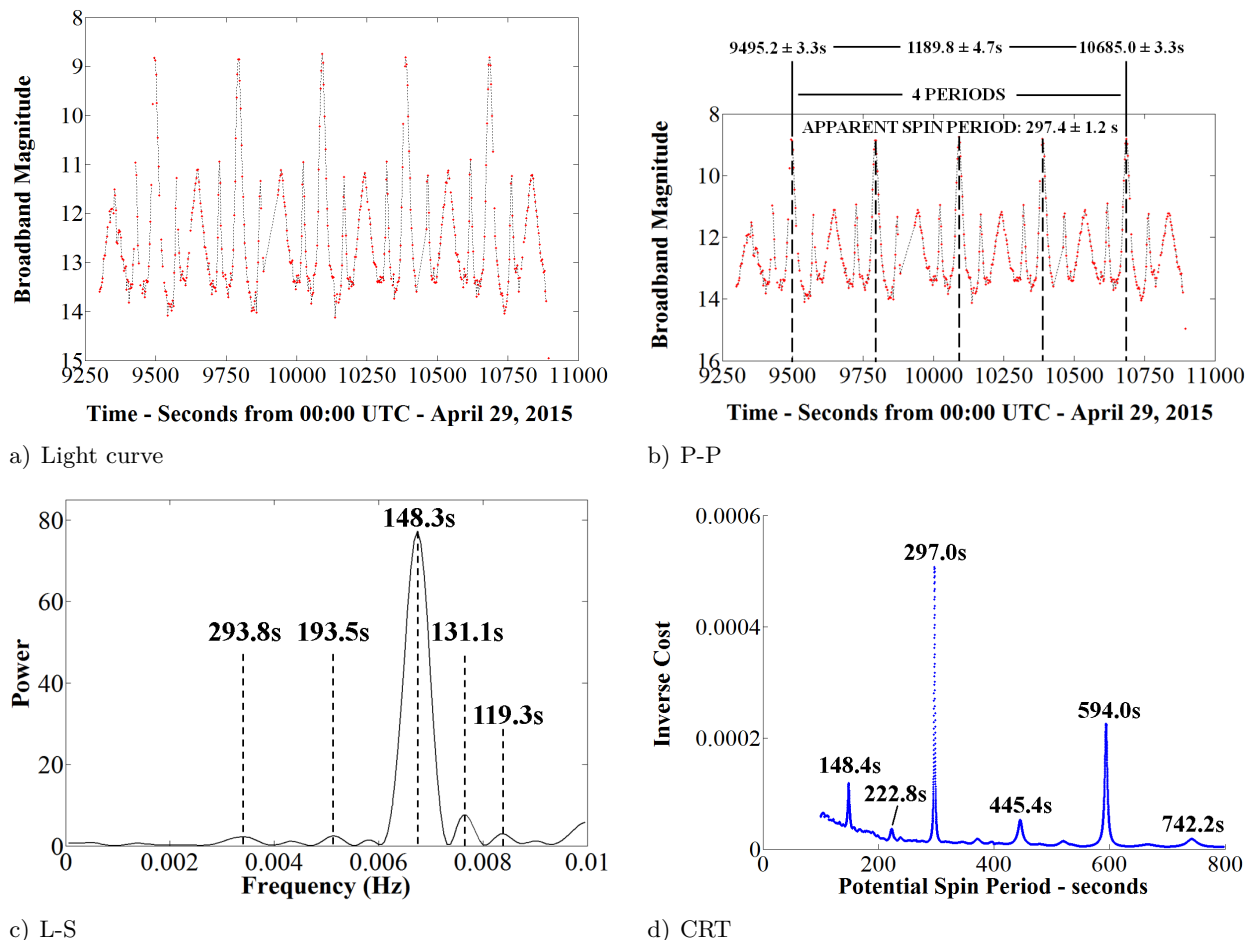

a) Light curve

b) P-P

c) L-S

d) CRT

Figure 5 Echostar-2 example light curve and spin period determination methods

1 Peak-to-Peak

The P-P method, described in [6][50] and illustrated in Fig. 5 (b), estimates the spin periods by the visual inspection of light curves to identify repeating (cyclical) characteristics. Once a repeating pattern has been identified, two similar light curve features, each containing a clearly visible maximum (typically from a thin, sharp feature due to a specular reflection), are chosen; one near the light curve's temporal beginning and the other near its temporal ending. Aliasing, due to a sampling rate less than the spin period's Nyquist frequency, is especially important when considering

---

[50]also Earl, M., Observation and Analysis of the Spin Period Variations of Inactive Box-wing Telecommunications Satellites in Geosynchronous Orbit, MSc thesis, RMCC, May 2013, http://www.castor2.ca/08_Papers/earl_thesis.pdf, Accessed 03/27/16.

this method. High resolution imaging was required to detect the maximum (broadband) detected signal and to minimize aliasing concerns. The temporal difference between these two extreme maxima is then divided by the integer number of cycles between the two maxima, assuming that the light curve has no significant gaps between the two chosen extreme maxima. Figure 5 (b) illustrates this process by identifying similar maxima of Fig. 5 (a) that are four cycles apart. The temporal uncertainty of each light curve data point was assumed to be 3.32s, the duty cycle of the CCD used to obtain the raw images, because the exact location of a light curve maximum could conceivably lie between the data points immediately adjacent to the apparent (chosen) maximum data point. The spin period of the light curve shown in Fig. 5 (a) was estimated by the P-P method (Fig. 5 (b)) to be 297.4±1.2s.

For those light curves with easily identifiable repeating cycles, the P-P method was assumed to be the most reliable spin period determination method because the method relied on visual (manual) inspection of the light curves. However, visual inspection is not practical when automating the spin period determination process. Two automated methods of spin period determination, specifically the L-S[51] (L-S) method, described in [22], and the CRT, described in [5], were used alongside the P-P method to determine the reliability of each of the three methods.

2   Lomb-Scargle

The L-S method uses a discrete Fourier transform to infer the most significant light curve frequencies (reciprocal of the periods) between 0 Hz and a user-specified upper frequency boundary. Figure 5 (c) illustrates the L-S periodogram of the example light curve shown in Fig. 5 (a), showing the most significant light curve frequencies, which were between 0 Hz and 0.01 Hz, and their corresponding periods. Figure 5 (c) suggests that the most significant potential spin period (corresponding to the largest periodogram maximum) is 148±5s. The uncertainty was determined from the full width at half maximum (FWHM) of the distribution corresponding to the highest power in the periodogram (the greatest power spectrum maximum) shown in Fig. 5 (c). The spin period corresponding to the largest periodogram significance (148±5s) was close to half of the period determined by the P-P method (297.4±1.2s) and had an uncertainty that was over 4 times larger than that from the P-P method. The periodogram in Fig. 5 (c) also suggests a period (293.8s) that differs by several seconds from the period determined by the P-P method. However, this L-S-determined period corresponds to a distribution maximum that has a much lower power (significance) when compared to the maximum power in the periodogram. Using multiple trials with different satellite light curves, it was determined that the L-S method was likely to indicate a statistically significant period which was approximately half the period identified by the P-P method. The investigation concluded that the L-S method was not as reliable as the P-P method when analyzing easily inferred light curve periods and therefore it could not be used for automated spin period determination.

3   Cross-Residual Technique

The CRT compares a temporal section of a light curve (for example, from a light curve's commencement to a potential spin period time (T) afterward) with subsequent sections of the same temporal duration, as described in [5]. This is done to automatically identify repeating patterns in the light curve, similar to the visual process in the P-P method, except that the comparisons are performed throughout the light curve, data point by data point.

---

[51]Specifically, the MATLAB 'lombscargle.m' L-S analysis program, originally written by Dr. Brett Shoelson, was modified for this analysis. http://www.mathworks.com/matlabcentral/fileexchange/993-lombscargle-m/content/lombscargle.m. Accessed 04/03/16.

A "cross-residual" (ϵ) (determined with Eq. (1)) is the difference between the measured broadband magnitude (m_{B}) at a time t_{j} and the measured broadband magnitude at time $t_{\mathrm{j}} + T$, as described in [5]. Most cross-residuals should be small (possibly near 0) when the time T is nearest to some multiple of the satellite's possibly true spin period. However, if the light curve characteristics change significantly over several cycles, then the minimum residuals will likely occur by comparing adjacent cycles. A "cost function" is the sum of the squares of all cross-residuals corresponding to a chosen potential spin period (T). The cost function is therefore minimized by choosing the spin period value (T) that minimizes the sum of these cross-residuals. The inverse of this cost function (J) (shown in Fig. 5 (d)) better discriminates the smaller cost function values and shows the most likely light curve period as a maximum rather than as a minimum.

The number of cycle comparisons (N) performed within a light curve will decrease as the potential period (T) increases. In order to maintain a fair comparison between all of the determined costs, a cost function average is calculated by dividing the cost function by N for each potential period. Equation (2) calculates the reciprocal of this cost function average. This process is similar to that described in [5].

$$\epsilon(t_{\mathrm{j}}) = m_{\mathrm{sat}}(t_{\mathrm{j}} + T) - m_{\mathrm{sat}}(t_{\mathrm{j}}) \tag{1}$$

$$J = N \left\{ \sum_{\mathrm{i}=1}^{\mathrm{N}} \sum_{\mathrm{j}=1}^{\mathrm{T}} \left[\epsilon_{\mathrm{i}}(t_{\mathrm{j}}) \right]^2 \right\}^{-1} \tag{2}$$

Figure 5 (d) illustrates the resulting CRT periodogram of the light curve shown in Fig. 5 (a), showing the most significant light curve periods. Figure 5 (d) suggests that the most significant potential spin period is 297.0±0.8s. The uncertainty was determined from the FWHM of the distribution corresponding to the highest inverse cost (J) in the periodogram shown in Fig. 5 (d). This spin period appeared consistent with (within 1s of) the 297.4±1.2s period determined by the P-P method. The periodogram in Fig. 5 (d) also indicates a half-period (148.4s) similar to that indicated by the L-S method; however its maximum inverse cost is significantly smaller than that corresponding to the 297.0s period. The CRT method typically identified the most likely light curve periods as those within 1s of those identified by the P-P method. However, the CRT had problems identifying periods from those light curves that exhibited varying amplitudes or varying phases between adjacent cycles. In these circumstances, the P-P method was preferred.

E   Phase Plots

A "phase plot" is a rotation-phased folded light curve whose temporal segments (with durations of the inferred period) are stacked (the process of light curve folding) such that the full horizontal axis corresponds to a single inferred period. Each was assigned a "phase percentage" (P) data point, according to Eq. (3). This allows us to more easily compare a satellite's light curve morphology over numerous spin periods. Each phase plot data point consisted of a "phase percentage" (P) (the percentage of the inferred period, ranging from 0% to 100%) coordinate, on a plot's horizontal axis and a broadband magnitude coordinate on a plot's vertical axis. Light curves were folded according to Eq. (3), where t_{lc} denotes the original light curve time coordinate, t_{ph} denotes a phase offset time (primarily used for phase-aligning two or more different phase plots), and T denotes the inferred light curve period. The "frac" operator refers to keeping only the decimal component of the result (subtract the integer portion).

$$P = (100\%) \ \mathrm{frac} \left\{ \frac{(t_{\mathrm{lc}} - t_{\mathrm{ph}})}{T} \right\} \tag{3}$$

A "coherent" phase plot was defined as a phase plot whose individual cycles (ranging from 0% to 100%) appear similar to each other in shape, amplitude, and phase. Consequently, an "incoherent

phase plot" was defined as a phase plot whose individual cycles appear significantly different from the others, in shape, amplitude, and/or phase.

All of the broadband photometric light curves, corresponding to the satellites shown in Table 2, were folded to produce phase plots. Example AS-7000 phase plots are shown in Figs. 6 (Telstar-401), 7 (Telstar-402R), 8 (AMOS-5i), 9 (Echostar-2), and 10 (Intelsat-802). Example HS-601 phase plots are shown in Figs. 11 (Solidaridad-1), 12 (DirecTV-2), 13 (Solidaridad-2), 14 (Intelsat-3R), 15 (Paksat-1), and 16 (HGS-1). Several phase plots of each satellite illustrate the variation of the light curve morphology over time; especially over different seasons. Each phase plot sub-caption indicates, from left to right; the observation's beginning and ending times (UTC) (hh:mm) indicating the image collection duration; the Gregorian date (mm-dd-yy) of the observation; the Julian day of the observation, elapsed since 00:00 UTC January 0, 2012 (December 31, 2011 or Julian date 2455926.5); the determined spin period; and the average (of the beginning and the ending of the observation) topocentric (azimuth and elevation) coordinates from the observation location. The default broadband magnitude range depicted is 17 (faintest) to 8 (brightest). The nearest integer broadband magnitude is indicated for those observations brighter than 8th magnitude. The majority of the 11 satellites show coherent phase plots, while a minority have shown incoherent phase plots, significantly varying in amplitude and/or phase from cycle to cycle.

A phase plot's phase depended on when (during the satellite spin) the observations had commenced. It was therefore very unlikely that a number of light curves of the same satellite obtained over a number of days would have the same phase. In order to allow easier and more convenient comparisons between phase plots, each satellite's phase plots were synchronized with each other by phase-shifting them in time (by varying the t_{ph} coordinate) such that a reference phase percentage was assigned to a specific repeating light curve feature (such as a specific brightness maximum).

1 AS-7000 Phase Plot Analysis

Telstar-401 and Telstar-402R (phase plots shown in Figs. 6 and 7, respectively) have identical designs[52]. Each became inactive due to catastrophic malfunction [24], but their phase plots appear to have different shapes and behaviors. This finding is similar to what Cognion had reported for the GOES satellites [4]. Typically, Telstar-401's phase plots appeared coherent. Prior to 2015, Telstar-402R's phase plots (Fig. 7 (a) and (b)) appeared incoherent. This finding is similar to what Cognion and Binz had reported for the GOES satellites. In 2015, Telstar-402R's phase plots appeared more coherent (Fig. 7 (c)).

A similarity between Telstar-401's, AMOS-5i's, and Echostar-2's phase plots was noticed when comparing Figs. 6, 8 (b) and (c), and 9, respectively. Each phase plot has two broad features and two thin features, which suggest four sides of a box-wing's cube structure. The two sharp, thin light curve features suggest specular reflections from the satellite box's two mirrored radiators[53] and not the solar panels, because each side of each box-wing solar panel is expected to have a different reflectivity and smoothness [25]. Therefore, the features corresponding to individual sides of a solar panel were expected to be noticeably different from one another. Such an expected difference was inconsistent with the observed similarity of the two sharp, thin features in Figs. 6, 8 (b) and (c), and 9.

---

[52]Encyclopedia Astronautica, Telstar, http://www.astronautix.com/t/telstarseries.html, Accessed 03/18/17.

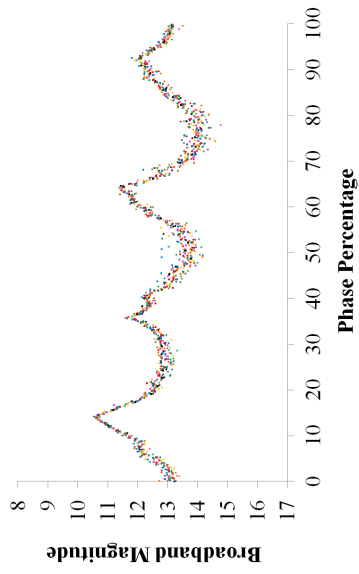[53]The radiators dissipate heat away from electrical components.
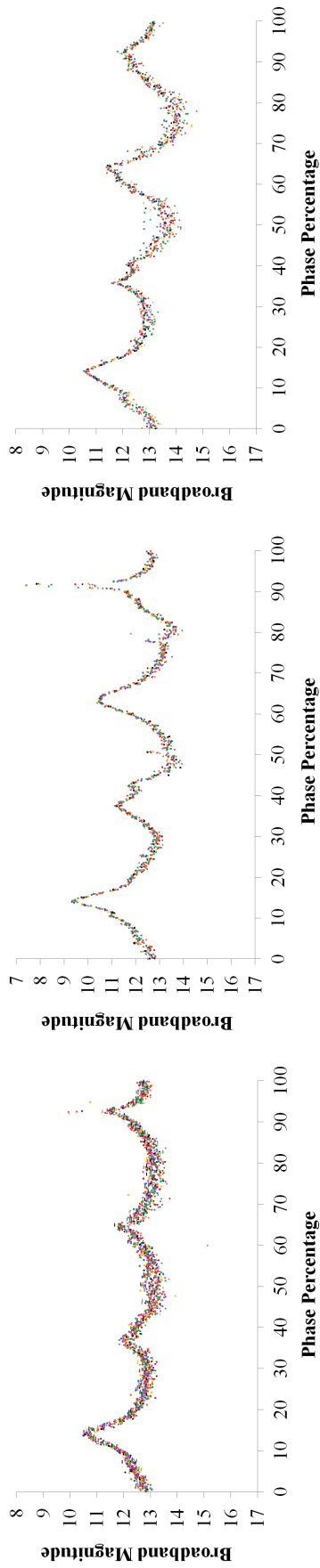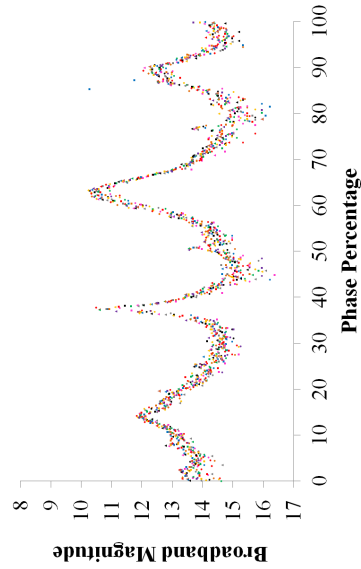
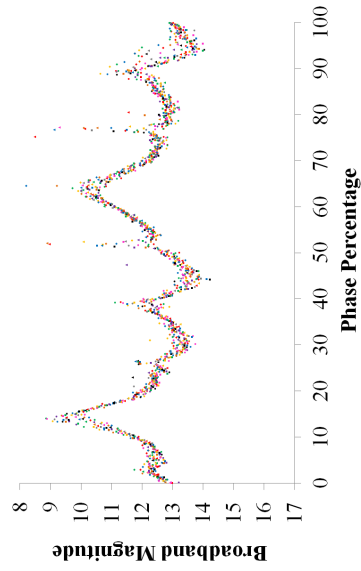a) 04:49-07:06; 06-11-12; 163; 160.9s; 209.6°, 27.8°
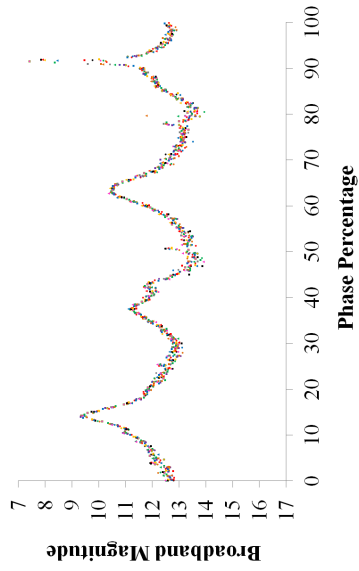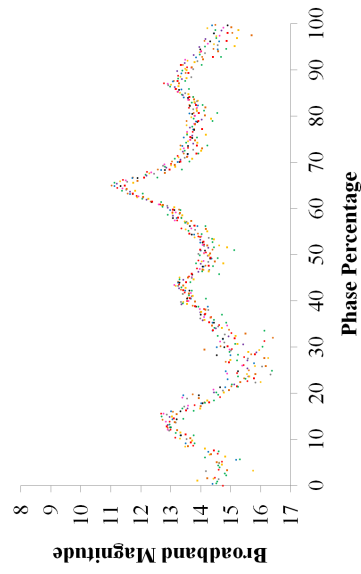
b) 05:10-06:11; 11-14-12; 319; 153.4s; 220.2°, 28.7°

c) 01:59-03:01; 03-30-13; 455; 164.6s; 236.2°, 38.8°

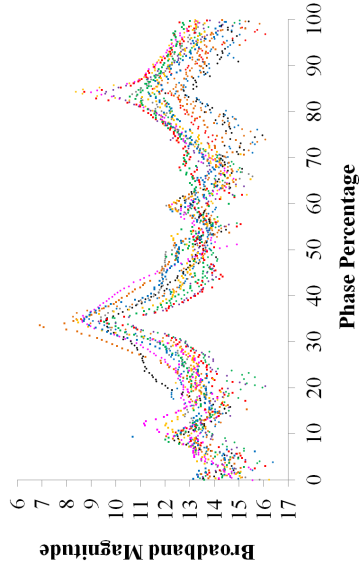d) 04:24-05:39; 08-30-13; 608; 151.2s; 217.1°, 16.5°

e) 04:11-05:41; 02-16-14; 778; 162.0s; 223.1°, 46.5°

f) 02:19-02:58; 07-10-15; 1287; 167.2s; 222.9°, 26.6°

Figure 6 Telstar-401 phase plots

a) 01:43-04:07; 10-29-13; 668; 635s; 195.2°, 31.4°
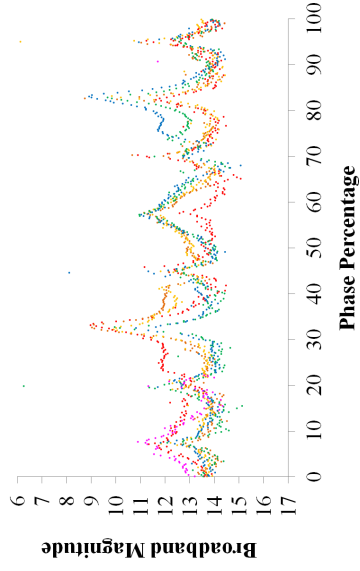
b) 09:24-11:17; 11-15-14; 1050; 1080s; 237.3°, 30.0°

c) 04:51-06:09; 05-14-15; 1230; 1568s; 234.2°, 29.1°

Figure 7 Telstar-402R phase plots
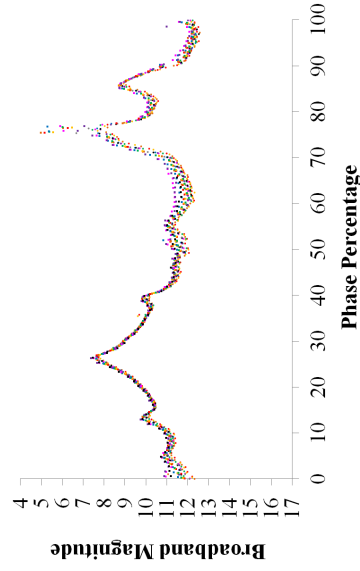
a) 03:34-04:52; 08-24-12; 237; 277.9s; 172.5°, 37.3°
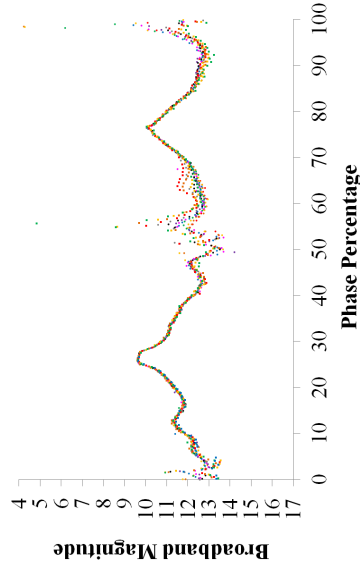
b) 01:41-03:09; 01-21-14; 752; 375.1s; 161.2°, 38.7°
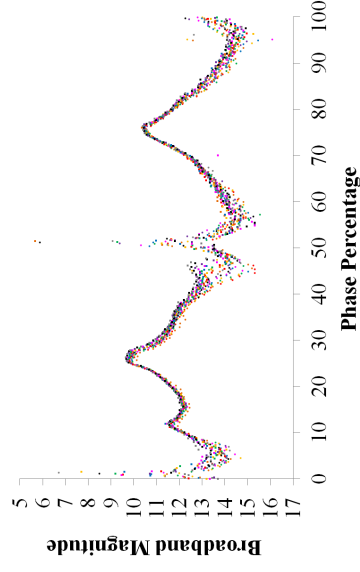
c) 01:19-03:07; 05-07-14; 858; 365.5s; 173.9°, 42.0°

Figure 8 AMOS-5i phase plots

28
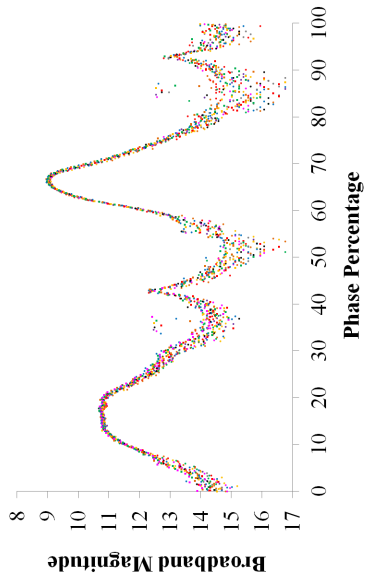
a) 01:37-03:21; 03-12-12; 72; 502.5s; 194.1°, 41.1°

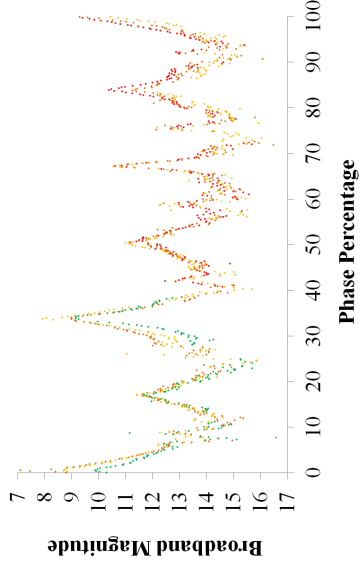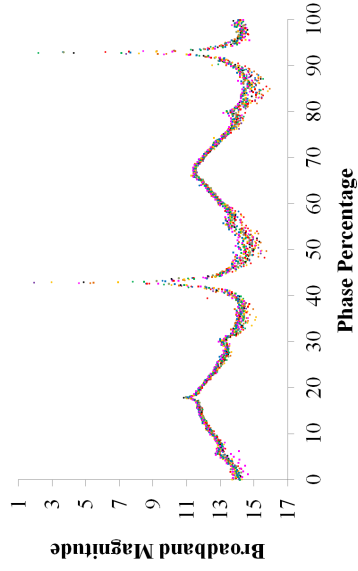b) 01:46-03:21; 09-12-12; 256; 375.9s; 157.6°, 32.6°
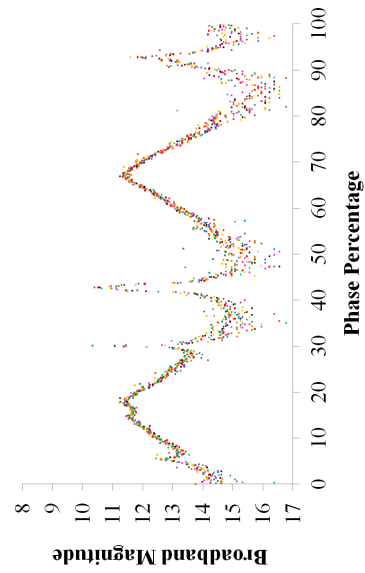
c) 23:16-01:09; 01-02-13; 367-68; 462.8s; 165.4°, 36.1°
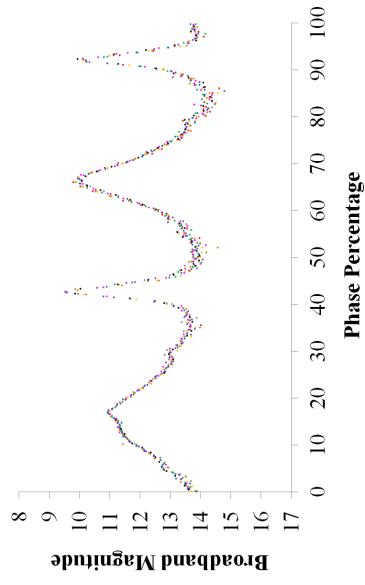
d) 04:40-05:57; 08-11-13; 589; 385.5s; 231.2°, 21.8°
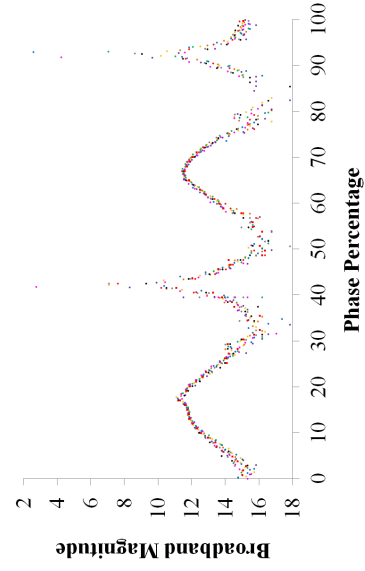
e) 00:29-01:13; 09-17-14; 991; 285.4s; 229.6°, 24.7°
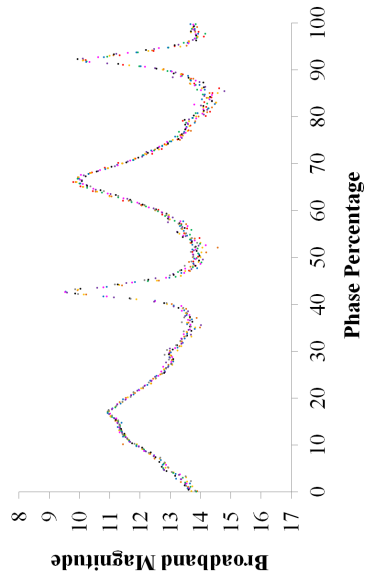
f) 02:09-02:49; 06-20-15; 1267; 292.0s; 157.7°, 35.8°

Figure 9 Echostar-2 phase plots
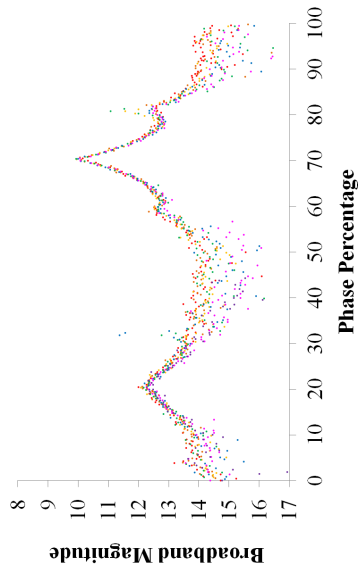
a) 02:03-03:09; 01-21-15; 1117; 611.6s; 118.7°, 22.3°
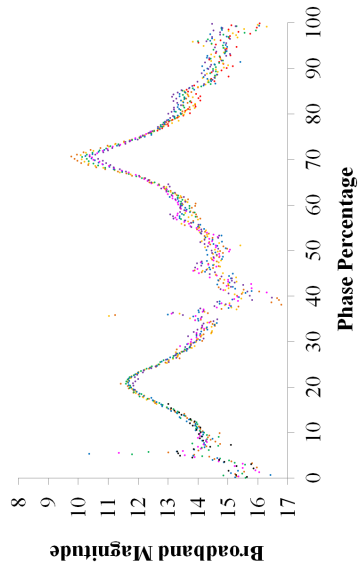
b) 02:21-03:28; 01-29-15; 1125; 624.1s; 198.3°, 38.5°
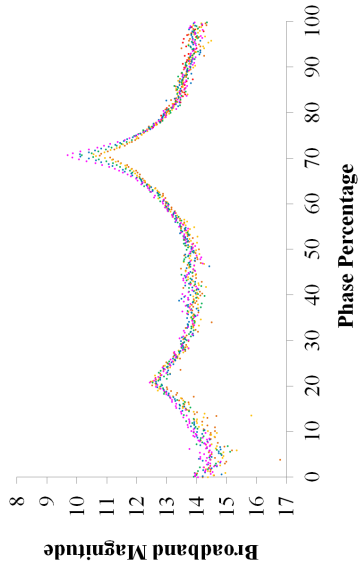
c) 00:15-01:17; 03-12-15; 1167; 690.0s; 150.3°, 38.2°
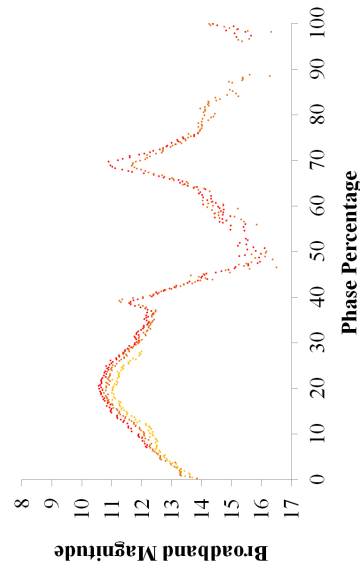
d) 04:34-05:11; 06-20-15; 1267; 993.6s; 230.5°, 27.2°
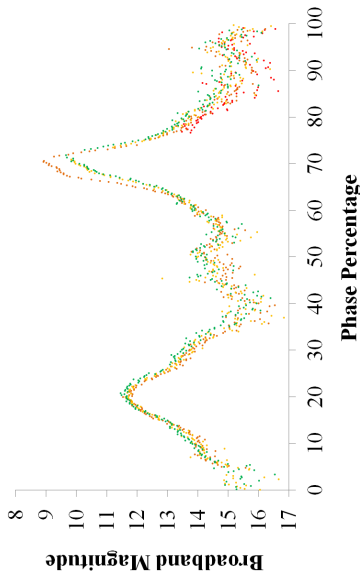
e) 03:58-05:07; 08-07-15; 1315; 1291.1s; 241.9°, 17.0°
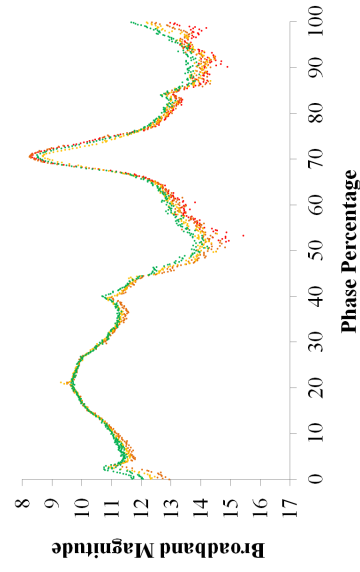
f) 01:18-03:04; 09-15-15; 1354; 1779.9s; 174.2°, 35.1°

Figure 10 Intelsat-802 phase plots

30
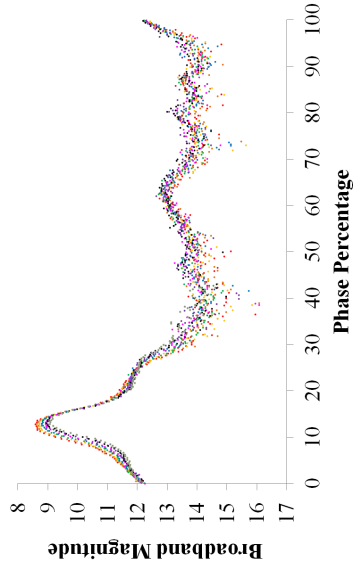
a) 02:23–04:38; 06-15-12; 167; 968s; 218.9°, 35.3°
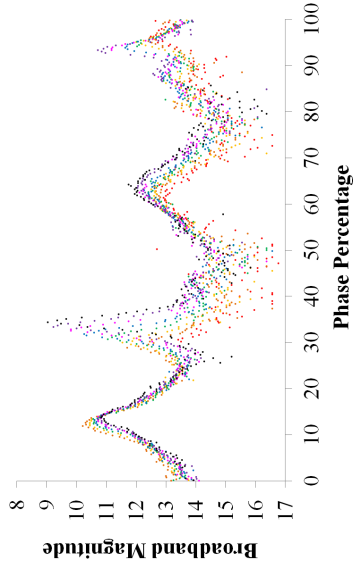
b) 05:17–07:03; 11-07-12; 312; 846s; 219.3°, 27.5°
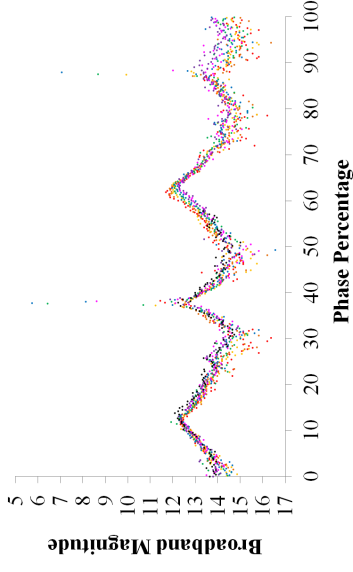
c) 05:11–06:52; 07-14-13; 561; 800s; 216.1°, 22.5°
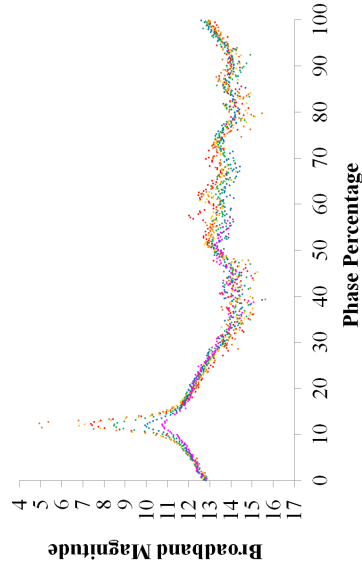
d) 05:40–07:04; 11-04-13; 674; 924s; 215.7° , 30.6°
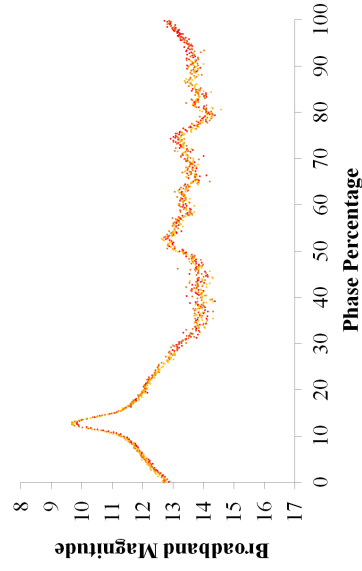
e) 07:06–08:11; 11-15-14; 1050; 1322s; 220.0° , 37.1°
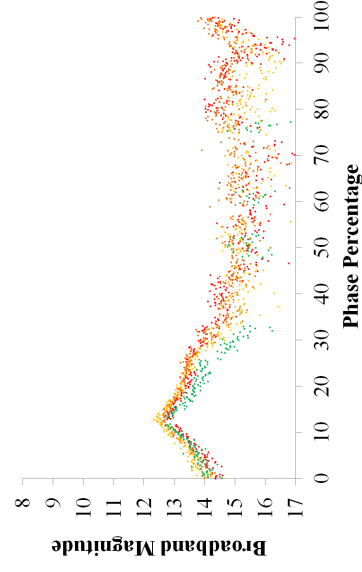
f) 03:01–05:00; 07-10-15; 1287; 1690s; 220.1°, 25.2°

Figure 11 Solidaridad-1 phase plots

31
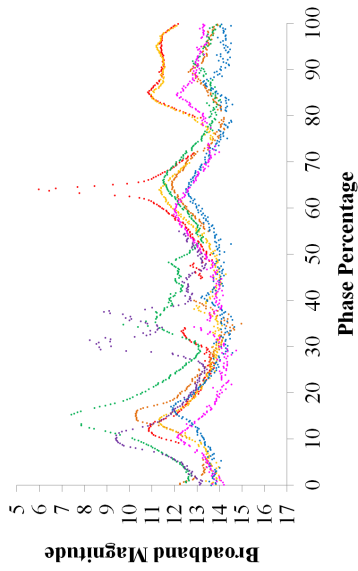
a) 03:20-05:23; 11-15-14; 1050; 1145s; 183.0°, 37.3°
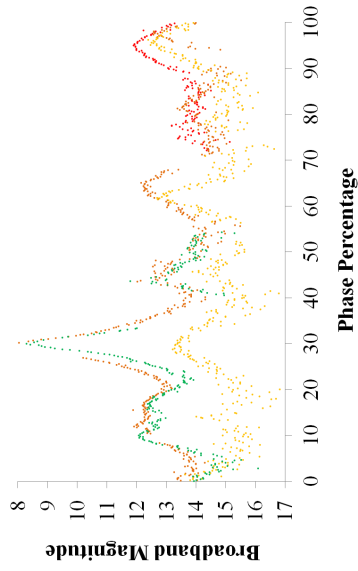
b) 07:09-08:29; 05-23-15; 1239; 1706s; 227.1°, 25.9°
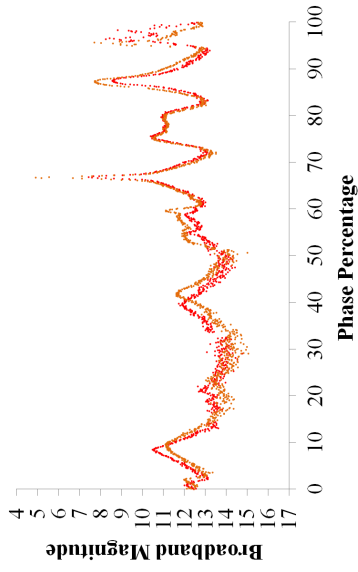
c) 01:51-04:20; 01-08-16; 1469; 4315s; 117.1°, 26.4°

Figure 12 DirecTV-2 phase plots
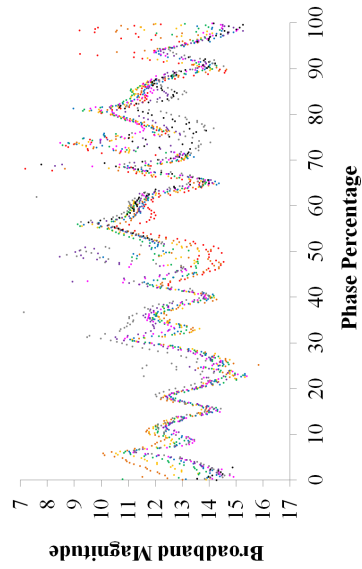
a) 01:14-03:15; 11-15-14; 1050; 855.0s; 136.0°, 27.4°
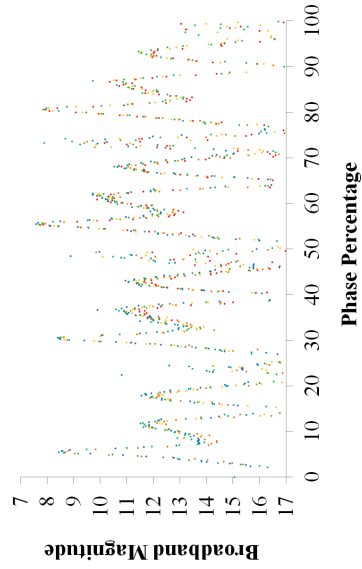
b) 01:10-02:21; 04-16-15; 1202; 959.0s; 204.1°, 43.0°
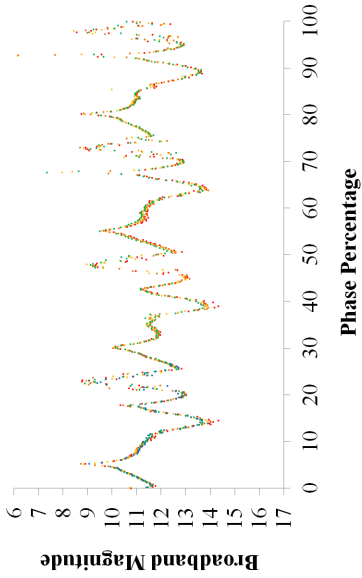
c) 02:50-04:05; 06-20-15; 1267; 1046.2s; 160.0°, 34.8°

Figure 13 Solidaridad-2 phase plots

32
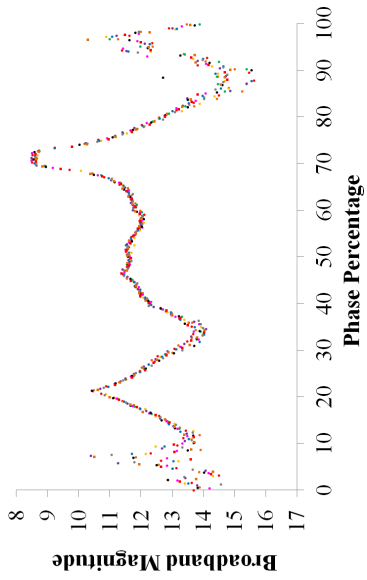
a) 23:30-00:24; 01-20-14; 750-51; 181.6s; 164.2°, 37.1°
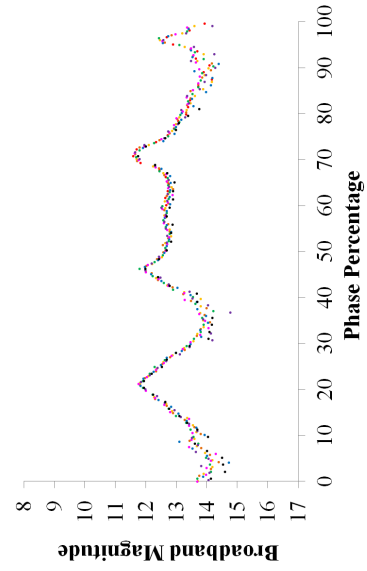
b) 03:00-03:23; 04-20-14; 841; 191.0s; 200.1°, 41.6°
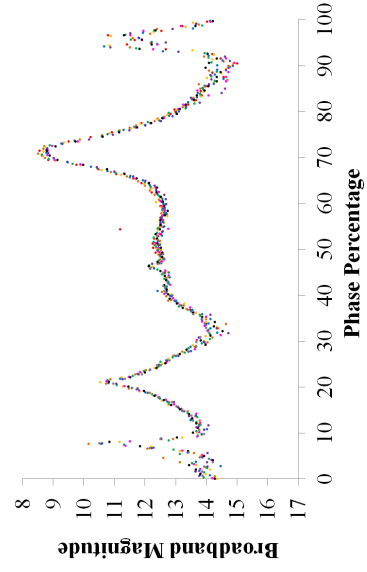
c) 04:43-05:22; 07-18-14; 930; 289.1s; 222.5°, 28.3°

Figure 14 Intelsat-3R phase plots
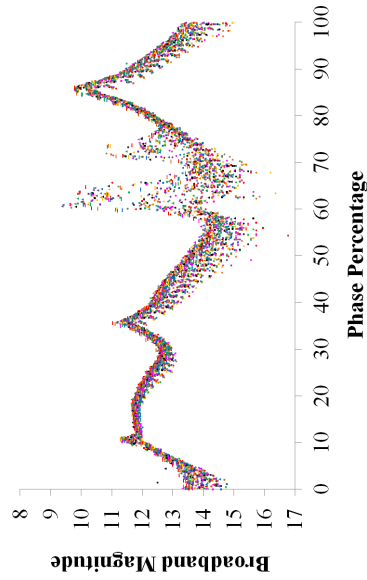
a) 23:50-04:44; 10-09-13; 647-48; 259.2s; 184.5°, 37.5°
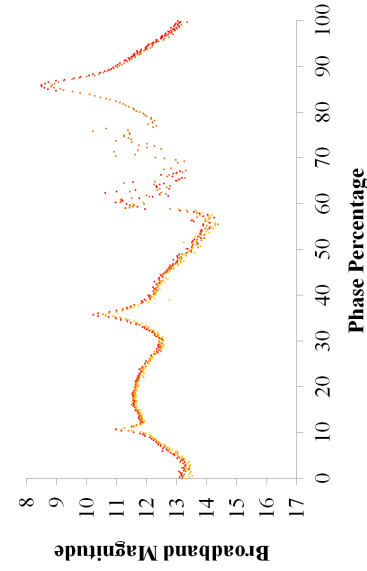
b) 04:01-04:44; 12-20-14; 1085; 974.1s; 168.1°, 39.2°
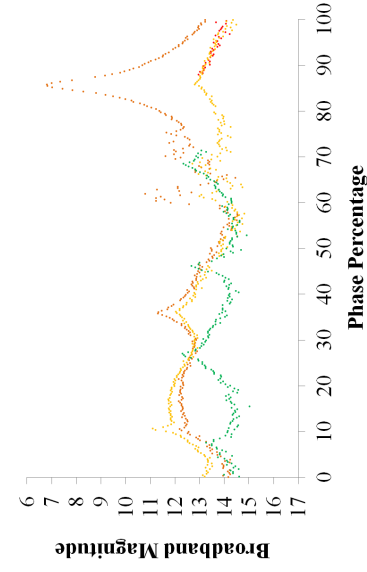
c) 01:33-02:16; 05-14-15; 1230; 913.0s; 159.6°, 39.6°

Figure 15 Paksat-1 phase plots

33
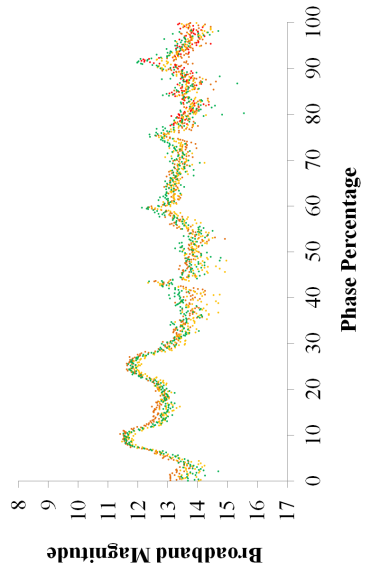
a) 07:01-08:29; 06-15-12; 167; 1648s; 129.9°, 20.4°
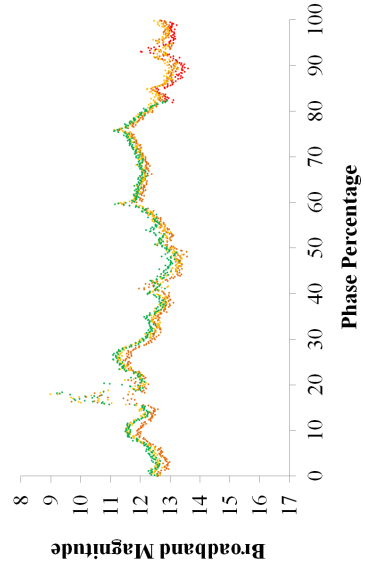
b) 00:27-02:01; 09-14-12; 258; 1847s; 135.4°, 23.6°
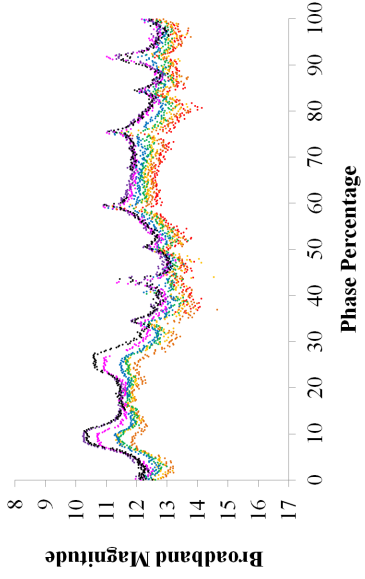
c) 22:49-01:55; 12-12-12; 346-47; 1445s; 151.1°, 31.1°
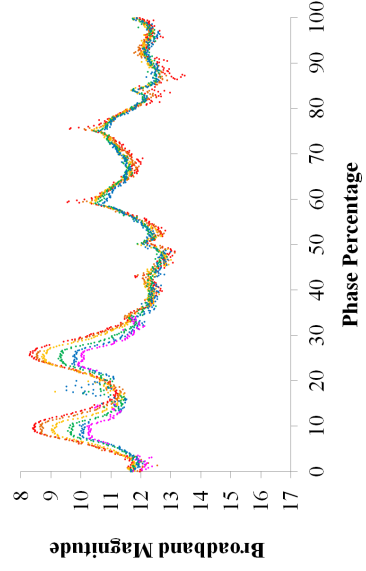
d) 05:45-08:10; 06-15-13; 532; 1608s; 231.3°, 25.7°
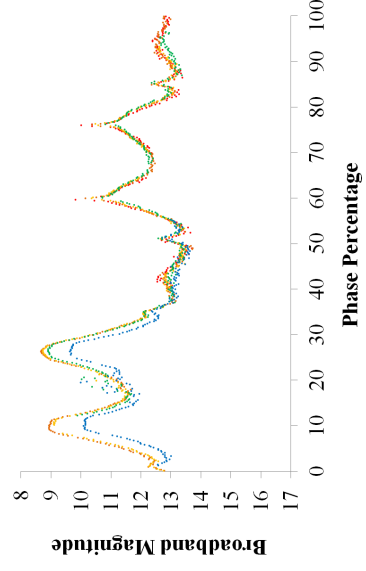
e) 00:34-02:03; 02-11-15; 1138; 1281s; 194.2°, 38.8°
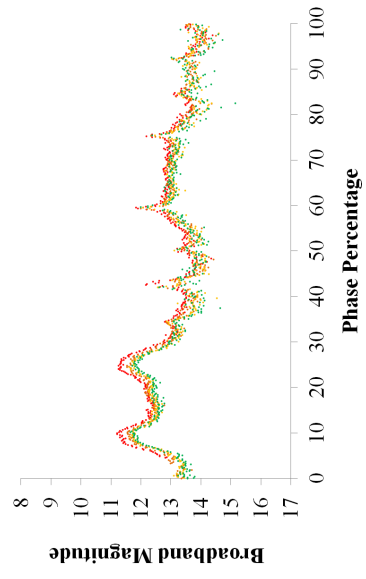
f) 06:38-08:26; 06-20-15; 1267; 1611s; 147.8°, 26.3°

Figure 16 HGS-1 phase plots

34

Echostar-2 suffered a catastrophic failure in 2008.[54]. All of its phase plots appeared to be coherent. AMOS-5i and Intelsat-802 were both retired[55] [56]. Their phase plots also appeared to be coherent. Intelsat-802's phase plots appear to vary significantly over the nine months it was observed in 2015.

2 HS-601 Phase Plot Analysis

Solidaridad-1 and Solidaridad-2 (phase plots are shown in Figs. 11 and 13, respectively) are identical in design and their phase plots appear to be both significantly different but consistently coherent. Solidaridad-1 suffered a catastrophic failure in August 2000[57] and Solidaridad-2 was retired in December 2013[58]. Solidaridad-1's phase plot in Fig. 11 (c) shows the four features (two broad and two thin) similar to those of Telstar-401, AMOS-5i, and Echostar-2. This suggests that a comparison of two single phase plots currently cannot be used to discriminate between the AS-7000 and HS-601 designs. The four phase plots could be suggesting some similarity of the satellite spin axis orientations with respect to the Sun and to the observer.

Solidaridad-2's phase plots (Fig. 13) appear significantly complex, containing at least 12 maxima per inferred cycle. The physical structure of the satellite is assumed to have 14 significant surfaces; comprising of all six sides of the box, both sides of each of the two fully deployed solar panels and both sides of each of the two large communications dishes. It is unclear whether or not the majority of these surfaces could reflect sunlight to an Earth-bound observer at unique phases over a single spin cycle.

The majority of DirecTV-2's phase plots (Fig. 12) suggest incoherence in both amplitude and phase, which is similar to what Cognion had reported for GOES-12 [4], Binz had reported for Superbird-A1 [5], and Ryan and Ryan had reported for GOES-8 [15]. However, Fig. 12 (c) shows that DirecTV-2's phase plot can also appear coherent. This phenomenon was reported by Cognion and Ryan and Ryan when independently observing GOES-8 [4, 15]. The phase plots suggest that DirecTV-2's spin period might have nearly quadrupled in over one year. These observations suggest that a long and increasing spin period is related to a coherent phase plot.

Intelsat-3R's phase plots (Fig. 14) appear to be similar in shape but not in amplitude. Similar to Echostar-2's phase plots over a one year timescale, some of the Intelsat-3R maxima could be as low as 8th magnitude or as high as 4th magnitude. All of the satellite's phase plots observed over 2015 appeared coherent.

From late 2013 to early 2015, Paksat-1's phase plots (Fig. 15) appeared coherent and similar in shape, amplitude, and phase. An observation conducted on May 14, 2015 (Fig. 15 (c)) revealed that its phase plot was incoherent, both in amplitude and in phase. Its phase plots remained incoherent throughout the remainder of the study. Between October 2013 and January 2015, the satellite's spin period varied from 259s to 1302s; an increase of over five times. GOES-8's spin period also appeared to be increasing in 2014; before Ryan and Ryan observed its incoherent phase plot in September 2015 [15]. These observations suggest that a long and increasing spin period is

[54] Bergin, C., "Sea Launch lofts EchoStar 11 - EchoStar 2 dies on orbit," https://www.nasaspaceflight.com/2008/07/sea-launch-lofts-echostar-11-echostar-2-dies-on-orbit/, July 2008, Accessed 04/01/16.

[55] Min, J. et al.,"Branching Out - Reaching New Heights," Tech. rep., Asia Satellite Telecommunications Holdings Limited, August 2012, http://www.asiasat.com/sites/default/files/ir_2012.pdf, Accessed 04/01/16.

[56] Intelsat, "Form 10-K: Annual Report Pursuant to Section 13 or 15(d) of the Securities Exchange Act Report," Tech. rep., US SEC, December 2012, https://www.sec.gov/Archives/edgar/data/1156871/000119312508062350/d10k.htm, Accessed 04/01/16.

[57] Jeffery, M., "SATMEX's Solidaridad 1 Satellite Lost" http://spaceflightnow.com/news/n0008/29solidaridad1, August 2000, Accessed 04/01/16.

[58] Personal correspondence with Dr. Jeremiah Salvatore, retired Boeing senior research fellow: October 23, 2014.

related to an incoherent phase plot. However, the opposite phenomenon (long and increasing spin period appearing to relate to a coherent phase plot) was observed for DirecTV-2.

HGS-1's phase plots (Fig. 16) contain two pairs of similar features. The first pair, (with maxima appearing at 10% and 26% of a cycle in Fig. 16) appear as two broad features. The second pair, (with maxima appearing at 60% and 76% of a cycle in Fig. 16) appear as two broad features with thin crests near each of their maxima. The components of each pair are separated by approximately 16% of a spin cycle. These characteristics did not vary throughout all of the observations; however, their amplitudes varied over time, even when comparing contiguous cycles within a single phase plot. The corresponding components of each pair (for example, the first broad feature maximum to the first crest maximum) are separated by 50% of a spin cycle. These observations could be suggesting two surfaces with an angular separation of 180°, such as two opposite sides of the box or the two opposite sides of the deployed solar panel. However, it is unclear how a fully deployed (planar) solar panel could be reflecting twice per side over a single spin cycle.

F Spin Period Variations

The instantaneous spin periods of the 11 satellites were inferred from their light curves using the P-P method and the CRT. The time evolution of the AS-7000 and HS-601 satellites' spin periods is shown in Figs. 17 and 18, respectively. Each of the 11 satellites' spin periods appeared to vary in some manner over time, similar to what Earl and Wade had reported in [6, 22]. When considering shape, amplitude, and variation timescale, the AS-7000 spin period variations appeared diverse with respect to one another. In contrast, several of the HS-601 satellites had spin period variations that revealed some similarities with respect to one another.

The "variation amplitude" was defined as the full minimum to adjacent maximum (or vice-versa) spin period range that is observed on a plot of spin period versus time. The "variation timescale" was defined as the amount of time between two adjacent maximum or two adjacent minimum spin periods on a plot of spin period versus time.

1 AS-7000 Spin Period Analysis

Telstar-401's spin period (Fig. 17 (a)) consistently appears to vary cyclically. Its variation amplitude decreased from 25s in 2012 to 13s in 2014, then increased to 25s by 2016. The variation timescale decreased from 270d in 2012 to 250d in 2014. The timescale then increased to nearly 300d in 2015. The decrease (or increase) in variation amplitude appeared to coincide with the decrease (or increase) in the variation timescale. Spin periods could not be easily inferred from Telstar-402R's light curves; therefore some of the estimated spin periods in Fig. 17 (b) might not necessarily indicate the true spin periods. This is similar to what Cognion had reported for GOES-12 [4].

AMOS-5i's spin period variation (Fig. 17 (c)) was more coarsely sampled than Telstar-401's because AMOS-5i was less accessible over a year. A cyclical spin period variation with a timescale of one year and an amplitude of 1025s is suggested. Although AMOS-5i's minimum spin period is of the same order of magnitude as that of Telstar-401, AMOS-5i's variation amplitude appears to be over 40 times larger than that of Telstar-401. AMOS-5i's maximum spin period variation rate (from day 584 to 600, since January 0, 2013) appears to be 10.5 s·d^{-1}; which is over 50 times larger than Telstar-401's maximum rate of 0.2 s·d^{-1}.

Echostar-2's spin period (Fig. 17 (d)) also appears to vary cyclically. However, Echostar-2's variation amplitude appears to vary significantly when compared with that of Telstar-401. In 2012-13, Echostar-2's variation amplitude was at least 190s and its average spin period was 439s. In 2014-15, its variation amplitude had decreased to 31s and its average spin period had decreased to 296s. Another significant difference between Echostar-2's and Telstar-401's spin period variations can be seen in Fig. 17 (d) as slight decreases (inflection points) in Echostar-2's spin period variation

rate around days 160, 370, 480, 1100, and 1230. This phenomenon does not appear in any of the other AS-7000 spin period variation plots. Echostar-2's spin period variation timescale decreased from nearly one year in 2012-2013 to 270d in 2014-15. This phenomenon is similar to what was observed for Telstar-401's spin period variation. The gap in Fig. 17 (d) from day 632 to 953 was caused by the satellite's inaccessibility due to a prolonged time of low elevation (less than 15°).

a) Telstar-401

b) Telstar-402R

c) AMOS-5i

d) Echostar-2
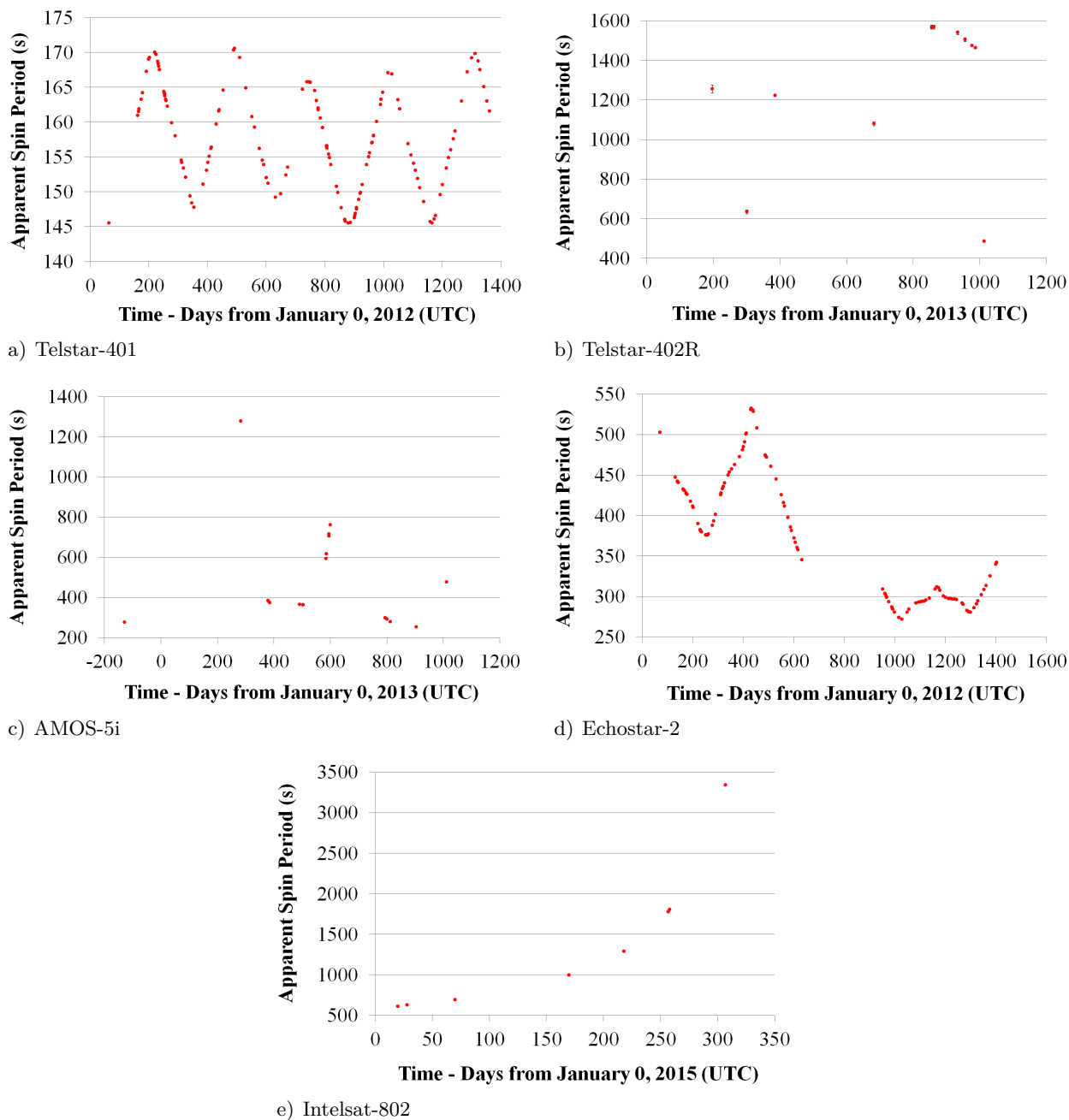
e) Intelsat-802

Figure 17   AS-7000 spin period variations
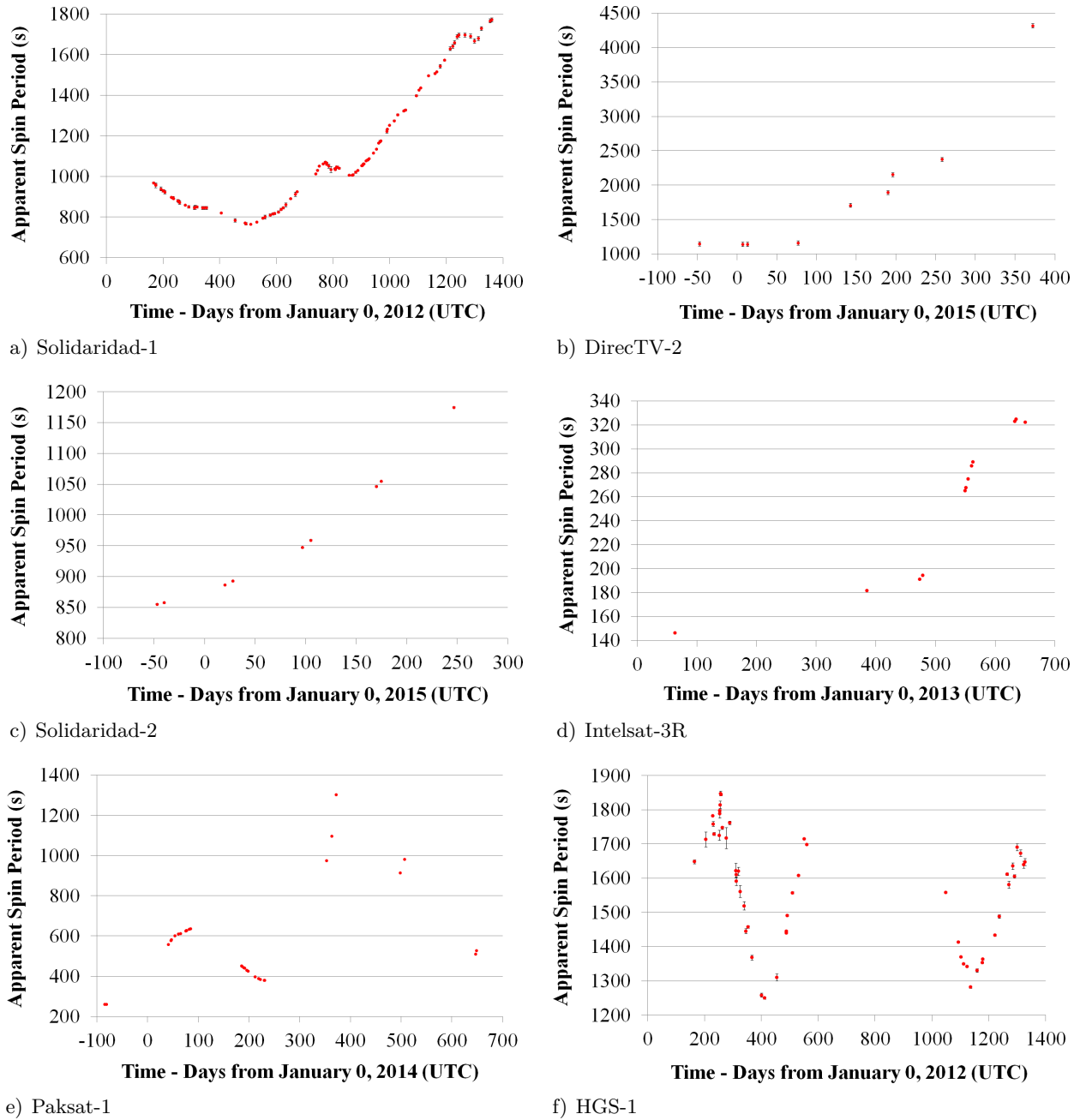
Figure 18 HS-601 spin period variations

Intelsat-802's spin period (Fig. 17 (e)) appears to be increasing slowly and secularly (possibly monotonically) such that it nearly tripled in nine months. This secular behavior is similar to what Papushev, et al. had reported for Gorizont-16 [3] and what Cognion and Ryan and Ryan had reported for GOES-8 [4, 15]. Intelsat-802's spin period variation rate appears to be increasing with time, which is similar to what was observed for AMOS-5i. If Intelsat-802's variation is cyclical, then the cycle could be longer than 300d. Intelsat-802 was also observed by Binz, et al. between January and May 2012; before the observations in this study began. They estimated its spin angular rate to be 0.47º· s^{-1} [5], which corresponds to a spin period of 766s. This suggests that Intelsat-802's spin period was larger before the observations in this study began, thus suggesting a long-period,

cyclical spin period variation.

2 HS-601 Spin Period Analysis

Solidaridad-1's spin period (Fig. 18 (a)) appears to steadily decrease from day 165 to day 510, then it increases from day 510 to day 1400, with two exceptions, near days 800 and 1275. This suggests a very long cyclical variation timescale which is greater than 1200d (3.3y). Solidaridad-2's spin period (Fig. 18 (c)) appears to steadily and smoothly increase in a secular fashion; however, this could also be a long term cyclical variation. Solidaridad-2's spin period appears to be within the range observed for Solidaridad-1. It is not known if the Solidaridad-2 phase plots represent a full, multiple, or even a fraction of the true spin period.

DirecTV-2's spin period (Fig. 18 (b)) appears to increase from 1140s to 4315s, smoothly and secularly, over time. As with Telstar-402R, some of DirecTV-2's estimated periods might not be indicative of the satellite's true spin periods, as indicated by the satellite's mainly incoherent phase plots in Fig. 12.

Intelsat-3R's spin period (Fig. 18 (d)) also appears to increase smoothly and secularly over time, which is similar to the variations observed for Intelsat-802, Solidaridad-2, and DirecTV-2. Its spin period of 146s, at around day 65 (since January 0, 2013) was comparable to that of Telstar-401, but it increases to 290s by day 565, which is comparable to Echostar-2's shortest observed spin period. Intelsat-3R's spin period variation rate reached 1.9 s·d^{-1} between days 550 and 565.

Paksat-1's spin period (Fig. 18 (e)) might be varying cyclically, with a variation amplitude of at least 1045s and a variation timescale of greater than 200d. However, more data is required in order to confirm this. The spin period variation rate reached 22.9 s·d^{-1} between days 363 and 372. Paksat-1's phase plots (Fig. 15 (a) and (b)) appeared coherent up to May 2015. The phase plot corresponding to May 14, 2015 (Fig. 15 (c)) appears to be incoherent; after the spin period reached a maximum of 1302s.

HGS-1's spin period (Fig. 18 (f)) also appears to vary cyclically but includes short term fluctuations. Between days 252 and 257 (since January 0, 2012), the spin period increases significantly from 1725s to 1847s at a rate of 24.4 s·d^{-1}, which is similar to Paksat-1's maximum observed spin period variation rate. Despite HGS-1's long average spin period, its phase plots have remained relatively coherent when compared to those of Telstar-402R and DirecTV-2. The variation timescale appears to be 310d in 2012-13 and 330d in 2014-15; yet, when comparing the two spin period minima on days 412 and 1137, the average variation timescale appears to be 362s.

3 Summary of Spin Period Analysis

Table 4 summarizes the observed spin period characteristics of the 11 satellites. AS-7000 and HS-601 satellites are listed in the top and bottom sections, respectively. Figure 19 plots the 11 satellites' spin period variation amplitudes against their average spin periods. The number next to each data point indicates the satellite's NORAD designation, as shown and cross-referenced with its COSPAR and common identifications in Table 2. Arrows depict spin period variation amplitudes that are likely larger than the plot indicates. Data points without arrows depict the known spin period variation amplitudes and average spin periods. Data points with arrows depict uncertain spin period amplitudes and/or uncertain average spin periods. Vertical error bars depict the full extent of the known variation amplitudes. The linear trend line depicts the relationship between the spin period variation amplitude and the average spin period proposed in [22].

Table 4 Observed spin period characteristics

Satellite	Minimum Period (s)	Maximum Period (s)	Cycle Amplitude (Fraction of Minimum Period) (s)	Average Period (s)	Variation Timescale (d)
Telstar-401	145.5	170.6	25.1 (0.173)	158.0	275±25
Telstar-402R	487	1568	>1081 (>2.22)	1028	Unknown
AMOS-5i	254	1277	>1023 (>4.03)	766	>316
Echostar-2	272.1	532.2	260.1 (0.956)	402.2	315±50
Intelsat-802	612	3345	>2733 (>4.47)	1978	>300
Solidaridad-1	764	1771	>1007 (>1.32)	1268	>1200
Solidaridad-2	855	1174	>319 (>0.373)	1014	>300
DirecTV-2	1140	4315	>3175 (>2.78)	2728	>400
Intelsat-3R	146.0	289.1	>143 (>0.979)	218	Unknown
Paksat-1	259.2	1301.6	>1042 (>4.02)	780.4	>200
HGS-1	1249	1847	598 (0.479)	1548	335±25
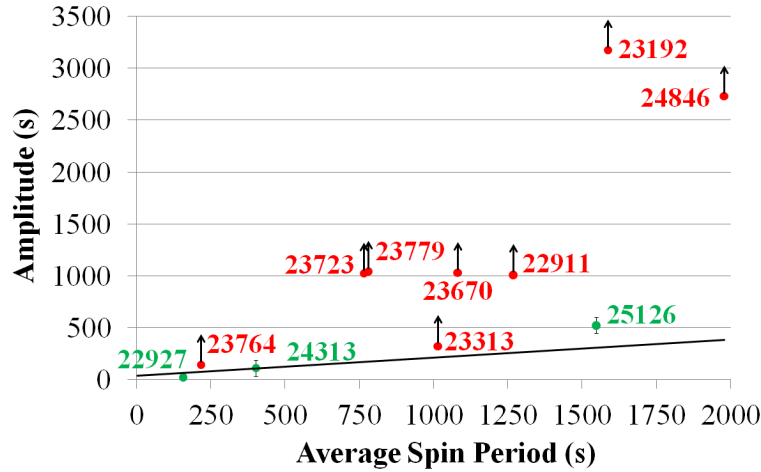
Figure 19 Spin period variation amplitude versus average spin period

Figure 19 shows that the linear trend line proposed in [22] does not fit the new data. The position of Solidaridad-1's data point has moved far above the proposed trend line after December 2013. The data points pertaining to Telstar-402R, AMOS-5i, Intelsat-802, DirecTV-2, and Paksat-1 also appear far above the trend line. HGS-1's and DirecTV-2's average spin periods are 40s apart, but their amplitudes are nearly 2700s apart. This significant discrepancy might be due to HGS-1's undeployed solar panel and/or DirecTV-2's incoherent phase plots.

AMOS-5i's and Paksat-1's data points (Fig. 19) appear to be in close proximity to each other. This suggests that their spin period variations are similar to each other, both in average spin period and in amplitude. Telstar-402R's and Solidaridad-1's amplitudes appear to be similar to those of AMOS-5i and Paksat-1.

Intelsat-802's and DirecTV-2's data points indicate a larger variation amplitude and a larger

average spin period than those of the other nine satellites. Telstar-402R's, Paksat-1's (in 2015), and DirecTV-2's incoherent phase plots and long spin periods suggest that the phase plot becomes incoherent as the spin period becomes longer. However, AMOS-5i's, Intelsat-802's, Solidaridad-1's, and Solidaridad-2's coherent phase plots and long spin periods suggest that the phase plot does not become incoherent as the spin period lengthens. The reasons and possible consequences of this contradiction are currently unknown.

G Quantifying Light Curve Features: Power Spectrum Ratios

Visual inspection of the phase plots offer some suggestions concerning how a light curve's morphology varies with time. However, it is reasonable to assume that a satellite's light curve morphology and its spin period variation will be related if the observed spin period variations are associated with the satellite's varying orientation relative to the Sun (and the consequential SRP), as Earl and Wade proposed in [6]. Although L-S periodograms could not determine satellite spin periods as reliably as the P-P method or the CRT, such periodograms could be used to quantify how the overall light curve morphology varies over time.

The maximum full-period power (P_{full}) was defined to be the maximum detected power corresponding to the Lomb-Scargle frequency of the most likely spin period. Subesequently, the maximum half-period power (P_{half}) was defined to be the maximum detected power corresponding to the Lomb-Scargle frequency of half the most likely spin period. The PSR was defined to be the full/half ratio of these two maxima within a single L-S periodogram, as described in Eq. (4). By comparing several PSRs from several light curves, basic information about how a light curve's morphology can be analyzed.

$$PSR = \frac{P_{full}}{P_{half}} \tag{4}$$

L-S periodograms were extracted[59] from all light curves of the five most frequently observed satellites: Telstar-401, Echostar-2, Solidaridad-1, Paksat-1, and HGS-1. Power spectrum maxima corresponding to the full, half, fourth, and eighth of the corresponding (P-P or CRT) inferred spin periods (1, 2, 4, and 8 times the corresponding spin frequencies) were inferred from each periodogram. The PSRs were plotted against time (from early 2012 to late 2015) to investigate how the PSRs were varying over time. Of all PSR combinations, the strongest evidence of a cyclical PSR variation was observed for the full/half period PSRs of Telstar-401 and Echostar-2, as shown in Fig. 20 (a) and (b), respectively.

Figure 20 (a) suggests that Telstar-401's full/half period PSR behaves cyclically over time with a time duration of between 100d and 200d; approximately half the duration of Telstar-401's spin period variation. Telstar-401's PSR variation amplitude appears to be between 3 and 5 between day 0 and day 500, then appears to decrease to less than 1 between days 500 and day 900. Finally, Telstar-401's PSR variation amplitude appears to slowly increase to between 4 and 5 between days 900 and 1300. Figure 20 (b) suggests that Echostar-2's full/half period PSR behaves somewhat cyclically with a variable duration. Since the largest PSR is between 0.5 and 0.6, noise might be a more significant contributor to Echostar 2's PSR plot than Telstar-401's PSR plot. Figure 20 (b) suggests that Echostar 2's PSR variation amplitude decreased from between 0.2 and 0.5 from between 2012 and 2013 to less than 0.2 after 2013.

---

[59]with the modified lombscargle.m software.

a) Telstar-401

b) Echostar-2
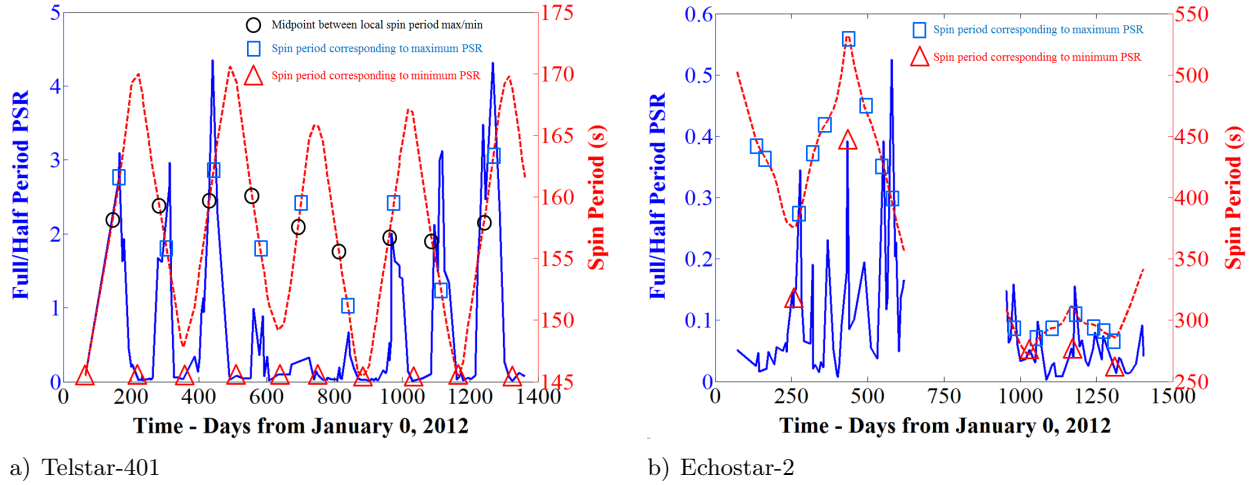
Figure 20 Full/half period PSR versus spin period

Figure 20 (a) suggests that results of the L-S method of spin period determination for Telstar-401's light curves might better concur with the P-P method's results when the full/half PSR was greater than 1 (corresponding to a full period power spectrum maximum being greater than the half period power spectrum maximum). This assumes that the full period power spectrum maximum is the greatest within the entire periodogram. In contrast, Fig. 20 (b) suggests that results of the L-S method would likely result in the half spin period determined by the P-P method or the CRT method, assuming that the half period power spectrum maximum is the greatest within the periodogram. Both of these results concur with the conclusions reached for the L-S method in Section D.

Telstar-401's and Echostar-2's PSR variations (solid blue curve) were compared to their corresponding spin period variations (dashed red curve), as shown in Fig. 20 (a) and (b), respectively. Each black circle in Fig. 20 (a) represents a midpoint between a maximum and a minimum in the Telstar-401 spin period curve. In Fig. 20, each blue square represents a location on the spin period curve corresponding to the time of a PSR maximum. In Fig. 20, each red triangle represents the location on the PSR curve which corresponds to the time of a spin period maximum or minimum.

The strongest correlation between PSR variation and spin period variation was found for Telstar-401 (Fig. 20 (a)). Each maximum and minimum spin period in Fig. 20 (a) correlate in time to a PSR minimum. Each PSR maximum in Fig. 20 (a) correlates in time to a point on the spin period curve between a circle and a maximum or minimum. Where Telstar-401's spin period amplitude appears to be large, the maximum PSR also appears to be relatively large. Conversely, where Telstar-401's spin period amplitude appears to be small, the maximum PSR also appears to be relatively small. Echostar-2 had similar, albeit weaker (possibly due to noise) correlations (Fig. 20 (b)). Some maximum or minimum spin periods roughly correlate in time with PSR maxima. Other PSR maxima appear to correlate in time with Echostar-2's spin period curve's inflection points (described in Section F). The remaining PSR maxima do not appear to correlate in time with any significant spin period curve feature. Echostar-2's maximum PSRs appear to increase (or decrease) as the spin period amplitude increases (or decreases).

These quantitative correlations suggest a relationship between the two satellites' spin period behaviors and their light curve morphologies. Since a satellite's spin geometry with respect to the Sun and to the observer is a major contributor to its observed light curve morphology [6], the relationships shown in Fig. 20 imply a direct connection between these two satellites' spin geometries and the spin period variations presented in this paper. Once this relationship is further

studied and verified, this evidence might be used to verify attitude dynamics models of a number of inactive box-wing GEO satellites.

H   Conclusions

A long term and high temporal resolution observations of 11 inactive box-wing GEO satellites was conducted, comprising of five AS-7000 and six HS-601 designs, from March 2012 to January 2016 in order to carefully compare their light curve morphologies and their spin period variations. This research confirms previously published results of shorter term and lower resolution surveys of Russian and American box-wing satellites and have revealed additional phenomena not previously discovered. Despite similar designs and with few exceptions, the 11 satellites' phase plots appeared diverse with respect to one another. Some of the phase plots of Telstar-401, AMOS-5i, Echostar-2, and Solidaridad-1 appeared to be similar, each consisting of two broad features and two tall, thin features. Despite this finding, the phase plots alone could not be used to discriminate between the AS-7000 designs and the HS-601 designs. The unexpected variations of DirecTV-2's (incoherent to coherent) and Paksat-1's (coherent to incoherent) phase plots have indicated that this research requires additional observations, possibly with larger-aperture telescopes and color photometric methods.

Consistently cyclical spin period variations were observed for Telstar-401, AMOS-5i, Echostar-2, Paksat-1, and HGS-1. More secular spin period variations were observed for Intelsat-802, Solidaridad-1, Solidaridad-2, Intelsat-3R, and DirecTV-2. Telstar-402R's spin period variation could not be deemed cyclical or secular due to its apparently incoherent phase plots. The proposed linear relationship between the original four satellites' spin period variation amplitudes and their average spin periods could not adequately model the additional data.

Correlations were found between Telstar-401's and Echostar-2's full/half period PSRs and their spin periods. Telstar-401's PSR minima appeared to correlate in time with its spin period maxima and minima. Telstar-401's PSR maxima appeared to correlate in time with its spin period curve between its spin period extrema and its midpoints between extrema. Some of Echostar-2's PSR maxima appeared to correlate in time with its spin period maxima and minima. Telstar-401's and Echostar-2's power spectrum maxima were observed to increase or decrease as the spin period variation amplitude increased or decreased, respectively. These correlations are important because they could be indicating a relationship between Telstar-401's light curve morphology (spin attitude and sunlight geometry being contributors) and its spin period variations.

Some of the box-wing light curves can vary little over weeks and months, as was observed for Echostar-2. However, light curves can also vary substantially over a single (synodic) spin period, as was observed for Telstar-402R and DirecTV-2. In addition, a single box-wing's light curve can significantly change from coherent to incoherent (or vice-versa), as was observed for DirecTV-2 and Paksat-1. Therefore, observing consistent similarity between inactive box-wing GEO satellites' broadband photometric behaviors will be difficult. An implication of this is that OOS missions might have to contend with highly variable attitude dynamics with diverse and varying timescales.

This study has provided additional photometric data that can be used to determine attitude dynamics modeling constraints. These data include: the spin period variation timescales, amplitudes, and inflections (and their respective variations); the width and amplitude of noticeable light curve features; the coherence of light curves; and the PSR variations, including PSR comparisons with spin period variations.

Although this research has been comprehensive, additional observations will be required to confirm the coherence or incoherence of DirecTV-2's, Telstar-402R's and Paksat-1's phase plots, confirm the suggested PSR to spin period relationship of Telstar-401 and Echostar-2 (as well as other box-wing satellites), and to increase the sample size to over 11 satellites in order to observe and analyze additional phenomena that could assist with space object characterization efforts. It

is hoped that this paper will motivate future space surveillance professionals to frequently monitor the inactive satellite population and to discover how their attitudes vary.

CHAPTER 4: SPIN AXIS ORIENTATION

The previous paper (Chapter 3) concluded that the Echostar-2 satellite exhibited the most stable light curve morphology, suggesting that the satellite's attitude is the most stable relative to the other ten satellites studied. Echostar-2's light curves also exhibited evidence of bright specular reflections, which suggested two highly reflective surfaces, positioned at approximately 180º from each other. It was for these reasons that Echostar-2 was chosen to be the best candidate for box-wing spin axis orientation determination.

As of April 2017, there had been no published quantitative estimations of any inactive box-wing GEO satellite's spin axis orientation. This might be due to the fact that the traditional "Epoch Method" of spin axis orientation estimation relies on the critical assumption that the satellite's spin state is stable; meaning that both the spin angular velocity magnitude and its direction in an inertial frame are assumed to be constant with time. Earlier research by the author has revealed that the spin angular velocity vectors of inactive box-wing GEO satellites are likely constantly varying with time. The largest contributor to the external torque that was causing this variation was determined to be SRP. Lorentz (magnetic) and gravity-gradient forces were less significant contributors to the overall torque.

A GEO satellite's relative motion with respect to a ground-based observer is very small when compared to that of a Low Earth Orbit (LEO) satellite. A GEO satellite's nearly 24-hour orbit period results in a very slow motion with respect to the Sun. Since an inactive GEO satellite's motion with respect to the observer and to the Sun causes the synodic spin period variation, the variation of the spin period due to SRP is likely comparable to, or greater than, the synodic spin period variation due to the satellite's relative motion. It is for this reason that the Epoch Method might not be a trustworthy tool for either synodic-sidereal spin period transformation or for spin axis orientation estimation of inactive GEO satellites.

This Chapter investigates the most likely attitude of Echostar-2, assuming no external torques, a reflectance model considering all critical sides of Echostar-2, and the spin axis orientation estimation of Echostar-2, based on two bright specular reflections (for each spin period) that were detected in March and in September of 2012, 2013, and 2015. For the first time, this research has estimated the orientation of an inactive box-wing GEO satellite through the photometric measurement of its detected flux during bright specular reflections.

Estimating the Spin Axis Orientation of the Echostar-2 Box-wing Geosynchronous Satellite

Michael A. Earl[‡] and Gregg A. Wade[§]

Royal Military College of Canada, Kingston, Ontario, Canada, K7K 7B4

This paper is being prepared for submission to the COSPAR Advances in Space Research by the fall of 2017.

A   Introduction

NEARLY 60 years after the launch of Sputnik, SSA continues to protect our highly valuable active satellite population from threats that include satellite collision, malevolent physical interference, and communications interference. SSA involves many forms of surveillance, including space object characterization. Space object characterization is used to determine a satellite's identity, nation of origin, status (active or inactive), orbit characteristics, attitude (orientation), size, and/or component make-up[60]. The ability to perform suitably high cadence SSA has recently become much more complicated, mainly because of the significantly increased satellite population due to the Chinese Fengyun-1C ASAT test and the Iridium-Cosmos satellite collision. Every single piece of orbiting debris created by these two events has the capability of colliding with and causing serious damage to active satellites in the sun-synchronous orbit region and to satellites being launched into and beyond this region. Therefore, performing high cadence space object characterization on both active and inactive satellites is equally important to prevent serious harm to the active satellite population.

The attitude determination aspect of space object characterization involves estimating the inertial orientation of a satellite. An active satellite can determine its attitude with an on-board system. This is likely to be its ADCS. Access to a specific active satellite's ADCS data is normally restricted to the satellite owner(s) and operator(s). Inactive satellites have either catastrophically malfunctioned or have been permanently deactivated (colloquially known as "retired"). In either case, an inactive satellite's ADCS system is no longer functioning. Therefore, determining the attitude of restricted active satellites or inactive satellites requires a different method other than analyzing ADCS data.

The most direct, most accessible, and least expensive satellite detection method is ground-based optical observation, which involves detecting sunlight reflected from the satellite with ground-based telescopes and CCDs. Studies performed by Earl (2007 and 2011) between 2007 and 2011 concluded that over 4,200 individual satellites residing in the LEO to the HEO realms could be detected with COTS small-aperture (less than 0.3m) telescopes and CCD cameras [26][61]. The study concluded

---

[‡]PhD Candidate, Department of Physics, Royal Military College of Canada, P.O. Box 17000 Station Forces Kingston, Ontario, Canada, K7K 7B4.

[§]Department Head, Department of Physics, Royal Military College of Canada, P.O. Box 17000 Station Forces Kingston, Ontario, Canada, K7K 7B4.

[60]National Space Studies Center, "AU-18 Space Primer - Chapter 19: Space Surveillance Network", http://space.au.af.mil/au-18-2009/au-18_chap19.pdf, Accessed 10/09/16.

[61]Earl, M., The CASTOR Satellite Catalogue, http://www.castor2.ca/13_Catalogue/index.html, Accessed 10/09/16.

that nearly 70% of the GEO satellite population could be detected with a single ground-based optical facility based in a single location[62]. The GEO satellite population resides at approximately 35,785 km in altitude with nearly circular prograde orbits inclined at between 0º and 15º from the Earth's equatorial plane[63].

Attitude determination of inactive GEO satellites is becoming more important because of robotic OOS missions[64]. Cognion (2014), Binz (2014), and Earl and Wade (2015 and 2016) have conducted optical surveys of inactive box-wing GEO satellites to conduct qualitative assessments of their attitude variations [4, 5, 6, 16]. A box-wing GEO satellite (illustrated in Fig. 21[65]) consists of a central cube-shaped bus portion, with side lengths of approximately 2.5m, and two large solar panels, each about 25m^2 in area. Cognion, Binz, and Earl and Wade analyzed photometric light curves of box-wing satellites and reported that they appeared to spin with diverse synodic periods, ranging from several seconds to several hours. Cognion (2014) and Earl and Wade (2016) reported that the light curve morphology of some box-wings appears to vary over long timescales (weeks or months), while other box-wing satellites appear to have a varying morphology over shorter timescales, such as within a single spin period [4, 16]. Some of these satellites' light curves had such complex morphologies that spin period inference was difficult or indeterminable, suggesting complex attitude dynamics [4, 5, 16]. Cognion (2014), Binz (2014), and Earl and Wade (2016) concluded that the attitude dynamics of inactive box-wing GEO satellites appeared to be more complex than once thought [4, 5, 16], suggesting that an OOS mission to GEO might need to carefully assess each GEO box-wing satellite's attitude when planning a service or salvage mission.
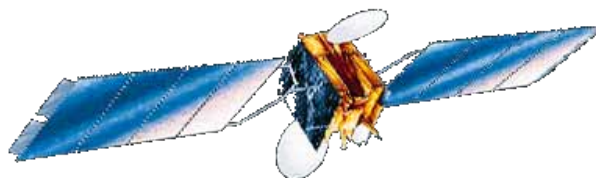
Figure 21   The Echostar-2 box-wing satellite

The "spin axis orientation" was defined as the inertial RA (α_{spin}) and dec (δ_{spin}) direction of a satellite's spin angular velocity vector ($\vec{\omega}$). This paper presents an estimation of Echostar-2's spin axis orientation in 2012, 2013, 2014, and 2015 based on geometrical models centered around its bright specular reflections. First to be discussed is Echostar-2's most likely stable spin axis orientation with respect to its body frame. Next, an ideal physical box-wing model and a corresponding reflectance model are discussed. Next, the Eulerian transformations between the spin axis orientation and the satellite body axis, and the spin axis orientation and the equatorial (RA and dec) inertial coordinate system are described. Next, a discussion of the geometrical model that estimates the spin axis orientation is conducted. Then, Echostar-2's estimated spin axis orientations are presented and discussed. Finally, light curve simulations corresponding to the dates of the estimated spin axis orientations are presented and discussed.

---

[62]Earl, M., The CASTOR Satellite Catalogue - Statistics, http://www.castor2.ca/13_Catalogue/05_Stats/index.html, Accessed 10/09/16.

[63]JFCC SPACE/J3, Space Track, https://www.space-track.org, Accessed 10/09/16.

[64]DARPA, Program Aims to Facilitate Robotic Servicing of Geosynchronous Satellites, http://www.darpa.mil/news-events/2016-03-25, Accessed 10/09/16.

[65]Krebs, G., Gunter's Space Page - EchoStar 1,2, http://space.skyrocket.de/doc_sdat/echostar-1.htm, Accessed 10/09/16.

B   Background

1   The Echostar-2 Satellite

Echostar-2 is a telecommunications satellite originally designed by GE's AS with an AS-7000[66] bus design. The satellite was launched on September 11, 1996[67] to service customers in North and South America[68] for 15 years. The satellite was primarily used as a back-up satellite to Echostar-1, with a nominal operational longitude slot of 148º west[69].

On July 14, 2008, the satellite suffered "a substantial failure that appears to have rendered the satellite a total loss"[70]. Echostar-2 could no longer be controlled from the ground and therefore could not be parked in the GEO graveyard orbit. Echostar-2 has been observed to oscillate about the 105º west geopotential well [6].

2   Echostar-2 Observations and Light Curves

In late-2010, about 2.5 years after the satellite's catastrophic malfunction, amateur satellite observers reported that Echostar-2 was flashing "very brightly" to the naked eye (likely due to brief specular sunlight reflections), with an apparent period of 240.3s[71]. In this paper, the term "broadband" was defined to refer to an unfiltered optical system with a detected flux spanning the entire detectable optical spectrum. Long term and high temporal resolution broadband photometric observations of Echostar-2 were conducted from March 2012 to November 2015 [16] with the equipment and procedure described in [6]. Earl and Wade (2016) reported that Echostar-2's spin period varied cyclically, with a minimum of 272.1s and a maximum of 532.2s [16, 17]. The satellite's spin period variation amplitude was observed to decrease from 186.8s (in 2012-13) to 31.3s (in 2014-15) [16]. Brief and bright (naked eye brightness) specular flares from Echostar-2 were observed in March and September of 2012, 2014, and 2015. Two contiguous specular flares corresponded to half an inferred spin period[72].

Earl and Wade reported that all light curves of Echostar-2 contained four distinct and alternating features over each inferred spin period; two broad (likely diffuse reflection) features and two thin and sharp (likely specular reflection) features that suggested four sides of the box-wing satellite's box portion [16, 17]. Figure 22 shows an example of an Echostar-2 folded broadband light curve for September 12, 2012 [16]. The thin, sharp features appeared similar in shape and amplitude and were consistently separated by 50% of a spin period [16], suggesting that two reflective surfaces, 180º of a rotation apart, were specularly reflecting sunlight to the observer during each satellite rotation. This further suggested that the two highly reflective mirrored radiators[73], and not the solar panels, were the sources of the bright specular flares observed in 2012, 2014, and 2015 [16].

---

[66] Also known as "LM-7000".

[67] JFCC SPACE/J3, Space Track, https://www.space-track.org, Accessed 05/01/16.

[68] Krebs, G., Gunter's Space Page - Echostar 1, 2, http://space.skyrocket.de/doc_sdat/echostar-1.htm, Accessed 05/01/16.

[69] Bergin, C., "Sea Launch lofts EchoStar 11 - EchoStar 2 dies on orbit," https://www.nasaspaceflight.com/2008/07/sea-launch-lofts-echostar-11-echostar-2-dies-on-orbit/, July 2008, Accessed 04/01/16.

[70] US SEC, "Form 8-K: Current Report Pursuant to Section 13 or 15(d) of the Securities Exchange Act of 1934", http://apps.shareholder.com/sec/viewerContent.aspx?companyid=DISH&docid=6046093, Accessed 05/01/16.

[71] McCants, M., "Very bright flashes from Echostar-2", http://www.satobs.org/seesat/Nov-2010/0052.html, Accessed 05/01/16.

[72] Earl, M., Observation and Analysis of the Spin Period Variations of Inactive Box-wing Telecommunications Satellites in Geosynchronous Orbit, MSc thesis, RMCC, May 2013, http://www.castor2.ca/08_Papers/earl_thesis.pdf, Accessed 03/27/16.

[73] The radiators dissipate heat away from the temperature-sensitive electrical components within the box portion.
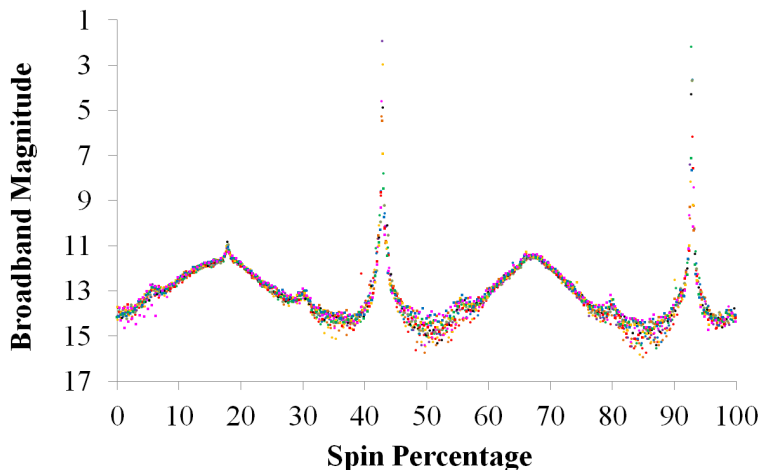
Figure 22 Echostar-2 folded light curve: September 12, 2012

An inactive box-wing satellite's light curve morphology depends on the satellite's spin axis orientation with respect to the satellite's body frame, to the Sun, and to the observer. Earl and Wade reported that Echostar-2's light curve morphology was similar over time; always containing the two alternating broad (diffuse) and sharp (specular) features over an inferred spin period (as shown in Fig. 22), but with varying specular brightness amplitudes over a weekly timescale. The light curve morphologies of the remaining ten satellites listed in [16] were observed to vary significantly over timescales between a single spin period (typically minutes or hours) and several months [16]. Echostar-2's light curve specular magnitude amplitudes appeared to vary cyclically with a timescale of approximately half a year [16]. Echostar-2's brightest broadband specular magnitudes were consistently observed in several weeks of March and September of 2012, 2014, and 2015. One of the brightest specular flares, of approximately broadband magnitude 2 (Fig. 22), was observed on September 12, 2012.

3 Synodic and Sidereal Spin Periods

An extreme example of the difference between synodic and sidereal spin periods (also known as the "synodic effect") would be when a non-spinning (infinitely long sidereal spin period) GEO satellite was observed from a location on the Earth's surface. The observer would see the satellite appear to spin with a 24-hour (synodic) period because the GEO satellite is orbiting the Earth at the same angular rate as the Earth's rotation and it is moving with the Earth as it orbits the Sun[74]. Therefore, the satellite's light curve would appear to have a 24-hour period, even though the satellite is not spinning at all.

Evidence of the synodic effect was presented by Lambert, et al. (2003) based on their observations of the cylindrical SBS-B and SBS-C HS-376 [75] design GEO satellites with the AEOS facility in Maui, Hawaii from 2002 to 2003 [18]. Lambert, et al. observed bright reflections which were seen as brief temporal duration and bright magnitude features on their I-band photometric light curves, as shown in [18]. They reported that on June 15, 2003, SBS-B's light curve period (inferred from the light curve features) appeared to lengthen from 50s to nearly 200s over a timescale of 2.5 hours from 10:30 to 13:00 UTC. They also reported that on December 20, 2002, SBS-C's light

---

[74]Earl, M., Observation and Analysis of the Spin Period Variations of Inactive Box-wing Telecommunications Satellites in Geosynchronous Orbit, MSc thesis, RMCC, May 2013, http://www.castor2.ca/08_Papers/earl_thesis.pdf, Accessed 10/11/16.

[75]Hughes 376, later Boeing 376.

curve period appeared to suddenly increase from 30s to 60s at approximately 08:40 UTC [18].

Lambert, et al. concluded that the SBS-B and SBS-C light curves they observed were inconsistent with those of active HS-376 satellites. They suggested that after these spacecraft were retired, they underwent a change in their dynamics, wherein their spin axes transitioned from their minimum to their maximum MOIs, resulting in a pure tumble [18]. Lambert, et al. reported that the satellites' synodic spin periods increased suddenly and significantly. They suggested that the cause in each case was the PAB (corresponding to a satellite surface responsible for the bright reflections), nearly aligning with the satellite's spin axis [18]. An extreme example of such a lengthening of synodic period occurs when a surface's PAB is aligned with the spin axis and the observer can see a sunlight reflection from the corresponding surface. In this case, the light curve should show a continuous and constant reflected brightness until the PAB is no longer aligned with the spin axis, or, until the viewing geometry between the Sun, the observer, and the satellite ceases to be favorable for a sunlight reflection to the observer.

4   Satellite Spin Axis Orientation Determination

A spinning satellite's synodic-sidereal spin period difference depends on its spin axis orientation [19] with respect to its inertial frame. Hall, et al. estimated the IMAGE satellite's spin axis orientation from their synodic spin period measurements inferred from I-band photometric light curves obtained with the AEOS facility.

Hall, et al. estimated IMAGE's spin axis orientation with the "Epoch Method", a method which is also used within the asteroid observation community, as described in [19]. An advantage of the epoch method is that it does not depend on the satellite's shape and its reflectivity characteristics. This method assumes that the satellite's spin axis state is stable (not chaotic) and that the measured synodic spin period corresponds to a full rotation of the PAB (responsible for the observed reflections and the inferred spin periods) about the satellite's spin axis [19].

Earl and Wade (2015) studied the apparent angular accelerations of four inactive box-wing GEO satellites. They concluded that SRP was a primary contributor to a net external torque causing each of the accelerations. In the case of box-wing GEO satellites, the epoch method might not be a viable option for spin axis orientation determination because of the constantly varying apparent spin periods that are not solely caused by geometry between the satellite, the Sun and the observer. Since inactive GEO satellites appear to move very slowly with respect to an observer relative to satellites in other orbits, the primary contributor to the apparent spin period variations would likely be the effects of SRP on the GEO satellites' sidereal spin periods and not the varying geometry. If this is the case, then an alternative method of spin axis orientation determination will be required. This paper describes, in detail, a geometrical method that relies on very bright specular reflections observed over several days.

C   Rotation Kinematics

An unconstrained and freely rotating body will have three principal axes of rotation, each with its own MOI. Echostar-2's x_b, y_b, and z_b principal body frame axes were defined as shown in Fig. 23. When Echostar-2 was active, its solar panels rotated about the satellite's x_b axis to track the Sun. After the satellite's malfunction, Echostar-2's solar panels remained fixed in the satellite's body frame, assuming that the entire satellite is a rigid body.

A spinning satellite's angular momentum vector ($\vec{L}$) is related to its spin axis vector ($\vec{\omega}$) by its second rank inertia tensor (**I**). Echostar-2's estimated specifications and inertia tensor are both discussed in Appendix A. Echostar-2's three individual MOIs, corresponding to each principal axis shown in Fig. 23, are determined with Eqs. (44), (45), and (46) in Appendix A. Echostar-2's resultant inertia tensor is shown in Eq. (47) in Appendix A. The off-diagonal components (products of inertia) were assumed to be negligible relative to the diagonal components (principal MOIs). The

rationale for this assumption was based on the known MOI tensors of the two Solidaridad box-wing satellites[76].
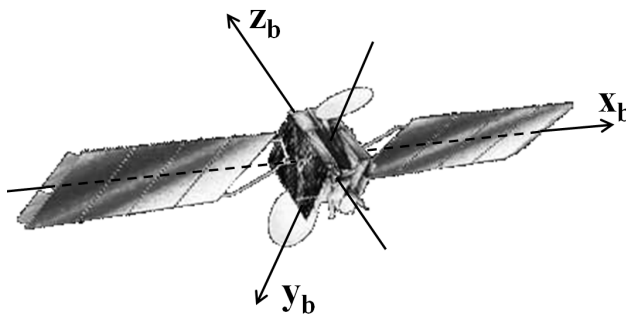
Figure 23 Echostar-2's principal body rotation axes

1 Preliminary Evolution of Body Frame Spin Axis without External Torques

An active box-wing GEO satellite's typical spin axis orientation in both the body frame and inertial frame is located along the x_b body frame axis and perpendicular to the Earth's equatorial plane (the equatorial z-axis), respectively [9]. This is done to align the solar panels and box portion with the Sun and with the Earth's surface, respectively. Immediately after a box-wing satellite becomes inactive, it was assumed that it will continue to spin solely about its x_b-axis as the momentum wheels slow down and transfer their angular momentum into the entire system through a small friction force. This assumption is based on the fact that the satellite's total angular momentum can only be varied by external torques and not by internal ones [27, 28]. Assuming a negligible net external torque, Echostar-2's possible stable spin axis orientation was determined with respect to its body frame and to the equatorial frame, corresponding to a time shortly after it malfunctioned. The example Echostar-2 light curve shown in Fig. 22 suggests that the satellite is inactive and therefore has an inactive internal attitude control system. Assuming negligible external torques, if Echostar-2 is solely comprised of rigid body components, then the satellite would continue to spin about its principal x_b-axis indefinitely. The $\vec{L}$ and $\vec{\omega}$ vectors would coincide (same orientation) and would have magnitudes that would differ by an I_{xx} order of magnitude. Lambert, et al. might have alluded to this when they referred to the spin axis as the "angular momentum vector" instead of the angular velocity vector [18].

It was assumed that Echostar-2's box portion is the most rigid component of the satellite and that its solar panels and communications dishes are more mechanically flexible than the box portion. Motion of the solar panels and/or the dishes with respect to the body frame will cause the satellite's rotational kinetic energy (T) to decrease through friction. Assuming a negligible external net torque, the $\vec{L}$ vector will remain constant. The translational component of the satellite's kinetic energy was not considered as a contributor to this process.

The dot product of the angular momentum vector ($\vec{L}$) with itself was determined and rearranged to result in Eq. (5), which is in the form of an "angular momentum ellipsoid" (L-ellipsoid) with coordinates consisting of the body frame angular velocity components (ω-space). The ellipsoid's three semi-axes depend on the three principal MOIs (I_{xx}, I_{yy}, and I_{zz}) and the magnitude of $\vec{L}$ (L).

$$\frac{\omega_x^2}{(\frac{L}{I_{xx}})^2} + \frac{\omega_y^2}{(\frac{L}{I_{yy}})^2} + \frac{\omega_z^2}{(\frac{L}{I_{zz}})^2} = 1 \tag{5}$$

---

[76]Solidaridad-1 coordinate system definition, dimensions, and MOIs; provided by Dr. Jeremiah Salvatore, retired Boeing senior research fellow.

A similar ellipsoid equation containing the rotational kinetic energy (T) (assuming the inertia tensor in Eq. (47)) is shown in Eq. (6), which is the "rotational kinetic energy ellipsoid" (T-ellipsoid) in ω-space. The ellipsoid's three semi-axes depend on I_{xx}, I_{yy}, I_{zz}, and T. Since both L and T have to exist for any $\vec{\omega}$, it was assumed that $\vec{\omega}$ can only exist where the L-ellipsoid and T-ellipsoid intersect.

$$\frac{\omega_x^2}{(\sqrt{\frac{2T}{I_{xx}}})^2} + \frac{\omega_y^2}{(\sqrt{\frac{2T}{I_{yy}}})^2} + \frac{\omega_z^2}{(\sqrt{\frac{2T}{I_{zz}}})^2} = 1 \tag{6}$$

From spin period observations of Echostar-2 from 2012 to 2015 [16], the satellite's average spin period was estimated to be 373.9s, corresponding to a spin angular velocity of 0.0168044 rad·s^{-1}. It was initially assumed that the satellite's spin axis is currently oriented along the equatorial z-axis and along the body frame's z-axis (maximum MOI). Soon after the satellite malfunctioned and before the satellite reached its steady state motion, it was assumed that the satellite was spinning solely about its x_b body axis and about the equatorial z-axis. Using the conservation of angular momentum, it was determined that the satellite's initial spin period soon after its malfunction was 69±13s, an angular velocity magnitude of 0.091±0.017 rad·s^{-1}. The corresponding initial angular momentum vector was 161±41 J·s, oriented parallel to the equatorial $\vec{\omega}$ orientation. The corresponding initial rotational kinetic energy was 7.3±3.0 J.

Figure 24 (a) shows the corresponding L-ellipsoid (smaller, thinner) and T-ellipsoid (larger). The dark spot shows one assumed intersection of the two ellipsoids, where the only assumed physically possible directions of $\vec{\omega}$ in ω-space can exist, which is along the x_b-axis. The second dark spot (not shown) is located at the opposite end of the L-ellipsoid from the first dark spot, signifying the same $\vec{\omega}$ magnitude, but spinning in the opposite direction. Figure 24 illustrates Echostar-2's assumed L-ellipsoid and T-ellipsoid as T decreased after the satellite's malfunction. Figures 24 (a), (b), (c), and (d) refer to rotational kinetic energies of 6.4 J, 3.0 J, 1.5 J, and 1.3 J, respectively. As T decreased, the (smaller) L-ellipsoid in Fig. 24 (b) remained a constant size while the (larger) T-ellipsoid shrunk, keeping its semi-axis ratio constant.

Figure 24 shows that as T decreases, the $\vec{\omega}$ vector migrates away from the x_b-axis and heads towards the z_b-axis. The z_b-axis corresponds to the satellite's maximum MOI, according to Fig. 46 and Eqs. (46) and (47). Figure 24 (b) and (c) show that $\vec{\omega}$ is comprised of ω_x, ω_y, and ω_z components and that $\vec{\omega}$ will precess about the x_b-axis in a roughly circular fashion. From Fig. 24 (c) to (d), $\vec{\omega}$ ceases precessing about the x_b-axis and finally aligns with the z_b-axis. Fig. 24 (d) shows the point at which T has reached its final state. At this point $\vec{L}$ is still constant in magnitude and direction and T has dropped to 1.3 J. If T decreased any further, it is assumed that $\vec{\omega}$ will not be physically possible because the two ellipsoids can no longer intersect.

Fig. 24 shows that Echostar-2's spin axis would settle on that principal axis having the largest MOI (the z_b-axis) at some time after the malfunction; assuming that no external torques are present and that the solar panel and dishes were moving with respect to the body frame. In inertial space, the angular momentum has not changed and therefore the final spin axis orientation will become parallel to $\vec{L}$ and the satellite will have reached "flat spin". Assuming no external torques, it was concluded that flat-spin is the most stable spin configuration of a box-wing satellite. In reality, a box-wing satellite is being affected by varying external torques, primarily SRP [6]. These torques will affect the satellite's $\vec{L}$ over time, depending on the satellite's characteristics, spin period, and varying solar panel orientation with respect to sunlight [6].

a) $T = 6.4$ J

b) $T = 3.0$ J

c) $T = 1.5$ J

d) $T = 1.3$ J
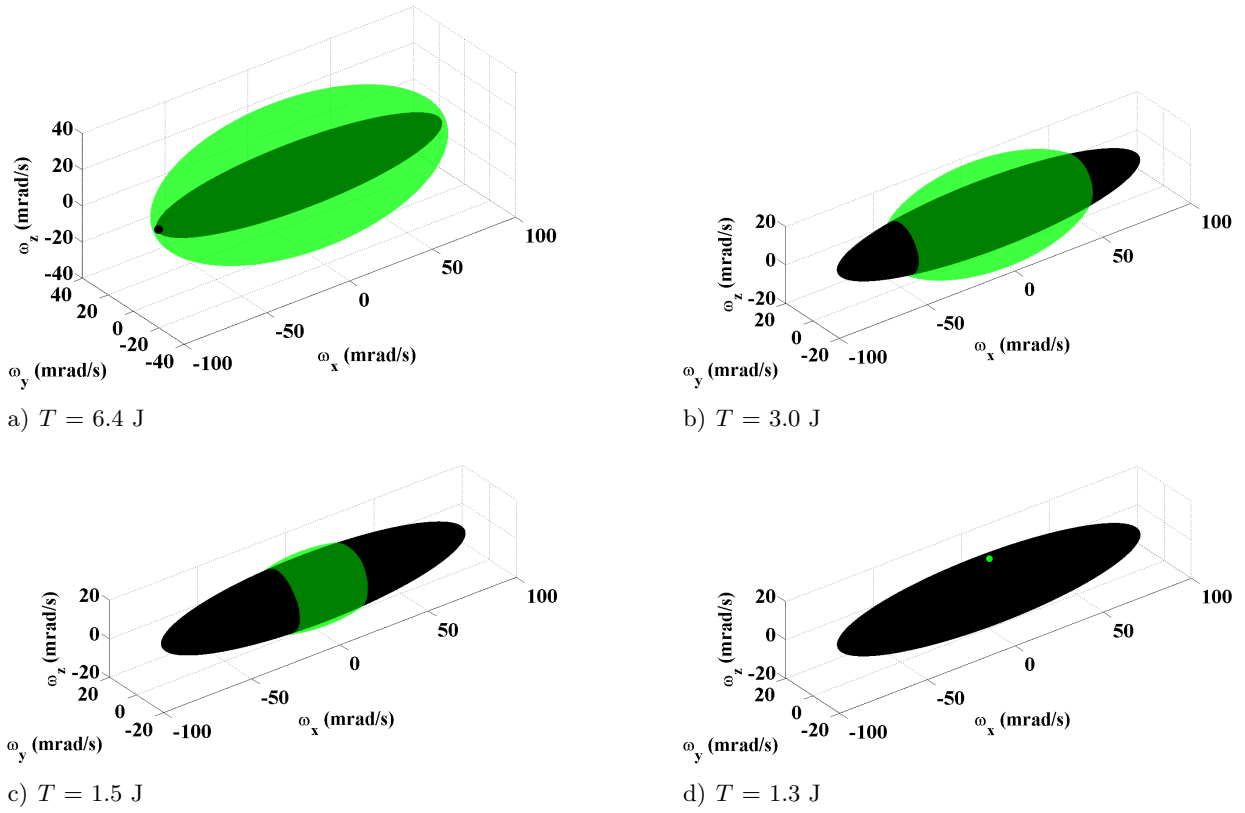
Figure 24   Simulation of Echostar-2's decreasing rotational kinetic energy after malfunction

2   Box-wing Satellite Model

In order to understand how a box-wing satellite's observed light curve could vary due to sun-satellite-observer geometry and satellite attitude, a numerical model in MATLAB that simulated the observed light curves using a simple 3-dimensional (3-D) model composed of geometric satellite forms was developed. Specifically, a box-wing model consisting of a flat-sided cube (the bus), flanked by two large and flat-sided rectangular plates (the solar panels), and two round, flat-sided, and large-diameter disks (the communications dishes) (Fig. 25), was used. It was assumed that each of these surfaces had a uniform, but unique, reflectivity and smoothness. Each surface was depicted by a specific color so that the surface(s) contributing the most to the brightness throughout the simulated light curves could be identified.

The normal unit vector of each surface shown in Fig. 25 with respect to the satellite's body frame coordinates was defined. "Cube side 1" was defined as the mirrored radiator surface whose normal was along the x_b-axis, as shown in Fig. 25. Using this system, "cube side 2" was defined as the cube surface whose normal unit vector was along the y_b-axis (Fig. 25). Using this system, "cube side 3" was defined as the surface with a normal unit vector anti-parallel to the x_b-axis and "cube side 4" was defined as the surface with a normal unit vector anti-parallel to the y_b-axis (Fig. 25). The two remaining cube sides, labeled "cube side 5" and "cube side 6" in Fig. 25, were defined as the surfaces oriented parallel and anti-parallel to the direction of the z_b-axis, respectively (Fig. 25).

"Solar panel 1" and "solar panel 2" were defined as the large rectangular plates that were connected to cube side 1 and cube side 3, respectively, as shown in Fig. 25. Figure 25 depicts both solar panels in the same orientation with respect to one another, such that the visible sides' normals are pointing parallel to the z_b-axis. However, solar panel 2 can be oriented differently than

solar panel 1.
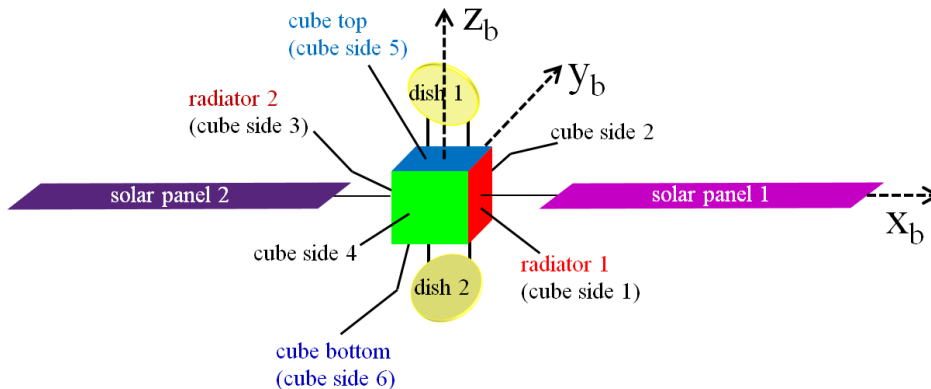
Figure 25 Box-wing satellite model

The two large communications dishes were defined as "dish 1" and "dish 2", as shown in Fig. 25. From artist's conceptions, it was estimated that the two dish surfaces were oriented at approximately 20º from the z_b body frame axis; corresponding to normal unit vectors oriented 20º below and above the body frame's x-y plane. The opposite sides of the solar panels and dishes, not visible in Fig. 25, were assumed to have normal unit vectors that were 180º from their corresponding visible sides.

3 Coordinate Transformations

In order to simulate the satellite's observed sunlight reflection light curves at any time, the position of the Sun and the observer with respect to each of the satellite's surfaces (as defined in Section 2) had to be expressed in a single, convenient coordinate system. Since the interest was primarily in the satellite spin axis orientation's inertial coordinates, the equatorial coordinate system was chosen. Therefore, the Sun's location, Echostar-2's surface normals, and the observer's location all had to be expressed in the equatorial (RA and dec) coordinate system. These unit vectors are all described in Appendix B and Appendix C.

The general coordinate transformation method that used was derived from the Euler rotation matrices shown in Appendix B. The order of the Euler transformation matrix application denotes the "x-convention", as described in [27]. From this general Eulerian x-convention coordinate transformation, the Sun's ecliptical to equatorial, the satellite surfaces' body frame to spin axis frame, and the satellite surfaces' spin axis frame to equatorial frame coordinate transformations were conducted, as fully described in Appendix B.

SOLAR: ECLIPTICAL TO EQUATORIAL FRAME   The Sun's location with respect to the Earth, and consequently to the GEO belt, were initially expressed in geocentric ecliptical longitude (λ_{sun}) and geocentric ecliptical latitude (β_{sun}) coordinates. It was assumed that the Sun's mean apparent path with respect to the Earth was along the ecliptic plane and consequently the Sun's ecliptical latitude was defined as being $\beta_{sun} = 0$ at all times.

The Sun's geocentric ecliptical longitude (λ_{sun}) varied cyclically over an (elliptical) Earth orbit timescale (one sidereal year) with 0º corresponding to the Vernal Equinox (at or near March 21). The Sun's geocentric ecliptical to equatorial (RA: α_{sun} and dec: δ_{sun}) coordinate transformation is shown in Eqs. (59) (Sun dec), (60) (sine of Sun RA), and (61) (cosine of Sun RA) in Appendix B. Equations (60) and (61) were used to determine the quadrant of α_{sun}, using the Euler conditions shown in Eq. (56) in Appendix B.

Satellite surface normal: body frame to equatorial frame   The surface normal unit vector coordinate transformation from the body frame to the equatorial frame required two Eulerian coordinate transformations because the surface normal orientation in the equatorial frame depended on the spin axis orientation with respect to the body frame and the spin axis orientation with respect to the equatorial frame. The first of the Euler rotations transformed the unit vector's body frame coordinates (defined as α_b and δ_b) to the spin frame coordinates (defined as α_ω and δ_ω), as illustrated in Fig. 48. The second of the Euler rotations transformed the spin frame coordinates to the equatorial frame coordinates (defined as α_{eq} and δ_{eq}), as illustrated in Fig. 49.

The body frame to spin frame coordinate transformations are shown in Eqs. (63) (elevation), (64) (sine of azimuthal spin axis angle), and (65) (cosine of azimuthal spin axis angle). Equations (64) and (65) determined the quadrant of α_ω, using the conditions shown in Eq. (56). The spin frame to equatorial frame coordinate transformations are shown in Eqs. (67) (dec), (68) (sine of spin axis RA), and (69) (cosine of spin axis RA). Equations (68) and (69) determined the quadrant of α_{eq}, using the conditions shown in Eq. (56). The Euler rotation angles required for the body frame to the spin frame transformation (ϕ_b, θ_b, and ψ_b) and those required for the spin frame to the equatorial frame transformation (ϕ_ω, θ_ω, and ψ_ω) were initially unknown. For this reason, comparisons of light curve simulations and observed light curves were required to determine Echostar-2's most likely spin axis orientation(s).

D   Reflectance Model

The instantaneous apparent brightness of a satellite surface's reflection will depend on the Sun's location, the observer's location, the satellite's location, the satellite's attitude (spin axis orientation with respect to the equatorial frame and to the body frame), and the surface's reflectance characteristics [19], including its albedo, diffuse reflectance, specular reflectance, and smoothness [29, 30]. As Echostar-2 spins, all of its surface normals' equatorial coordinates will constantly vary with time. If a GEO satellite's spin axis orientation is nearly constant (in both body frame and equatorial frame) over a number of spin periods, then, over several contiguous nights, the satellite's light curve should appear similar from cycle to cycle. This light curve stability (defined as "coherence" in [16]), has been observed in Echostar-2's light curves obtained at similar times of night over several contiguous nights [6]. In several weeks, the light curve should appear to change as the geometry between the satellite, the Sun, and the observer slowly varies. This phenomenon has been observed in Echostar-2's light curves obtained at similar times of night over several weeks [6, 16].

A reflecting surface will have specific properties that determine the intensity of the reflected light flux that an observer detects. The reflectance model used for Echostar-2 light curve simulations was based on Blinn (1977) [29] with specular reflection components based on statistical specular reflection models described by Blinn and Torrence and Sparrow (Torrence-Sparrow) (1967) [29, 30]. This Section discusses the components of this model that were considered and the assumptions that were used to determine each of the satellite surface's reflectance characteristics.

Blinn described the total normalized reflected light flux intensity as a function of the proportion of the ambient light flux reflected (p_a), the proportion of the diffuse light flux reflected (p_d), and the proportion of the specular light flux reflected (p_s), as shown in Eq. (7) [29]. The variables I_i and I_r are the total light flux intensity incident on the surface and the reflected light flux intensity from the surface, respectively. The variables d and s denote the specific normalized diffuse and specular reflection amounts, respectively, as described by Blinn [29].

$$I_r = I_i \left[p_a + d p_d + s p_s \right] \tag{7}$$

1 Incident Light Flux Contributors

To evaluate the reflected light flux intensity, sunlight was considered to be the primary contributor, with Earth-shine and moonlight as potential secondary and tertiary contributors, respectively. The Sun has an average visual magnitude of -26.83 [7] when viewed from the region of Earth orbit, including the GEO satellite region. Echostar-2's broadband magnitude was observed by Earl and Wade to be between 17 and 2 [16]. In this paper, the Sun was assumed to be a point source.

When observed from the GEO belt, the full Earth appears to have an average visual magnitude of -20, assuming an average solar constant of 1360.8 ± 0.5 W·m^{-2} [31] and an average clear sky Earth albedo of 0.3 [32]. The Earth's maximum apparent brightness at GEO is therefore nearly 7 broadband magnitudes fainter than the Sun's brightness at GEO. However, the observations of Echostar-2 described by [16] were conducted within two hours of midnight Eastern Time (04:00 or 05:00 UTC). When the satellite was observed, the Earth would have appeared as a wide crescent (at most) from the perspective of Echostar-2. Reducing the Earth's apparent phase from full to crescent reduces its maximum visual magnitude to approximately -18; nearly 9 broadband magnitudes fainter than the Sun.

If the sunlight flux reflected from the Earth has the same spectral characteristics as those of the Sun (with the exception of brightness), and that Earth-shine was the only light source, then Echostar-2's apparent broadband magnitude would range from 28 to 13. The magnitude 13 reflections would only occur during the brightest of specular reflections. Therefore, when simulating Echostar-2 light curves, Earth-shine was not considered to be a significant brightness contributor when compared to the Sun's contribution.

The full Moon at its perigee[77] has a visual magnitude of -12.9 at its closest distance to the GEO belt; approximately 327,400 km [7]. The full Moon's apparent brightness at GEO is therefore approximately 14 magnitudes fainter (nearly 400,000 times fainter) than the Sun's brightness at GEO. Since a full moon appears nearly 5 magnitudes fainter than a crescent Earth, the Moon was not considered to be a contributor to the Echostar-2 light curve.

2 Ambient and Diffuse Reflections

Blinn assumed that a component of the total incident light flux falling on a surface was an ambient light source. Blinn described this as a uniform light flux originating from all directions. When integrated, this ambient light flux would yield a constant flux value for any normal direction [29]. In Earth orbit, ambient light flux originates from the Milky Way stars (other than the Sun) and external galaxies. However, when compared to sunlight, this ambient light flux is negligible. As a result, it was assumed that the variable p_a in Eq. (7) was 0.

Diffuse light flux reflection was described by Blinn as the equal diffusion of the incident light flux in all directions by the illuminated surface [29], more commonly known as "Lambertian reflection" [29]. The Lambertian (diffuse) reflection (d) is calculated with the dot product of the surface's normal unit vector ($\hat{n}_{eq}$) and the solar unit vector ($\hat{n}_{sun}$), as shown in Eq. (8) and defined in Appendix C. The dot product results in the solar incidence angle (ξ) on the solar panel plane. The proportion of the diffuse reflection (p_d in Eq. (7)) depends on the surface's specific reflection characteristics, including its albedo. Assuming that the surface is perfectly opaque (no light transmission through the material) and the dot product result is negative, the diffuse flux is 0 (dark).

$$d = \cos(\xi) \tag{8}$$

---

[77] 363,400 km from the Earth's center.

3 Specular Reflection

The Torrence-Sparrow model involves a surface that is comprised of randomly orientated micro-facets [29, 30]. The Ψ angle was defined as the angle between a reflective surface's normal unit vector and the PAB, as shown in Fig. 50 and in Eq. (81). The specular component of the reflected light comes from those micro-facets whose surface normals are nearly aligned with the PAB, i.e. when their individual Ψ angles are nearly 0. As shown in Eq. (9), Blinn described the Torrence-Sparrow specular reflection component (s) as being comprised of a distribution function (D), a masking function (G), a Fresnel reflection function (F), and the cosine of the angle η (shown in Fig. 50 in Appendix C) [29]. The observer requires a direct line of sight to the surface in order to see any specular reflection from it. Therefore, the $\cos\eta$ term in Eq. (9) must be positive, as shown in Eq. (73). The variables D, G, and F can only have values between 0 and 1 [29].

$$s = \frac{DGF}{\cos(\eta)} \tag{9}$$

The distribution function (D) of Eq. (9) refers to the proportion (the probability density of the unit vector $\hat{n}_{\text{PAB}}$) of those micro-facets whose normals are nearly aligned with the PAB [33]. Torrence-Sparrow, Blinn, and Kelemen (2001) referred to a Gaussian distribution function, shown in Eq. (10), that depends on the Ψ angle (shown in Fig. 50) (in radians only) and a surface smoothness factor μ, which is also the slope of the specular reflection distribution [33]. The smoothness factor (μ) can have values between 0 (shiny) and 1 (dull) [29].

$$D = \exp\left[-\frac{\Psi}{\mu}\right]^2 \tag{10}$$

The masking function (G), a quantitative expression of self-shadowing, refers to the micro-facets that block incident light to other micro-facets or block the reflected light from other micro-facets. The masking function depends on the specific texture of the surface and the light's incidence angle on the surface (ξ) [29]. Echostar-2's reflecting surfaces were assumed to comprise of fine-textured materials with μ values of less than 0.1. Using this assumption, self-shadowing could only occur if the ξ angle was large or nearly 90º. Most of the observations were conducted when the phase angle (PA) at Echostar-2 was less than 50º, although the maximum PA allowed was 90º [6]. Therefore, it is likely that most of the high incidence angle sunlight would have been detected as diffuse and not specular reflection by the observer. As a result, the masking function (G) was assumed to have a value of 1 at all times.

The Fresnel reflection function (F) refers to the fraction of light being reflected (as opposed to being absorbed) by the surface. Metals have Fresnel values of nearly 1 [29]. Echostar-2 was assumed to have been primarily constructed of aluminum and other light-opaque materials, therefore the Fresnel value (F) was assumed to be 1 at all times.

4 Box-wing Reflectance Model

Equation (11) shows the expression for the total estimated reflected light intensity (I_{r}) from a box-wing satellite surface. Equation (11) is only non-zero when both the ξ and η angles have cosines that are positive, as shown in Eqs. (71) and (73), respectively. Equation (12) determines the total amount of reflected light flux ($I_{\text{r(tot)}}$) from all defined box-wing surface contributions at any instant. The subscript "(ci)" denotes the specific cube side (1, 2, 3, 4, 5, or 6) in Fig. 25. The subscript "(ps)" denotes the specific solar panel and specific panel side, respectively, in Fig. 25. The subscript "(ds)" denotes the specific communication dish and specific dish side, respectively, in Fig. 25.

Eqs. (7) to (12) do not take into account any surface occulting, shadowing of one surface by other surfaces, or multiple reflections between surfaces. As a result, some simulated broadband magnitudes appear brighter (or fainter) than expected.

$$
I_{\mathrm{r}} = \begin{cases} I_{\mathrm{i}} \left\{ p_{\mathrm{d}} \cos \xi + p_{\mathrm{s}} \left[\dfrac{\exp\left[-\frac{\Psi}{\mu}\right]^2}{\cos \eta} \right] \right\} & \text{if } \cos \xi > 0 \text{ and } \cos \eta > 0; \text{ and} \\ 0 \text{ otherwise.} \end{cases}
\tag{11}
$$

$$
I_{\mathrm{r(tot)}} = \sum_{\mathrm{i}=1}^{6} \left\{ I_{\mathrm{r(ci)}} \right\} + \sum_{\mathrm{p}=1}^{2} \sum_{\mathrm{s}=1}^{2} \left\{ I_{\mathrm{r(ps)}} \right\} + \sum_{\mathrm{d}=1}^{2} \sum_{\mathrm{s}=1}^{2} \left\{ I_{\mathrm{r(ds)}} \right\}
\tag{12}
$$

The free parameters in Eq. (11) are I_{i}, p_{d}, p_{s}, and μ. For each defined surface, these free parameters are unconstrained because the exact size and reflective properties of each of Echostar-2's surfaces were unknown.

E   Specular Reflection Geometry

The specular reflection distribution function (D), shown in Eq. (10), suggests that the maximum specular reflection flux would be observed (assuming a constant surface smoothness μ) when the angle Ψ between a surface PAB unit vector ($\hat{n}_{\mathrm{PAB}}$) and the same surface's normal unit vector ($\hat{n}_{\mathrm{eq}}$) is zero. In this case, these two unit vectors would be co-located. If a satellite's light curve exhibited a sufficient amount of specular reflections over a long timescale (months or years) and those specular reflections could be identified (or at least assumed) to be emanating from a particular satellite surface, then the maximum specular reflection flux observed over that time would correspond to the minimum Ψ angle. The many observations of Echostar-2 made over a nearly 4-year timescale were advantageous because a large statistical sampling of specular reflections enabled us to identify the maximum specular reflectance flux and be confident that it would constitute the minimum Ψ angle observed. Although this minimum Ψ angle would not necessarily be zero, it would be the closest to zero that was observed over the nearly 4-year timescale.

1   Geometry of Maximum Specular Reflection Flux

Of all the box-wing observations obtained between early-2012 and late-2015, Echostar-2's brightest specular reflections were observed to have broadband magnitudes of between 1 and 2 between September 9 and 20, 2012. It was assumed that the Ψ angles during these specular reflections were zero. An example illustration of the sunlight direction, the observer's position on the Earth, and the satellite surface's orientation, which collectively could have caused the maximum specular reflection observed on 02:10:39 UTC on September 12, 2012, is shown in Fig. 26. Figure 26 depicts the satellite surface as a radiator side of the model cube (shown without solar panels or dishes), which was originally shown in Fig. 25. The PA (ρ) has been slightly exaggerated in Fig. 26 (b) in order to permit easier reading of the labels.

The equatorial coordinates of the Sun and of the observer as viewed from the satellite at a time of maximum specular reflection were known; therefore the coordinates of the PAB unit vector could be determined using Eqs. (75) through to (80). Even if the identity of the specific surface causing the specular reflection was assumed, or had been identified, Echostar-2's attitude at the time of the observed maximum specular reflection could have any orientation about the surface normal unit vector, and consequently about the PAB unit vector. The spin axis orientation can be located anywhere that allows the surface normal unit vector to align with the PAB unit vector once per spin period.
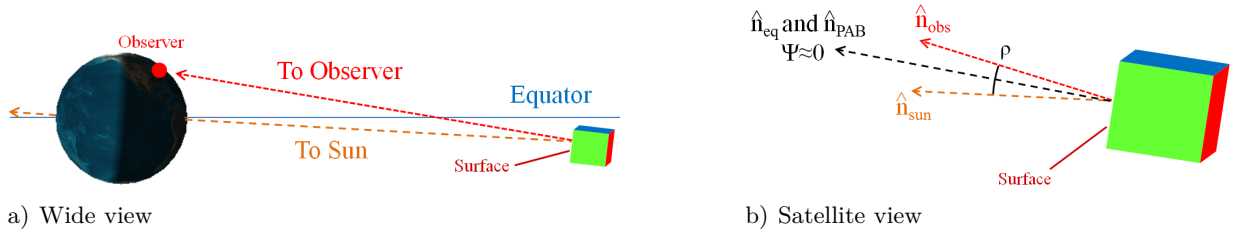
Figure 26 Sunlight direction, observer, and satellite surface at 02:10:39 UTC September 12, 2012

2   Spin Axis Plane Corresponding to Maximum Specular Reflection Flux

Figure 22 reveals that two bright specular reflections of approximately magnitude 2 were observed from Echostar-2, once every half spin period. These two specular reflections did not correspond to the same satellite surface because the two diffuse features in the same light curve (Fig. 22), also separated by 50% of the spin period, appear different from each other. This suggests that the two surfaces are located on opposite sides of the spacecraft. These two surfaces could be the two sides of the solar panels or the two mirrored radiators labeled in Fig. 25.

A box-wing satellite's solar panel is designed such that one side contains the power generating solar cells while the opposite side is painted with white or black paint [25]. As a result of this difference, the two sides of a solar panel would not likely exhibit similar reflection features in a light curve, such as the specular features shown in Fig. 22. The two radiators located on the satellite's box portion were assumed to have identical second-surface mirror specifications, whose highly reflective aluminum or silver tile backing is coated with quartz glass [34]. The aluminum or silver backing would make both radiators highly specularly reflective, similar to what had been observed in the light curves. Therefore, the bright specular reflections were likely caused by the two mirrored radiators, as depicted in Fig. 25.

It was assumed that both of Echostar-2's mirrored radiators have very similar specifications, including size and reflectivity. In this case, the only constraints on the satellite's attitude that would cause two specular reflections of similar brightness over one spin period, would be that the spin axis orientation vector (angular velocity vector) had to be directed parallel to both radiators (perpendicular to both radiators' surface normals). Therefore, the spin axis orientation in the body frame would be located in the y_b-z_b plane (Fig. 23) and the spin axis orientation in the equatorial frame would be located in a plane that is perpendicular to the PAB unit vector as shown in Fig. 26 (b) and at the time shown in its caption. The "flat spin" scenario, in which the satellite exclusively spins about its z_b axis (shown in Fig. 24 (d)), satisfies the body frame y_b-z_b plane condition. However, the MOI of a cube is the same for any axis passing through its geometrical center (assuming a uniform density throughout). Therefore, the satellite's y_b and z_b orthogonal body frame axes can be located anywhere within the y_b-z_b plane.

Table 5 lists all data required to determine the orientation of the PAB unit vector when the maximum specular reflection observed on September 12, 2012. The J2000.0 equatorial coordinates of the Sun and of the satellite were determined with Software Bisque's TheSky Level IV, Version 5 planetarium software. The three PAB Cartesian coordinates were determined with Eqs. (75) to (77). Finally, the PAB's J2000.0 equatorial coordinates were determined with Eqs. (78) to (80). Note that the sum of the squares of the PAB's Cartesian coordinates will not equal 1, because only the direction of the PAB unit vector was determined. The final row of Table 5 shows the determined PAB equatorial coordinates.

Table 5 Quantities required to determine Echostar-2's PAB unit vector on September 12, 2012

Variable	Value	Notes
$\lambda_{\text{sun}}(^{\text{o}})$	169.72611	J2000.0
$\alpha_{\text{sun}},\ \delta_{\text{sun}}(^{\text{o}})$	170.55542, 4.0663889	J2000.0
$\alpha_{\text{sat}},\ \delta_{\text{sat}}(^{\text{o}})$	326.16875, -10.591944	J2000.0
$\alpha_{\text{obs}},\ \delta_{\text{obs}}(^{\text{o}})$	146.16875, 10.591944	α_{sat} - 180$^{\text{o}}$, -δ_{sat}
$x_{\text{PAB}},\ y_{\text{PAB}},\ z_{\text{PAB}}$	-0.9002443, 0.3554714, 0.1273627	PAB's Cartesian x, y, and z coordinates
$\alpha_{\text{PAB}},\ \delta_{\text{PAB}}(^{\text{o}})$	158.45287, 7.4964117	J2000.0

The spin axis unit vector ($\hat{n}_{\text{spin}}$) and the PAB unit vector were assumed to have been orthogonal to each other at 02:10:39 UTC on September 12, 2012. The two mirrored reflectors' surface normal unit vectors aligned with the PAB unit vector, in an alternating fashion, twice per spin period. These alignments resulted in the narrow tall specular features of the light curve shown in Fig. 22. It was assumed that the light curve's remaining (diffuse) features were due to the satellite's other box sides, its dishes, and possibly its solar panels. The dot product of two orthogonal unit vectors is 0, as shown in Eq. (82). Equation (82) can be rearranged to yield an equation that analytically determines all of the possible spin axis equatorial coordinates, as is shown in Eq. (85). No matter what its orientation, the spin axis plane will span all RA coordinates (0 to 360°). The corresponding spin axis dec coordinates can be determined from a RA coordinate with Eq. (85). Figure 27 (a) shows all of the possible equatorial coordinates of Echostar-2's spin axis orientation on September 12, 2012, based on the analytical solutions of Eq. (85).

The analytical determination, as shown in Fig. 27 (a), was confirmed with specular reflection models, which determined the maximum specular reflection as the satellite spun. This was achieved by testing all spin axis orientation equatorial coordinates (involving all Euler angles between the spin axis and the equatorial frame). The radiators' (cube side 1 and cube side 3) reflective free parameters, including the incident solar radiation on each (expressed in Analog to Digital Units (ADUs)), were assumed to have the values shown in Table 6. It was assumed that the radiators exhibited totally specular reflections (no diffuse reflections). No other satellite surfaces other than the radiators were considered to be contributors to the reflected light flux. The free parameters were chosen such that the maximum specular reflection brightness was magnitude 2 when the reflected flux value was used in Eq. (13). Equation (13) was an empirical equation derived from CCD images of Landolt stars [16]. An angle increment of one degree was used for both RA and dec coordinates.

$$m_{\text{b}} = 21.4 - 1.182\ ln\left[I_{\text{r(ci)}}\right] \tag{13}$$

Figure 27 (b) presents the 3-D results of the analysis, showing the spin axis orientation coordinates and the broadband magnitude. Figure 27 (c) presents the 2-dimensional (2-D) results of the analysis, showing the spin axis orientation coordinates with different greyscale shading indicating different broadband magnitudes. The vertical scale corresponding to the broadband magnitude (depicting magnitude 14 to 2) can be used for both Figs. 27 (b) and (c).

Table 6 Values of radiator reflection free parameters

Variable	Value	Notes
I_{c1} and I_{c3}	1.31×10^7 ADU	CCD detection units
μ_{c1} and μ_{c3}	0.05	reflector smoothness factor
$p_{d(c1)}$ and $p_{d(c3)}$	0	no diffuse component
$p_{s(c1)}$ and $p_{s(c3)}$	1	100% specular component

a) Analytical method

b) 3-D Specular reflection simulation

c) 2-D Specular reflection simulation
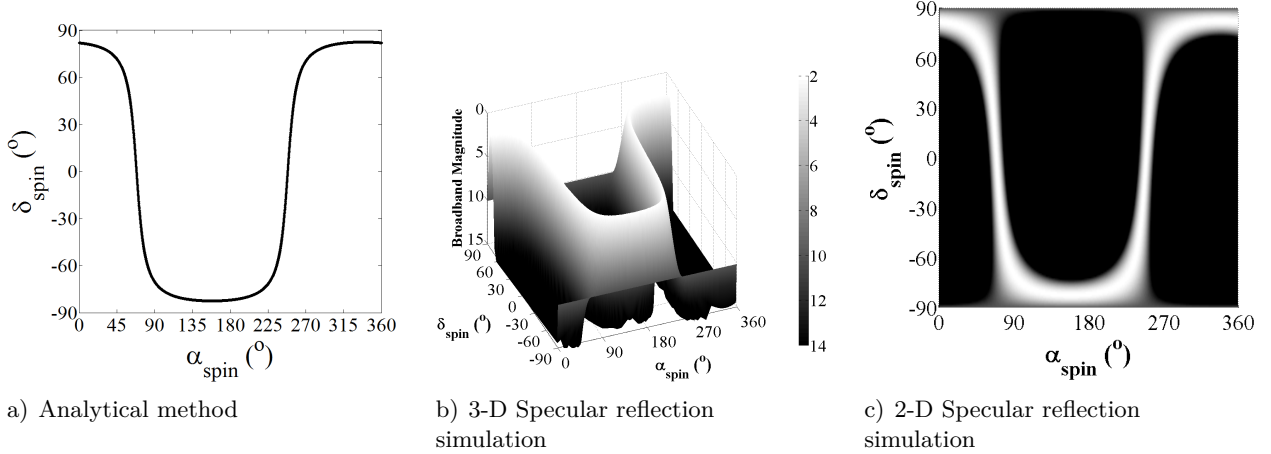
Figure 27 Echostar-2's possible spin axis orientation coordinates for September 12, 2012

Figure 27 (c) suggests that the analytical solution of the spin axis plane shown in Fig. 27 (a) was the correct one. Although the solution of the spin axis plane reduces the overall problem by one degree of freedom, the question of the most likely spin axis orientation, somewhere along the spin axis plane, still exists. Before investigating how to further reduce the degrees of freedom to solve for the spin axis orientation, one would need to address the question of determining the maximum angle between the surface normal and the PAB that would still be considered as a specular reflection.

3 Specular Reflection Curve Width

The width of the specular reflection features (Fig. 22) primarily depends on the smoothness of the mirrored radiators (μ). Within a folded light curve, a specular reflection will appear to have a smaller density of data points when compared to a diffuse reflection. This is because a specular reflection can normally occur in a much smaller timescale than a diffuse reflection and a specular reflection is more sensitive to the Ψ angle between the surface normal and the PAB.

Figure 22 shows alternating diffuse and specular reflections, with contributions from at least four cube sides, including the two sides containing the mirrored radiators. The specular reflection features appear to be thinner than those of the diffuse reflections; however, the specular reflections will also likely contain diffuse reflection contributions. Figure 28 shows all of the superimposed reflections, corresponding to both mirrored radiators, that were observed on September 12, 2012. Figure 28 shows the reflections corresponding to 38% to 48% (filled points) and from 88% to 98% (hollow points) of the spin percentage (horizontal axis), as shown in Fig. 22. Figure 28 shows the similarity between the two specular reflections with respect to one another. The horizontal line indicates the estimated border between the high density and low density data points, suggesting

the border between the mostly diffuse (below the line) and the mostly specular (above the line) reflections. The width of the curve at the divide (indicated by the horizontal line), was measured to be $0.672 \pm 0.077\%$ of a spin period, which corresponds to a rotation angle of $2.42 \pm 0.28^{\circ}$. The center of this angle corresponds to the maximum specular reflection flux. This suggests that a mirrored radiator surface unit vector must be within $1.21 \pm 0.14^{\circ}$ of the PAB to make it possible for the observer to view a specular reflection brighter than magnitude 9. However, this determination was based on the initial assumption that the maximum specular reflection flux observed on September 12, 2012 corresponded to a Ψ angle of 0.
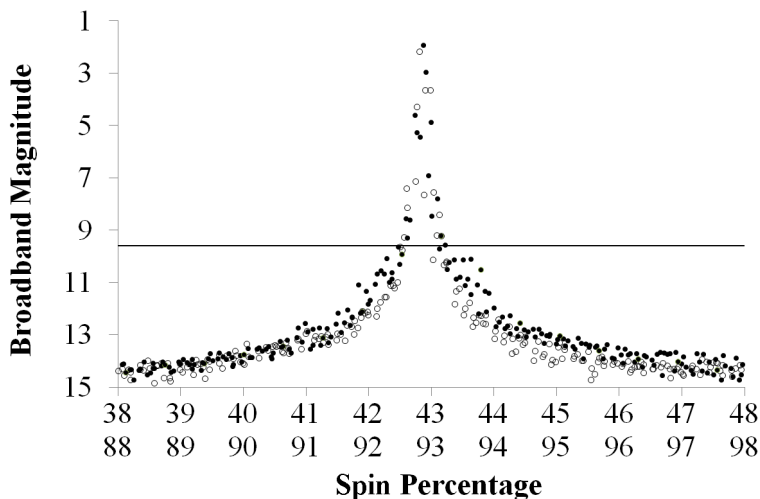
Figure 28   Overlay of Echostar-2 specular reflections observed on September 12, 2012

F   Analytical Spin Axis Orientation Determination

Additional bright specular reflections were observed on the nights of September 9, 10, 11, 13, 14, 16, 20, and October 10, 2012. Table 7 shows the date, the time, the Sun's equatorial coordinates, the observer's equatorial coordinates (with respect to Echostar-2), and the satellite's brightest estimated broadband magnitude corresponding to the brightest specular reflections observed. It was assumed that each one of these specular reflections corresponded to a radiator with a Ψ angle of 0. Consequently, each of these specular reflections corresponded to a PAB unit vector that was orthogonal to a spin axis plane.

1   Spin Axis Plane Intersections

Echostar-2's spin axis planes, that correspond to the dates and times shown in Table 7, will all be different because the PABs will all be different. However, should the spin axis orientation be identical over a number of days, then two points along these spin axis planes would have to be identical, or at least similar, to one another. One of these points would identify a prograde spin axis (positive dec) and the other would identify a retrograde spin axis (negative dec), located 180° from the prograde spin axis. The two spin axis points would therefore be identified as intersections between two or more spin axis curves, which correspond to the spin axis planes.

Table 7 Observed Echostar-2 bright specular reflections from September 9 to October 10, 2012

Date (mm/dd/yy)	Time (UTC)	λ_{sun} (°)	α_{obs}, δ_{obs} (°)	Brightest Magnitude
09/09/12	02:07:21	166.80667	142.30625, +10.51333	1.4
09/10/12	02:08:39	167.77944	143.64583, +10.54306	1.6
09/11/12	02:37:08	168.77111	151.81042, +10.66611	1.2
09/12/12	02:10:39	170.55542	146.16875, +10.59194	2.0
09/13/12	02:17:48	170.70444	148.97250, +10.63472	1.7
09/14/12	02:15:36	171.67722	149.42667, +10.64083	1.7
09/16/12	02:18:07	173.62889	152.06792, +10.67083	1.2
09/20/12	02:10:58	177.53000	154.28167, +10.69500	1.8
10/10/12	02:07:26	197.17972	173.02125, +10.64222	2.0

To demonstrate this intersection principle, suppose that the spin axis orientation of Echostar-2 was always constant, had a 0 dec, and was always orthogonal to the two radiators' surface unit vectors, as shown in Fig. 29. In this case, the only times the observer could see a bright specular reflection from the radiators would be when the PAB's RA coordinate was within 1.21 ± 0.14° of the Sun's RA coordinate. This would occur on several days separated by six months (half an Earth orbit). Therefore, the PAB's RA coordinate at six months later would be 180° away from the first PAB's RA coordinate. Figure 30 shows that the curve corresponding to the second spin axis plane (dashed line) would be phase-shifted 180° in RA from the curve corresponding to the first spin axis plane (dotted line). Figure 30 also shows that the two curves intersect at a dec of 0 and with the two RAs separated by 180°. This indicates that there are two spin axes that lie along the same line but with rotation in opposite directions, demonstrating that either spin axis could produce the observed specular reflections.

Figure 30 (a) depicts the spin axis curves from specular reflections viewed in March and September. Figure 30 (b) depicts the spin axis curves from specular reflections viewed in June and December. The two curves in Fig. 30 (b) have much different amplitudes when compared to those in Fig. 30 (a) because of the Sun's varying apparent dec, as viewed from Earth (and from the satellite) between June and December, as illustrated in Fig. 47. The only major difference between Fig. 30 (a) and (b) is that the spin axis orientation's RA coordinate is shifted by 90°, as expected.

Assuming that Echostar-2's spin axis orientation remained nearly constant between September 9 and October 10, 2012, the possible spin axis orientations (prograde and retrograde) can be determined from the intersections of two or more spin axis planes separated temporally. Echostar-2's synodic spin period was observed to increase from 376.0 ± 0.3s to 393.2 ± 0.3s during this time [16]; therefore a stable-state angular velocity magnitude could not be assumed. The RA coordinates of the spin axis curves' intersection points can be determined analytically from their respective PAB coordinates with Eq. (89). The dec coordinates can then be determined from either PAB coordinates with Eq. (85).
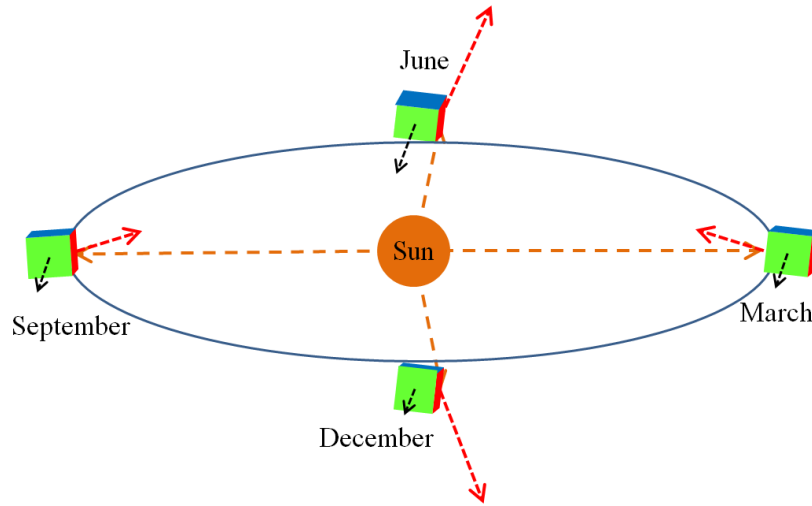
Figure 29 Specular reflections of radiators when spin axis orientation dec is 0
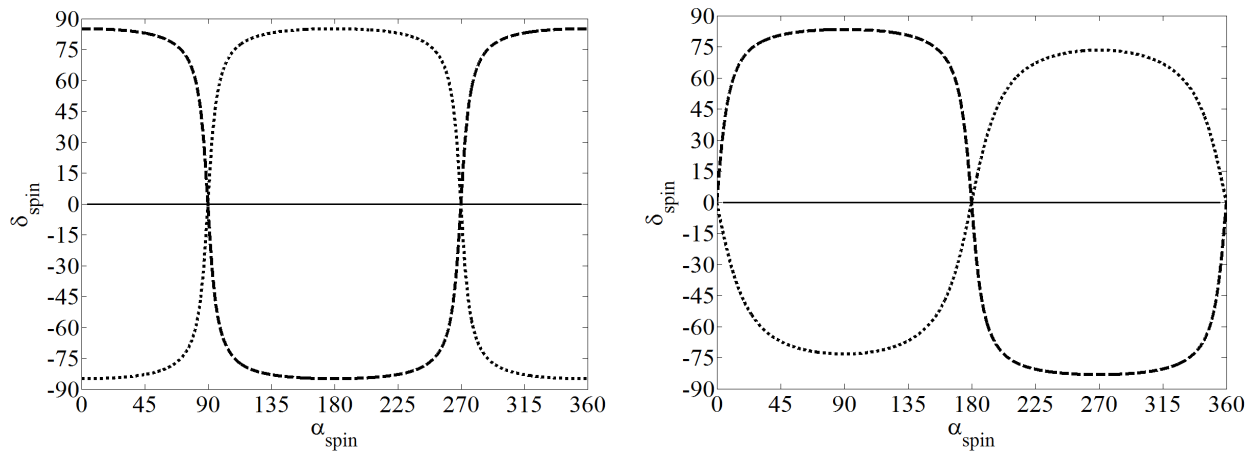
a) March and September specular reflections

b) June and December specular reflections

Figure 30 Intersection of spin axis curves corresponding to 0 dec spin axis orientation

G Spin Axis Orientation Estimations

Table 8 lists all of Echostar-2's potential spin axis orientations that are based on the brightest specular reflections as observed on September 9 and 10, 2012, September 10 and 11, 2012, and so on, until September 20 and October 10, 2012. The last two rows of Table 8 list comparisons of September 9 and September 16, 2012 (7 days apart) and September 16 and October 10, 2012 (24 days apart). Two coordinate pairs are listed for each pair of days; the first pair $(\alpha_{\text{spin(p)}}, \delta_{\text{spin(p)}})$ referring to a prograde spin axis and the other pair $(\alpha_{\text{spin(r)}}, \delta_{\text{spin(r)}})$ referring to a retrograde spin axis.

Table 8 Spin axis curve intersection coordinates - September and October 2012

Dates (mm/dd1-dd2)	$\alpha_{spin(p)}, \delta_{spin(p)}$ (°)	$\alpha_{spin(r)}, \delta_{spin(r)}$ (°)
09/09-10	285.4, +77.64	105.4, -77.64
09/10-11	318.0, +81.72	138.0, -81.72
09/11-12	54.1, +81.60	234.1, -81.60
09/12-13	299.2, +80.35	119.2, -80.35
09/13-14	275.0, +72.96	95.0, -72.96
09/14-16	286.5, +77.88	106.5, -77.88
09/16-20	277.4, +73.97	97.4, -73.97
09/20-10/10	283.2, +77.08	103.2, -77.08
09/09-16	286.8, +77.96	106.8, -77.96
09/16-10/10	282.9, +76.60	102.9, -76.60

With the exception of the spin axis orientations corresponding to September 11-12, 2012, all of the spin axis orientations range in RA from 275º to 318º (corresponding retrograde RAs ranging from 95º to 138º) and range in dec from 73º to 82º (corresponding retrograde decs ranging from -82º to -73º). However, the spin axis orientations corresponding to the two more widely spaced days between September 9-16 and between September 16 and October 10, 2012, suggest that Echostar-2's spin axis orientation falls between 282º and 287º in RA and between 77º and 78º in dec (prograde), or between 102º and 107º in RA and between -78º and -77º in dec (retrograde).

Figure 31 (a) shows the intersections of the spin axis curves corresponding to September 9 (solid curve), 13 (dotted curve), 20 (dash-dot curve), and October 10, 2012 (dashed curve). Figure 31 (a) shows the intersections with the analytical method and Fig. 31 (b) shows the intersections from specular reflection simulations. The two circles in each of Fig. 31 (a) and (b) indicate the most likely intersection points that correspond to the prograde and retrograde spin axis orientations. Figure 31 demonstrates that the likely spin axis orientation from September 9 to October 10, 2012 was located near the equatorial coordinates shown in the last two rows of Table 8.

a) Analytical method

b) Specular reflection simulations
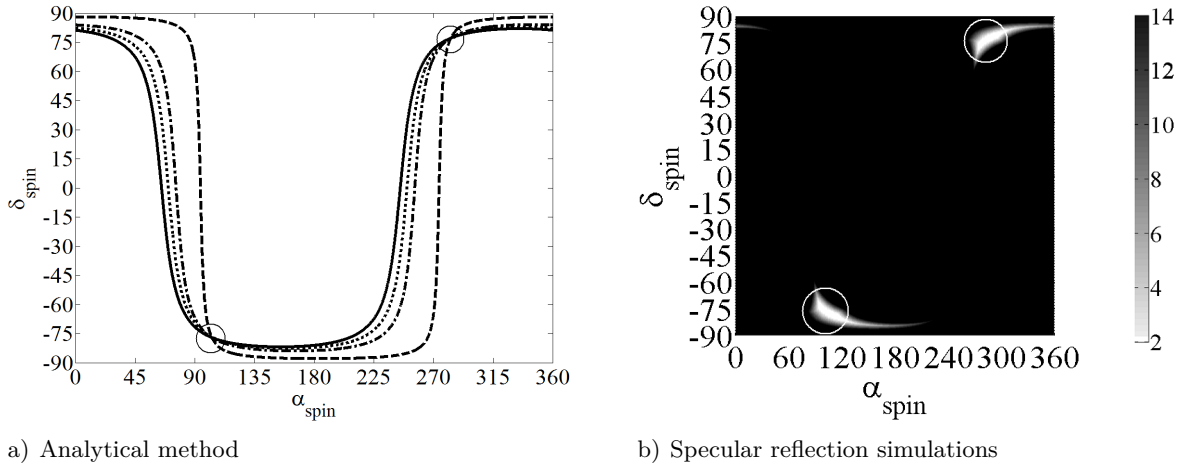
Figure 31 Spin axis curve intersections (September 9, 13, 20, and October 10, 2012)

Further analysis of Echostar-2's spin axis orientation was conducted based on observations conducted on March 5 to 29, 2013, August 19 to September 19, 2014, March 5 to 24, 2015, and July 25 to October 10, 2015. Table 9 shows the resulting intersection points of those spin axis curves which correspond to the date pairs shown. In all cases, specular reflections were observed that were assumed to have originated from the satellite's mirrored radiators. Table 9 suggests that although the spin axis orientation might have been stable in September-October 2012, the spin axis had moved to a different location by March 2013. The estimated spin axis orientations from the August-September 2014 observations suggest that Echostar-2's spin axis did not return to the same estimated location in September-October 2012. The observations from March, July, and September 2015 were not conducted as frequently as the earlier observations; however, they also suggest that the spin axis orientation varies over time.

From the results shown in Tables 8 and 9, the most likely prograde and retrograde spin axis orientations were determined and are shown in Table 10 and Fig. 32. The random uncertainties were determined by the standard deviation of the data for each date shown in Tables 8 and 9. All data that greatly deviated from the average were considered outliers and were omitted. In Fig. 32, the circles denote the prograde and retrograde spin axis orientations for September to October, 2012. The squares denote the orientations for March 2013. The triangles denote the orientations for August to September 2013. The diamonds denote the orientations for March 2015. Finally, the asterisks denote the orientations for July to October 2015. The labels "Spring" and "Autumn" indicate the spin axis orientations for the dates around March and the dates around September of each year, respectively, for easier comparison of the plots.
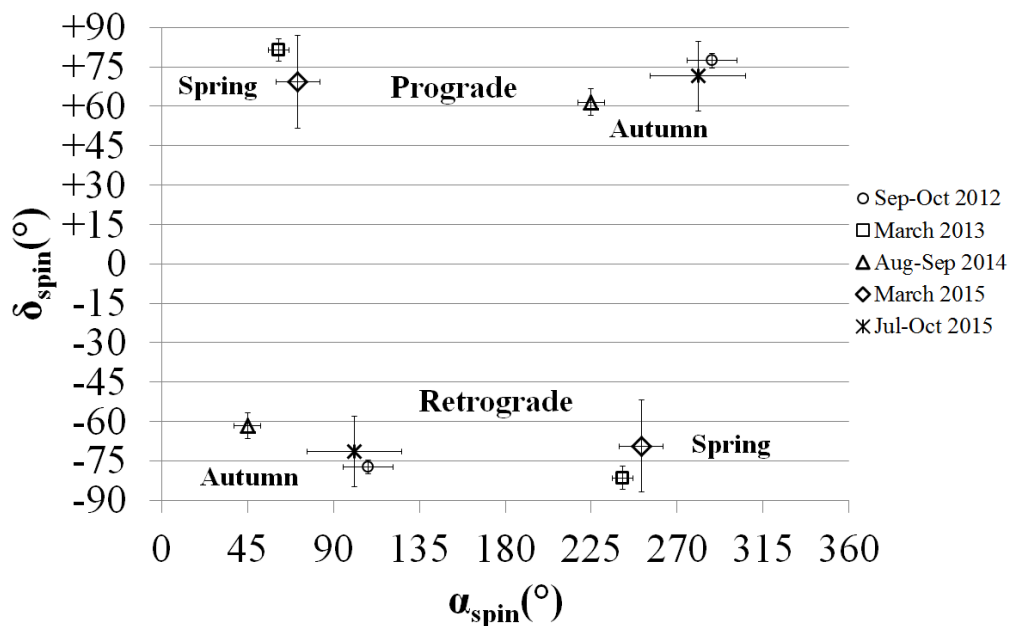
Figure 32   Estimated spin axis orientations of Echostar-2 - 2012 to 2015

Figure 32 suggests that Echostar-2's spin axis orientation, corresponding to the spring and autumn months, has significantly different coordinates. If the spin axis had been stable over the entire year, then specular reflections from the mirrored radiators would not have been observed in the spring because the satellite would have had the wrong orientation to reflect sunlight to the observer. Therefore, it is reasonable to conclude from this research and previous research shown in [6] that Echostar-2's angular velocity vector's magnitude and direction are both varying with time, primarily due to SRP torques.

Table 9   Estimated Echostar-2 Spin Axis Orientations - March 2013 to September 2015

Dates (mm/dd1-dd2)	$\alpha_{\text{spin(p)}}, \delta_{\text{spin(p)}}$ (°)	$\alpha_{\text{spin(r)}}, \delta_{\text{spin(r)}}$ (°)
March 2013		
03/05-08	66.7, +85.81	246.7, -85.81
03/05-14	58.5, +82.93	238.5, -82.93
03/05-16	69.8, +86.37	249.8, -86.37
03/08-14	57.2, +76.23	237.2, -76.23
03/08-16	59.1, +80.57	239.1, -80.57
03/14-16	57.3, +76.99	237.3, -76.99
August-September 2014		
08/19-20	225.7, +62.85	45.7, -62.85
08/19-24	217.3, +58.07	37.3, -58.07
08/19-26	212.1, +54.02	32.1, -54.02
08/20-24	223.9, +61.27	43.9, -61.27
08/24-25	226.6, +62.37	46.6, -62.37
08/25-26	225.3, +61.64	45.3, -61.64
08/26-09/04	352.3, +0.21	172.3, -0.21
09/04-15	224.1, +58.48	44.1, -58.48
09/04-19	226.3, +59.50	46.3, -59.50
09/15-16	228.9, +65.05	48.9, -65.05
09/16-19	238.8, +72.62	58.8, -72.62
March 2015		
03/06-12	66.7, +70.87	246.7, -70.87
03/06-24	62.7, +50.99	242.7, -50.99
03/12-24	84.3, +86.14	264.3, -86.14
July-October 2015		
07/25-08/07	34.4, +50.69	214.4, -50.69
08/07-09/24	263.3, +62.09	83.3, -62.09
09/24-10/10	298.5, +80.93	118.5, -80.93

H   Light Curve Simulations

The estimated spin axis orientations that are shown in Fig. 32 were tested by simulating light curves using the box-wing satellite model shown in Fig. 25 and the reflectance model described in Section D. The light curve simulations were compared with the corresponding observed Echostar-2 folded light curves (one example shown in Fig. 22). The two radiators' reflectance parameters (as listed in Table 6) and the reflectance parameters of the remaining box-wing surfaces shown in Table 11 were used to produce the reflectance models. Each of the parameters shown in Table 11 (including each surface's incident flux values, I_{i}) was chosen through trial and error, such that the resulting simulated light curve would be similar to the observed light curve of September 12, 2012.

Table 10 Estimated Echostar-2 spin axis orientations - 2012 to 2015

Dates	$\alpha_{\mathrm{spin(p)}}, \delta_{\mathrm{spin(p)}}$ (°)	$\alpha_{\mathrm{spin(r)}}, \delta_{\mathrm{spin(r)}}$ (°)
September 9 to October 10, 2012	$288 \pm 13, +77.4 \pm 2.7$	$108 \pm 13, -77.4 \pm 2.7$
March 5 to 16, 2013	$61.4 \pm 5.4, +81.5 \pm 4.3$	$241.4 \pm 5.4, -81.5 \pm 4.3$
August 19 to September 19, 2014	$224.9 \pm 7.0, +61.6 \pm 4.9$	$44.9 \pm 7.0, -61.6 \pm 4.9$
March 6 to 24, 2015	$71 \pm 11, +69 \pm 18$	$251 \pm 11, -69 \pm 18$
July 25 to October 10, 2015	$281 \pm 25, +72 \pm 13$	$101 \pm 25, -72 \pm 13$

The first block of values refers to the remaining cube sides (c2, c4, c5, and c6). The second block refers to the two solar panel surfaces (s11, s12, s21, and s22). The final block refers to the two large communications dishes (d11, d12, d21, and d22).

Table 11 Values of Echostar-2 remaining surfaces' free parameters

Parameter	Value	Same As
$I_{\mathrm{i(c2)}}$	2500 ADU	$I_{\mathrm{i(c4)}}$, $I_{\mathrm{i(c5)}}$, and $I_{\mathrm{i(c6)}}$
$\mu_{\mathrm{(c2)}}$	0.2	$\mu_{\mathrm{(c4)}}$, $\mu_{\mathrm{(c5)}}$, and $\mu_{\mathrm{(c6)}}$
$p_{\mathrm{d(c2)}}$	0.1	$p_{\mathrm{d(c4)}}$, $p_{\mathrm{d(c5)}}$, and $p_{\mathrm{d(c6)}}$,
$p_{\mathrm{s(c2)}}$	0.9	$p_{\mathrm{s(c4)}}$, $p_{\mathrm{s(c5)}}$, and $p_{\mathrm{s(c6)}}$
$I_{\mathrm{i(s11)}}$	$3\mathrm{x}10^7$ ADU	$I_{\mathrm{i(s21)}}$
$I_{\mathrm{i(s12)}}$	$1\mathrm{x}10^5$ ADU	$I_{\mathrm{i(s22)}}$
$\mu_{\mathrm{(s12)}}$	0.05	$\mu_{\mathrm{(s22)}}$
$\mu_{\mathrm{(s11)}}$	0.15	$\mu_{\mathrm{(s21)}}$
$p_{\mathrm{d(s11)}}$	0	$p_{\mathrm{d(s21)}}$
$p_{\mathrm{s(s11)}}$	1	$p_{\mathrm{s(s21)}}$
$p_{\mathrm{d(s12)}}$	0.2	$p_{\mathrm{d(s22)}}$
$p_{\mathrm{s(s12)}}$	0.9	$p_{\mathrm{s(s22)}}$
$I_{\mathrm{i(d11)}}$	3000 ADU	$I_{\mathrm{i(d12)}}$, $I_{\mathrm{i(d21)}}$, and $I_{\mathrm{i(d22)}}$
$\mu_{\mathrm{(d11)}}$	0.5	$\mu_{\mathrm{(d21)}}$
$\mu_{\mathrm{(d12)}}$	0.3	$\mu_{\mathrm{(d22)}}$
$p_{\mathrm{d(d11)}}$	0.1	$p_{\mathrm{d(d21)}}$, $p_{\mathrm{d(d12)}}$, and $p_{\mathrm{d(d22)}}$
$p_{\mathrm{s(d11)}}$	0.9	$p_{\mathrm{s(d21)}}$, $p_{\mathrm{s(d12)}}$, and $p_{\mathrm{s(d22)}}$

A least squares method, described in Appendix E, was used to determine the best fit between the simulated light curves and the observed folded light curves. This least squares method was used to minimize the sum of the residuals (ϵ_{m}) between the simulated broadband magnitudes (m_{sim}) and the observed broadband magnitudes (m_{obs}) for all points along the synodic spin period (ranging from 0 to 100%), with a 0.1% increment. The phases of the simulated light curves were varied over the observed folded light curves from 0.1% to 99.9% and the simulated light curve of best fit was

presented.

Figure 33 shows the simulated light curves (dotted line) and the observed folded light curves (small circles) for September 9 (a), 12 (b), 14 (c), and October 10 (d) of 2012, as well as March 6 (e) and 17 (f) of 2013. As was also reported in [16], Echostar-2's light curve features for these dates appear to be very similar to one another, with the minor exception of the fainter specular reflections observed in March 2013. All of these simulations assumed that the satellite's body frame was coincident with the equatorial frame ($\phi_b = 0$ and $\theta_b = 0$). The September and October 2012 simulations were conducted assuming that the spin axis orientation was prograde at coordinates $\alpha_{spin} = 288^o$ and $\delta_{spin} = +77.4^o$. The March 2013 simulations were conducted assuming that the spin axis orientation was prograde at coordinates $\alpha_{spin} = 61.4^o$ and $\delta_{spin} = 81.5^o$. Simulations of the remaining 2013, 2014, and 2015 observations yielded similar results.

Figures 34 (a), (b), and (c) show simulated light curves corresponding to September 12, 2012 in which the spin axis orientation coordinates did not coincide with the curve shown in Fig. 27 (a). Figures 34 (a), (b), and (c) also assumed that the satellite's body frame coincided with the equatorial frame ($\phi_b = 0$ and $\theta_b = 0$). In each case, the simulated light curve looked very different from what was observed, especially with respect to the two radiator specular reflections. Figure 34 (c) shows a special case in which the spin axis orientation is aligned with the PAB. In this case, the satellite's cube top (side c5 in Fig. 25) and sides s11 and s21 of the solar panel are perpetually reflecting sunlight to the observer over a spin period, hence the very bright and constant broadband magnitude shown in Fig. 34 (c).

Figures 34 (d) and (e) show two simulated light curves, which correspond to September 12, 2012, in which the spin axis orientation within the satellite's body frame is located off of the orthogonal plane shown in Fig. 51. The spin axis orientation in inertial space was assumed to be prograde at coordinates $\alpha_{spin} = 288^o$ and $\delta_{spin} = +77.4^o$. Figure 34 (f) shows a specific spin axis orientation within the satellite's body frame and the inertial frame, which results in a single bright specular reflection off of one of the radiators but not the other, as the satellite spins. Figure 34 (f) therefore shows the largest offset between the two radiators' specular reflections.

Figure 34 (d) shows that if the spin axis orientation's equatorial coordinates are orthogonal to the PAB and the spin axis orientation's body frame coordinates are not quite orthogonal to the radiators' surface normals, then the resultant light curve would contain two specular reflections with different amplitudes. Figure 34 (e) shows that if the satellite's body frame coordinates are rotated 90° to the spin axis orientation (along the orthogonal plane shown in Fig. 51), then the two specular reflections from the radiators will remain. However, the solar panels will also be reflecting sunlight to the observer when the two radiators' surface unit vectors are orthogonal to the PAB. Finally, Fig. 34 (f) shows that if the spin axis orientation is not orthogonal to the two radiators' surface unit vectors and is also not orthogonal to the PAB's equatorial coordinates, then observing two bright and equal brightness specular reflections from both radiators during a single spin period is not possible. Figures 33 and 34 illustrate that the estimated spin axis orientations are geometrically correct such that the light curves that have been observed in September-October 2012 and March 2013 can be correctly simulated.
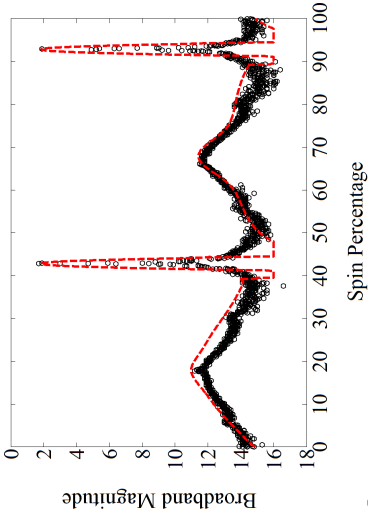
a) September 9, 2012
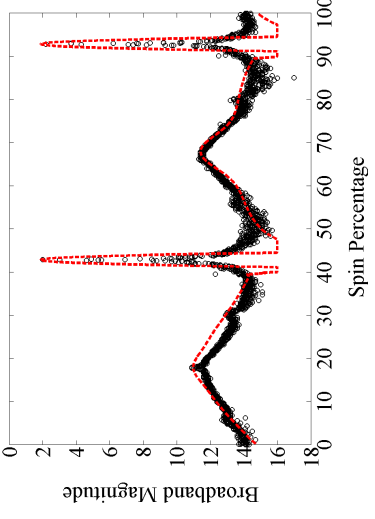
b) September 12, 2012
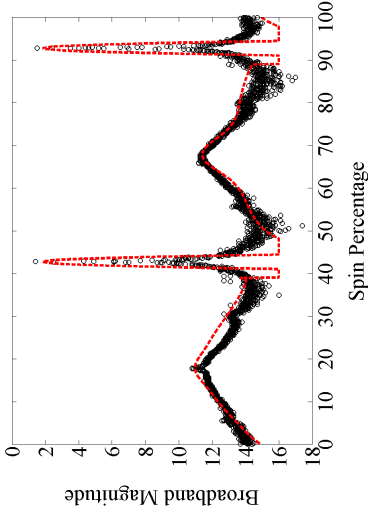
c) September 14, 2012
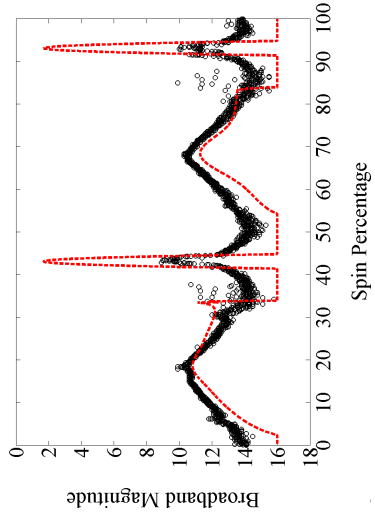
d) October 10, 2012

e) March 6, 2013

f) March 17, 2013
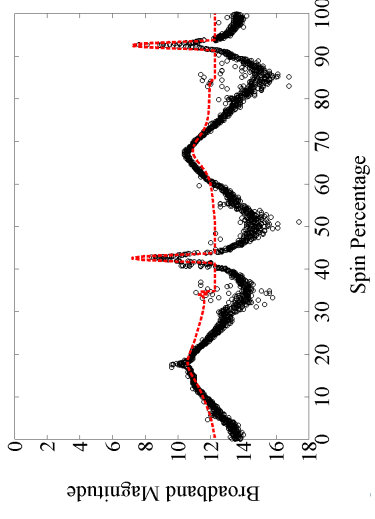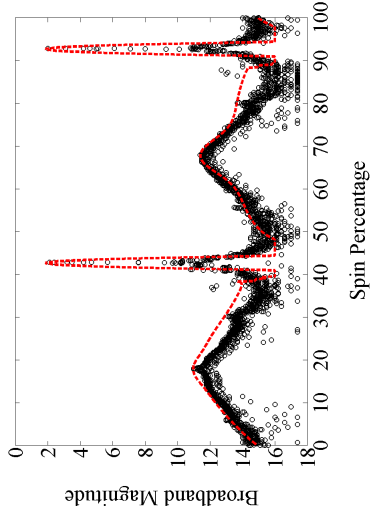
Figure 33 Echostar-2 light curve simulations: September and October 2012, and March 2013

c) $\phi_b = 0°$, $\theta_b = 0°$, $\alpha_{spin} = 158.4°$, $\delta_{spin} = 7.5°$

b) $\phi_b = 0°$, $\theta_b = 0°$, $\alpha_{spin} = 180°$, $\delta_{spin} = 30°$

a) $\phi_b = 0°$, $\theta_b = 0°$, $\alpha_{spin} = 45°$, $\delta_{spin} = 61°$
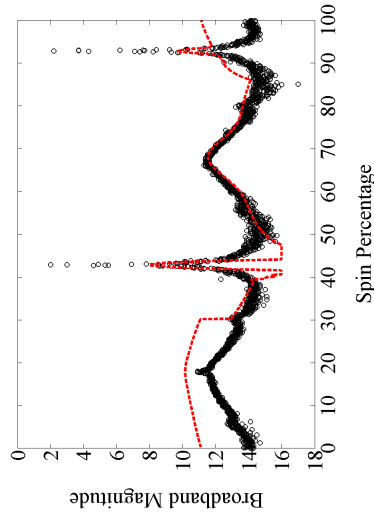
f) $\phi_b = 54°$, $\theta_b = 45°$, $\alpha_{spin} = 0°$, $\delta_{spin} = 45°$

e) $\phi_b = 0°$, $\theta_b = 90°$, $\alpha_{spin} = 288°$, $\delta_{spin} = 77°$

d) $\phi_b = 25°$, $\theta_b = 10°$, $\alpha_{spin} = 288°$, $\delta_{spin} = 77°$
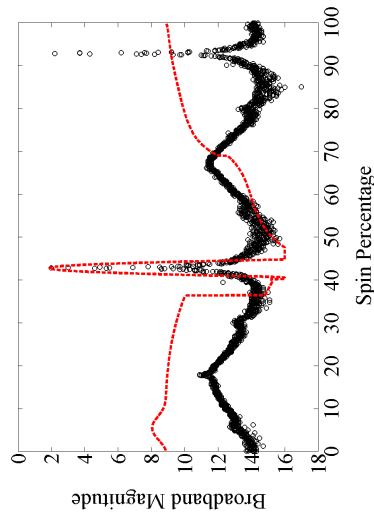
Figure 34 Light curve simulations (September 12, 2012)

71

The synodic spin period variations of Echostar-2 that were reported by Earl and Wade in [16] were likely caused by SRP acting on the satellite's large solar panels. If the spin axis orientation varies, as is reported in this paper, then so will the external SRP torque acting on the system. If the spin axis orientation varies at a rate comparable to the Earth's orbit motion, then synodic effects could cause the apparent angular acceleration magnitude to increase or decrease, depending on the spin axis' motion. The conclusions reached in this paper suggest that Echostar-2's spin axis is precessing, thereby causing a spin axis orientation variation over time that can affect the satellite's apparent spin angular acceleration. Using the estimated spin axis orientations and their suggested motions, angular acceleration models based on SRP torques can be developed for Echostar-2, which could further verify the findings of this paper and determine the satellite's true (sidereal) spin periods between 2012 and 2015.

I   Conclusions

This research has successfully estimated the spin axis orientation of the Echostar-2 inactive box-wing GEO satellite through analytical and simulation models. These estimations were verified by comparing simulated light curves with broadband, long term, and high temporal resolution observations conducted from 2012 to 2015. One of the satellite's brightest observed specular reflections, which occurred on September 12, 2012, was used to determine the most likely spin axis plane, thus reducing the degrees of freedom. Bright specular reflections observed on a number of other days in September 2012 and again on October 10, 2012 were used to determine the most likely spin axis orientations by analyzing intersections of the resulting spin axis curves.

This research has found that Echostar-2's most likely steady-state body frame spin axis orientation would correspond to a flat spin about the satellite's largest MOI, inertially oriented perpendicular to Earth's equatorial plane, assuming negligible external torques acting on the system. Echostar-2's maximum MOI corresponds to that principal axis running through the geometric center of the box structure that ideally is parallel to the surface normals of both its solar panels.

Echostar-2's spin axis orientation was estimated to have been located at 288 ± 13, +77.4 ± 2.7 (prograde spin) or 108 ± 13, -77.4 ± 2.7 (retrograde spin) between September 9 and October 10, 2012. Its spin axis orientation was estimated to have been located at 61.4 ± 5.4, +81.5 ± 4.3 (prograde spin) or 241.4 ± 5.4, -81.5 ± 4.3 (retrograde spin) in March 2013. Similar estimations were performed for August-September 2014, March 2015, and July-October 2015. Echostar-2's spin axis orientation appears to be moving over time, thus strongly suggesting spin axis precession.

For the first time, the spin axis orientation of an inactive box-wing GEO satellite was estimated with ground-based, small-aperture, broadband observations. The spin axis orientation determination method presented here can potentially be used to conduct additional attitude surveys of the inactive GEO satellite population in advance of OOS missions. This research can also enhance space object characterization efforts within the GEO satellite population, thereby creating a more robust SSA capability. This research and its conclusions was strongly supported by long term and dedicated ground-based broadband optical observations of 11 inactive box-wing GEO satellites that were conducted from March 2012 to January 2016.

CHAPTER 5:   SPIN PERIOD VARIATION SIMULATION

The previous paper (Chapter 4) discussed the estimations of the spin axis orientation of the Echostar-2 box-wing GEO satellite. These estimations were based on photometric observations obtained from March 2012 to November 2015 (described in Chapter 3). These estimations did not directly explain Echostar-2's spin angular velocity characteristics or its spin period variation characteristics over the observations' time span. Explanations of these characteristics required a SRP model that considered the satellite's largest area surfaces, which suggested the large-area solar panels.

This Chapter of the thesis investigated; the differences between the synodic and sidereal spin periods using the estimated spin axis orientations; and simulations of the net SRP torque, spin angular acceleration, and spin period variations based on SRP models that considered all contributions from all sides of Echostar-2's solar panels over each (varying) spin period.

The SRP torque model was based on assumptions of the reflectivity, orientation, and relative orientation (canting angle) of Echostar-2's two solar panels. Additional assumptions included; the dimensions and masses of each of the satellite's critical components; and the satellite's three MOIs. These assumptions had to be made because the manufacturers of all 11 satellites that were originally observed did not divulge to the author any information concerning these satellites.

This research represents the first time that an inactive box-wing GEO satellite's spin angular acceleration and spin period variation has been simulated using a SRP torque model that used previously estimated spin axis orientations. These simulations would not have been possible without the long term photometric observations obtained that were used to estimate Echostar-2's spin axis orientations.

Simulations of the Sidereal Spin Period Variation of the Echostar-2 Geosynchronous Satellite

Michael A. Earl[¶] and Gregg A. Wade[‖]

Royal Military College of Canada, Kingston, Ontario, Canada, K7K 7B4

This paper is being prepared for submission to the COSPAR Advances in Space Research by the winter of 2017.

A   Introduction

SINCE the launch of Sputnik, SSA has been protecting the active satellite population from threats that include collision, physical interference, and communications interference. SSA includes the determination of a satellite's; identity; nation of origin; activity; orbit characteristics; attitude; size; and/or component make-up. The ability to perform suitably high temporal frequency SSA has become more difficult because of increases in the satellite population due to significant events, such as the 2007 Fengyun-1C destruction and the 2009 Iridium-Cosmos collision. In most of the orbit realms, orbiting debris has the potential to cause significant damage to active satellites.

The probability of collision between two satellites will depend on several factors, including their respective orbit elements, their overall sizes (volume), their shapes, and their attitudes in inertial space. The difference between a "near miss" and a collision could depend on the relative attitudes of the two satellites involved, especially if one of (or both of) the satellites has a large dimension. The "box-wing" is one such satellite design, consisting of a central cube-shaped bus portion with side lengths of approximately 2.5m and two large solar panels, each about 25m^2 in area, as illustrated in [6, 16, 20, 22]. A box-wing satellite's "wing span" (largest dimension) can be as large as 30m.

The GEO population consists of satellites orbiting at approximately 35,785 km in altitude with nearly circular prograde orbits inclined at between 0º and 15º from the Earth's equatorial plane[78]. Recent observations of inactive GEO box-wing satellites have revealed rotational motion with diverse spin periods ranging from several seconds to several hours [3, 4, 5, 16], suggesting complicated attitude dynamics, in general.

Echostar-2 is an inactive[79] box-wing GEO telecommunications satellite originally designed by GE's AS[80] with an AS-7000[81] design. The satellite's power system and attitude control systems are no longer functioning, therefore it is free to move and spin with negligible constraints.

This paper first presents the estimated sidereal spin periods of the Echostar-2 box-wing GEO satellite, on the dates corresponding to the spin axis orientations estimated in [20]. Next, this paper presents simulations of Echostar-2's spin period variations, based on the spin axis orientations

---

[¶]PhD Candidate, Department of Physics, Royal Military College of Canada, P.O. Box 17000 Station Forces Kingston, Ontario, Canada, K7K 7B4.

[‖]Professor and Department Head, Department of Physics, Royal Military College of Canada, P.O. Box 17000 Station Forces Kingston, Ontario, Canada, K7K 7B4.

[78]JFCC SPACE/J3, Space Track, https://www.space-track.org, Accessed 03/25/16.

[79]Echostar-2 has been inactive since June 2008.

[80]Acquired by Martin Marietta in 1993 which subsequently became Lockheed Martin in 1995.

[81]Also known as LM-7000.

estimated in [20]. Finally, the individual and relative solar panel orientations that resulted in the best least squares fit of the observed angular acceleration curves and spin period variation curves are discussed.

B   Background

1   Box-wing Light Curves

Papushev, et al. (2009) conducted a long term survey of inactive Raduga, Ekran and Gorizont GEO satellites [3]. They reported that their resulting light curves were diverse and had inferred (synodic) periods that varied over time. They presented several reasons for the reported spin period variations, including: light pressure force (interpreted as the force originating from SRP); Lorentz force acting upon the charged satellite surfaces by the Earth's magnetic field; and micro-jet (internal) forces caused by small fissures in the hermetically sealed satellite buses [3]. They reported that these forces were on the order of between 30 and 100 mdyn (between 0.3 and 1 μN). Papushev, et al. did not present models or calculations that verified the hypothesized spin period variation causes or the force magnitude range.

A paper by Earl and Wade (2015) featured the observed angular accelerations of four inactive box-wing GEO satellites and the maximum possible angular acceleration determined from a first-order box-wing external torque model [6]. They concluded that SRP was the largest contributor to the observed angular accelerations and therefore contributed to the apparent spin period variations. They reported that Lorentz forces were too small to account for the observed angular accelerations, due to the large distance of the GEO circular orbit radius from the Earth's magnetic poles. The micro-jet hypothesis that was originally proposed by Papushev, et al., was not tested because the four box-wing satellites studied had been inactive for at least four years [6] when the study commenced.

In this paper, the term "broadband" was defined to refer to an unfiltered optical system with a detected flux spanning the entire detectable optical spectrum. Another paper by Earl and Wade (2017) featured the long term[82] and high temporal resolution[83] broadband photometric observations of 11 inactive box-wing GEO satellites to further study their light curve morphologies and their apparent spin period variations [16]. It was concluded that all 11 satellites' light curves and inferred spin period variations were diverse, when compared to each other, with few similarities [16]. Light curves of some satellites varied slowly over a timescale of weeks or months, while the light curves of other satellites varied more quickly over timescales of minutes or hours. Echostar-2's light curves appeared to be the most stable, with similar features observed over a nearly 4-year timescale. It was suggested in [16] that Echostar-2's spin axis orientation was either nearly constant or that it could have a small precession angle [16].

2   Angular Acceleration and Spin Period Variation

Earl and Wade (2015) presented evidence that suggested that a box-wing satellite's spin angular acceleration (and therefore its spin period variation), shown in Fig. 35 (a), is dependent upon; the satellite's orientation with respect to the Sun; the solar panel(s) orientation(s) with respect to the Sun; the solar panels' orientations with respect to each other (if more than one); and the solar panel reflectivity (on each of the panel sides) [6]. They presented a simple first order model to simulate the HGS-1 satellite's spin angular acceleration and its spin period variation from mid-2012 to late-2013. HGS-1 has only one deployed solar panel[84] [6] and therefore is not the typical example of a

---

[82]Early March 2012 to early January 2016.

[83]One observation of each satellite per week, weather and access permitting.

[84]HGS-1's southern solar panel could not be deployed after launch.

2-panel box-wing satellite. Echostar-2 has two fully deployed solar panels.

Earl and Wade (2015 and 2017) reported that Echostar-2's spin period variation, shown in Fig. 35 (b), appeared to be cyclical [6, 16]. However, the variations were not sinusoidal and included points of inflection where the spin period variation magnitude would appear to decrease for a number of days before resuming its previous rate of change, as illustrated in [16]. Echostar-2's spin period variation amplitude also appeared to decrease over time; from 156.2s in 2012-13 to 39.4s in 2015, as described in [16]. This decrease appeared to correlate with the overall decrease in Echostar-2's average spin period.

a) Angular acceleration curve

b) Spin period variation curve
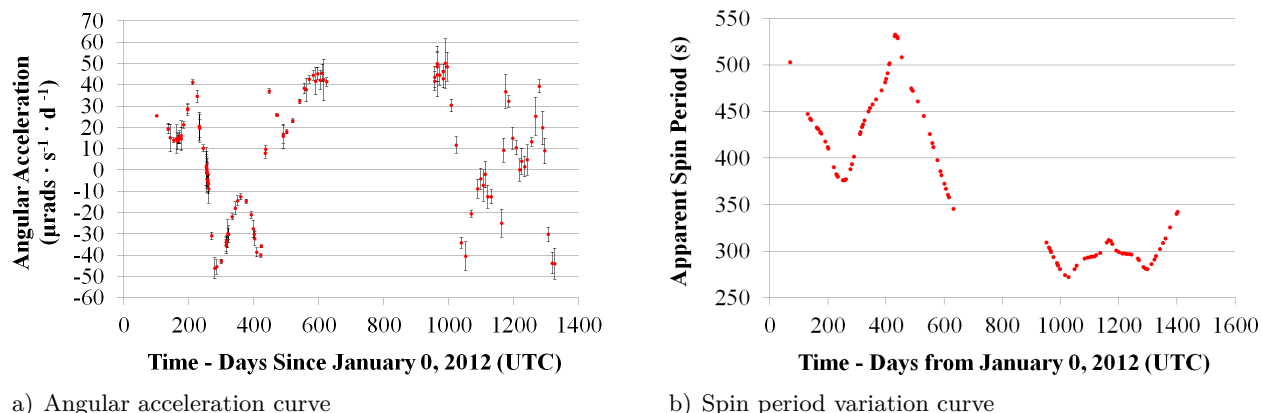
Figure 35 Echostar-2 angular acceleration and spin period variation curves

Earl and Wade (2017) reported a strong quantitative relationship between Telstar-401's light curve morphology and its spin period, suggesting a quantitative relationship between the satellite's attitude and its spin period variation [16]. This relationship suggests that SRP is varying Telstar-401's attitude, which in turn is varying the satellite's spin period over time. A similar, albeit weaker, correlation was also found for Echostar-2 [16].

3 Spin Axis Orientation

The "spin axis orientation" was defined in [20] as the inertial RA (α_{spin}) and dec (δ_{spin}) direction of a satellite's spin angular velocity vector ($\vec{\omega}$). These two angles are related to the Euler transformation angles between a satellite's spin axis reference frame and the equatorial (inertial) reference frame, as described in [20].

In Earl and Wade (2017), Echostar-2's spin axis orientation was estimated in [20] using bright specular reflections that were assumed to have originated from the satellite's two mirrored radiators [20]. It was concluded that Echostar-2's spin period orientation is precessing with a period of approximately one sidereal year. Knowledge of the spin axis orientation and its precession rate reduces the number of free parameters involved when conducting simulations of the effects of SRP on the spin period. However, the orientation of the solar panels with respect to the satellite's body frame remains a free parameter because there was no evidence of bright specular sunlight reflections from Echostar-2's solar panels [20].

4 Synodic and Sidereal Spin Periods

An extreme example of the difference between synodic and sidereal spin periods (also known as the "synodic effect") would be when a non-spinning (infinitely long sidereal spin period) GEO satellite was observed from a location on the Earth's surface. The observer would see the satellite appear to spin with a 24-hour (synodic) period because the GEO satellite is orbiting the Earth at

nearly the same angular rate as the Earth's rotation and it is moving with the Earth as it orbits the Sun[85]. Therefore, the satellite's light curve would appear to have a 24-hour period, even though the satellite is not spinning at all.

Evidence of the synodic effect for GEO satellites was presented by Lambert, et al. (2003) based on their observations of the cylindrical design SBS-B and SBS-C HS-376 [86] satellites with the AEOS facility in Maui, Hawaii [18]. They reported that SBS-B's light curve period appeared to lengthen from 50s to nearly 200s over a timescale of 2.5 hours. They also reported that SBS-C's light curve period appeared to suddenly increase from 30s to 60s [18]. They suggested that the cause of the spin period lengthening in each case was the satellite's spin axis nearly aligning with its PAB [18].

Hall, et al. (2006) obtained I-band light curves of NASA's IMAGE polar-orbiting satellite with the AEOS facility soon after the satellite permanently ceased transmitting telemetry [19]. Hall, et al. reported varying synodic spin periods of between 121.6s and 126.5s (rates of between 0.49342 and 0.47431 min^{-1}) over a timescale of approximately 45 minutes. These estimations were compared with the sidereal spin rate contained within the final IMAGE telemetry received by NASA; 0.47594$\pm$0.00012 min^{-1}, corresponding to a spin period of 126.066$\pm$0.032s [19].

A satellite's synodic spin period can be varied by relative motions of the satellite, the observer, and the Sun. This includes the satellite's spin axis orientation with respect to the PAB [19]. For example, if a spinning satellite is moving quickly with respect to an observer, that observer will measure a synodic spin period that might significantly deviate from its sidereal spin period [19]. In the case of most GEO satellites (observed by Cognion, Binz, Earl and Wade, and Lambert, et al.), the relative motion between the satellite and observer is very small and therefore could be negligible when compared to the relative motion between the observer and a lower-altitude satellite.

C Echostar-2 Satellite Body Frame Unit Vector Conventions

The body frame unit vector conventions for Echostar-2's two solar panels are shown in Fig. 36. The normal unit vector of each solar panel side was labeled $\hat{n}_{ps}$, where "p" is the panel number (1 or 2) and "s" is the side number (1 or 2). For example, the unit vector $\hat{n}_{11}$ refers to the first side of the first panel, $\hat{n}_{22}$ refers to the second side of the second panel, and so on. The choice of which solar panel is labeled "1" and which is labeled "2" is arbitrary, provided that the convention is not varied mid-analysis. The choice of side "1" and side "2" is also arbitrary and subject to the same restriction. The solar panels' external force subscripts "$\vec{F}_{ps}$" follow the same convention as the solar panel unit vectors. The term l_{tot} refers to Echostar-2's wing span, as quantified in [20]. The terms l_p and w_p refer to the length and width, respectively, of either of Echostar-2's solar panels, as indicated in [20]. The unit vectors $\hat{r}_p$ refer to the radial unit vectors directed along solar panel "p" (1 or 2) from the geometric center of Echostar-2's box portion, as shown in Fig. 36.

D Synodic to Sidereal Spin Period Transformation

A box-wing GEO satellite's synodic spin period (T_{syn}) can be inferred from ground-based observations of periodic sunlight reflections from one or more of the satellite's surfaces [6, 16]. The inferred synodic spin period will likely not be identical to the sidereal (real) spin period (T_{sid}). The temporal difference between a synodic and sidereal spin period will depend on factors that include; the sidereal period; the satellite orbit period; the satellite spin axis' orientation with respect to the orbit plane; and the satellite spin axis' orientation with respect to the PAB.

---

[85]Earl, M., Observation and Analysis of the Spin Period Variations of Inactive Box-wing Telecommunications Satellites in Geosynchronous Orbit, MSc thesis, RMCC, May 2013, http://www.castor2.ca/08_Papers/earl_thesis.pdf, Accessed 10/11/16.

[86]Hughes 376, later Boeing 376.
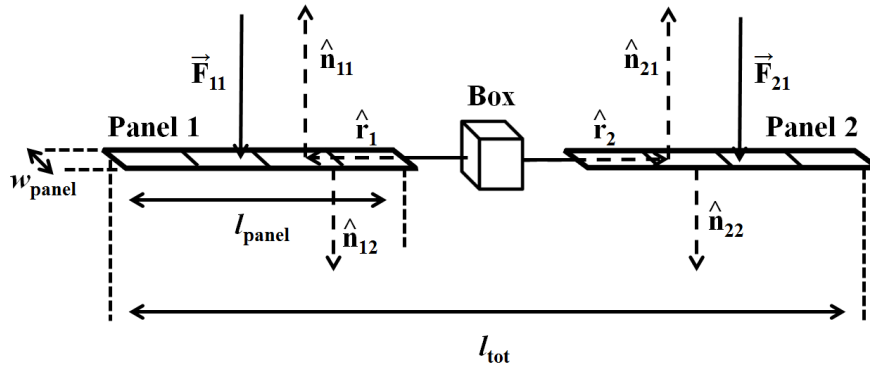
Figure 36 Echostar-2 dimension and unit vector conventions

Synodic to sidereal transformations were investigated by considering two specific but very different scenarios. The first (ideal) scenario considered a geostationary satellite, consisting of a single reflective surface, with a spin axis orientation that was always orthogonal to the orbit plane and to the PAB, as shown in Fig. 37. The second (general) scenario considered the general case of a GEO satellite (having a nearly zero orbit eccentricity and an orbit inclination of less than 15º) with an arbitrary spin axis orientation, an example of which is shown in Fig. 39. The general scenario was used to simulate the apparent spin periods of Echostar-2, based on the estimated spin axis orientations shown in [20]. Results from the ideal scenario were presented to verify the order of magnitude of the synodic-sidereal differences determined by the general scenario.

1   Ideal Scenario

Figure 37 illustrates the ideal scenario. The orientation of the geostationary orbit in equatorial inertial space is shown at the top right corner (α and δ) of Fig. 37. The ideal scenario also considers the sunlight vector as lying within the equatorial plane and therefore coincides with either the Vernal or Autumnal Equinox, as seen from the Earth.

Figure 37 shows two instances of the geostationary satellite, depicted as the thin rectangles. An observer on the Earth's equator is depicted by points P_1 and P_2, both at the same geodetic location but at two different times during the Earth's rotation. The observer detects a bright sunlight reflection at time t_1 because the reflective surface's normal unit vector ($\hat{n}$) coincides with the satellite's PAB. The PA at time t_1 is shown as ρ_1 in Fig. 37. The reflective surface is rotating with some sidereal spin period about the spin axis (depicted as the dot on the rectangle at S_1). As the circular arrow at S_1 shows, the direction of the spin is prograde.

After one sidereal spin period (time $t_1 + T_{sid}$), the reflecting surface will have the same orientation in inertial space as it had at time t_1, as the gray hashed rectangle in Fig. 37 shows. The observer at point P_2 will not see a bright reflection at time $t_1 + T_{sid}$ because the orbit motion has changed the surface's orientation with respect to the Earth. Once the surface spins the additional angle ϵ (shown in Fig. 37), the observer would once again detect a bright reflection. This additional rotation would require an additional time (ΔT), which is the temporal difference between the sidereal and synodic spin periods.

The angles β_1 and β_2 in Fig. 37 refer to the PA half angles, which are the dot products of the solar unit vector and the PAB unit vector at times t_1 and $t_1 + T_{syn}$, respectively. The angle ϵ is equal to the difference between the two β angles, as shown in Eq. (14). The angle ϵ can also be expressed as a function of the difference of the two PA (ρ) angles, as shown in Eq. (14). The variation of the satellite's true anomaly (ν) during orbit is the primary contributor to the PA variation because the solar parallax is negligible at 1 Astronomical Unit (AU). The ϵ angle can

therefore be expressed as a fraction of the satellite's geostationary orbit period. Equation (15) shows that this fraction is based on the satellite's synodic spin period and its sidereal orbit period.
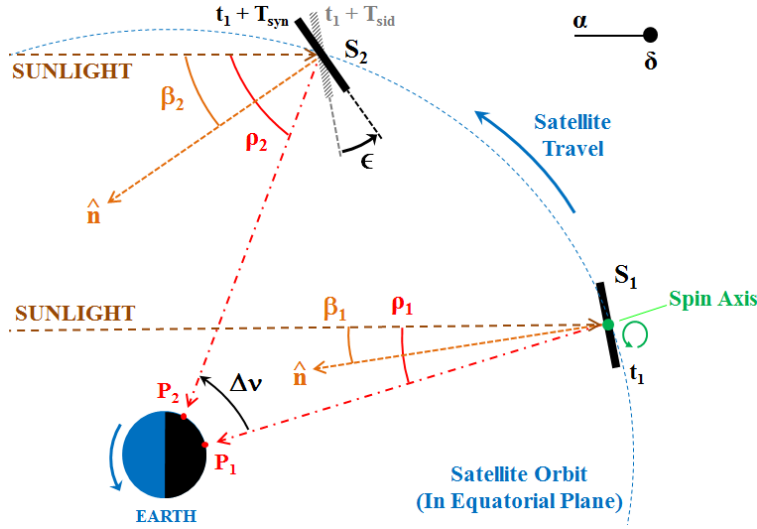
Figure 37 Ideal scenario

$$\epsilon = \beta_2 - \beta_1 = \frac{\rho_2 - \rho_1}{2} \tag{14}$$

$$\epsilon = \frac{\Delta\nu}{2} = \pi \left(\frac{T_{\text{syn}}}{T_{\text{orb}}} \right) \tag{15}$$

The satellite's sidereal spin period is a function of its synodic spin period and the temporal difference (ΔT) between the sidereal and synodic spin periods, as shown in Eq. (16). The time ΔT can also be expressed as a function of the ϵ angle and the satellite's sidereal spin period, as shown in Eq. (17). Substituting Eq. (15) for the ϵ angle in Eq. (17), Eq. (18) results.

$$T_{\text{sid}} = T_{\text{syn}} - \Delta T \tag{16}$$

$$\Delta T = \frac{\epsilon}{2\pi} T_{\text{sid}} \tag{17}$$

$$\Delta T = \frac{T_{\text{sid}} T_{\text{syn}}}{2 T_{\text{orb}}} \tag{18}$$

Substituting Eq. (18) for ΔT in Eq. (16) results in Eq. (19), the synodic to sidereal spin period transformation equation for the ideal scenario. The '$\pm$' sign in Eq. (19) refers to the direction of the satellite spin. The '+' is used for a prograde spin and the '-' is used for a retrograde spin. A geostationary satellite's sidereal orbit period (T_{orb}) is 86,164.1s (one sidereal day).

$$T_{\text{sid}} = \left[\frac{1}{T_{\text{syn}}} \pm \frac{1}{2 T_{\text{orb}}} \right]^{-1} \tag{19}$$

Figure 38 (a) shows the resulting ΔT values for a geostationary satellite with a synodic spin period between 0 and 4500s (a). Figure 38 (b) shows the ΔT values for Echostar-2's range of synodic spin periods (between 250s and 550s), as stated in [16]. The solid line depicts prograde spin and the dashed line depicts retrograde spin. Figure 38 (b) suggests that Echostar-2's synodic-sidereal spin period difference would be between 0.36s and 1.75s (for either a prograde or a retrograde spin), assuming that Echostar-2's spin axis orientation had the same ideal scenario characteristics.

79

a) T_{syn} between 0 and 4500s

b) Echostar-2 T_{syn} values: between 250s and 550s
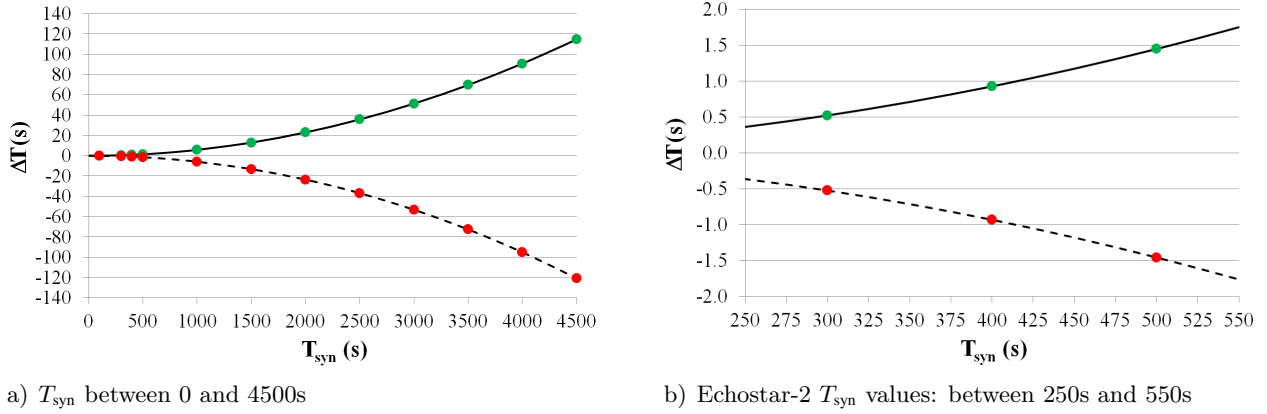
Figure 38 ΔT versus T_{syn} for ideal scenario

Simulations of the synodic effect for the ideal scenario were also conducted with MATLAB software that simulated a geostationary satellite comprised of a spinning plane with an adjustable sidereal spin period. The dots that overlay the lines in Fig. 38 show the resulting ΔT values, for both prograde and retrograde spin directions, based on specifically selected sidereal spin periods.

2   General Scenario

Echostar-2's orbit and attitude characteristics would not fit the stringent conditions of the ideal scenario shown in Fig. 37 because its orbit inclination is greater than 0. The Sun is on one of the Equinoxes only twice per year (specifically, around March 21 and September 21). The ground-based observer will also be at a different latitude than the equator. Finally, Echostar-2's spin axis orientation was determined in [20] to not be orthogonal to its orbit plane or to the Earth's equatorial plane. Figure 39 illustrates an example of the general scenario. Determining an analytical relationship between the synodic spin period and the sidereal spin period becomes more difficult in the general scenario because of the larger number of variables involved. However, simulations of Echostar-2's synodic spin period, based on the aforementioned free parameters of the satellite, were performed with a modified version of the MATLAB software originally used to verify the ideal scenario's analytical synodic-sidereal equation (Eq. (19) and Fig. 38).
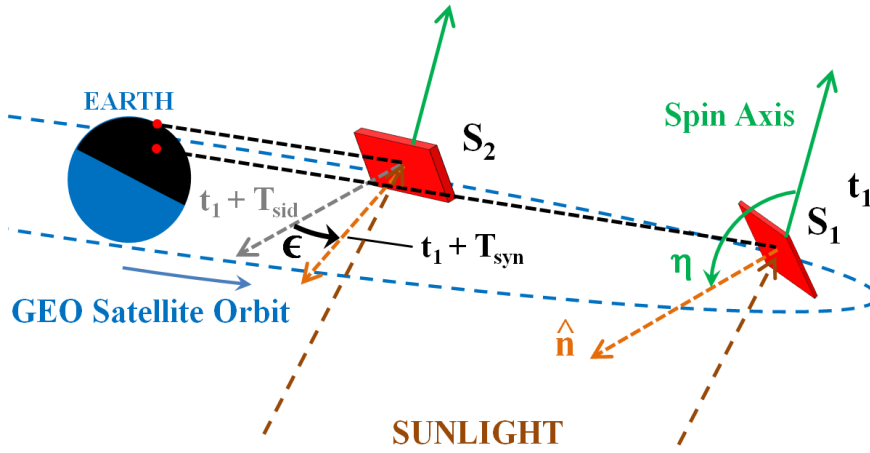
Figure 39   General scenario

Echostar-2's spin axis orientation was estimated in [20] from light curves containing two bright

(broadband magnitude at or near 2) specular reflections per inferred spin period. These specular reflections were assumed to be caused by the satellite's two highly reflective mirrored radiators and not its two solar panels [20]. Fig. 40 shows Echostar-2's spin axis orientations from 2012 to 2015 [20]. For each of these estimated spin axis orientations, the mirrored radiators' surface normals were assumed to be nearly orthogonal to the spin axis orientations because the specular reflections were observed to have nearly identical maximum broadband magnitudes [20]. The axes shown in Fig. 40 are the spin J2000.0 epoch equatorial (inertial) RA (α_{spin}) and dec (δ_{spin}) coordinates with respect to the Earth's equatorial plane and the First Point of Aries.
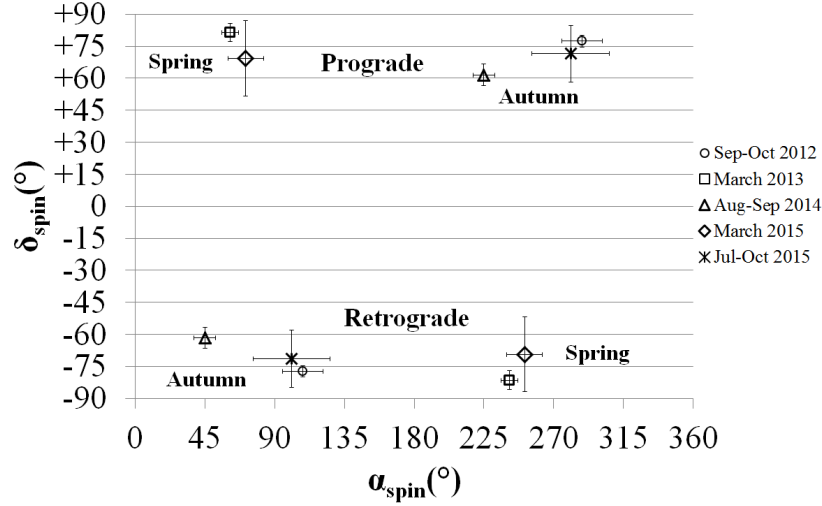
Figure 40   Estimated Echostar-2 spin axis orientations: 2012 to 2015

3   Echostar-2 Synodic-Sidereal Difference

The varying spin axis orientation shown in Fig. 40 suggests that Echostar-2's spin axis orientation was precessing with a period of approximately one sidereal year. Spin axis precession implies that the sidereal-synodic temporal difference (ΔT) will vary with time due to factors including; the spin axis orientation variation; the synodic (observed) spin period variation; the satellite's slowly increasing orbit inclination; and the Sun's varying apparent equatorial coordinates.

Equation (16) can be rearranged to determine ΔT from the sidereal and synodic spin periods, as shown in Eq. (20). The MATLAB simulation software was used to estimate the synodic spin period from inputs that included; the sidereal spin period; the Sun's ecliptic longitude; Echostar-2's location with respect to the ground-based observer (determined with propagated orbit elements); and Echostar-2's estimated spin axis orientation with respect to the equatorial coordinate system. In each simulation, the sidereal spin period that could result in the observed synodic spin period on the corresponding date and time was determined, for both prograde and retrograde spin directions.

$$\Delta T = T_{\text{syn}} - T_{\text{sid}} \tag{20}$$

Table 12 shows the observed synodic spin periods, the determined sidereal spin periods, both prograde (T_{p}) and retrograde (T_{r}), and the resultant ΔT values for both spin directions, for September 9 to October 10, 2012. Note that the ΔT values for the prograde direction (ΔT_{p}) are not identical to those for the retrograde direction (ΔT_{r}). Figure 38 shows that ΔT_{p} and ΔT_{r} are not identical, even in the ideal scenario, especially for the longer synodic spin periods.

Table 12 Observed synodic and estimated sidereal spin periods: September-October 2012

Date (mm/dd/yy)	T_{syn} (s)	T_{p} (s)	T_{r} (s)	ΔT_{p} (s)	ΔT_{r} (s)
09/09/12	376.0	375.2007	376.8030	0.7993	-0.8030
09/10/12	375.8	375.0019	376.6020	0.7981	-0.8020
09/11/12	375.8	374.9940	376.6095	0.8060	-0.8095
09/12/12	375.9	375.0963	376.7072	0.8037	-0.8072
09/13/12	375.8	374.9966	376.6071	0.8034	-0.8071
09/14/12	375.9	375.1185	376.6854	0.7815	-0.7854
09/16/12	376.0	375.2022	376.8015	0.7978	-0.8015
09/20/12	376.8	376.0118	377.5917	0.7882	-0.7917
10/10/12	393.2	392.3290	394.0751	0.8710	-0.8751

Figure 41 shows the synodic-sidereal time difference (ΔT) for each of the inferred synodic spin periods corresponding to the dates in [20]. Over the 2012 to 2015 observation time, the estimated spin axis orientation appeared to vary but remain within 30º from the orthogonal to the equatorial plane. This meant that none of the estimated spin axis orientations were predicted to be near the PABs, which were nearer to the equatorial plane for the entire time. This, in addition to the short synodic spin periods, means that the simulated prograde and retrograde sidereal spin periods should be similar to those predicted in the ideal geostationary case. However, in several cases, especially near the 290s synodic spin period, there are noticeable differences between the two scenarios. These differences are likely the result of the spin axis orientation and not the sidereal spin period.
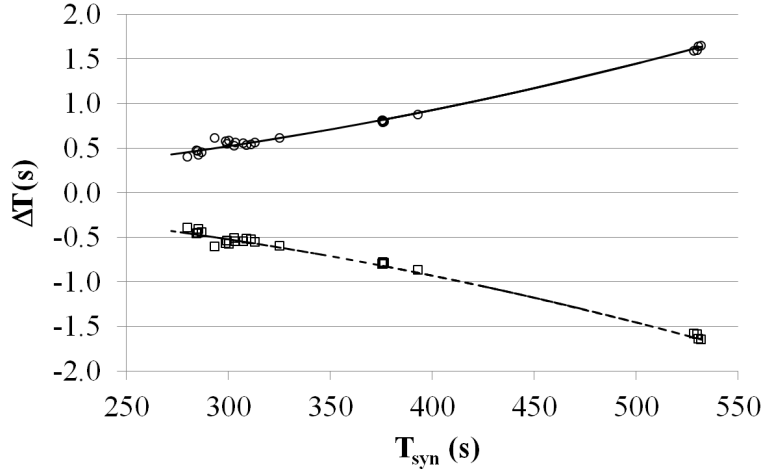
Figure 41 Echostar-2 synodic-sidereal time difference

The circles and squares in Fig. 41 refer to the simulated prograde and retrograde sidereal spin periods, respectively, based on the observed synodic spin periods. The solid and dashed lines in Fig. 41 refer to the prograde and retrograde results of the ideal scenario, respectively. Figure 41 suggests that the temporal differences between the Echostar-2 and ideal scenarios are very similar, but not identical, as had been expected.

E Solar Radiation Pressure

1 Basics

SRP (P_{SRP}) is the pressure that is exerted by solar photons. The SRP at an average distance of 1 AU is determined by the solar constant (the solar energy flux at 1 AU) (Φ_{s}) at this distance and the speed of light in a vacuum (c), as shown in Eq. (21). Kopp and Lean (2011) reported the value of Φ_{s} to be 1360.8 $\pm$ 0.5 W·m^{-2} [31]. Using this value of Φ_{s} in Eq. (21), the SRP at 1 AU is 4.539 $\pm$ 0.002 μPa.

$$P_{\text{SRP}} = \frac{\Phi_{\text{s}}}{c} \tag{21}$$

2 Force and Torque

Figure 42 illustrates sunlight illuminating one side of a solar panel, having an area A and a reflectivity q_{ps}, at an incidence angle ϕ_{ps} to the panel's normal unit vector $\hat{n}_{\text{ps}}$. The $\cos(\phi_{\text{ps}})$ term is the dot product of the sun's location unit vector (as viewed by the satellite) and the $\hat{n}_{\text{ps}}$ unit vector. The surface in Fig. 42 can be considered as being a transparent surface, a reflective surface, an absorptive surface, or a combination of all three. Generally, a satellite solar array is designed to absorb sunlight, while the "box" portion is designed to reflect sunlight to prevent overheating [35]. The instantaneous force vector that is caused by absorbed SRP on a single solar panel of area A ($\vec{F}_{\text{ps}}$) is determined with Eq. (22) [35]. Figure 42 shows that the SRP force direction is negative with respect to the surface's $\hat{n}_{\text{ps}}$ unit vector direction. This is the reason for the negative sign in Eq. (22).

As seen from the Earth, the Sun appears to be an extended light source having an angular diameter of approximately 0.5º. This means that in reality the solar panels do not see light from a point source but a summation of point sources. In this paper, we assume that the Sun is a point source for the purposes of a first-order dynamics model.
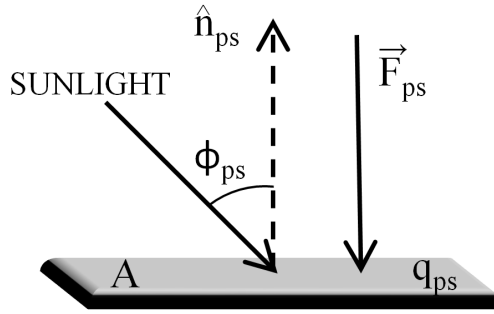
Figure 42 Force due to SRP

$$\vec{F}_{\text{ps}} = \left[(P_{\text{SRP}}A)(1 + q_{\text{ps}}) \cos(\phi_{\text{ps}}) \right] (-\hat{n}_{\text{ps}}) \tag{22}$$

The instantaneous external torque ($\vec{\tau}_{\text{ps}}$), which is caused by the instantaneous SRP force acting on the solar panel ($\vec{F}_{\text{ps}}$), is determined with Eq. (23) [35]. This external torque will change the satellite's angular momentum vector ($\vec{L}$) (as described in Appendix F), which includes its angular velocity ($\vec{\omega}$) and therefore its sidereal spin period (T_{sid}).

It was assumed that P_{SRP}, l_{tot}, l_{p}, and w_{p} were all constants. Consequently, the panel area (the product of l_{p} and w_{p}) was also assumed to be of a constant value. These constants were amalgamated to define the constant torque scalar τ_{c}, as shown in Eq. (24). Equation (23) was then represented using τ_{c} as shown in Eq. (25). Echostar-2's value of τ_{c}, estimated from P_{SRP} and the

dimensions of the Echostar-2 solar panels (shown in [6]), was 923 ± 50 μN·m.

$$\vec{\tau}_{\text{ps}} = \left[0.5(P_{\text{SRP}}A)(l_{\text{tot}} - l_{\text{p}}) \right] (1 + q_{\text{ps}}) \cos(\phi_{\text{ps}}) \left[\hat{r}_{\text{p}} \times (-\hat{n}_{\text{ps}}) \right] \tag{23}$$

$$\tau_{\text{c}} \equiv 0.5(P_{\text{SRP}}A)(l_{\text{tot}} - l_{\text{p}}) \tag{24}$$

$$\vec{\tau}_{\text{ps}} = \tau_{\text{c}}(1 + q_{\text{ps}}) \cos(\phi_{\text{ps}}) \left[\hat{r}_{\text{p}} \times (-\hat{n}_{\text{ps}}) \right] \tag{25}$$

3 Instantaneous Net SRP Torque

Sunlight may illuminate both solar panels at the same time. The instantaneous SRP contributions of all sunlit solar panel sides will result in an instantaneous net SRP torque ($\vec{\tau}_{\text{net}}$). It was assumed that both of Echostar-2's solar panels were rigid and perfect planes; therefore, only two of the four panel sides can be sunlit at any one time. A negative $\cos(\phi_{\text{ps}})$ value corresponds to a solar panel side in shadow (not sunlit). A shadowed panel side's SRP torque was considered to be negligible relative to an SRP torque due to a sunlit panel side. As the satellite spins, the originally shadowed solar panel side will eventually become sunlit. In this case, the $\cos(\phi_{\text{ps}})$ term corresponding to that panel side would become positive and consequently its instantaneous SRP torque contribution would no longer be negligible.

The normal unit vector corresponding to side 2 of a specific solar panel ($\hat{n}_{12}$ or $\hat{n}_{22}$) was assumed to be in the opposite direction to the corresponding panel's first side unit vector ($\hat{n}_{11}$ or $\hat{n}_{21}$, respectively), as shown in Eq. (26). Consequently, $\cos(\phi_{\text{p2}})$ was assumed to be the negative of $\cos(\phi_{\text{p1}})$, as shown in Eq. (26). Echostar-2's solar panel axes might be slightly misaligned with respect to one another. Therefore, the $\hat{r}_1$ and $\hat{r}_2$ unit vectors were not assumed to be negatives of one other, despite what Fig. 36 suggests.

$$\hat{n}_{\text{p2}} = -\hat{n}_{\text{p1}} \quad \text{and} \quad \cos(\phi_{\text{p2}}) = -\cos(\phi_{\text{p1}}) \tag{26}$$

Assuming the identities shown in Eq. (26), the instantaneous net SRP torque ($\vec{\tau}_{\text{net}}$) is expressed as shown in Eq. (27). The $\delta_{1,\text{s}}$ and $\delta_{2,\text{s}}$ terms are Kronecker Deltas comparing the solar panel side ('s') with the number '1' and the number '2', respectively. The only possible values of $(-1)^{\delta_{1,\text{s}}}$ and $(-1)^{\delta_{2,\text{s}}}$ are 1 or -1. Any value that is negative within the angle brackets is to be considered zero. This makes sure that none of the non-sunlit solar panel sides can be considered as contributors to the instantaneous net SRP torque.

$$\vec{\tau}_{\text{net}} = \tau_{\text{c}} \left\{ \sum_{\text{p}=1}^{2} \sum_{\text{s}=1}^{2} \left\{ (1 + q_{\text{ps}}) \left\langle (-1)^{\delta_{2,\text{s}}} \cos(\phi_{\text{p1}}) \right\rangle (-1)^{\delta_{1,\text{s}}} \left[\hat{r}_{\text{p}} \times \hat{n}_{\text{p1}} \right] \right\} \right\} \tag{27}$$

It was assumed that the unit vectors $\hat{r}_{\text{p}}$ and $\hat{n}_{\text{p1}}$ (both corresponding to the same panel) are always perpendicular to each other. As a result of this assumption, the cross product of the two unit vectors were assumed to be always perpendicular to each of the original two unit vectors. However, $\hat{r}_1$ might not necessarily lie in the same line as $\hat{r}_2$ and $\hat{n}_{11}$ might not be in the same direction as $\hat{n}_{21}$. Therefore, the two cross products (each corresponding to one solar panel) might not necessarily be equal and opposite to one other, thereby allowing a non-zero net instantaneous net torque to affect Echostar-2's spin angular momentum. This net torque could be the primary reason that Echostar-2's spin period has been observed to vary over time, as was originally suggested in [3] and as was discussed more thoroughly in both [6] and this paper.

The instantaneous net SRP torque, shown in Eq. (27), would act to vary the spin angular velocity's magnitude and direction. Earl and Wade (2017) reported that Echostar-2's light curves were not observed to vary significantly over nearly four years [16]. It was concluded that the lack of light curve variation could be due to a stable spin axis whose direction was not varying

significantly [16]. However, it was concluded in [20] that Echostar-2's spin axis was in motion between the months of September and March in each year of 2012 to 2015, suggesting a precession of the satellite's spin axis orientation.

It was reported in Earl and Wade (2017) that no significant evidence of sunlight reflections from Echostar-2's solar panels was observed. This suggested that the satellite was at or near a flat spin state, as described in [20]. In a flat spin state, the satellite is rotating about the principal rotation axis that corresponds to its largest MOI. Echostar-2's three MOIs, coinciding with its three principal rotation axes, were estimated in [6]. The largest MOI (I_{zz}) coincided with the satellite's z_b body frame axis, with the I_{yy} MOI possibly possessing a similar value to I_{zz}. However, comparing the equations that determined both I_{yy} and I_{zz} confirm that I_{zz} must be at least slightly larger than I_{yy} [6].

F   Torque Components

Equation (27) suggests that if Echostar-2's solar panels had identical dimensions, identical reflectivity (both panel sides 1 and 2) and an identical orientation with respect to one other (canting angle (χ_δ) of 0), then the instantaneous net SRP torque on the satellite would constantly be zero and therefore the spin's angular velocity (spin period) would not vary over time. However, even if the solar panels were designed with identical specifications, natural events, including; uneven solar exposure; collisions with micro-meteors and other debris; and warping, possibly causing a slight canting angle between the two panels, will cause the net SRP torque to be other than zero. Echostar-2 is generally unconstrained with respect to any rotational motion, therefore even a significantly small net external torque can vary the angular momentum (according to Eq. (94)), thereby varying both the spin's angular velocity (spin period) and the spin axis' orientation in inertial space. As a result, there can be two components of the net SRP torque; one that will be aligned with the spin axis orientation, causing an increase (or a decrease) in the spin angular velocity; and one that will be perpendicular to the spin axis orientation, causing a secular or cyclical variation (precession) of the spin axis' orientation.

The free parameters that were considered when conducting the angular velocity variation simulations included each solar panel's body frame orientation (including the canting angle between the two panels) and each panel side's reflectivity. These simulations were required to determine the likely solar panel orientations that would result in the simulated spin period variations most closely resembling the observed spin period variations.

The Euler coordinate transformation equations required to transform the body-frame coordinates to the spin axis frame coordinates and to transform the spin axis frame coordinates to the equatorial (inertial) frame coordinates are described in [20]. Appendix F discusses the Euler equations required to describe the rotational motion of a rigid body based on components of the net torque that are applied to each of the three principal axes of rotation. The Euler equations shown in Eqs. (111), (112), and (113) exclusively refer to the body-frame components of the SRP torque (τ_x, τ_y, and τ_z), angular velocity (ω_x, ω_y, and ω_z), and angular acceleration ($\frac{d\omega_x}{dt}$), ($\frac{d\omega_y}{dt}$), and ($\frac{d\omega_z}{dt}$). Equation (27) can only determine the torque components in the equatorial (inertial) frame because the Sun's apparent direction with respect to the satellite, both solar panels' radial unit vectors, and both panels' normal unit vectors were all expressed in the equatorial coordinate frame to determine this torque. To reduce the amount of free parameters required to solve the Euler rotational motion equations, a number of assumptions were made, which were based on the observational evidence reported in [6] and [16].

As reported in [16, 20], no evidence of sunlight reflections from Echostar-2's solar panels was observed from 2012 to 2015. This was based on the assumption that the sources of the bright specular reflections were the two mirrored radiators. Any rotation component about the satellite's body frame x-axis over such a long time frame would result in evidence of reflections from both

the solar panels and the mirrored radiators over time. As was reported in [20], the bright specular reflections had roughly the same shape and only their brightness varied over time, suggesting that only two specific surfaces, separated by 180º from each other, had been observed over the long term. Therefore, there was enough evidence from the observations to conclude that the rotation about the satellite x-axis was either much smaller compared to the other two components or was zero for the entire time. By extension, the torque component about the body frame's x-axis was also very small compared to the other two components or was zero because any torque about this axis would cause an angular velocity and therefore would eventually reveal sunlight reflections off of the solar panels. When considering these assumptions, the three Euler rotational motion equations shown in Eqs. (111), (112), and (113) reduced to as shown in Eqs. (28), (29), and (30), respectively.

$$0 = (I_{zz} - I_{yy})\omega_y\omega_z \tag{28}$$

$$\tau_y = I_{yy}\frac{d\omega_y}{dt} \tag{29}$$

$$\tau_z = I_{zz}\frac{d\omega_z}{dt} \tag{30}$$

In order for Eq. (28) to be true, one of the following must also be true: the two MOIs I_{yy} and I_{zz} are equal, ω_y is zero, and/or ω_z is zero. Echostar-2's spin axis was estimated to be oriented somewhere within the satellite's y_b-z_b plane, as illustrated in Fig. 43 [20]. This meant that neither ω_y nor ω_z could likely be zero. On the other hand, Echostar-2's three MOIs were estimated and presented in [16, 20]. The I_{yy} and I_{zz} MOI components were determined to be very similar to one another. As a result, it was assumed that I_{yy} and I_{zz} were equal to one another because their values and uncertainties were similar to one another. As a result, Eq. (28) was considered to be true and was therefore removed from consideration for Echostar-2's rotational motion, leaving Eqs. (31) and (32).
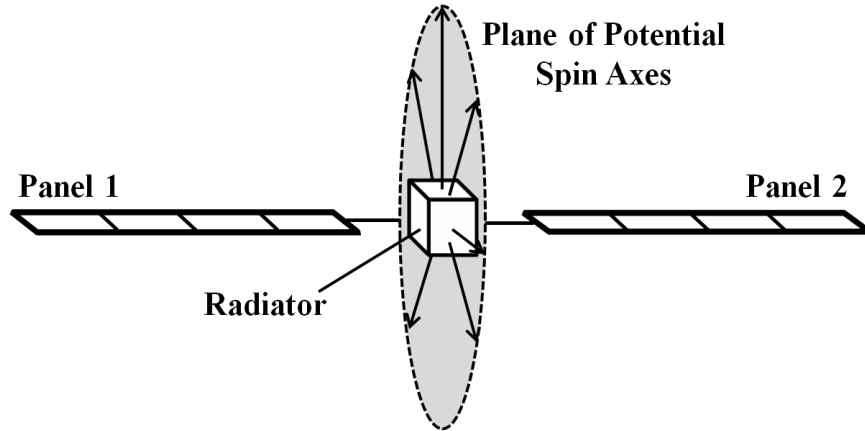
Figure 43 Potential Echostar-2 body frame spin axis orientations

$$\tau_y = I_{zz}\frac{d\omega_y}{dt} \tag{31}$$

$$\tau_z = I_{zz}\frac{d\omega_z}{dt} \tag{32}$$

The SRP-based force on each solar panel would be perpendicular to each of the corresponding panel surfaces, as illustrated in Figs. 36 and 42. The instantaneous SRP torque caused by a solar panel would therefore be orthogonal to the SRP force on the corresponding panel ($\vec{F}_p$) and orthogonal to the panel's radial unit vector $\hat{r}_p$. The SRP torque arising from each panel can be

split into two components comprised of; a torque that is aligned along the spin angular velocity vector; and a torque that is aligned orthogonal to the spin angular velocity vector.

The MOI of a solid uniform density cube is the same for any axis passing through the cube's center of mass, which, in this case, is in the same location as the cube's geometric center [36]. This means that the satellite's MOIs are not affected by a rotation of the box about the $\hat{r}_\mathrm{p}$ unit vectors, as long as the y_b and z_b axes are fixed with respect to the solar panels. Since it was assumed that the MOIs I_{yy} and I_{zz} were equal, the choice of the y_b and z_b axes are arbitrary with respect to the box portion only, provided that they are still orthogonal to each other and to the x_b axis.

For a flat spin scenario, the satellite's body frame axis that corresponds to the maximum MOI (along the z_b axis) has to be oriented nearly parallel to the panels' normal unit vectors. It is likely that Echostar-2's two solar panels have a small (as opposed to large) canting angle (less than several degrees) between them, or the satellite's power generation would have been compromised when it was active and the (larger) SRP torque would have been more difficult to compensate for.

The instantaneous net torque vector ($\vec{\tau}_\mathrm{net}$) can likely be located anywhere within the y_b-z_b plane because this vector is the addition of two similar, yet not identical, instantaneous panel torques. The net torque components (along-axis and precession) will depend on the solar panels' orientations with respect to the spin axis orientation and therefore will critically depend on the canting angle between the two solar panels.

Assuming that the net torque is directed parallel to the spin axis orientation (the angular velocity vector), this would result in the spin's angular velocity increasing with the angular acceleration magnitude shown in Eq. (32). Assuming that the net torque is directed anti-parallel to the spin axis orientation, the spin's angular velocity will decrease with the angular acceleration magnitude shown in Eq. (32). Either case represents the maximum angular acceleration that is possible, considering the specific characteristics of the two solar panels. The net torque can also have a direction that is orthogonal to the spin axis orientation. In this case, the torque acts to change the direction of the spin axis orientation, thus causing precession motion. It is likely that the spin angular velocity's magnitude and direction are varying with time, as was reported in [6], [16], and [20].

As the satellite spins, the instantaneous net torque (from the two solar panels) will vary nearly cyclically. However, the satellite will be moving in its orbit with respect to the Sun and the Sun will appear to slightly change its RA and dec with every additional spin period. The total torque vector ($\vec{\tau}_\mathrm{tot}$) is the addition of all instantaneous net torques over one complete satellite spin period. The total torque vector's Cartesian inertial coordinates can be obtained by summing each individual torque component (resulting in $\vec{\tau}_\mathrm{tot,x}$, $\vec{\tau}_\mathrm{tot,y}$, and $\vec{\tau}_\mathrm{tot,z}$), as shown in Eqs. (33), (34), and (35). The incrementation value should be a small fraction of the total spin period. In this way, the total torque vector's magnitude and the direction can be determined for each spin period. Since the body frame x-component of all instantaneous net torques were assumed to be zero, the total torque vector should be oriented somewhere within the body frame's y_b-z_b plane. The total torque vector's inertial equatorial coordinates ($\alpha_{\tau\mathrm{tot}}$ and $\delta_{\tau\mathrm{tot}}$) can be determined with Eq. (36) and Eq. (37), respectively.

$$\tau_\mathrm{tot,x} = \sum_{t=0}^{T} \tau_\mathrm{net,x}(t) \tag{33}$$

$$\tau_\mathrm{tot,y} = \sum_{t=0}^{T} \tau_\mathrm{net,y}(t) \tag{34}$$

$$\tau_\mathrm{tot,z} = \sum_{t=0}^{T} \tau_\mathrm{net,z}(t) \tag{35}$$

$$\alpha_{\tau\text{tot}} = \tan^{-1}\left[\frac{\tau_{\text{tot,y}}}{\tau_{\text{tot,x}}}\right] \tag{36}$$

$$\delta_{\tau\text{tot}} = \sin^{-1}(\tau_{\text{tot,z}}) \tag{37}$$

The quantity "γ" was defined as being the angle between the spin axis orientation (angular velocity vector) and the total (summed) torque vector. The dot product of the spin axis orientation's unit vector and the total torque's unit vector results in the cosine of this γ angle, as shown in Eq. (38). Simulations of the satellite's varying spin angular velocity would depend on the net torque's orientation with respect to the spin axis orientation.

In order to determine the instantaneous net SRP torque component that varies Echostar-2's angular velocity (not the spin axis orientation), the result of Eq. (27) had to be multiplied by the cosine of the γ angle, as shown in Eq. (39). Equation (39) was considered as a vector component directed parallel (or anti-parallel) to the angular velocity (spin) vector, resulting in the increase (or decrease) of the spin angular velocity. Equation (40) shows the complementary component to τ_{spin} causing the spin axis orientation variation (precession).

$$\cos(\gamma) = \sin(\delta_{\text{axis}})\sin(\delta_{\tau\text{tot}}) + \cos(\delta_{\text{axis}})\cos(\delta_{\tau\text{tot}})\cos\left[\alpha_{\text{axis}} - \alpha_{\tau\text{tot}}\right] \tag{38}$$

$$\tau_{\text{spin}} = \tau_{\text{tot}}\cos(\gamma) \tag{39}$$

$$\tau_{\text{prec}} = \tau_{\text{tot}}\sin(\gamma) \tag{40}$$

The spin angular acceleration (α_{spin}) is determined with Eq. (41). When α_{spin} is positive, the total torque will act to assist the spin angular velocity. Conversely, when α_{spin} is negative, the total torque will act to oppose the spin angular velocity. After each complete spin has been simulated, the new angular velocity is determined with Eq. (42). The new angular velocity after one complete spin is determined from the angular acceleration over the preceding complete spin period (T_{o}). The new spin period is determined from the new angular velocity with Eq. (43). After this calculation, the new spin period T becomes the new (T_{o}), another spin period is simulated, and another new spin period is calculated.

$$\alpha_{\text{spin}}(T_{\text{o}}) = \frac{\tau_{\text{spin}}(T_{\text{o}})}{I_{zz}} \tag{41}$$

$$\omega_{\text{spin}}(T) = \omega_{\text{spin0}} + T_{\text{o}}\alpha_{\text{spin}}(T_{\text{o}}) \tag{42}$$

$$T(T_{\text{o}}) = \frac{2\pi}{\omega_{\text{spin}}(T_{\text{o}})} \tag{43}$$

With each subsequent spin, the total torque is determined, the spin angular acceleration is determined, the new spin angular velocity magnitude is determined, and finally the new spin period is determined. Assuming an identical sun angle with each spin, the total torque will increase as the spin period increases and will decrease as the spin period decreases. This variation occurs because the time that the SRP can affect the satellite's spin period grows with increasing spin period and shrinks with decreasing spin period. This effect should result in longer durations at the lower spin periods and shorter durations at the higher spin periods. This phenomenon has been observed for a number of box-wing GEO satellites, including AMOS-5i and Paksat-1 [16].

1   Precession Torque Component

Precession is the apparent motion (variation) of the spin axis orientation over time. The torque component τ_y in Eq. (31) determines the specific precession motion. This motion consists of a precession angle (from the angular momentum vector) and a precession rate. Although this precession motion could be hypothetically determined from the SRP torque precession components,

the precession motion can also be inferred from the observed variation of the spin axis orientation, as shown in Fig. 40. It was assumed that the angular momentum vector was roughly in the direction of the North Celestial Pole (NCP). This assumption was based on the flat-spin analysis conducted in [20]. As a result, the space cone would be centered on the NCP, with the angular velocity vector circling around it with an angle $\psi_{\omega L}$ between the angular momentum and the angular velocity vectors.

Figure 40 implies that between 2012 and 2015, the angular velocity vector was at least 8⁰ and at most 30⁰ from the angular momentum vector. The largest $\psi_{\omega L}$ angle of 30⁰ was initially assumed; however this angle could be changed. Figure 40 also shows that the angle between the "spring" and "autumn" spin axis orientations was roughly 180⁰, suggesting that the precession period is approximately one sidereal year. Figure 44 illustrates the presumed relationship between Echostar-2's spin axis and the angular momentum vectors.
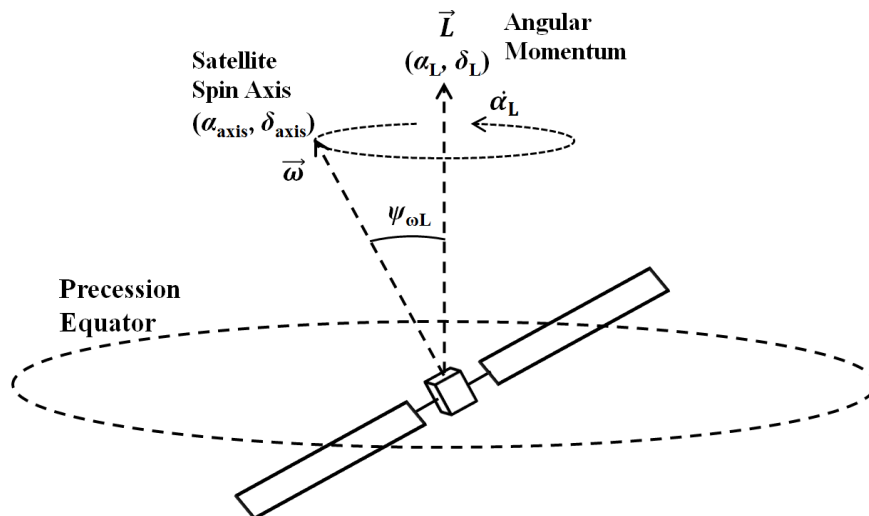
Figure 44   Echostar-2 spin axis precession

G   Spin Period Variation Simulations

Observations previously conducted and reported in [6] and [16] suggested that Echostar-2's spin period varied cyclically with an amplitude that decreased significantly over time. Echostar-2's spin angular acceleration also varied cyclically, but its amplitude appeared to be nearly constant, ranging from -50 to 50 μrad $\cdot$s$^{-1}\cdot$d^{-1}. The torque (both instantaneous net magnitude and spin axis component), spin angular acceleration, and spin period were simulated, with software designed in MATLAB, for a ten-year time frame, beginning with the date of the first observation (March 11, 2012). The values of the free parameters that were used to produce the results are shown in Table 13. The reflectivity parameters of Echostar-2's solar panels have been assumed because most of the satellite's specifications are proprietary.

The results of the simulations are shown in Fig. 45. Figure 45 (a) shows the simulated magnitude of the instantaneous net torque vector, based on the sum of all of the SRP torque components of each solar panel contribution, over a ten-year time span from March 11, 2012. Figure 45 (a) suggests that there is a much larger cyclical envelope with a period of approximately one sidereal year (365.256 days); corresponding to the orbit period of the Earth. Figure 45 (b) shows the integrated result, over each individual sidereal spin period, of the SRP torques over the same ten-year time span. Figure 45 (c) and (d) show the simulated (solid line) and observed (dots) angular acceleration variation over a four-year and ten-year time span, respectively. Finally, Fig. 45 (d)

and (e) show the simulated (solid line) and observed (dots) spin period variation over a four-year and ten-year time span, respectively.

Table 13 Values of free parameters

Free Parameter	Symbol	Value	Notes / References
Time increment	t_{inc}	10s	Resolution / run time trade-off
Panel 1 Side 1 body coordinates	$\alpha_{n(11)}, \delta_{n(11)}$	270°, 85°	normal unit vector
Panel 1 Side 1 reflectivity	q_{11}	0.6	[35]
Panel 1 Side 2 reflectivity	q_{12}	0.1	Assuming black paint
Panel 2 Side 1 reflectivity	q_{21}	0.6	[35]
Panel 2 Side 2 reflectivity	q_{22}	0.1	Assuming black paint
Panel 2 RA offset	χ_α	0	RA offset from Panel 1
Panel 2 dec offset	χ_δ	0.01^o	dec offset from Panel 1
Precession angle between $\vec{\omega}$ and $\vec{L}$	$\psi_{\omega L}$	30°	Estimated from [20]
Coordinates of $\vec{L}$	α_L, δ_L	N/A, 90°	Assumed from [20]
Precession rate	$\dot{\alpha}_L$	$720^o \cdot y^{-1}$	Best rate for simulations

Figure 45 (a) presents the magnitude (not the direction) of the instantaneous net SRP torque on Echostar-2. Figure 45 (b) is the result of integrating (summing) the instantaneous net SRP torque components (x, y, and z) over each satellite spin over the ten-year time span and applying Eq. (39) to determine the total torque on the satellite's spin axis after every individual spin period. Figure 45 (b) shows that the SRP torque's overall amplitude is decreasing with time, suggesting that the angular acceleration amplitude will also decrease with time.

Figure 45 (c) and (d) compare (for the first time) the long term observed and simulated angular acceleration variation along an inactive box-wing GEO satellite's (Echostar-2) spin axis. Assuming that the angular velocity vector is always prograde, a positive angular acceleration denotes the assistance to the spin, while a negative angular acceleration denotes the opposition to the spin. Figure 45 (c) and (d) are the results of applying Eq. (41) to the simulation results shown in Fig. 45 (b).

Figure 45 (c) and (d) suggest that the general shape of the angular acceleration variation is similar for both the observed (dotted) and the simulated (solid line) cases. There are some deviations of the simulated curve from the observed curve. Such deviations are expected because many of the critical free parameters shown in Table 13 were assumed. None of the actual values of the free parameters shown in Table 13 could be obtained from Echostar-2's manufacturer, despite the fact that the satellite has been inactive since mid-2008 [87].

The shape of the simulated angular acceleration variation shown in Fig. 45 (c) and (d) could only be obtained by assuming that the precession rate of the angular velocity vector ($\vec{\omega}$) about the angular momentum vector ($\vec{L}$) is $720^o \cdot y^{-1}$ (4π rad·y^{-1}). This assumed precession rate is twice the rate suggested by [20]. However, further research might reveal a common link between the results of [20] and this paper that will explain Fig. 45 (c) and (d).

---
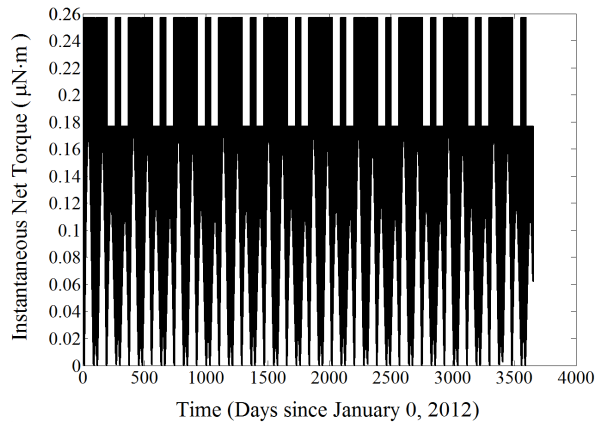
a) Instantaneous net torque magnitude
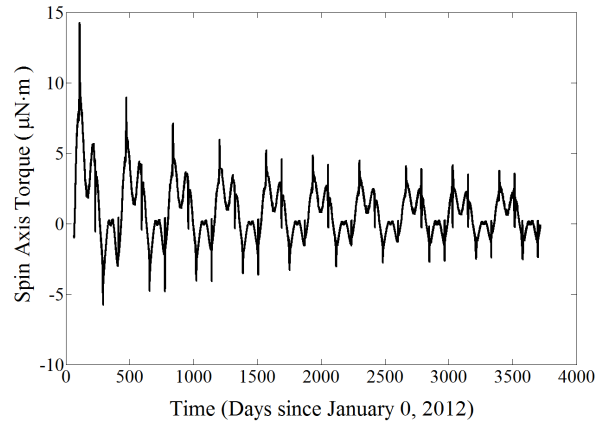
b) Torque along spin axis
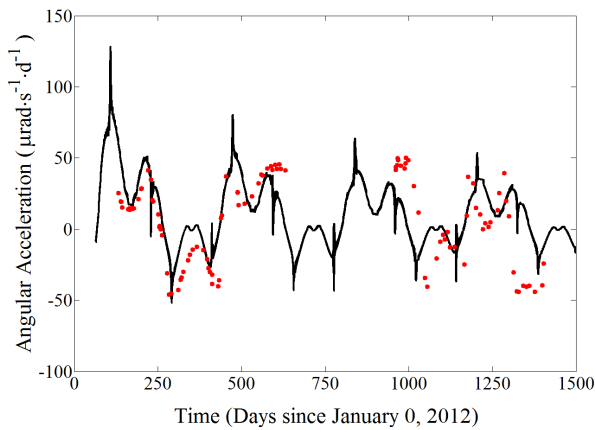
c) Angular acceleration along spin axis - 4 years
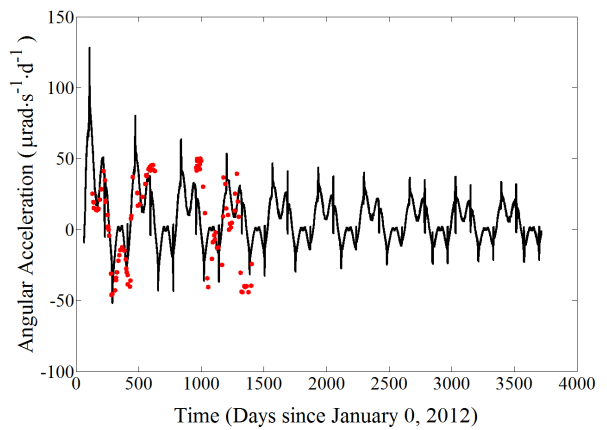
d) Angular acceleration along spin axis - 10 years
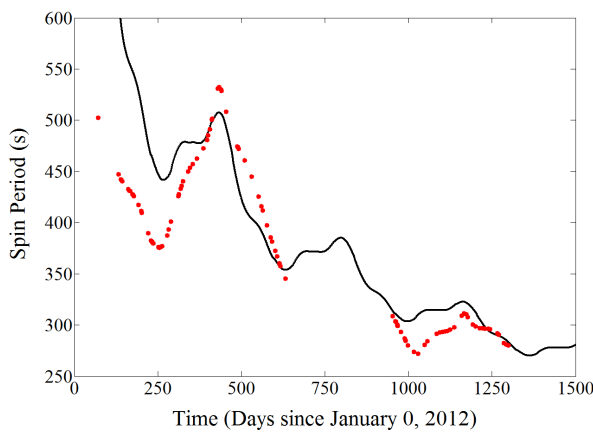
e) Spin period - 4 years
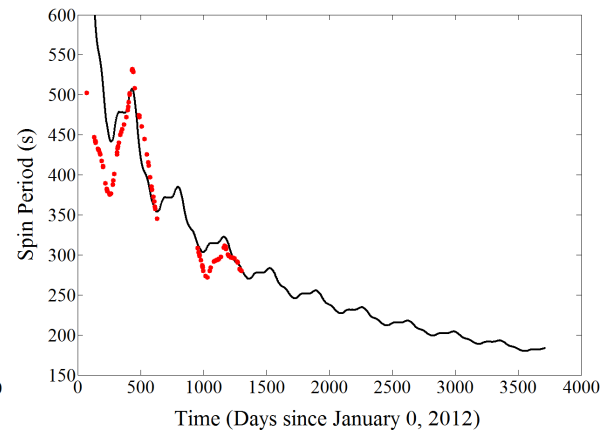
f) Spin period - 10 years

Figure 45 Simulation results

For the first time, the simulated angular acceleration variation shown in Fig. 45 (c) and (d) successfully models the phenomenon of the decreasing angular acceleration magnitude in between angular acceleration maxima and minima that was first reported in [6]. This phenomenon seems to

be exclusively apparent in the case of Echostar-2; however other box-wing satellites might exhibit this behavior if their individual characteristics are similar to those shown in Table 13.

The simulated angular acceleration curves shown in Fig. 45 (c) and (d) suggest a decreasing amplitude over time, which is analogous to dampening. The observed amplitude reported in [6] does not appear to decrease; however further observation might reveal how the amplitude varies over time.

Figure 45 (d) and (e) compare (for the first time) the observed and simulated spin period variation of an inactive box-wing GEO satellite (Echostar-2) over a ten-year and a nearly four-year time span, respectively. Figure 45 (d) and (e) suggest that the general shape of the spin period variation is similar for both the observed (dotted) and the simulated (solid line) cases. There are some deviations of the simulated curve from the observed curve, as was previously described for Fig. 45 (c). This simulation successfully predicted the overall decrease of the spin period and the decrease of the spin period amplitude over time. This simulation also successfully predicted the existence of the spin period inflection points where the spin period variation rate decreases momentarily before resuming toward the global maximum or global minimum spin period. The precise location of the inflection points in the variation curve could not be simulated accurately; however with supplementary research and observations, the simulation model could be improved.

The spin period simulations presented in Fig. 45 (d) and (e) suggest that the amplitude will steadily decrease for a number of years. This phenomenon has been observed for other box-wing satellites, including Solidaridad-1, Paksat-1, and AMOS-5i. However, only observations of Solidaridad-1 has resulted in a very long spin period variation period. An interesting similarity between Echostar-2's and Telstar-401's spin period variations can be seen in the simulations when considering that as the spin period decreases, so does the amplitude. Telstar-401's average spin period is very low when compared to the largest spin period for Echostar-2. The simulation correctly predicts the decrease of the amplitude with a decrease in the overall spin period.

Telstar-401's average spin period is 158s [6]. The satellite's spin period amplitude was observed to be small at approximately 26s over four years. The Echostar-2 spin period simulation might be revealing that Telstar-401's short period and smaller amplitude might not be permanent and that the satellite was observed at a time when its spin period was at a minimum. Over a larger period of time, Telstar-401's spin period might increase and its amplitude might eventually resemble Echostar-2's. Since both satellites are of a similar box-wing design and both suffered catastrophic malfunctions, they might have a very long and cyclical overall spin period variation in common.

However, another hypothesis can be put forward. Telstar-401 became inactive in January 1997 due to a catastrophic power failure. Echostar-2 became inactive in July 2008, for the same reason. This means that Telstar-401 has been inactive for approximately 11.5 years longer than Echostar-2. The spin period variation scenario shown in Fig. 45 (e) predicts that Echostar-2's average spin period will continue to decrease to under 200s in several years; near the 158s spin period that Telstar-401 has at present. In the four years of observation, Telstar-401's spin period variation amplitude has not varied significantly. However, Echostar-2's spin period variation amplitude has been observed to significantly decrease over four years. This suggests that Telstar-401's spin period has reached a stable point in nearly 20 years in which the spin period and its amplitude have stabilized such that neither vary significantly over time. In contrast, Echostar-2's spin period and its variation have not yet reached the same stability after being inactive for under half the time of Telstar-401.

It is reasonable to hypothesize that despite a cyclical SRP torque during a satellite's spin and during a sidereal year, there would be an overall secular spin axis torque, causing an overall spin angular acceleration that would either assist or oppose the spin's angular velocity. In Echostar-2's case, the overall torque would assist the spin, thereby decreasing the spin period and its amplitude over the long term. However, there would be a limit to how much the SRP torque can increase

the spin's angular velocity. This limit could be reached in the form of the amount of time the SRP has to affect the spin angular velocity. As the spin period decreases, the amount of time the SRP has to affect the spin period (for each spin) also decreases. A larger angular velocity would also result in a larger angular momentum. The SRP torque could become so small with respect to the angular momentum that the spin period and the spin axis orientation will eventually be negligibly affected by the SRP torque. Therefore, the spin period and its amplitude variation would reach their respective minima and would not vary significantly over time, as was observed for Telstar-401 for nearly four years.

Based on the satellites' diverse photometric characteristics and diverse spin period variations reported in [6] and [16], the models described in this paper might apply exclusively to Echostar-2 (and possibly Telstar-401) only. However, additional observations of an additional number of inactive box-wing GEO satellites could reveal similar photometric and spin period variation characteristics to those exhibited by Echostar-2. Such "Echostar-2"-type box-wing satellites could provide an additional opportunity to improve sidereal spin period variation curve modeling, using this paper as a starting point.

H   Conclusions

The research featured in this paper has demonstrated, for the first time, that an inactive box-wing GEO satellite's sidereal spin period can be estimated and that its spin period variation can be simulated, to a first-order approximation, when applying the basic assumptions of its solar panel reflectance and attitude characteristics. The results presented here were the result of several years of high temporal resolution photometric observation, coupled with geometric and numerical modeling. It must be stressed that a long term and temporally high resolution observation schedule is vital to building a simulation model to describe any inactive satellite's attitude dynamics.

This research has shown that Echostar-2's sidereal (true) spin period differs from its synodic (observed) spin period. This difference is not substantial because of the satellite's short spin period and the large angle of the satellite's spin axis orientation with respect to its PAB orientation.

Echostar-2's angular acceleration variation and spin period variation have been simulated with very encouraging results. In both cases, the observed trends and amplitude variations over time were successfully simulated by the first-order models discussed. In the case of the angular acceleration, the simulations suggest a slowly decreasing amplitude over time. The simulations also offer an explanation as to why the angular acceleration magnitude decreases momentarily, then increases again, at some time between a global maximum and a global minimum.

Throughout this paper, the Sun was assumed to be a point source of light and not the extended light source that it truly is when viewed from the Earth's orbit radius. More robust dynamics models of a box-wing satellite's spin period should include the extended light source model, with the Sun's apparent angular diameter being approximately 0.5^{o}.

The simulations presented here successfully show the observed spin period variation's overall decreasing spin period trend as well as the decreasing amplitude trend over four years. The simulations also successfully model (within a first-order approximation) the temporary decrease of the spin period variation rate in between a global maximum and global minimum spin period. The model had to use a $720^{\text{o}} \cdot \text{y}^{-1}$ precession rate rather than the $360^{\text{o}} \cdot \text{y}^{-1}$ precession rate that was previously reported.

The simulations included a time frame of 10 years from the date of the first observation of the Echostar-2 satellite (March 11, 2012). The simulations predict that the Echostar-2 satellite's angular acceleration amplitude will continue to slowly decrease. The simulations also predict that the satellite's overall spin period and spin period amplitude will decrease, suggesting that its spin period will vary in a similar manner to the Telstar-401 satellite's spin period variation. The very long, possibly cyclical, trend might indicate a combination of the yearly cyclical spin period observed

for Paksat-1 with a very long cyclical trend observed for the Solidaridad-1 satellite.

The solar panel orientations that resulted in the most accurate simulations corresponded to a canting angle of 0.01º and a panel normal orientation of 85º with respect to the body frame of the satellite. A deviation of even 0.001º in the canting angle would result in simulations that are at variance with the angular acceleration and spin period variation observations. The reflectivity free parameters corresponded to 0.6 and 0.1 for the first side and the second side of the two solar panels, respectively.

The three papers presented in Michael A. Earl's PhD thesis represent the first steps to understanding the attitude dynamics of inactive box-wing GEO satellites. The first paper introduced the observation strategy that can be used to obtain photometric light curves to study these satellites' unique long term morphologies. The second paper introduced geometrical and statistical methods that can be used to identify these satellites' highly reflective components so that the satellite's most likely attitudes and attitude variations can be estimated. This third paper has introduced the physical dynamics models that can be used to simulate these satellites' angular acceleration variations and spin period variations over the long term.

Together, these three papers propose the observation, geometrical modeling, and numerical modeling processes that space scientists can use to observe and study inactive box-wing GEO satellites' long term attitude dynamics. Frequent observation and modeling will enable space scientists to develop a database that can be used by the space surveillance community to characterize the inactive satellite population for use in OOS and conjunction analysis.

CHAPTER 6: SUMMARY

The three papers presented in this thesis represent the first steps to understanding the attitude dynamics of inactive box-wing GEO satellites, based on long term and high resolution ground-based broadband photometric observations. The first paper introduces the observation and analysis strategies that can be used to study box-wing satellites' photometric light curve morphologies, spin period variations and angular acceleration variations. The second paper introduces geometrical and statistical methods that can be used to estimate these satellites' specular components and their most likely attitudes and attitude variations. The third paper introduces the physical dynamics models that can be used to simulate and predict these satellites' long term angular acceleration variations and long term spin period variations.

A   Observations and Photometric Light Curve Analysis

A sample of 11 inactive box-wing GEO telecommunications satellites were observed at least once per week (weather and access permitting) from March 2012 to January 2016 in order to obtain high resolution (high sample rate) broadband photometric light curves. Synodic spin period, angular acceleration, and periodogram data were inferred from each of these light curves in order to investigate how each satellite's light curve morphology, spin period and angular acceleration appeared to vary over the short term (minutes to days) and the long term (weeks to months).

Three methods of spin period determination (P-P, L-S, and CRT) (inferred from light curves) were carefully evaluated in order to assess their practicality and their relative accuracy. This analysis was performed to determine which of these three methods would result in the most practical and accurate spin period determination with the consistently lowest statistical uncertainty.

Each of the 11 satellites' light curves obtained were carefully studied to investigate how they varied over the short term (minutes to days) and over the long term (weeks to months). A satellite's light curve morphology could suggest the satellite's attitude variation over time and the variation rate. The satellite with the smallest light curve variation over the long term was assumed to have the most stable attitude of the 11 satellites over the study's 4-year timescale. The "most stable" satellite's geometric and reflective properties were then assessed to estimate its spin axis orientation.

The additional photometric light curve data that was obtained allowed the further study of a previously postulated relationship between box-wing satellites' spin period variation amplitudes and their average spin periods. This analysis investigated whether or not an inactive box-wing satellite's spin period variation amplitude could be predicted from its average spin period, or vice-versa.

Telstar-401's and Echostar-2's light curve morphologies were quantified by extracting the maximum spectrum powers, corresponding to a full light curve period and a half light curve period, from each of their L-S periodograms and determining the full-to-half PSR. The PSR and the spin period were both plotted against time in order to investigate any relationships between the satellites' PSRs and the spin periods. A strong relationship between the PSR and the spin period could suggest a relationship between a box-wing satellite's orientation and its attitude dynamics.

B   Estimation of Echostar-2's Spin Axis Orientation

The likely attitude dynamics of Echostar-2 immediately after its malfunction (assuming that no external disturbance torques were present), were investigated. This "flat spin" scenario demonstrated Echostar-2's possible attitude dynamics, assuming a constant angular momentum. Since the disturbance torque from SRP has been determined to be very small for box-wing satellites (in the order of μNs), a flat spin state represented a logical first-order scenario.

Echostar-2's geometrical and (diffuse and specular) reflectance models were presented. These box-wing models included all six sides of a uniform density cube (the box), two large flat plates

(representing the solar panels), and two large and angled flat disks (representing the two large communications dishes).

The time of Echostar-2's brightest observed specular reflections were chosen from the light curves to represent the time in which a highly reflective surface's normal unit vector and the satellite's PAB were co-located (an angle of 0 between them). The maximum angle between this surface normal and the PAB that constituted a specular reflection, was estimated. It was assumed that Echostar-2's bright specular reflections were the result of sunlight reflecting off of the two mirrored radiators, located on two opposite sides of the box portion. Based on the inertial coordinates of the Sun, the ground-based observer, and the satellite, the most likely attitudes that would result in a specular reflection to the observer were estimated analytically and with simulations based on Echostar-2's reflectance model. These attitudes corresponded to a great circle with a plane oriented orthogonally to the unit vector directed along the solar panels' longest dimensions.

Other bright specular reflections from Echostar-2 were observed on a number of days before and after the time of the brightest specular reflection. The attitude planes (great circles) that corresponded to the other bright specular reflections were plotted with the original attitude circle (brightest specular reflection). The intersections of these plots indicated Echostar-2's most likely spin axis orientations. Two intersection points were observed; the first corresponding to the prograde rotation angular velocity vector and the second corresponding to the retrograde angular velocity vector. All of the plot intersections were determined with analytical and simulation methods. Additional Echostar-2 specular reflections corresponding to approximately 6, 24, 30, and 36 months after the brightest specular reflection were analyzed to investigate how the satellite's spin axis orientation varied over the long term.

C   Echostar-2 Spin Period and Angular Acceleration Simulations

The temporal difference between Echostar-2's synodic and sidereal spin periods (assuming the previously estimated spin period orientations), were compared to the ideal synodic-sidereal differences ("ideal" refers to assuming a spin axis orientation that was approximately orthogonal to the satellite's orbit plane). This comparison was performed to investigate how the synodic spin period differed when assuming the satellite's estimated spin axis orientation and assuming an ideal flat spin orientation.

Simulations of Echostar-2's spin period variation and angular acceleration variation were conducted using SRP torque modeling that was based on numerical analysis. The instantaneous SRP torque contribution from all sunlit solar panel surfaces were integrated over each simulated satellite spin period. The net angular acceleration due to the total SRP torque over each spin period was determined and was then added to the angular velocity after each spin period. A number of solar panel orientations, with respect to the spacecraft body frame and with respect to each other (canting angle) were used in the SRP torque model to determine the best simulated spin period curve and to determine the angular acceleration curve that would fit the observed spin period and angular acceleration curves that were inferred from the light curves.

CHAPTER 7: DISCUSSION AND FUTURE WORK

The research presented in this thesis provides a solid foundation for future research because it includes; a significant amount of long term and high resolution photometric observations of 11 box-wing satellites; a careful assessment of the practicality and accuracy of three well known spin period inference methods; a comprehensive qualitative and quantitative comparison of these satellites' light curve morphologies, spin period variations, and angular acceleration variations; a first-time estimation of a box-wing satellite's spin axis orientation; a first-time assessment of a box-wing satellite's synodic-sidereal spin period difference; and first-time simulations of a box-wing satellite's spin period curve and angular acceleration curve. However, a number of interesting questions have arisen from this research.

This research has found that even box-wing satellites of the same model (AS-7000 or HS-601) could have significantly diverse light curve characteristics and diverse spin period variations. Would all inactive box-wing satellites in the GEO population have a diverse light curve morphology, spin period variation and angular acceleration variation when compared to one another? Would these findings also indicate that each satellite has a unique set of attitude dynamics? Future research should be conducted in order to investigate these questions further.

With a larger satellite sample and additional photometric observations, it was determined that the suggested linear trend between the original four satellites' spin period variation amplitude and their average spin periods no longer fit the new data. Does this indicate that a more complicated relationship between the spin period variation amplitude and the average spin period exists or does this indicate that no relationship between them exists? Additional photometric observations should be conducted so that more data points are available for analysis.

Why is the relationship between the full/half period PSR and spin period so strong for Telstar-401, much weaker for Echostar-2, and nearly non-existent for the remaining nine satellites in the sample? The reasons could include; a larger PSR signal relative to the background signal in the Telstar-401 periodograms; Telstar-401's much shorter average spin period (a larger angular velocity and angular momentum magnitude) in relation to the other 10 satellites; some traits that are present in Telstar-401's (and possibly Echostar-2's) attitude dynamics are not present in the other 10 satellites; and/or an image sampling frequency that favored Telstar-401 over the remaining 10 satellites. Additional observations and PSR analyses should be conducted in order to determine if another box-wing satellite of comparable average spin period and variation amplitude can have similar results to what was observed for Telstar-401.

The estimation of Echostar-2's spin axis orientation suggested that its spin axis is precessing with an angle of at least 8º and at most 30º from the orthogonal to the Earth's equatorial plane, with a period of approximately one sidereal year. Is this angle of precession solely due to SRP torque effects or are there more disturbance torques that can cause and/or vary this angle? Are there any other box-wing satellites that have similar spin axis orientations? Future work should include additional observations or a more detailed precession model that includes SRP and other potential disturbance torques.

The estimation of Echostar-2's spin axis orientation used the assumption that the source of the two nearly equally bright specular reflections, observed over a complete spin period, were the sunlit mirrored radiators and not the two solar panels. It may be possible that the reflections from the solar panels (or some other reflective surfaces) were being observed. A number of color photometric observations of Echostar-2 should be conducted in order to confirm that the bright specular reflections originate from a nearly perfectly reflective surface (such as a mirror), a partially absorptive colored specular surface (such as the solar panels), or some other reflective surface.

The box-wing specifications (masses and dimensions), solar panel reflectivity, and reflectance models presented in this thesis were all assumed based on artist's conceptions and average values found in the literature. The author had attempted to obtain this information directly from the

American manufacturers of the 11 satellites listed. Unfortunately, none of the manufacturers were willing to divulge any information concerning these 11 (inactive) box-wing satellites. For the benefit of all future space science and space surveillance professionals, it is strongly suggested that the satellite manufacturing industry should begin to reconsider their strict information control policies, especially with respect to those inactive box-wing satellites that are greater than 20 years old (outdated technology). In order for present-day space science graduate students to accurately model the disturbance torques' effects on orbiting debris, they must have more concrete information and a reduction in the number of assumptions of critical free parameters, including the effective dimensions and masses of the satellites' largest components.

This thesis reported several estimates of Echostar-2's spin axis orientation. The spin axis orientation's equatorial coordinates estimated from the September 9 to October 10, 2012 photometric data appears coherent to within 10º; however, several data points (in the minority) appear to be nearly 180º away from the majority of the data points. The cause of such a large discrepancy is unknown; however it could be due to the high decs (nearly 90º) causing a large uncertainty in the RA coordinates. This uncertainty could also be caused by the image sampling rate (data point cadence). In order to develop a more highly resolved profile of each of the two specular reflections, Echostar-2's light curves were folded. However, if the sampling rate were to be increased, there might be some improvement in the spin axis orientation uncertainty.

Some of the estimations suggested that the spin axis orientation did not move for nearly several weeks. This was observed from the September 9 to October 10, 2012 specular reflection data. However, estimations of later dates suggest that the spin axis orientation varies. The estimations could be suggesting that the spin axis orientation can move over several months, stop for several weeks, then resume varying again. However, the spin period and angular acceleration variations do not support this hypothesis. More observations and spin axis variation analysis are recommended to resolve this issue.

When estimating Echostar-2's synodic-sidereal spin period differences, it was assumed that the brightest observed specular reflection corresponded to the co-location of the reflective surface's normal unit vector and the satellite's PAB. This might have been the case at the time; however, it is likely that the angle between the two vectors was significantly small but still not zero. Therefore, there would be some unknown, yet significantly small, bias for all of the estimated spin axis orientations, since they were all based on this initial assumption. Additional observations of Echostar-2 might reveal even brighter specular reflections than those observed during this research; suggesting an even smaller angle between the two vectors.

Previous research has suggested that a satellite's synodic spin period could increase in the event that the satellite's spin axis orientation is nearly aligned with the satellite's PAB. The synodic-sidereal spin period difference presented in this thesis suggests that the synodic spin period will vary from the ideal synodic spin period curve predicted by the orthogonal spin axis case. This suggests that the synodic spin period can be affected by the angle between the spin axis orientation and the PAB. However, further research is required in order to confirm and expand upon these findings.

Simulations of Echostar-2's spin period and angular acceleration variations appear to share some of the characteristics of the observed spin period and angular acceleration variations including; the decreasing overall spin period over time; the decreasing spin period variation amplitude over time; the general shapes of the angular acceleration and spin period variation curves; the momentarily decreasing angular acceleration magnitude in between the curve's two adjacent maxima or two adjacent minima; and the spin period variation plateaus between maxima and minima. The simulations predict that during the 6 years after the final observation, the angular acceleration variation amplitude will continue to decrease, the overall spin period will continue to decrease, and the spin period variation will continue to decrease. Further observations of Echostar-2's spin period

and angular acceleration are strongly suggested in order to verify the predictions and the overall dynamics model.

The free parameters that were assumed in order to produce the angular acceleration and spin period variation curves were mostly reasonably in line with expected and observed physical values, with the exception of one. In order for the spin angular acceleration and spin period variations to resemble the observed curves, the precession rate free parameter had to be set to approximately $720^\text{o} \cdot \text{s}^{-1}$ (4π rad$\cdot \text{s}^{-1}$). This precession rate is approximately twice the rate suggested by the spin axis orientation estimations. The possible reasons for this apparent discrepancy are unknown; however the SRP torque about the satellite's x_b axis might not be precisely zero, as was assumed in this thesis to simplify the Euler rotational motion equations. If the x_b torque component were to be reintroduced, the work required to solve these equations would be significantly more difficult; requiring a significantly longer time to model and simulate.

The estimated canting angle between the solar panels was very low; 0.01^o (36 arc-seconds) when compared with previously reported values. This suggests a very small canting angle, which might be suggesting one of two possibilities. The first possibility is that the manufacturing precision for this satellite was so great that a tolerance of approximately an arc-minute was allowed for the canting angle. The second possibility is that the large amount of assumptions in this thesis have resulted in an underestimation of this canting angle.

The value of the solar constant was assumed to be a constant value over the entire year. Between solar maximum and solar minimum, the solar constant can vary by as much as 0.1%. More importantly, the solar constant can vary by as much as 6% between the Earth's perihelion (in January) and its aphelion (in July). A more statistically meaningful spin period variation curve might be obtained once more accurate specifications are obtained for Echostar-2.

Throughout this thesis, the Sun was assumed to be a point source of light and not the extended light source that it truly is when viewed from the Earth's orbit radius. More robust dynamics models of a box-wing satellite's spin period should include the extended light source model, with the Sun's apparent angular diameter being approximately 0.5^o.

Most of the observations conducted for this thesis were conducted at times when the satellites were not in or near eclipse. Future work could include detailed photometric observations (in broadband, color and I-band) of these satellites when entering, within, and exiting eclipse. Thermal gradients could be causing the satellites to suddenly flex (thermal snapping) and slowly change the satellites' spin periods over subsequent eclipses.

One method of resolving the issues surrounding the estimated spin axis orientation and precession rate is to design an OOS mission that will rendezvous with the inactive Echostar-2 satellite and obtain images of the satellite's attitude over a one year timescale or longer. At the same time, photometric observations of the satellite, similar to those discussed in this thesis, can be conducted over the same timescale. Any discrepancies between the ground-based models, ground-based observations, and space-based observations can be carefully analyzed and quantified such that future research can investigate the possible sources of uncertainty.

Finally, it is strongly suggested that the photometric observations conducted for this thesis research be continued as well as expanded to include; an additional number of box-wing satellites (a larger sample of satellites); color photometric observations (including I-band); spectroscopic observations; satellites of similar and different box-wing designs (other than AS-7000 and HS-601); and satellites with spin periods shorter than 145s and longer then 4315s. Such an effort will likely involve dedicated space surveillance professionals and privately-owned observatories equipped with research-grade color photometric and spectroscopic equipment. This effort could eventually be compiled into a significant database that can be accessed by present and future space surveillance professionals. Such a database might be able to reduce the amount of assumptions that researchers would need to make when modeling and simulating satellites' attitude dynamics.

CHAPTER 8: POTENTIAL BENEFITS OF THIS RESEARCH

Previous box-wing observation projects involving obtaining photometric light curves have revealed some preliminary data concerning light curve morphology and spin period variations. However, the previous research has not been comprehensive enough to answer the difficult questions surrounding their attitude dynamics. The research conducted in this thesis has, for the first time, suggested an end-to-end research program that includes, long term and high resolution photometric observations, spin axis orientation estimation, SRP disturbance torque modeling, and spin period variation simulation and prediction. Further research has the potential to obtain and provide long term and high resolution photometric data for all box-wing GEO satellites in orbit that can be accessed by graduate students, space science professionals and space surveillance professionals to assist them in their research. Frequent observation and modeling will enable space scientists to develop a database that can be used by the space surveillance community to characterize the inactive satellite population for use in OOS and conjunction analysis efforts.

Several OOS demonstration missions by DARPA, NASA, and Orbital ATK have been planned for 2018 and later. It is unclear whether or not they have conducted ground-based photometric observations of the target satellites in advance of these missions. This thesis has shown that such advance observations can provide some qualitative and quantitative information concerning the target satellites' attitude dynamics, including; their average spin periods; their spin period variations (including variation amplitude); their angular accelerations; their spin axis orientations; their spin axis precession; and their precession rates. When designing the robotic servicing modules for OOS, some advance information concerning the target satellites' attitude dynamics can possibly avoid over-design (saving time and money) and can provide some suggestions that can assist in avoiding and mitigating mission risk.

In the event that OOS missions are already taking place, this research can also be beneficial by providing attitude dynamics observations in advance of each OOS mission. An additional advantage is that the ground-based observing facilities can observe the rendezvous and docking (if weather and access permits) and can also observe the real-time spin period variation after docking has taken place.

At the present time, SSA efforts in the GEO population have been restricted to tracking data and space object characterization purposes. Unless the target is very large, radar facilities do not normally observe satellites that are in GEO orbits. The ground-based optical SSA facilities cannot routinely obtain light curves of GEO satellites because their schedules primarily involve obtaining tracking data of thousands of satellites every several days. An additional ground-based optical capability that primarily focuses on satellite photometric observations, similar to the methods described in this thesis, can be used to enhance space object characterization efforts within the box-wing GEO satellite population, thereby creating a more robust SSA capability. This thesis focused on the results of using a single ground-based facility consisting of a single small-aperture telescope and a COTS CCD camera. If this research is duplicated throughout Canada, the US and other nations containing SSN facilities, then a robust satellite photometric observation network can work alongside the existing SSN satellite tracking network in order to provide a more complete picture of our existing satellite population.

Together, the three papers presented within this thesis propose the observation, geometrical modeling, and numerical modeling processes that space scientists can use to observe and study inactive box-wing GEO satellites' long term attitude dynamics. The observations that were conducted can already constitute the beginning of a significant and important photometric database that can be accessed and amended by space science professionals worldwide.

CHAPTER 9:   CONCLUSIONS

Long term and high temporal resolution observations of 11 inactive box-wing GEO satellites were conducted, comprising of five AS-7000 and six HS-601 designs, from March 2012 to January 2016 in order to carefully compare their light curve morphologies and their spin period variations. This thesis has confirmed previously published results of shorter term and lower resolution surveys of Russian and American box-wing satellites and has revealed additional phenomena not previously discovered. Despite similar designs and with few exceptions, the 11 satellites' phase plots appeared diverse with respect to one another. Some of the phase plots of Telstar-401, AMOS-5i, Echostar-2, and Solidaridad-1 appeared to be similar, each consisting of two broad features and two tall, thin features. Despite this finding, it was concluded that phase plots alone could not be used to discriminate between the AS-7000 designs and the HS-601 designs. The unexpected variations of DirecTV-2's (incoherent to coherent) and Paksat-1's (coherent to incoherent) phase plots have indicated that this research requires additional observations, possibly with larger-aperture telescopes and requires color photometry.

Consistently cyclical spin period variations were observed for Telstar-401, AMOS-5i, Echostar-2, Paksat-1, and HGS-1. More secular spin period variations were observed for Intelsat-802, Solidaridad-1, Solidaridad-2, Intelsat-3R, and DirecTV-2. Telstar-402R's spin period variation could not be deemed cyclical or secular due to its apparently incoherent phase plots. The proposed linear relationship between the original four satellites' (Telstar-401, Echostar-2, Solidaridad-1, and HGS-1) spin period variation amplitudes and their average spin periods could not adequately model the additional data.

With respect to Telstar-401 and Echostar-2, correlations were found between full/half period PSRs and spin periods. Telstar-401's PSR minima appeared to correlate in time with its spin period maxima and minima. Telstar-401's PSR maxima appeared to correlate in time with its spin period curve between its spin period extrema and its midpoints between extrema. Some of Echostar-2's PSR maxima appeared to correlate in time with its spin period maxima and minima. Telstar-401's and Echostar-2's power spectrum maxima were observed to increase or decrease as the spin period variation amplitude increased or decreased, respectively. These correlations are considered to be important because they suggest a relationship between Telstar-401's light curve morphology (spin attitude and sunlight geometry being contributors) and its spin period variations.

It was found that some box-wing light curves can vary little over weeks and months, as was observed for Echostar-2. However, light curves can also vary substantially over a single (synodic) spin period, as was observed for Telstar-402R and DirecTV-2. It was also found that a single box-wing's light curve can significantly change from coherent to incoherent (or vice-versa), as was observed for DirecTV-2 and Paksat-1. Therefore, it will be difficult to find consistent similarity between inactive box-wing GEO satellites' broadband photometric behaviors. A likely implication of this is that OOS missions will have to contend with highly variable attitude dynamics with diverse and varying timescales.

This study has provided additional photometric data that can be used to determine attitude dynamics modeling constraints. These data include: the spin period variation timescales, amplitudes, and inflections (and their respective variations); the width and amplitude of noticeable light curve features; the coherence of light curves; and the PSR variations, including PSR comparisons with spin period variations.

This research has found that Echostar-2's most likely steady-state body frame spin axis orientation would correspond to a flat spin about the satellite's largest MOI, inertially oriented perpendicular to Earth's equatorial plane, assuming negligible external torques acting on the system. Echostar-2's maximum MOI corresponds to that principal axis running through the geometric center of the box structure that ideally, is parallel to the surface normals of both its solar panels.

For the first time, the spin axis orientation of an inactive box-wing GEO satellite (specifically,

Echostar-2), was estimated using analytical, geometrical, and simulation modeling. These estimations were verified by comparing simulated light curves with broadband, long term, and high temporal resolution observations conducted from 2012 to 2015. Echostar-2's spin axis orientation was estimated to have been located at 288 ± 13, +77.4 ± 2.7 (prograde spin) or 108 ± 13, -77.4 ± 2.7 (retrograde spin) between September 9 and October 10, 2012. Its spin axis orientation was estimated to have been located at 61.4 ± 5.4, +81.5 ± 4.3 (prograde spin) or 241.4 ± 5.4, -81.5 ± 4.3 (retrograde spin) in March 2013. Similar estimations were performed for August-September 2014, March 2015, and July-October 2015. Echostar-2's spin axis orientation appears to be moving over time, thus strongly supporting a spin axis precession motion.

This research has demonstrated, for the first time, that an inactive box-wing GEO satellite's sidereal spin period can be estimated and that its spin period variation can be simulated, to a first-order approximation, when applying the basic assumptions of its solar panel reflectance and attitude characteristics. Echostar-2's sidereal spin period differs from its synodic spin period. This difference is not substantial because of the satellite's short spin period and the large angle of the satellite's spin axis orientation with respect to its PAB orientation.

Echostar-2's angular acceleration variation and spin period variation have been simulated with very encouraging results. In both cases, the observed trends and amplitude variations over time were successfully simulated by the first-order models discussed. In the case of the angular acceleration, the simulations suggest a slowly decreasing amplitude over time. The simulations also offer an explanation as to why the angular acceleration magnitude decreases momentarily, then increases again at some time between a global maximum and a global minimum.

The simulations presented here successfully show the observed spin period variation's overall decreasing spin period trend as well as the decreasing amplitude trend over four years. The simulations also successfully model (within a first-order approximation) the temporary decrease of the spin period variation rate in between a global maximum and global minimum spin period. The model used a $720^{\circ} \cdot y^{-1}$ precession rate rather than the $360^{\circ} \cdot y^{-1}$ precession rate that was previously reported.

The simulations presented in this thesis included a time frame of 10 years from the date of the first observation of the Echostar-2 satellite (March 11, 2012). The simulations predict that the Echostar-2 satellite's angular acceleration amplitude will continue to slowly decrease. The simulations also predict that the satellite's overall spin period and spin period amplitude will decrease, suggesting that its spin period will vary in a similar manner to the Telstar-401 satellite's spin period variation. The very long, possibly cyclical, trend might indicate a combination of the yearly cyclical spin period observed for Paksat-1 with a very long cyclical trend observed for the Solidaridad-1 satellite.

The solar panel orientations that resulted in the most accurate simulations corresponded to a canting angle of 0.01° and a panel normal orientation of 85° with respect to the body frame of the satellite. A deviation of even 0.001° in the canting angle would result in simulations that are at variance with the angular acceleration and spin period variation observations. The reflectivity free parameters corresponded to 0.6 and 0.1 for the first side and the second side of the two solar panels, respectively.

The results presented in this thesis were the result of several years of high temporal resolution photometric observation, coupled with geometric and numerical modeling. It must be stressed that a long term and temporally high resolution observation schedule is vital to building a simulation model to describe any inactive satellite's attitude dynamics.

REFERENCES

[1] Uhlig, T., Sellmaier, F., and Schmidhuber, M., editors, *Spacecraft Operations*, Springer, 2015, p. 54, doi:10.1007/978-3-7091-1803-0.

[2] Cheruku, D. R., *Satellite Communication*, I.K. International Publishing House Pvt. Ltd., 2009, p. 88.

[3] Papushev, P., Karavaev, Y., and Mishina, M., "Investigations of the evolution of optical characteristics and dynamics of proper rotation of uncontrolled geostationary artificial satellites," *Advances in Space Research*, Vol. 43, February 2009, pp. 1416–1422, doi:10.1016/j.asr.2009.02.007.

[4] Cognion, R., "Rotation rates of inactive satellites near geosynchronous earth orbit," *Proceedings of the 2014 Advanced Maui Optical and Space Surveillance (AMOS) Technologies Conference*, edited by S. Ryan, Maui Economic Development Board, September 2014.

[5] Binz, C., Davis, M., Kelm, B., and Moore, C., "Optical Survey of the Tumble Rates of Retired GEO Satellites," *Proceedings of the 2014 Advanced Maui Optical and Space Surveillance (AMOS) Technologies Conference*, edited by S. Ryan, Maui Economic Development Board, September 2014.

[6] Earl, M. A. and Wade, G. A., "Observations of the Spin-Period Variations of Inactive Box-Wing Geosynchronous Satellites," *Journal of Spacecraft and Rockets*, Vol. 52, 2015, pp. 968–977, doi:10.2514/1.A33077.

[7] Chapman, D. M., editor, *Observer's Handbook 2016*, Vol. 108, Webcom Inc., 2016.

[8] Chartrand, M. R., *Satellite Communications for the Nonspecialist*, Spie Press, 2004, p. 238.

[9] Miller, M. J., Vucetic, B., and Berry, L., editors, *Satellite Communications - Mobile and Fixed Services*, Springer Science+Business Media LLC, 1st ed., 1993, doi:10.1007/978-1-4615-3230-9.

[10] Darrin, A. G. and O'Leary, B. L., editors, *Handbook of Space Engineering, Archaeology, and Heritage*, CRC Press, 2009, p. 73.

[11] Smirnov, N. N., editor, *Space Debris: Hazard Evaluation and Debris*, Taylor and Francis, 2002, p. 114.

[12] Lam, H.-L., Boteler, D. H., Burlton, B., and Evans, J., "Anik-E1 and E2 satellite failures of January 1994 revisited," *Space Weather*, Vol. 10, No. 10, October 2012, doi:10.1029/2012SW000811.

[13] Berchem, J., El-Alaoui, M., and Ashour-Abdalla, M., *Space Weather*, chap. Modeling Extreme Compression of the Magnetosphere: Results From a Global MHD Simulation of the May 4, 1998 Event, American Geophysical Union, Washington, D. C., 2001, pp. 241–248, doi:10.1029/GM125p0241.

[14] Payne, T., Gregory, S., Tombasco, J., Luu, K., and Durr, L., "Satellite Monitoring, Change Detection, and Characterization Using Non-Resolved Electro-Optical Data From a Small Aperture Telescope," *Proceedings of the 2007 Advanced Maui Optical and Space Surveillance (AMOS) Technologies Conference*, edited by S. Ryan, Maui Economic Development Board, September 2007.

[15] Ryan, W. and Ryan, E., "Photometric Studies of Rapidly Spinning Decommissioned GEO Satellites," *Proceedings of the 2015 Advanced Maui Optical and Space Surveillance (AMOS) Technologies Conference*, edited by S. Ryan, Maui Economic Development Board, September 2015.

[16] Earl, M. and Wade, G., "Analysis of the Long-term Photometric Variations of Inactive Box-wing Geosynchronous Satellites," Technical Note Submitted to the AIAA Journal of Spacecraft and Rockets, December 2016, Peer Review in Progress.

[17] Earl, M. A. and Wade, G. A., "The long-term broadband photometric surveys of inactive AS-7000 and HS-601 box-wing geosynchronous satellites," *Proceedings of the 17th Canadian Aeronautic and Space Institute (CASI) "ASTRO2016" Conference*, June 2016.

[18] Lambert, J., Hall, D., Africano, J., Kremeyer, K., and Kervin, P., "Observations of Retired Boeing 376 Spacecraft," *The 2003 AMOS Technical Conference Proceedings*, Maui Economic Development Board, 2003.

[19] Hall, D., Africano, J., Archambeault, D., Birge, B., Witte, D., and Kervin, P., "AMOS Observations of NASA's IMAGE Satellite," *The 2006 AMOS Technical Conference Proceedings*, Maui Economic Development Board, 2006.

[20] Earl, M. and Wade, G., "Estimating the Spin Axis Orientation of the Echostar-2 Box-wing Geosynchronous Satellite," Unpublished. To be Submitted to the COSPAR Advances in Space Research by the fall of 2017.

[21] Skinner, M., Russell, R., Kelecy, T., Gregory, S., Rudy, R., Kim, D., and Crawford, K., "Observations in the thermal IR and visible of a retired satellite in the graveyard orbit, and comparisons to active satellites in GEO," *Acta Astronautica*, Vol. 105, August 2014, pp. 1–10, doi:10.1016/j.actaastro.2014.08.016.

[22] Earl, M. A. and Wade, G. A., "Observation and Analysis of the Apparent Spin Period Variations of Inactive Box-wing Geosynchronous Resident Space Objects," *Proceedings of the 65th International Astronautical Congress, Toronto, Canada*, International Aeronautical Federation, 2014, Vol. 3, 2014, pp. 1753-1767.

[23] Skinner, M., Russell, R., Kelecy, T., Gregory, S., Rudy, R., and Kim, D., "Comparison of thermal IR and visible signatures of graveyard orbit objects," *Proceedings of the 66th International Astronautical Congress, Jerusalem, Israel*, International Astronautical Federation, 2015.

[24] Carlowicz, M. and Lopez, R., *Storms from the Sun: The Emerging Science of Space Weather*, Joseph Henry Press, 2002.

[25] List, M., Bremer, S., Rievers, B., and Selig, H., "Modelling of Solar Radiation Pressure Effects: Parameter Analysis for the MICROSCOPE Mission," *International Journal of Aerospace Engineering*, Vol. 2015, October 2015, pp. 6.

[26] Earl, M. A., "The CASTOR Sputnik 50th anniversary satellite tracking bonanza: project overview and preliminary analysis," *Journal of the Royal Astronomical Society of Canada*, Vol. 102, No. 4, August 2008, pp. 152–158.

[27] Goldstein, H., Poole, C., and Safko, J., *Classical Mechanics*, Addison-Wesley, 3rd ed., 2000.

[28] Symon, K. R., *Mechanics*, Addison-Wesley, 3rd ed., 1971.

[29] Blinn, J. F., "Models of Light Reflection for Computer Synthesized Pictures," *SIGGRAPH '77: Proceedings of the 4th annual conference on computer graphics and interactive techniques*, ACM New York NY, USA, 1977, doi:10.1145/563858.563893.

[30] Torrance, K. E. and Sparrow, E. M., "Theory for Off-Specular Reflection from Roughened Surfaces," *Journal of the Optical Society of America*, Vol. 57, No. 9, September 1967, pp. 1105–1114, doi:10.1364/JOSA.57.001105.

[31] Kopp, G. and Lean, J. L., "A new, lower value of total solar irradiance: Evidence and climate significance," *Geophysical Research Letters*, Vol. 38, No. 1, January 2011, pp. 7 pp., doi:10.1029/2010GL045777.

[32] Pistone, K., Eisenman, I., and Ramanathan, V., "Observational determination of albedo decrease caused by vanishing Arctic sea ice," *Proceedings of the National Academy of Sciences of the United States of America*, Vol. 111, No. 9, March 2014, pp. 3322–3326, doi:10.1073/pnas.1318201111.

[33] Kelemen, C. and Szirmay-Kalos, L., "A Microfacet Based Coupled Specular-Matte BRDF Model with Importance Sampling," *Eurographics Conference Proceedings*, 2001, Short Presentations.

[34] Gilmore, D. G., editor, *Spacecraft Thermal Control Handbook - Volume 1: Fundamental Technologies*, The Aerospace Press, 2nd ed., 2002, pp. 140-141.

[35] Wertz, J. R., *Orbit and Constellation Design and Management*, Microcosm Press, 2nd ed., 2009, p. 171.

[36] Taylor, J. R., *Classical Mechanics*, University Science Books, 2005, pp. 381-384.

[37] Reddy, M. R., "Space solar cells - tradeoff analysis," *Solar Energy Materials and Solar Cells*, Vol. 77, No. 2, May 2003, pp. 175–208, doi:10.1016/S0927-0248(02)00320-3.

APPENDIX A - Echostar-2 Inertia Tensor

Echostar-2 was assumed to be comprised of a central uniform density cube (the "box"), flanked by two large, flat, and uniform density plates (the "wings"), as illustrated in Fig. 46. The masses and dimensions of these critical components are listed in Table 14. The majority of the satellite's specifications is considered proprietary information, therefore the referenced values and their corresponding uncertainties were assumed to be correct. The communications dishes were omitted from the model because they were assumed to be negligible contributors to the satellite's inertia tensor.
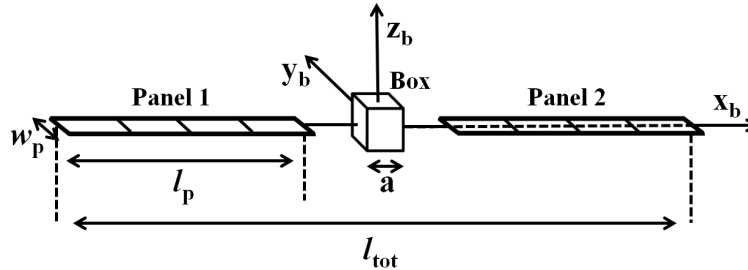
Figure 46   Echostar-2 box-wing satellite model

Table 14   Echostar-2 model masses and dimensions

Specification	Symbol	Value	Notes and Assumptions
Expected lifetime	N/A	12y [88]	
Active lifetime	N/A	11.8y [89] [90]	Negligible maneuvering fuel
Solar panel area density	σ_p	2.25 kg·m^{-2} [37]	Black silicon
Wing span	l_{tot}	23.9±0.5 m [6]	Both deployed solar panels
Solar panel length	l_p	8.5±0.2 m [6]	Single solar panel
Solar panel width	w_p	3.1±0.1 m [6]	Single solar panel
Box side length	a	2.3±0.2 m [6]	Ideal cube
On-orbit mass	m_{BOL}[91]	2885±50 kg [92]	Orbit insertion fuel depleted
Dry mass	m_{dry}	2000±50 kg [6]	Satellite mass without fuel
On-orbit fuel mass	m_{fBOL}	885±70 kg	On-orbit mass - dry mass
Estimated fuel mass remaining	m_{fEOL}	14±98 kg	After malfunction
Estimated total mass	m_{tot}	2020±80 kg	Constant fuel consumption rate
Solar panel mass	m_p	60±2 kg [6]	Single solar panel
Box mass	m_{box}	1900±80 kg [6]	total mass - panel masses

The diagonal inertia tensor components (I_{xx}, I_{yy}, and I_{zz}) were estimated with Eqs. (44), (45), and (46), respectively [6]. Note that despite the uncertainty of the three diagonal components,

---

[88]Satbeams SPRL, Echostar-2, http://www.satbeams.com/satellites?norad=24313, Accessed 10/30/16.

[89]JFCC SPACE/J3, Space Track, https://www.space-track.org, Accessed 10/30/16.

[90]Bergin, C., "Sea Launch lofts EchoStar 11 - EchoStar 2 dies on orbit," https://www.nasaspaceflight.com/2008/07/sea-launch-lofts-echostar-11-echostar-2-dies-on-orbit, July 2008, Accessed 10/30/16.

[91]Beginning of Life

[92]Satbeams SPRL, Echostar-2, http://www.satbeams.com/satellites?norad=24313, Accessed 10/30/16.

the I_{zz} component is always greater than the I_{yy} component, which is always greater than the I_{xx} component. All of the inertia products (off-diagonal inertia tensor components) were assumed to be negligible compared to the diagonal components. The MOI of a uniform density cube is identical for all axes passing through the cube's geometric center. This means that the inertia tensor of the model shown in Fig. 46 will be the same no matter what the orientation of the solar panels about the x_b axis, as long as this axis remains in the same plane as the solar panels.

The true MOI of Echostar-2 might vary as the satellite spins because of the sloshing of any remaining maneuvering fuel. However, Echostar-2 became inactive nearly 12 years into its expected 12-year lifetime, therefore the amount of maneuvering fuel remaining was assumed to be negligible.

$$I_{xx} = \frac{1}{6} \left[m_{box} a^2 + m_p (w_p)^2 \right] \tag{44}$$

$$I_{yy} = \frac{1}{6} \left\{ m_{box} a^2 + m_p \left[4(l_p)^2 + 3l_{tot}(l_{tot} - 2l_p) \right] \right\} \tag{45}$$

$$I_{zz} = \frac{1}{6} \left\{ m_{box} a^2 + m_p \left[4(l_p)^2 + 3l_{tot}(l_{tot} - 2l_p) + (w_p)^2 \right] \right\} \tag{46}$$

$$\mathbf{I} = \begin{bmatrix} 1770 \pm 300 & 0 & 0 \\ 0 & 9510 \pm 630 & 0 \\ 0 & 0 & 9610 \pm 630 \end{bmatrix} \text{kg} \cdot \text{m}^2 \tag{47}$$

APPENDIX B - Euler Coordinate Transformations

Providing that two coordinate systems share the same origin, the Euler x-convention coordinate transformation relates one orthogonal coordinate system to the other [27, 28]. The x-convention involves a rotation of angle ϕ about the original coordinate system's z-axis, a second rotation of angle θ about the new coordinate system's x-axis (called the line of nodes), and finally a third rotation of angle ψ about the new z-axis, as described in [27]. Note that only the coordinate system is rotating in each case and not the body in question.

The original coordinate system is a 3x1 matrix called A, containing the components of a unit vector x, y, and z. The resultant coordinate system is a 3x1 matrix called A', containing the components of the resulting unit vector x', y', and z'. The first, second, and third rotations are 3x3 matrices called B, C, and D, as shown in Eq. (48). The matrix form of the general coordinate transformation is shown in Eq. (49).

$$\mathbf{A'} = \mathbf{DCBA} \tag{48}$$

$$\begin{bmatrix} x' \\ y' \\ z' \end{bmatrix} = \begin{bmatrix} \cos(\psi) & \sin(\psi) & 0 \\ -\sin(\psi) & \cos(\psi) & 0 \\ 0 & 0 & 1 \end{bmatrix} \begin{bmatrix} 1 & 0 & 0 \\ 0 & \cos(\theta) & \sin(\theta) \\ 0 & -\sin(\theta) & \cos(\theta) \end{bmatrix} \begin{bmatrix} \cos(\phi) & \sin(\phi) & 0 \\ -\sin(\phi) & \cos(\phi) & 0 \\ 0 & 0 & 1 \end{bmatrix} \begin{bmatrix} x \\ y \\ z \end{bmatrix} \tag{49}$$

The coordinate systems' unit vector components can be represented with respect to their spherical coordinates β, γ (for the original coordinate system) and β', γ' (for the resulting coordinate system), as shown in Eqs. (50), (51), and (52). Substituting these three equations into Eq. (49) and expanding results in the general Eulerian coordinate transformation equations shown in Eqs. (53), (54), and (55).

Equations (54) and (55) are used to relieve the quadrant ambiguity of the resulting β' coordinate. Its conditions are shown in Eq. (56).

$$x = \cos(\beta)\cos(\gamma) \quad \text{and} \quad x' = \cos(\beta')\cos(\gamma') \tag{50}$$

$$y = \sin(\beta)\cos(\gamma) \quad \text{and} \quad y' = \sin(\beta')\cos(\gamma') \tag{51}$$

$$z = \sin(\gamma) \quad \text{and} \quad z' = \sin(\gamma') \tag{52}$$

$$\sin(\gamma') = \cos(\theta)\sin(\gamma) - \sin(\theta)\sin(\beta - \phi)\cos(\gamma) \tag{53}$$

$$\sin(\beta') = \frac{\cos(\psi)\left[\cos(\theta)\cos(\gamma)\sin(\beta - \phi) + \sin(\theta)\sin(\gamma)\right] - \sin(\psi)\cos(\gamma)\cos(\beta - \phi)}{\cos(\gamma')} \tag{54}$$

$$\cos(\beta') = \frac{\sin(\psi)\left[\cos(\theta)\cos(\gamma)\sin(\beta - \phi) + \sin(\theta)\sin(\gamma)\right] + \cos(\psi)\cos(\gamma)\cos(\beta - \phi)}{\cos(\gamma')} \tag{55}$$

$$\beta' = \begin{cases} 180° - \sin^{-1}\left[\sin(\beta')\right] & \text{if } \cos(\beta') < 0; \\ 360° + \sin^{-1}\left[\sin(\beta')\right] & \text{if } \cos(\beta') > 0 \text{ and } \sin(\beta') < 0; \text{ and} \\ \sin^{-1}\left[\sin(\beta')\right] & \text{otherwise.} \end{cases} \tag{56}$$

A   Sun: Ecliptical to Equatorial

In this paper, the Sun's initial coordinate system was considered to be geocentric ecliptical, consisting of ecliptic longitude (λ_{sun}) and ecliptic latitude (β_{sun}). The required coordinates after transformation is the equatorial RA (α_{sun}) and dec (δ_{sun}). Therefore, the corresponding β and γ coordinates in the Eulerian transformations are shown in Eq. (57).

$$\beta = \lambda_{\text{sun}}, \quad \gamma = \beta_{\text{sun}}, \quad \beta' = \alpha_{\text{sun}}, \quad \text{and} \quad \gamma' = \delta_{\text{sun}} \tag{57}$$

The θ rotation angle in the Sun's Eulerian transformation is the obliquity of the ecliptic plane

(ϵ). The ϵ angle is rotated according to a right-handed sense about the line of nodes. In order to accomplish this for an ecliptical to equatorial transformation, both the ϕ and ψ rotation angles have to be 180º in order for the line of nodes to be in the right position for the transformation. This ecliptical to equatorial coordinate transformation can also be accomplished with the inverse Euler transformation of the combined DCB matrices shown in Eq. (49). The angles required to perform the Sun coordinate transformation are shown in Eq. (58). Finally, the Sun's equatorial coordinates are determined from its ecliptical coordinates with Eqs. (59), (60), and (61). The conditions to relieve the α_{sun} quadrant ambiguity are the same as shown in Eq. (56), but replacing β' with α_{sun}, as shown in Eq. (57).

A plot of the Sun's RA and dec coordinates as seen from the Earth over one year is plotted in Fig. 47. The plot is based on Eqs. (59), (60), and (61) with the Sun's ecliptical coordinates as the initial arguments. The plot's origin point (0, 0) refers to the Vernal Equinox.

$$\beta_{\text{sun}} = 0, \quad \phi = 180º, \quad \theta = \epsilon, \quad \text{and} \quad \psi = 180º \tag{58}$$

$$\sin(\delta_{\text{sun}}) = \sin(\epsilon)\sin(\lambda_{\text{sun}}) \tag{59}$$

$$\sin(\alpha_{\text{sun}}) = \frac{\cos(\epsilon)\sin(\lambda_{\text{sun}})}{\cos(\delta_{\text{sun}})} \tag{60}$$

$$\cos(\alpha_{\text{sun}}) = \frac{\cos(\lambda_{\text{sun}})}{\cos(\delta_{\text{sun}})} \tag{61}$$
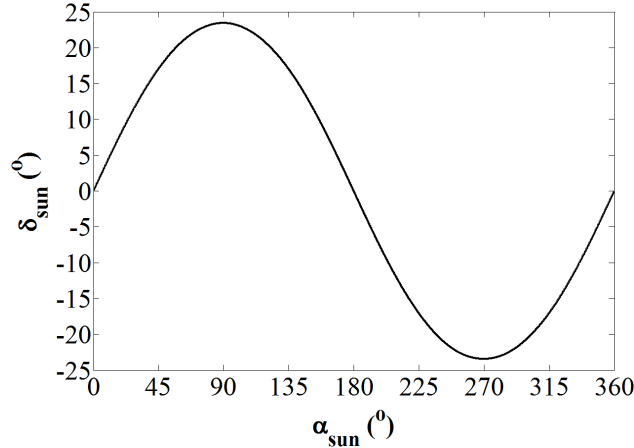
Figure 47   Sun's RA and dec seen from Earth over one year

B   Satellite: Body Frame to Spin Frame

A satellite surface's body frame unit vector coordinates (α_{b} and δ_{b}) can be transformed to the inertial equatorial coordinate system (α_{eq} and δ_{eq}) by performing two steps. The first step is to transform the body frame coordinates to the satellite's spin axis coordinates (α_{ω} and δ_{ω}), as illustrated in Fig. 48. The corresponding β and γ coordinates in the Eulerian transformations are shown in Eq. (62). The three Euler angles required for this transformation were defined (in the order of rotation performed), to be ϕ_{b}, θ_{b} (shown in Fig. 48), and ψ_{b}. The ψ_{b} rotation angle is result of the satellite's spin about the spin axis and therefore only depends on the time elapsed and the satellite's spin period.

The satellite surface's spin frame coordinates are determined from its body frame coordinates with Eqs. (63), (64), and (65). The conditions to relieve the α_{ω} quadrant ambiguity are the same as shown in Eq. (56), but replacing β' with α_{ω}, as shown in Eq. (62).

109
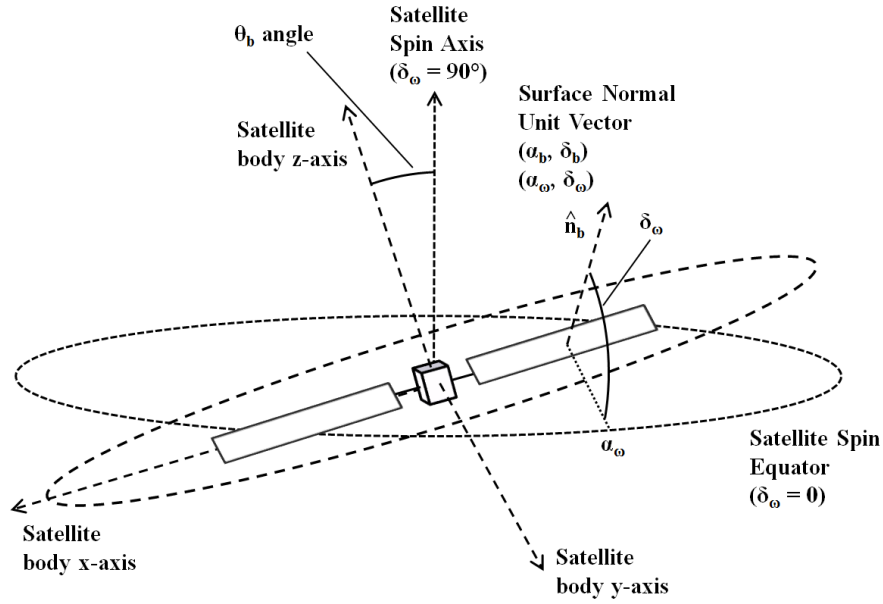
Figure 48 Surface normal unit vector in body frame and spin frame

$$\beta = \alpha_{\mathrm{b}}, \quad \gamma = \delta_{\mathrm{b}}, \quad \beta' = \alpha_{\omega}, \quad \text{and} \quad \gamma' = \delta_{\omega} \tag{62}$$

$$\sin(\delta_{\omega}) = \cos(\theta_{\mathrm{b}})\sin(\delta_{\mathrm{b}}) - \sin(\theta_{\mathrm{b}})\sin(\alpha_{\mathrm{b}} - \phi_{\mathrm{b}})\cos(\delta_{\mathrm{b}}) \tag{63}$$

$$\sin(\alpha_{\omega}) = \frac{\cos(\psi_{\mathrm{b}})\left[\cos(\theta_{\mathrm{b}})\sin(\alpha_{\mathrm{b}} - \phi_{\mathrm{b}})\cos(\delta_{\mathrm{b}}) + \sin(\theta_{\mathrm{b}})\sin(\delta_{\mathrm{b}})\right] - \sin(\psi_{\mathrm{b}})\cos(\alpha_{\mathrm{b}} - \phi_{\mathrm{b}})\cos(\delta_{\mathrm{b}})}{\cos(\delta_{\omega})} \tag{64}$$

$$\cos(\alpha_{\omega}) = \frac{\sin(\psi_{\mathrm{b}})\left[\cos(\theta_{\mathrm{b}})\sin(\alpha_{\mathrm{b}} - \phi_{\mathrm{b}})\cos(\delta_{\mathrm{b}}) + \sin(\theta_{\mathrm{b}})\sin(\delta_{\mathrm{b}})\right] + \cos(\psi_{\mathrm{b}})\cos(\alpha_{\mathrm{b}} - \phi_{\mathrm{b}})\cos(\delta_{\mathrm{b}})}{\cos(\delta_{\omega})} \tag{65}$$

C Satellite: Spin Frame to Equatorial Frame

The second step to transform a satellite surface's normal unit vector coordinates to the inertial equatorial frame is to transform the resulting spin axis frame coordinates (determined in Section B) to the equatorial coordinate system, as illustrated in Fig. 49. The corresponding β and γ coordinates in the Eulerian transformations are shown in Eq. (66). The three Euler angles required for this transformation were defined to be (in the order of rotation performed), ϕ_{ω}, θ_{ω} (shown in Fig. 49), and ψ_{ω}. The ϕ_{ω} rotation angle is the satellite's spin about the spin axis and therefore depends on the time elapsed and the satellite's spin period.

The satellite surface's equatorial coordinates are determined with Eqs. (67), (68), and (69). The conditions to relieve the α_{eq} quadrant ambiguity are the same as shown in Eq. (56), but replacing β' with α_{eq}, as shown in Eq. (66).

$$\beta = \alpha_{\omega}, \quad \gamma = \delta_{\omega}, \quad \beta' = \alpha_{\mathrm{eq}}, \quad \text{and} \quad \gamma' = \delta_{\mathrm{eq}} \tag{66}$$
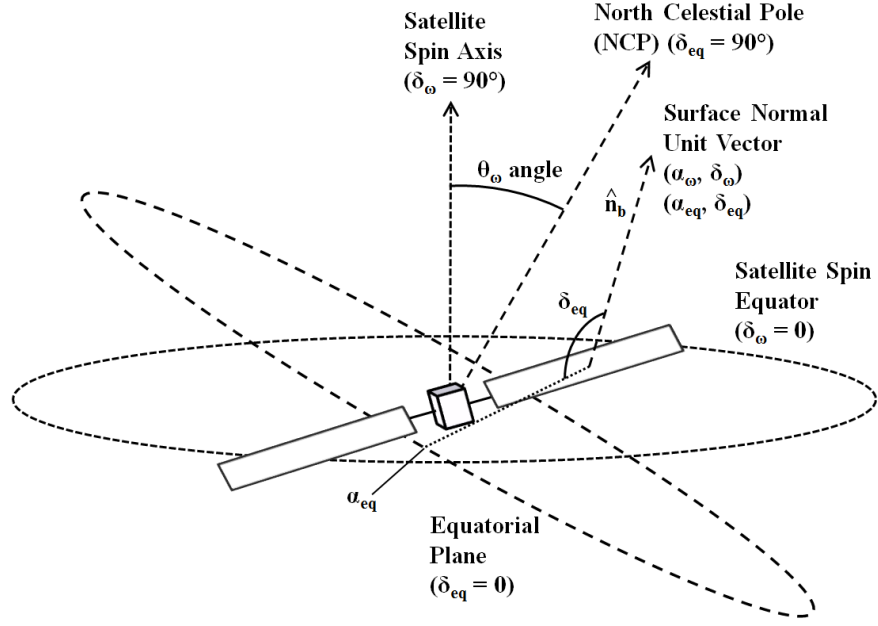
Figure 49   Surface normal unit vector in spin frame and equatorial frame

$$\sin(\delta_{\text{eq}}) = \cos(\theta_\omega)\sin(\delta_\omega) - \sin(\theta_\omega)\sin(\alpha_\omega - \phi_\omega)\cos(\delta_\omega) \tag{67}$$

$$\sin(\alpha_{\text{eq}}) = \frac{\cos(\psi_\omega)\left[\cos(\theta_\omega)\sin(\alpha_\omega - \phi_\omega)\cos(\delta_\omega) + \sin(\theta_\omega)\sin(\delta_\omega)\right] - \sin(\psi_\omega)\cos(\alpha_\omega - \phi_\omega)\cos(\delta_\omega)}{\cos(\delta_{\text{eq}})} \tag{68}$$

$$\cos(\alpha_{\text{eq}}) = \frac{\sin(\psi_\omega)\left[\cos(\theta_\omega)\sin(\alpha_\omega - \phi_\omega)\cos(\delta_\omega) + \sin(\theta_\omega)\sin(\delta_\omega)\right] + \cos(\psi_\omega)\cos(\alpha_\omega - \phi_\omega)\cos(\delta_\omega)}{\cos(\delta_{\text{eq}})} \tag{69}$$

APPENDIX C - Critical Sunlight Reflectance Angles

A   Unit Vectors and Coordinates

For each critical satellite surface considered in this paper, a solar unit vector ($\hat{n}_{sun}$), a surface normal unit vector ($\hat{n}_b$) (described in Appendix B), an observer unit vector ($\hat{n}_{obs}$), and a PAB unit vector ($\hat{n}_{PAB}$) have been defined. An illustration of each of these unit vectors is shown in Fig. 50.

The $\hat{n}_{sun}$ unit vector is directed from the satellite surface to the Sun's location, as shown in Fig. 50. This unit vector is assumed to be the same for all satellite surfaces at an instantaneous time because of the negligible parallax from surface to surface due to the very large range of the Sun from the satellite. The equatorial coordinates of the Sun were defined as α_{sun} and δ_{sun}. The $\hat{n}_b$ unit vector is always orthogonal to the specific satellite surface, as shown in Fig. 50 with equatorial coordinates of α_{eq} and δ_{eq}, as described in Appendix B. The $\hat{n}_{obs}$ unit vector is directed from the specific satellite surface to the observer, as shown in Fig. 50. The equatorial coordinates of the observer were defined as α_{obs} and δ_{obs}. The observer's equatorial coordinates with respect to the satellite are related to the satellite's equatorial coordinates with respect to the observer (α_{sat} and δ_{sat}) by Eq. (70). The $\hat{n}_{PAB}$ unit vector is described in Section B.

The solar incidence angle (ξ) represents the angle at the surface subtended by the Sun unit vector and the surface normal unit vector. This angle is determined by the dot product of $\hat{n}_{sun}$ and $\hat{n}_{eq}$, as shown in Eq. (71). The solar incidence angle is important for both the diffuse and specular reflection components. The angle brackets denote the positive angle condition shown in Eq. (72).

The "surface observation angle" (η) was defined as the angle at the satellite surface subtended by the surface normal unit vector and the observer unit vector, as shown in Fig. 50 (a). It was determined with Eq. (73) and the condition defined in Eq. (72).

a) Sun, surface normal, and observer

b) PA, PAB, and Ψ angle
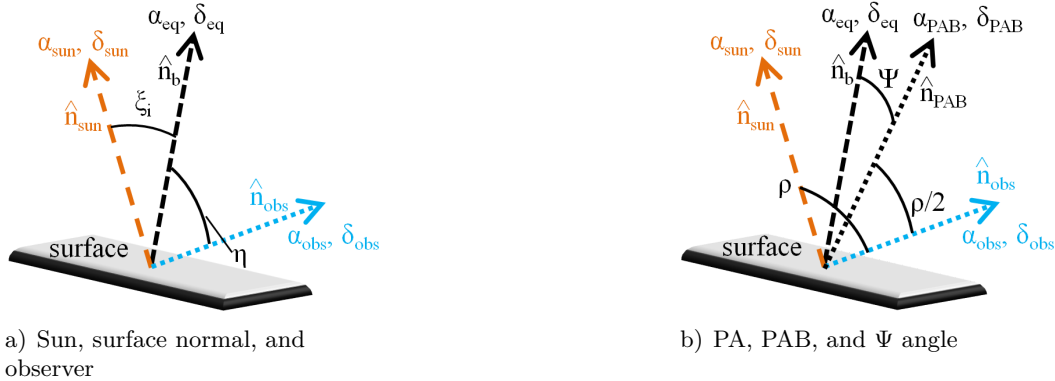
Figure 50   Sunlight reflectance angles

$$\alpha_{obs} = 180^o - \alpha_{sat} \quad \text{and} \quad \delta_{obs} = -\delta_{sat} \tag{70}$$

$$\cos(\xi) = \langle \hat{n}_{sun} \cdot \hat{n}_{eq} \rangle = \langle \sin(\delta_{sun})\sin(\delta_{eq}) + \cos(\delta_{sun})\cos(\delta_{eq})\cos(\alpha_{sun} - \alpha_{eq}) \rangle \tag{71}$$

$$\langle x \rangle = \begin{cases} x & \text{if} \quad x > 0; \text{and} \\ 0 & \text{otherwise.} \end{cases} \tag{72}$$

$$\cos(\eta) = \langle \hat{n}_{eq} \cdot \hat{n}_{obs} \rangle = \langle \sin(\delta_{eq})\sin(\delta_{obs}) + \cos(\delta_{eq})\cos(\delta_{obs})\cos(\alpha_{eq} - \alpha_{obs}) \rangle \tag{73}$$

B   Phase Angle and Phase Angle Bisector

The PA (ρ) is the instantaneous angle at the satellite, subtended by the solar unit vector ($\hat{n}_{sun}$) and the observer unit vector ($\hat{n}_{obs}$), as shown in Fig. 50 (b). The PA is determined by the dot

product of these two unit vectors, as described in Eq. (74).

$$\cos(\rho) = \hat{n}_{\text{sun}} \cdot \hat{n}_{\text{obs}} = \sin(\delta_{\text{sun}})\sin(\delta_{\text{obs}}) + \cos(\delta_{\text{sun}})\cos(\delta_{\text{obs}})\cos(\alpha_{\text{sun}} - \alpha_{\text{obs}}) \tag{74}$$

The PAB divides the PA into two equal half-angles of 0.5ρ, as shown in Fig. 50 (b). Therefore, the PAB unit vector $\hat{n}_{\text{PAB}}$ lies on a plane, in between the $\hat{n}_{\text{sun}}$ and the $\hat{n}_{\text{obs}}$ unit vectors, as shown in Fig. 50. The PAB unit vector's equatorial coordinates are determined from its Cartesian coordinates (x_{PAB}, y_{PAB}, and z_{PAB}) (determined with Eqs. (75), (76), and (77)) with Eqs. (78), (79), and (80). The conditions to relieve the α_{PAB} quadrant ambiguity are the same as shown in Eq. (56) (in Appendix B), but replacing β' with α_{PAB}.

An observer will see the maximum specular reflection brightness from a satellite's surface when the angle Ψ between the surface's PAB unit vector and the surface normal unit vector (shown in in Fig. 50 (b)) is 0, as long as the surface's PAB unit vector lies between the Sun unit vector and the observer unit vector as defined on the surface. The Ψ angle is determined with the dot product of the $\hat{n}_{\text{eq}}$ and the $\hat{n}_{\text{PAB}}$ unit vectors, as shown in Eq. (81).

$$x_{\text{PAB}} = 0.5\left[\cos\alpha_{\text{sun}}\cos\delta_{\text{sun}} + \cos\alpha_{\text{obs}}\cos\delta_{\text{obs}}\right] \tag{75}$$

$$y_{\text{PAB}} = 0.5\left[\sin\alpha_{\text{sun}}\cos\delta_{\text{sun}} + \sin\alpha_{\text{obs}}\cos\delta_{\text{obs}}\right] \tag{76}$$

$$z_{\text{PAB}} = 0.5\left[\sin\delta_{\text{sun}} + \sin\delta_{\text{obs}}\right] \tag{77}$$

$$\delta_{\text{PAB}} = \sin^{-1}\left[\frac{z_{\text{PAB}}}{\sqrt{0.5\left[1 + \cos(\alpha_{\text{sun}} - \alpha_{\text{obs}})\cos(\delta_{\text{sun}})\cos(\delta_{\text{obs}}) + \sin(\delta_{\text{sun}})\sin(\delta_{\text{obs}})\right]}}\right] \tag{78}$$

$$\sin\alpha_{\text{PAB}} = \frac{y_{\text{PAB}}}{\sqrt{(x_{\text{PAB}})^2 + (y_{\text{PAB}})^2}} \tag{79}$$

$$\cos\alpha_{\text{PAB}} = \frac{x_{\text{PAB}}}{\sqrt{(x_{\text{PAB}})^2 + (y_{\text{PAB}})^2}} \tag{80}$$

$$\cos\Psi = \hat{n}_{\text{eq}} \cdot \hat{n}_{\text{PAB}} = \sin\delta_{\text{eq}}\sin\delta_{\text{PAB}} + \cos\delta_{\text{eq}}\cos\delta_{\text{PAB}}\cos(\alpha_{\text{PAB}} - \alpha_{\text{eq}}) \tag{81}$$

APPENDIX D - Spin Axis Plane Intersection

A   Spin Axis Plane Coordinates

When a maximum specular reflection flux is observed from a location, some reflective surface's PAB unit vector and its surface normal unit vector are aligned (Ψ angle is 0). If the surface was rotated about its normal unit vector at the time of the specular reflection, the specular reflection should not disappear. If two surfaces that are parallel to each other are observed to exhibit alternating maximum specular reflections, then the spin axis is likely located somewhere in a plane that is perpendicular to both surface normal unit vectors and the PAB unit vector, as shown in Fig. 51. The dot product of the PAB unit vector and the spin axis unit vector ($\hat{n}_{\text{spin}}$) is therefore zero, as shown in Eq. (82).
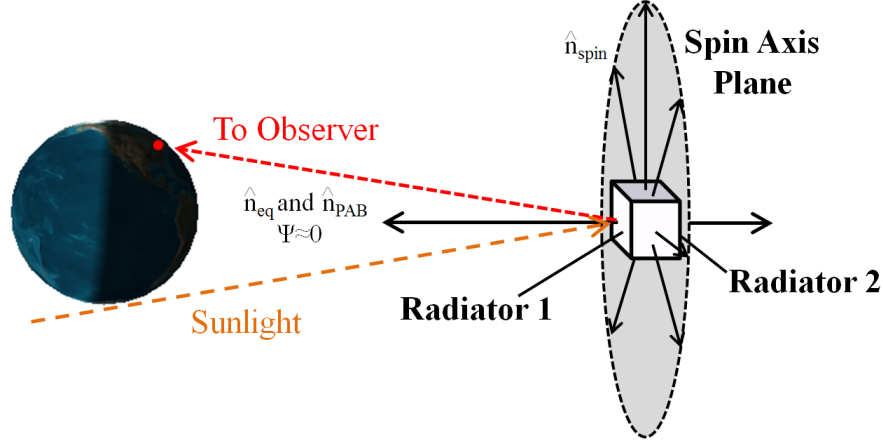

Figure 51   Spin axis plane perpendicular to a surface's PAB unit vector during specular reflection

Since the two unit vectors are orthogonal, the spin axis plane will consist of all RA angles from 0 to 360º. Equation (82) can be solved for δ_{spin} by dividing by $\cos(\delta_{\text{PAB}})$ and $\cos(\delta_{\text{spin}})$ to yield Eq. (83).

$$\hat{n}_{\text{PAB}} \cdot \hat{n}_{\text{spin}} = 0 = \sin(\delta_{\text{PAB}}) \sin(\delta_{\text{spin}}) + \cos(\delta_{\text{PAB}}) \cos(\delta_{\text{spin}}) \cos(\alpha_{\text{PAB}} - \alpha_{\text{spin}}) \tag{82}$$

$$\tan(\delta_{\text{spin}}) = -\frac{\cos(\alpha_{\text{PAB}} - \alpha_{\text{spin}})}{\tan(\delta_{\text{PAB}})} \tag{83}$$

Although Eq. (83) can be used easily, there can be singularity difficulties because of the two tangent functions. For instance, if the PAB unit vector is directed along the equatorial plane ($\delta_{\text{PAB}} = 0$) or along either of the celestial poles ($\delta_{\text{PAB}} = +90$º or -90º), then Eq. (83) will not work. For this reason, Eq. (83) was reconfigured to contain only sine and cosine terms.

Equation (84) results when the tangent terms of Eq. (83) are decomposed into their respective sine and cosine terms, the $\cos(\delta_{\text{spin}})$ term is expressed in terms of the Pythagorean trigonometric identity, and the entire resulting expression is squared. Equation (85) shows the final form after like terms are collected and a final Pythagorean trigonometric identity is applied.

$$\frac{\sin^2(\delta_{\text{spin}})}{1 - \sin^2(\delta_{\text{spin}})} = \left[\frac{\cos(\delta_{\text{PAB}}) \cos(\alpha_{\text{PAB}} - \alpha_{\text{spin}})}{\sin(\delta_{\text{PAB}})} \right]^2 \tag{84}$$

$$\sin(\delta_{\text{spin}}) = -\left[\frac{\cos(\delta_{\text{PAB}}) \cos(\alpha_{\text{PAB}} - \alpha_{\text{spin}})}{\sqrt{1 - \cos^2(\delta_{\text{PAB}}) \sin^2(\alpha_{\text{PAB}} - \alpha_{\text{spin}})}} \right] \tag{85}$$

B Spin Axis Plane Intersection Coordinates

If specular reflections are observed for some amount of time, the PAB unit vector will move according to the motion of the Earth in its orbit and also according to the satellite's motion with respect to the observer on the Earth. There will be two spin axis planes corresponding to two PAB unit vectors. Assuming that the spin axis orientation's equatorial coordinates are not varying over the time between the two specular reflection observations, the two spin axis planes will intersect at two specific equatorial coordinates that are 180° apart from one another. One of these locations refers to the prograde spin axis (positive angular velocity dec) and the other refers to the retrograde spin axis (negative angular velocity dec).

The two potential spin axis orientations can be determined analytically by dividing Eq. (83) corresponding to the first spin axis plane by the same equation corresponding to the second spin axis plane, as shown in Eq. (86). The α_{spin1} and α_{spin2} terms and the δ_{spin1} and δ_{spin2} terms are equal to each other at the two intersection points. As a result, these variables' number subscripts can be dropped and the tangent ratio on the left hand side of Eq. (86) is equal to 1, as shown in Eq. (87). However, the two PAB unit vector coordinates are still different from each other, mainly because of the Earth's orbit motion.

$$\frac{\tan(\delta_{\mathrm{spin1}})}{\tan(\delta_{\mathrm{spin2}})} = \frac{\tan(\delta_{\mathrm{PAB2}})\cos(\alpha_{\mathrm{PAB1}} - \alpha_{\mathrm{spin1}})}{\tan(\delta_{\mathrm{PAB1}})\cos(\alpha_{\mathrm{PAB2}} - \alpha_{\mathrm{spin2}})} \tag{86}$$

$$1 = \frac{\tan(\delta_{\mathrm{PAB2}})\cos(\alpha_{\mathrm{PAB1}} - \alpha_{\mathrm{spin}})}{\tan(\delta_{\mathrm{PAB1}})\cos(\alpha_{\mathrm{PAB2}} - \alpha_{\mathrm{spin}})} \tag{87}$$

As with Eq. (83), the tangent terms in Eq. (87) will cause problems at singularities. All of the tangent terms in Eq. (87) were decomposed into their respective sine and cosine terms, as shown in Eq. (88). The cosines of the RA differences were then expanded, like terms were gathered and then solved for $\sin(\alpha_{\mathrm{spin}})$ resulting in Eq. (89). The dec of the intersection point can be determined from the α_{spin} coordinate using Eq. (85).

$$1 = \frac{\sin(\delta_{\mathrm{PAB2}})\cos(\delta_{\mathrm{PAB1}})\cos(\alpha_{\mathrm{PAB1}} - \alpha_{\mathrm{spin}})}{\sin(\delta_{\mathrm{PAB1}})\cos(\delta_{\mathrm{PAB2}})\cos(\alpha_{\mathrm{PAB2}} - \alpha_{\mathrm{spin}})} \tag{88}$$

$$\sin(\alpha_{\mathrm{spin}}) = \frac{\tau_{21}\cos(\alpha_{\mathrm{PAB1}}) - \tau_{12}(\alpha_{\mathrm{PAB2}})}{\sqrt{\tau_{12}^2 + \tau_{21}^2 - 2\tau_{12}^2\tau_{21}^2\cos(\alpha_{\mathrm{PAB1}} - \alpha_{\mathrm{PAB2}})}}; \quad \text{where} \quad \tau_{\mathrm{ij}} = \sin(\delta_{\mathrm{PABi}})\cos(\delta_{\mathrm{PABj}}) \tag{89}$$

APPENDIX E - Least Squares Fitting of Simulated Light Curves

A light curve simulation consists of a plot of estimated broadband magnitudes (m_b) versus spin period percentages (spin percentages) ranging from 0 to 100%, representing one complete synodic spin period. When a simulated light curve is compared to an observed light curve, the two curves will not likely be in phase with one another, as shown in Fig. 52. Comparisons between out of phase light curves would likely be more difficult. Bringing the simulated and observed light curves in phase with one another will therefore enable easier comparison.

Figure 52 (a) illustrates how easily the simulated light curve (dashed) can be out of phase with the observed light curve (scattered circles). Figure 52 (b) shows the zoomed bottom-left corner of Fig. 52 (a) to show the difference between a simulated broadband magnitude (labeled m_{sim} and indicated with a dot) and an observed broadband magnitude (labeled m_{obs} and indicated with a rectangle). Figure 52 (b) illustrates that an m_{sim} value cannot be compared to a single m_{obs} value when using the scatter of observations alone. However, the m_{obs} values can be binned in a histogram, with each bin having a specific % size (b). In each bin, an average m_{obs} value, defined as m_{aveobs}, can be compared to each single m_{sim} value corresponding to a % value (c) in the center of each bin. Figure 52 (c) shows the comparison of the simulated curve with an averaged observed curve with a bin size of 0.3%. When averaged, each individual m_{aveobs} value can be compared to a corresponding m_{sim} value.
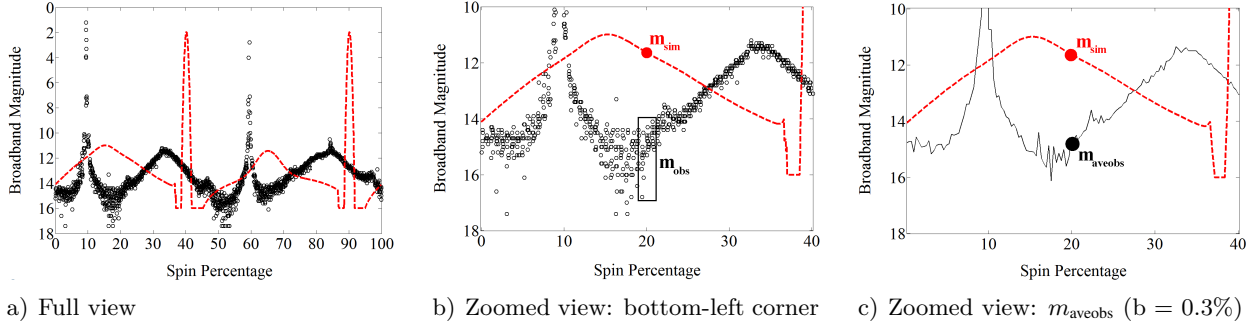

a) Full view   b) Zoomed view: bottom-left corner   c) Zoomed view: m_{aveobs} (b = 0.3%)

Figure 52   Simulated light curve out of phase with an observed light curve

A magnitude residual (ϵ_B) consists of the difference between the broadband magnitude of a simulated light curve (m_{sim}) and the broadband magnitude of the average observed light curve (m_{aveobs}) corresponding to a specific bin value (c) in the observed curve histogram, as shown in Eq. (90). The entire light curve will consist of N bins, determined by the chosen bin size (b) with Eq. (91). A bin's central value (c) is determined by the bin size and the bin number (B) with Eq. (92). The squares of the residuals corresponding to all specific bins are summed over all N bins, as shown in Eq. (93). The inverse of the least squares sum (J) is determined in Eq. (93) to more conveniently locate the best fit using a larger number (as opposed to a smaller number) and to more easily discriminate between smaller residual sums.

$$\epsilon_B = m_{sim} - m_{aveobs} \tag{90}$$

$$N = \frac{100\%}{b} \tag{91}$$

$$c = 0.5b + (B - 1) \tag{92}$$

$$J = \left[\sum_{B=1}^{N} (\epsilon_B)^2 \right]^{-1} \tag{93}$$

After a specific residual sum corresponding to a specific phase has been completed, the broad-

116

band magnitudes corresponding to specific bins in the simulated light curve are all shifted in phase by one bin number, thus shifting the entire simulated light curve by one bin size. Equation (93) is then performed again using the shifted magnitude values. This process is repeated until the original first phase that was analyzed is reached once again (100% phase shift). The simulated light curve phase that corresponds to the largest J value in Eq. (93) is considered to be the best fit to the observed average light curve. The simulated light curve is plotted against the original observed light curve, as shown in Fig. 53.
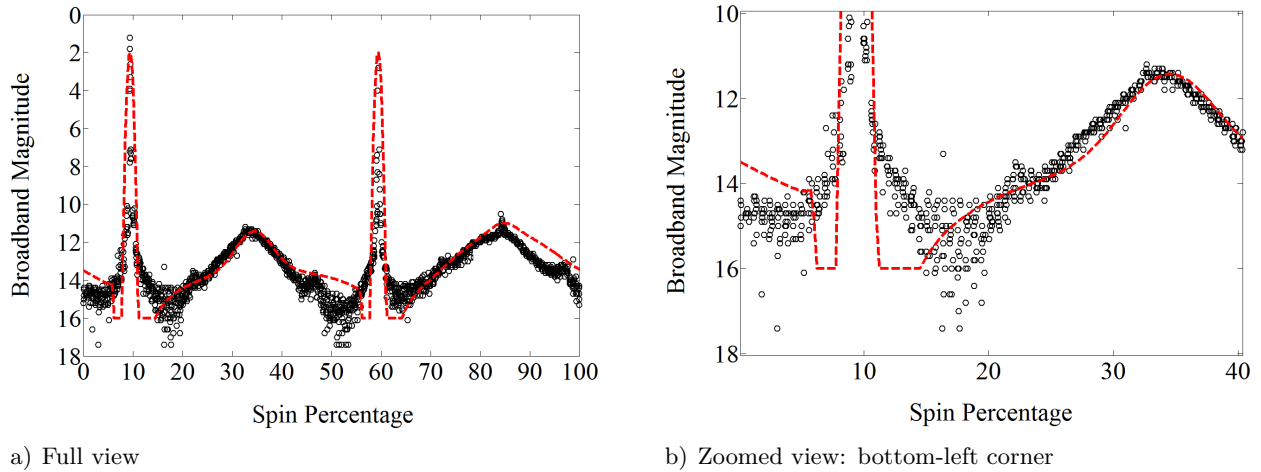

a) Full view

b) Zoomed view: bottom-left corner

Figure 53   Result of least squares fit of simulated light curve to observed light curve

APPENDIX F - Euler's Relations for Rigid Body Rotation

A   Time Derivative of Angular Momentum

An external torque ($\vec{\tau}$) that is applied to a rotating body will change that body's angular momentum ($\vec{L}$), as shown in Eq. (94). The definition of the angular momentum's time derivative is also shown in Eq. (94). At any specific time, the angular momentum vector will have specific coordinates in inertial space and another set of coordinates in the rotating body's body frame. Assuming that the angular momentum vector is constant in inertial space, it cannot be constant in the body frame coordinate system because the body frame is rotating about its angular velocity vector ($\vec{\omega}$), thus giving the body frame coordinates a time dependence. At time t+Δt, the two coordinate systems will not agree as to which $\vec{L}$(t) is the real one. Therefore, the time derivative of the angular momentum will be different in the two different coordinate systems [27, 28].

$$\vec{\tau} = \frac{d\vec{L}}{dt} = \lim_{t \to 0} \left[\frac{\vec{L}(t + \Delta t) - \vec{L}(t)}{\Delta t} \right] \tag{94}$$

The coordinates of the angular momentum (at some specific time t) in both inertial (L_x, L_y, and L_z) and body frame (L_bx, L_by, and L_bxz) coordinate systems are shown in Eq. (95) and Eq. (96), respectively. The subscript b denotes the body frame of reference. Equations (95) and (96) suggest that depending on the reference frame used, the angular momentum vector has two different sets of coordinates. The time derivative of $\vec{L}$ will also be dependent on which reference frame is used, as shown in Eq. (97) and Eq. (98). The superscript b in Eq. (98) denotes that the time derivative is being taken with respect to the rotating body frame reference system.

$$\vec{L}(t) = L_\text{x}\hat{x} + L_\text{y}\hat{y} + L_\text{z}\hat{z} \tag{95}$$

$$\vec{L}(t) = L_\text{bx}\hat{x}_\text{b} + L_\text{by}\hat{y}_\text{b} + L_\text{bz}\hat{z}_\text{b} \tag{96}$$

$$\frac{d\vec{L}}{dt} = \left(\frac{dL_\text{x}}{dt} \right) \hat{x} + \left(\frac{dL_\text{y}}{dt} \right) \hat{y} + \left(\frac{dL_\text{z}}{dt} \right) \hat{z} \tag{97}$$

$$\frac{d^\text{b}\vec{L}}{dt} = \left(\frac{dL_\text{bx}}{dt} \right) \hat{x}_\text{b} + \left(\frac{dL_\text{by}}{dt} \right) \hat{y}_\text{b} + \left(\frac{dL_\text{bz}}{dt} \right) \hat{z}_\text{b} \tag{98}$$

The derivative of Eq. (96) can also be performed with respect to the inertial reference frame, as shown in Eq. (99). Substituting Eq. (98) into Eq. (99) results in Eq. (100).

$$\frac{d\vec{L}}{dt} = \left(\frac{dL_\text{bx}}{dt} \right) \hat{x}_\text{b} + \left(\frac{dL_\text{by}}{dt} \right) \hat{y}_\text{b} + \left(\frac{dL_\text{bz}}{dt} \right) \hat{z}_\text{b} + L_\text{bx} \left(\frac{d\hat{x}_\text{b}}{dt} \right) + L_\text{by} \left(\frac{d\hat{y}_\text{b}}{dt} \right) + L_\text{bz} \left(\frac{d\hat{z}_\text{b}}{dt} \right) \tag{99}$$

$$\frac{d\vec{L}}{dt} = \frac{d^\text{b}\vec{L}}{dt} + L_\text{bx} \left(\frac{d\hat{x}_\text{b}}{dt} \right) + L_\text{by} \left(\frac{d\hat{y}_\text{b}}{dt} \right) + L_\text{bz} \left(\frac{d\hat{z}_\text{b}}{dt} \right) \tag{100}$$

The time derivatives of $\hat{x}_\text{b}$, $\hat{y}_\text{b}$, and $\hat{z}_\text{b}$ are the tangential velocities of the three unit vectors as they rotate about the angular velocity vector $\vec{\omega}$. The unit vectors' magnitudes cannot change over time, because they have magnitudes of unity at all times.

A simple example in which $\vec{\omega}$ is constant and aligned in the same direction as the object's $\hat{z}_\text{b}$ body frame axis is shown in Fig. 54. The time derivatives of the unit vectors are perpendicular to their respective unit vectors. In the case of Fig. 54, the time derivative of $\hat{z}_\text{b}$ is zero since it is aligned with the angular velocity vector $\vec{\omega}$.

Assuming that $\vec{\omega}$ and $\vec{r}$ are perpendicular to each other, the tangential velocity magnitude ($||\vec{v}_\phi||$) is related to the angular velocity magnitude by Eq. (101). The $\vec{r}$ vector is arbitrary in this case. The general case of Eq. (101) is shown in Eq. (102). The tangential velocity shown in Eq. (102) is the same as the time derivative shown in Fig. 54. Therefore, in general, Eq. (103) is true. Equation (100) can therefore be rewritten as Eq. (104) when substituting the unit vector
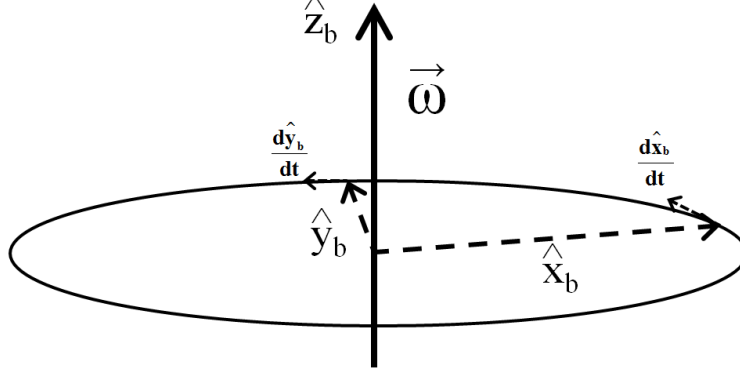
time derivatives with Eq. (103).

Figure 54   Body frame unit vector time derivatives

$$\|\vec{v}_\phi\| = \|\vec{\omega}\| \, \|\vec{r}\| \tag{101}$$

$$\vec{v}_\phi = \vec{\omega} \times \vec{r} \tag{102}$$

$$\frac{d\hat{x}_\mathsf{b}}{dt} = \vec{\omega} \times \hat{x}_\mathsf{b}; \quad \frac{d\hat{y}_\mathsf{b}}{dt} = \vec{\omega} \times \hat{y}_\mathsf{b}; \quad \text{and} \quad \frac{d\hat{z}_\mathsf{b}}{dt} = \vec{\omega} \times \hat{z}_\mathsf{b} \tag{103}$$

$$\frac{d\vec{L}}{dt} = \frac{d^\mathsf{b}\vec{L}}{dt} + L_\mathsf{bx} \left(\vec{\omega} \times \hat{x}_\mathsf{b} \right) + L_\mathsf{by} \left(\vec{\omega} \times \hat{y}_\mathsf{b} \right) + L_\mathsf{bz} \left(\vec{\omega} \times \hat{z}_\mathsf{b} \right) \tag{104}$$

The angular momentum components L_bx, L_by, and L_bz in Eq. (104) can be placed within their corresponding cross products, as shown in Eq. (105). Therefore, the relationship between the time derivatives of angular momentum with respect to an inertial frame and with respect a body frame is shown in Eq. (106).

$$\frac{d\vec{L}}{dt} = \frac{d^\mathsf{b}\vec{L}}{dt} + \left(\vec{\omega} \times L_\mathsf{bx}\hat{x}_\mathsf{b} \right) + \left(\vec{\omega} \times L_\mathsf{by}\hat{y}_\mathsf{b} \right) + \left(\vec{\omega} \times L_\mathsf{bz}\hat{z}_\mathsf{b} \right) \tag{105}$$

$$\frac{d\vec{L}}{dt} = \frac{d^\mathsf{b}\vec{L}}{dt} + \left(\vec{\omega} \times \vec{L} \right) \tag{106}$$

B   Torque and Angular Velocity Components

The fundamental equations for torque ($\vec{\tau}$) and angular momentum ($\vec{L}$) are shown in Eqs. (107) and (108), respectively. Equation (107) is directly related to Eq. (106) through the time derivative of the angular momentum with respect to the inertial reference frame. Equations (107) and (108) can be substituted into Eq. (106) to result in Eq. (109).

$$\vec{\tau} = \frac{d\vec{L}}{dt} \tag{107}$$

$$\vec{L} = \mathbf{I}\vec{\omega} \tag{108}$$

$$\mathbf{I}\frac{d\vec{\omega}}{dt} = \frac{d^\mathsf{b}\mathbf{I}\vec{\omega}}{dt} + (\vec{\omega} \times \mathbf{I}\vec{\omega}) \tag{109}$$

The time derivative of the angular velocity shown in Eq. (109) is the same with respect to both the inertial frame and body frame [28]. The inertia tensor shown in Eq. (109) is only a constant within the body frame of reference (not the inertial frame). Therefore, the entirety of Eq. (109) has to be considered with respect to the body frame so that the inertia tensor can be considered to be constant throughout the analysis.

Treating the inertia tensor as a constant results in Eq. (110). Expanding Eq. (110), which includes taking the cross product, with respect to the three principal rotation axes of the satellite in the body frame, results in Eqs. (111), (112), and (113). In all three cases, the products of inertia were all assumed to be negligible with respect to the principal MOIs, as described in [20].

$$\mathbf{I}\frac{d\vec{\omega}}{dt} = \mathbf{I}\frac{d^b\vec{\omega}}{dt} + (\vec{\omega} \times \mathbf{I}\vec{\omega}) \tag{110}$$

$$\tau_{\mathrm{x}} = I_{\mathrm{xx}}\frac{d\omega_{\mathrm{x}}}{dt} + (I_{\mathrm{zz}} - I_{\mathrm{yy}})\,\omega_{\mathrm{y}}\omega_{\mathrm{z}} \tag{111}$$

$$\tau_{\mathrm{y}} = I_{\mathrm{yy}}\frac{d\omega_{\mathrm{y}}}{dt} - (I_{\mathrm{zz}} - I_{\mathrm{xx}})\,\omega_{\mathrm{x}}\omega_{\mathrm{z}} \tag{112}$$

$$\tau_{\mathrm{z}} = I_{\mathrm{zz}}\frac{d\omega_{\mathrm{z}}}{dt} + (I_{\mathrm{yy}} - I_{\mathrm{xx}})\,\omega_{\mathrm{x}}\omega_{\mathrm{y}} \tag{113}$$

Equations (111), (112), and (113) are the Eulerian relationships describing a rigid body's rotational motion. The components of torque (τ_{x}, τ_{y}, and τ_{z}), as well as the components of the angular velocity (ω_{x}, ω_{y}, and ω_{z}) are all with respect to the principal axes of rotation in the body frame of reference.